University of Nevada, Reno

GPS Imaging of Vertical Land Motion and Earthquake Coseismic Displacements in the GPS Mega-Network

A dissertation submitted in partial fulfillment of the requirements for the degree of Doctor of Philosophy in Geophysics

by

Justine Overacker

Dr. William C. Hammond
Dissertation Advisor

August, 2023

© by Justine Overacker, 2023
All Rights Reserved.

THE GRADUATE SCHOOL

We recommend that the dissertation
prepared under our supervision by

JUSTINE OVERACKER

entitled

GPS Imaging of Vertical Land Motion and Earthquake Coseismic Displacements in the GPS Mega-Network

be accepted in partial fulfillment of the
requirements for the degree of

DOCTOR OF PHILOSOPHY

William C. Hammond, Ph.D.
Advisor

Geoffrey Blewitt, Ph.D.
Committee Member

Corné Kreemer, Ph.D.
Committee Member

John N. Louie, Ph.D.
Committee Member

Anna Panorska, Ph.D.
Graduate School Representative

Markus Kemmelmeier, Ph.D., Dean
Graduate School

August, 2023

Abstract of the Dissertation

The Nevada Geodetic Laboratory's (NGL) Global Positioning Systems (GPS) worldwide data holdings number nearly 21,000 GPS stations that comprise the GPS Mega-Network today. Advances in data processing software, final orbit and clock products, atmospheric modeling, and reference frames have improved the precision and accuracy of GPS positioning solutions to the sub-millimeter level. The rates of change in these GPS position time series can be calculated by the MIDAS robust trend estimator to identify the patterns and styles of crustal deformation. Additionally, the large number of global stations improves the spatial resolution of observable geophysical signals. Together, these improvements helped motivate the GPS Imaging technique, an analysis method that interpolates spatiotemporal GPS trends between stations to construct a crustal velocity field representative of coherent movement of the solid Earth. The research presented in this dissertation uses the GPS Imaging technique to identify and analyze a number of geophysical signals related to vertical land motion and earthquake deformation.

Two studies examine vertical land motion trends in regions of the United States and try to pinpoint the underlying geological sources for their signals. In the first study, GPS Imaging is used to identify the scope and extent of a subsidence signal observed in the Pacific Northwest. This signal is subsiding at approximately –2 mm/year, a rate higher than surrounding subsidence, and is located at latitudes corresponding to the Cascadia subduction zone and approximate longitude of the Cascadia arc. Several methods tested the resolution of GPS Imaging and changes to the regional signal over time. GPS data was then compared to predictions of various hypothesized loading sources that might contribute to the subsidence feature. GPS Imaging and realistic regional geological properties constrained volcanic loading and end loading models. This revealed that both styles of loading matched the width of the subsidence feature. A postseismic relaxation model from the 1700 M9.1 Cascadia Earthquake was compared to the GPS Imaging result, and accounted for approximately half of the subsidence signal concentrated around the Cascadia arc. Glacial isostatic adjustment modeling of the region determined that lithospheric flexure contributes about –1 mm/year of subsidence to the region. By combining the postseismic relaxation and glacial isostatic adjustment models, the subsidence feature was removed, suggesting that these two processes are likely the dominant sources of the subsidence signal. However, climatic and hydrological data compared to vertical land motion trends indicate possible contributions from hydrological loading. This work demonstrates a way to analyze subsidence signals in geologically complex regions, and laid important groundwork for other vertical land motion research.

The second vertical land motion study was located in the Great Plains, United States. Vertical velocity data indicated there was an enigmatic source of regional uplift of approximately ~2 mm/year centered around the Texas Panhandle, with uplift extending through to the surrounding ~670 km x 280 km area. This region is home to the High Plains aquifer, the largest aquifer in the country and a major source of groundwater for agriculture. Water levels for the southern part of the aquifer have declined over 45 m, with greatest declines centered near the Texas Panhandle. Hydrological unloading was

investigated as the principal source of the uplift signal. Climatic and hydrological data indicate a correlation between periods of drought and an increased rate of uplift observed by GPS data in the region. A hydrological unloading model was constrained by GPS Imaging by locating the greatest water mass loss where the uplift signal was ≥1 mm/year. Results indicated that a water volume loss of –5.1 km^3/ year was sufficient to create the uplift signal observed by GPS Imaging, and this unloading rate is substantiated by other estimated rates of High Plains aquifer depletion. Our results indicated that hydrological unloading from aquifer deletion from climatic and anthropogenic influences is causing vertical land motion in the southern High Plains aquifer. This challenges the common conception that aquifer depletion equates to a subsidence signal, and also proves that GPS Imaging can be used as a tool to monitor groundwater changes remotely.

The last study shifts away from regional vertical land motion investigations to apply GPS Imaging to global earthquake research. Some of the ~21,000 GPS stations in GPS Mega-Network are situated in earthquake prone regions experiencing tectonic deformation from plate interactions and/or induced seismicity. Earthquakes captured by the GPS Mega-Network are recorded in GPS time series as immediate discontinuities that represent coseismic displacement. Several different strategies are first tested to estimate coseismic displacements for the NGL. Analysis of coseismic displacements, aided by GPS Imaging, suggests that estimations are improved by a hierarchical strategy and radius of influence used to approximate which stations may be potentially affected by an earthquake. Next, the coverage, completeness, and resolution of coseismic displacements in the GPS Mega-Network is examined using the GPS Global Earthquake Catalog built from the coseismic displacement data. Comparisons of the GPS Global Earthquake

Catalog to the USGS National Earthquake Information Center Earthquake Catalog for events occurring between 1 Jan. 1994–20 Apr. 2022 reveal that the GPS Mega-Network's ability to capture global earthquake activity has increased over time and that the availability of estimated GPS coseismic displacements is greatest for earthquakes $M \geq 7$. Of the 427 earthquakes $M \geq 7$ recorded by the USGS, 93% of earthquakes $7 \leq M < 7.5$ have estimated GPS displacements, and 100% of earthquakes $7.5 \leq M \leq 9.1$ have coseismic displacement data available.

To my grandparents.

Acknowledgements

When I was once again considering an advanced degree, I turned to mentors that have given me perspective throughout my geophysics career both inside and outside of academia: Dr. Wendy Calvin, Dr. Louise Pellerin, and Dr. John Louie. John, in particular, was responsible for telling me about the fully-funded opportunity with the Nevada Geodetic Laboratory (NGL), and he ultimately convinced me to apply for a doctorate by making a compelling argument that a Ph.D. didn't mean I had to become a professor. Lu Pellerin was the exemplary proof of that point, and though she passed away in March this year, she will always be my geophysicist role model and template for success. Thank you all for your abundant advice; you share part of the blame for this, and I am forever indebted.

Of course, none of this would have been possible if the folks at NGL didn't take a chance on me. Before I started at NGL, I had only a rudimentary awareness of GPS geodesy, instead working on near surface exploration geophysics. I appreciate Dr. Bill Hammond, Dr. Geoff Blewitt, and Dr. Corné Kreemer for their passion, patience, and collaboration that propelled me to become the scientist I am today. Many thanks also to Bret Pecoraro for bringing me on field work adventures and training me on hands-on GPS. But foremost, I am grateful to my advisor, Bill Hammond. He has been an artesian well of knowledge, creativity, and enthusiasm. Bill's mentorship gave me the freedom to exercise my curiosity and try new things with this research. His acceptance allowed me space to grow during summer internships, at conferences, and routinely got me out into the field. "Justine follows her own path…" Thank you for your understanding and for being a continued beacon of inspiration and guidance.

Additionally, I would like to extend my appreciation to all the members of my committee, Drs. Bill Hammond, Geoff Blewitt, Corné Kreemer, John Louie, and Anna Panorska. I especially want to thank Anna for stepping out of her mathematical comfort zone to take on the challenge of geophysics. I know it's been an adjustment, and I appreciate all the efforts you've made to learn about our strange and exciting world.

My transition from industry back to student life was made much easier by the graduate student friends I made during my time at University of Nevada, Reno (UNR), starting with my office mates in the NGL. Aren Crandall-Bear, Meredith Kraner, Nina Miller, Eduard Nastase, and Zack Young made the last 7 years a joy by sharing much more than space with me. The ups and downs of this journey were celebrated and commiserated with all of you over the course of our time together. Many other faculty members and graduate students in my cohort made this second go-around at UNR a pleasure, but I would specifically like to acknowledge Ph.D. students Heather Winslow, Sarah Trubovitz, Pooja Sheevam, Michelle Scalise, Ian Pierce, Drew Levy, Kurt Kraal, Ellyn Huggins, Scott Feehan, and Conni De Masi. I have been blessed along the way to befriend many other geoscientists outside UNR during this time, and I would be remiss if I failed to properly mention Sean Malloy and Justin Rittgers from the 2018 UNAVCO and 2019 US Bureau of Reclamation internships respectively. What do we say to imposter syndrome?! NOT TODAY.

I must also thank my non-geoscience inner circle who have watched me in bewildered amazement during this whole process and have supported me nonetheless with their love: Surachany, Seth, Ashley, and Sasha; my siblings Karina and Joe, my parents Jan and Steve, my aunts and uncles, and particularly my Grandma Marilyn. I've heard a dozen times that some of you guys (still??) have no idea what I'm doing, but having you in my cheering section makes a world of difference anyway. And though it may seem silly to acknowledge my dogs, the endless affection from Shelby and Rex kept me grounded throughout this process, especially during the COVID-19 pandemic. I honestly couldn't have done this without them. Rest in peace, Shelby.

Saving the best for last, words cannot adequately express the depths of gratitude I have for my loving husband and partner Colin. Colin, you always encourage me to follow my cockamamie dreams and you are a sustaining force in every possible way while I achieve them. You are my rock… and we all know how much I love rocks. And though you will disagree with me in a very self-deprecating way out of pure modesty, none of this would've been possible if you weren't by my side. From the bottom of my heart, thank you for being the anchor that keeps this Trusty Shellback from floating adrift.

Table of Contents

List of Tables

List of Figures

1

Introduction

1.1 Identifying Spatiotemporal Signals of Active Earth Processes with GPS Imaging

Global Positioning Systems (GPS) record the position of the station in east, north, and up directions. Trends in positioning data over time uncover motion of the Earth's crust and, when combined with data from other nearby GPS stations, can reveal regional spatiotemporal patterns of crustal deformation. The Nevada Geodetic Laboratory (NGL) processes data for ~21,000 GPS stations worldwide that comprise the GPS Mega-Network (Blewitt et al., 2018). The distribution of GPS stations in the global network enhances the spatial resolution of observable geophysical signals. This improved resolution helps identify underlying geologic processes at the source of crustal deformation. Aiding these crustal motion investigations are advances in data processing (Bertiger et al., 2020; Kreemer et al., 2020) and revisions to global reference frames (Altamimi et al., 2016) that improve the precision and accuracy of GPS positioning solutions to the sub-millimeter level. The MIDAS robust trend estimator further improves accuracy and reduces uncertainties by estimating crustal velocities that are insensitive to the effects of outliers, seasonality, and undocumented displacements caused by earthquakes or equipment changes (Blewitt et al., 2016).

Together, these improvements are incorporated into the GPS Imaging technique, an analysis method that interpolates spatiotemporal GPS trends between stations to construct a velocity field of crustal motions representative of coherent movement of the solid Earth. In recent studies, NGL applied the vast GPS Mega-Network and the GPS Imaging technique to locate and reveal geodynamic processes such as drought accelerated tectonic uplift (e.g., Hammond et al., 2016), strain rates and velocities from glacial isostatic adjustment (e.g., Kreemer et al., 2018), and contributions of vertical land motion to global sea-level rise (e.g., Hammond et al., 2021). The potential applications for the GPS Imaging technique are as expansive as the GPS Mega-Network itself.

In this dissertation, I explore different applications of the GPS Imaging technique using stations within the GPS Mega-Network. Two vertical land motion studies investigate enigmatic geophysical signals in active and in relatively stable geologic provinces in the United States. The third study uses global earthquake data collected by the GPS Mega-Network to design a database of coseismic displacements, testing displacement estimation strategies with GPS Imaging. These studies are summarized in the following section.

1.2 Summary of Dissertation Chapters

1.2.1 Cascade Arc Subsidence in the Pacific Northwest United States

In Chapter 2, I describe the capabilities of GPS Imaging by applying it to understand the source of a downward vertical signal centralized in the Pacific Northwest United States interior. The subsidence signal of interest is approximately double the rate of surrounding regional subsidence at around –2 mm/year, and the pattern, though diffuse near the state border of Washington and Oregon, is approximately located along the Cascade Arc. The Pacific Northwest is at the convergence of the Juan de Fuca and North

American plates, and as such experiences tectonism and volcanism related to the motion and melt of the subducting oceanic plate that can cause crustal deformation (Orr and Orr, 2002). Additionally, Cascadia experienced a M9.1 megathrust earthquake in 1700 that may still be affecting crustal motions today (Pollitz et al., 2008). Though the Cascadia subduction zone geologic processes might seem like the obvious sources of the subsidence signal, this active and complex region not only undergoes crustal deformation from plate tectonics. In the Late Pleistocene, the Laurentide and Western Cordilleran ice sheets melted rapidly (Orr and Orr, 2002), causing present day glacial isostatic adjustment (GIA). The northern part of the study area in Canada flexes the lithosphere approximately south of the Canadian border downward (Peltier et al. 2015; Peltier et al., 2018; Argus et al. 2014) by a process called forebulge collapse (Watts, 2001). Additionally, proximity to the ocean and high topographic relief creates a cool, wet climate which can cause vertical land motions from cyclical loading from orographic precipitation and snowpack (Fu et al., 2015). I examine each of these possible loading signals in an attempt to distinguish how they might contribute to the spatiotemporal patterns of the subsidence feature.

To understand the vertical land motion of the Pacific Northwest, I first create a regional vertical velocity field with GPS Imaging. I examine the extent of the feature and compare velocity profiles with latitude transects of topographic features. I also test the resolution of the GPS Imaging result to ensure the subsidence feature is not adversely affected by GPS station spacing. Models of GIA are also compared to the GPS Imaging result to determine if and how GIA contributes to the subsidence signal. GIA models contribute a widespread signal of subsidence in the Pacific Northwest area, but its fastest subsidence is not geographically concentrated along the Cascade Arc. Climate data for districts approximately overlapping the subsidence feature and hydrological time series help define wet and dry patterns to investigate how the subsidence feature changes during early, middle, and late time periods. Results show that the swath of subsidence is shrinking and the rate is decreasing over time. Plate flexure models for volcanic loading and end loading from a subducting plate are tested against the width of the subsidence feature identified by GPS Imaging. These results indicate that the volcanic and end loading models create signals that are predicted to be within the range required to create the subsidence signal. Lastly, a postseismic relaxation model for the 1700 Cascadia megathrust earthquake was compared to GPS observations. The geographic extent of the subsidence signal is concentrated along the Cascade Arc, and residual rates of subsidence were approximately of the same rate as the GIA model. Combining the postseismic and GIA models solved for nearly the entirety of the subsidence signal of interest, though the other possible sources tested could minorly contribute to the subsidence feature as well.

Portions of this material or previous iterations of this project were presented at the 2017 EarthScope National Workshop (Overacker et al., 2017a), 2017 American Geophysical Union (AGU) Annual Meeting (Overacker et al., 2017b), 2018 UNAVCO Science Workshop (Overacker et al., 2018), and 2019 International Union of Geodetic Geophysicists Conference (Overacker et. al, 2019). I performed analysis, authored the main text, and produced all the figures herein. Bill Hammond supervised this research and assisted with programming by providing me with vital GPS Imaging scripts (Hammond et al., 2016), access to and the scripts for MIDAS time series analysis (Blewitt et al., 2016), checkerboard test script, GIA modeling scripts (Peltier et al. 2015;

Peltier et al., 2018; Argus, Peltier, et al. 2014), GRACE mass concentration script (Loomis et al., 2019), GMT scripts and files for topography and plate boundaries (Bird, 2003), and direction for loading models (Turcotte and Schubert, 2002). Additionally, he contributed substantial editorial advice. Zachary Young provided the 1700 M9.1 Cascadia postseismic positioning time series model from Pollitz et al. (2008) and provided advice on the model results. Geoff Blewitt and Corné Kreemer also reviewed presented materials and provided comments and edits that this research benefited from. Program troubleshooting was made possible throughout much of the earlier iterations of this research by the generosity and patience of Meredith Kraner and Eduard Nastase.

1.2.2 Vertical Land Motion of the High Plains Aquifer Region of the United States: Effect of Aquifer Confinement Style, Climate Variability, and Anthropogenic Activity

In Chapter 3, I build upon lessons learned in Chapter 2 to investigate an enigmatic signal of vertical uplift located in the southern Great Plains of the United States. The pattern and extent of the vertical land motion observed by GPS Imaging correlates with the southern extent of the High Plains aquifer. This region of the aquifer has witnessed significant declines in aquifer levels in the past century, over 45 m in areas located near the highest rate of uplift (McGuire, 2017), and an estimated 330 km^3 of water volume was removed between 1950 and 2007 (Scanlon et al., 2012). Commonly, vertical land motion signals related to aquifer depletion are associated with subsidence owing to poroelastic contraction and/or compaction. Here, we investigate whether this uplift could be associated with a different mechanism: elastic unloading caused by the loss of mass associated with aquifer depletion.

To understand the possible relation between the uplift and the aquifer, I use GPS, geologic, satellite gravity, hydrologic, and climate data to understand what drives the spatial and temporal patterns of the observed GPS signals. The High Plains aquifer is divided into northern and southern regions because the signals of vertical land motion are very different. GPS Imaging is used to create uplift maps from GPS data for the regional vertical land motion trend, seasonality, and early and late period testing which uses Palmer Drought Severity Index (PDSI) climate data as an analog for wet and dry seasons. These maps are compared to the equivalent water height spatiotemporal data from Gravity Recovery and Climate Experiment (GRACE), which measures gravity perturbations from the changing distribution of water mass, to determine whether the uplift signal can be attributed to seasonal and/or long-term hydrological unloading. GPS time series are compared to GRACE time series and PDSI time series intersecting with and within the High Plains aquifer boundary to examine vertical land motion trends and compare them to water mass and climate trends. Well data serve as an indicator of the impact of human activities on the aquifer. Finally, we use GPS Imaging to create a simplified model to estimate how much water mass would be required to cause the uplift signal. The findings indicate that a water volume loss of –5.1 km^3/year is sufficient to cause the observed uplift.

This material was published by: Overacker, J., Hammond, W. C., Blewitt, G., & Kreemer, C. (2022). Vertical Land Motion of the High Plains Aquifer Region of the United States: Effect of Aquifer Confinement Style, Climate Variability, and

Anthropogenic Activity. *Water Resources Research*, *58*(6), e2021WR031635, https://doi.org/10.1029/2021WR031635. For this project, I identified the uplift signal, performed analysis and interpretation of signals using GPS, GRACE, hydrological, and climatic data, and designed the unloading model for the uplift signal. I authored the main text and made all figures except for Figure 3.15 (McGuire, 2017) which beautifully demonstrates how groundwater levels have changed in the High Plains aquifer.

Throughout the project, Bill Hammond provided invaluable guidance and revisions that helped craft the initial vision of this project into its final published product. Additionally, he shared template GPS Imaging scripts (Hammond et al., 2016) for vertical trends, seasonality, checkerboard tests, and the glacial isostatic adjustment model (Peltier et al. 2015; Peltier et al., 2018; Argus, Peltier, et al. 2014), as well as the GRACE mascons (Loomis et al., 2019) and the LoadDef (Martens et al., 2019) unloading models. Geoff Blewitt and Corné Kreemer assisted greatly by brainstorming with me during the early stages of the project and contributing edits to the manuscript. Additionally, reviews by Donald Argus, Manoo Shirzaei, an anonymous reviewer, and the Associate Editor Kamini Singha helped improve the manuscript. Special thanks to Scott McCoy for sharing the Google Earth file with the High Plains aquifer boundaries from research by Willett et al., 2018, Rina Schumer for discussions on aquifer mechanics, and to Zachary Young for helping me build the initial loading model.

1.2.3 Coverage, Completeness, and Resolution of Coseismic Displacements in the GPS Mega-Network Global Earthquake Catalog

In Chapter 4, I diverge from the previous track of using GPS Imaging to examine vertical land motion signals and instead apply the algorithm directly towards earthquake science. The Nevada Geodetic Laboratory (NGL) collects GPS data from many networks globally. I refer to all the stations collectively as the GPS Mega-Network. When a station within the network experiences an earthquake, coseismic displacement presents on the GPS time series as an immediate discontinuity in the position time series. These coseismic displacements can provide information on the scope, style, and direction of crustal deformation which can help refine the properties of the earthquake. Coseismic displacements can also be used as a correction factor when studying subtle signals of crustal deformation, and/or as an indicator of GPS station stability when defining accurate reference frames. The NGL estimates coseismic displacements for the GPS Mega-Network after each earthquake event. Here, I design a method to calculate the displacements in part using GPS Imaging. I evaluate how the completeness of the GPS Mega-Network Global Earthquake Catalog, comprised of the coseismic displacement estimates, compares to that of the USGS National Earthquake and Information Center (NEIC) Earthquake Catalog. I consider all earthquakes with M≥5.5 that occurred between 1 Jan. 1994 and 20 Apr. 2022. This provides insight into spatiotemporal patterns of coverage, completeness, and resolution for the ability of the GPS Mega-Network to capture earthquake deformation over time.

I first define two basic methods for estimating coseismic displacements, the Data Near Event (DNE) and the Time Series Model (TSM). I develop a model hierarchy that applies displacement estimation strategy according to the data content of each station affected by a given earthquake event. Then I define the radius of influence equation which is used to flag GPS stations near the earthquake epicenter for displacement estimation. I use GPS Imaging to interpolate horizontal displacement magnitudes surrounding the event to characterize the fall off of displacement with distance from the epicenter. Finally, I compare the USGS NEIC Earthquake Catalog with the database constructed from 20,224 stations worldwide, 7,486 of which are affected by the 14,059 earthquakes worldwide and account for 63,122 displacement estimates flagged for potential coseismic deformation that comprise the GPS Mega-Network Global Earthquake Catalog. These findings improve displacement estimates for GPS stations affected by earthquakes worldwide and illuminate how far the GPS Mega-Network has come at capturing earthquake information as well as paths for improvement going forward.

For this project, I designed and tested the DNE estimation strategy and the radius of influence. I also built the GPS Mega-Network Global Earthquake Catalog and performed comparative analysis. I authored the main text and made all figures except for Figure 4.2, which was contributed by Bill Hammond, and Figure 4.4 which was generated by the NGL (Blewitt et al., 2018).

This chapter would not have been possible without the joint efforts of the NGL. This research builds on ideas that were put into place as an operational requirement of the GPS Mega-Network. The Time Series model and the original radius of influence which keeps track of potential coseismic displacements on the NGL website (http://geodesy.unr.edu/NGLStationPages/steps.txt) using USGS NEIC data were originally proposed by Bill Hammond, who recognized a need for a refined estimation strategy so the NGL can develop a publicly accessible data product. The incredible amount of data is largely due to the efforts of Corné Kreemer who, in part, amasses the database from networks in the GPS Mega-Network and keeps them up to date. The data processing and development of algorithms is done by Geoff Blewitt. This research brings systematic coseismic displacement data products close to being available to the broader community.

I was able to devise and refine the strategies described in Chapter 4 with Bill Hammond's continual advice and support. He provided me with an early version of a script that I developed to deploy the DNE model, the GMT scripts used to plot the GPS Mega-Network, and the GPS Imaging script that was adapted from vertical land motion into the horizontal displacement magnitude maps. He also made copious comments and edits on the chapter manuscript for submission to a peer-reviewed journal in the near future. Some of this research and figures were previously presented at the 2020 and 2021 AGU Annual Meetings (Overacker et al., 2020; Overacker et al., 2021) and GAGE-SAGE Community Workshop meetings (Overacker et al., 2021); many thanks for the reviews and edits by Bill Hammond, Corné Kreemer, and Geoff Blewitt during that time that helped contribute to this project. Finally, much gratitude to David Phillips for hiring me to develop much of this work in partnership with the NGL during my 2018 UNAVCO USIP summer internship.

1.3 References

Altamimi, Z., Rebischung, P., Métivier, L., & Collilieux, X. (2016). ITRF2014: A new release of the International Terrestrial Reference Frame modeling nonlinear station motions. *J. Geophys. Res. - Solid Earth*, *121*(8), 6109-6131.

Argus, D. F., Peltier, W. R., Drummond, R., & Moore, A. W. (2014). The Antarctica component of postglacial rebound model ICE-6G_C (VM5a) based on GPS positioning, exposure age dating of ice thicknesses, and relative sea level histories. *Geophysical Journal International*, *198*(1), 537-563.

Bertiger, W., Bar-Sever, Y., Dorsey, A., Haines, B., Harvey, N., Hemberger, D., et al. (2020). GipsyX/RTGx, a new tool set for space geodetic operations and research. *Advances in Space Research*, *66*(3), 469–489, https://doi.org/10.1016/j.asr.2020.04.015.

Bird, P. (2003). An updated digital model of plate boundaries. *Geochemistry, Geophysics, Geosystems*, *4*(3).

Blewitt, G., Kreemer, C., Hammond, W.C., & Gazeaux, J. (2016). MIDAS Robust Trend Estimator for Accurate GPS Station Velocities Without Step Detection. *J. Geophys. Res. - Solid Earth*, *121*(3), 2054-2068, https://doi.org/10.1002/2015JB012552.

Blewitt, G., Hammond, W.C., & Kreemer, C. (2018). Harnessing the GPS data explosion for interdisciplinary science. *Eos*, *99*, https://doi.org/10.1029/2018EO104623.

Fu, Y., Argus, D. F., & Landerer, F. W. (2015). GPS as an independent measurement to estimate terrestrial water storage variations in Washington and Oregon. *J. of Geophys. Res. - Solid Earth*, *120*(1), 552-566.

Hammond, W. C., Blewitt, G., & Kreemer, C. (2016). GPS Imaging of vertical land motion in California and Nevada: Implications for Sierra Nevada uplift. *J. Geophys. Res. - Solid Earth*, *121*(10), 7681–7703, https://doi.org/10.1002/2016JB013458.

Hammond, W. C., Blewitt, G., Kreemer, C., & Nerem, R. S. (2021). GPS imaging of global vertical land motion for studies of sea level rise. *J. of Geophys. Res. - Solid Earth*, *126*(7), e2021JB022355.

Kreemer, C., Blewitt, G., & Davis, P. (2020). Geodetic evidence for a buoyant mantle plume beneath the Eifel volcanic area, NW Europe. *Geophysical Journal International*, *222*(2), 1316–1332, https://doi.org/10.1093/gji/ggaa227.

Kreemer, C., Hammond, W. C., & Blewitt, G. (2018), A robust estimation of the 3-D intraplate deformation of the North American plate from GPS. *J. Geophys. Res. - Solid Earth*, *123,* 4,388–4,412, https://doi.org/10.1029/2017JB015257.

Loomis, B. D., Luthcke, S. B., & Sabaka, T. J. (2019). Regularization and error characterization of GRACE mascons. *Journal of Geodesy*, *93*, 1381–1398, https://doi.org/10.1007/s00190-019-01252-y.

Martens, H. R., Rivera, L., & Simons, M. (2019). LoadDef: A Python-based toolkit to model elastic deformation caused by surface mass loading on spherically symmetric bodies. *Earth and Space Science*, *6*(2), 311-323.

McGuire, V. L. (2017). Water-level and recoverable water in storage changes, High Plains aquifer, predevelopment to 2015 and 2013–15. *Scientific Investigations Report*, https://doi.org/10.3133/sir20175040.

Orr, W. N., & Orr, E. L. (2006). *Geology of the Pacific Northwest*, p. 2-18. Waveland Press.

Overacker, J., Hammond, W. C., Blewitt, G., & Kreemer, C. (2022). Vertical Land Motion of the High Plains Aquifer Region of the United States: Effect of Aquifer Confinement Style, Climate Variability, and Anthropogenic Activity. *Water Resources Research*, *58*(6), e2021WR031635, https://doi.org/10.1029/2021WR031635.

Overacker, J., Hammond, W. C., Blewitt, G., & Kreemer, C. (Mar. 2018). *Investigating Vertical Deformation in the Interior Pacific Northwest with GPS Imaging*. UNAVCO Science Workshop, Broomfield, CO.

Overacker, J., Hammond, W. C., Blewitt, G., & Kreemer, C. (Jul. 2019). *GPS Imaging and Interpretation of Vertical Motion of the Cascade Arc*. International Union of Geodetic Geophysicists, Montréal, Canada.

Overacker, J., Hammond, W.C., Kraner, M.L., & Blewitt, G. (May 2017). *GPS Imaging of Vertical Land Motions in the Pacific Northwest.* EarthScope National Meeting, Anchorage, AK.

Overacker, J., Hammond, W.C., Kraner, M.L., & Blewitt, G. (Dec. 2017). *Using GPS Imaging to Unravel Vertical Land Motions in the Interior Pacific Northwest*. Fall American Geophysical Union Meeting, New Orleans, LA. https://agu.confex.com/agu/fm17/meetingapp.cgi/Paper/233457.

Overacker, J., Hammond, W.C., Kreemer, C., & Blewitt, G. (Dec. 2020). *Exploring the Limits of Earthquake Offset Detection in GPS Geodesy*. Poster session presented virtually at American Geophysical Union Meeting.

Overacker, J., Hammond, W.C., Kreemer, C., & Blewitt, G. (Aug. 2021). *Evaluating a Global Dataset of GPS Earthquake Offsets for Catalog Completeness*. E-Lightning poster session presented virtually at GAGE/SAGE Community Science Workshop.

Overacker, J., Hammond, W.C., Kreemer, C., & Blewitt, G. (Dec. 2021). *Capturing Global Earthquakes with the GPS Mega-Network*. Presented at G21A-05 session, American Geophysical Union Meeting, New Orleans, LA, https://youtu.be/dmBfYn8W0-o.

Peltier, W. R., Argus, D. F., & Drummond, R. (2015). Space geodesy constrains ice age terminal deglaciation: The global ICE-6G_C (VM5a) model. *J. Geophys. Res. – Solid Earth*, *120*, 450–487, https://doi.org/10.1002/2014JB011176.

Peltier, W.R., Argus, D. F., & Drummond, R. (2018). Comment on "An assessment of the ICE-6G_C (VM5a) glacial isostatic adjustment model" by Purcell et al. *J. Geophys. Res. – Solid Earth*, *123*(2), 2019-2028.

Pollitz, F. F., McCrory, P., Svarc, J., & Murray, J. (2008). Dislocation models of interseismic deformation in the western United States. *J. of Geophys. Res. – Solid Earth*, *113*(B4), B04413-n/a, https://doi.org/10.1029/2007JB005174.

Scanlon, B. R., Faunt, C. C., Longuevergne, L., Reedy, R. C., Alley, W. M., McGuire, V. L., & McMahon, P. B. (2012). Groundwater depletion and sustainability of irrigation in the US High Plains and Central Valley. *Proceedings of the national academy of sciences*, *109*(24), 9320-9325.

Turcotte, D. L., & Schubert, G. (2002). *Geodynamics*, p. 123-129. Cambridge, United Kingdom: Cambridge University Press.

Watts, A. B. (2001). *Isostasy and Flexure of the Lithosphere*, p. 114-121. Cambridge, United Kingdom: Cambridge University Press.

Willett, S. D., McCoy, S. W., & Beeson, H. W. (2018). Transience of the North American High Plains landscape and its impact on surface water. *Nature*, *561*(7724), 528-532.

2

Cascade Arc Subsidence in the Pacific Northwest United States

2.1 Abstract

I construct a vertical land motion velocity field of the Pacific Northwest United States using data from 648 GPS stations. The result shows a 50–250 km wide swath of nearly –2 mm/year subsidence that approximately spans Cascade Arc longitudes and the length of the Cascadia subduction zone. I model several possible sources for the subsidence feature. Climatic and hydrological data indicate limited contribution to the subsidence. Glacial isostatic adjustment models identify a probable source of subsidence, though they do not fully explain the signal rate or pattern. I use the vertical velocity field as a constraint for plate scale modeling. Numerical modeling of volcanic loading and end loading from Juan de Fuca plate subduction suggest that both possibly contribute to downward motion. Lastly, I model postseismic relaxation from the 1700 M9.1 Cascadia Earthquake. The result shows a north-south extent of subsidence concentrated along the Cascade Arc and, when this model was combined with the glacial isostatic adjustment model, the subsidence feature was completely removed. The combination of these postseismic relaxation and glacial isostatic adjustment geophysical processes best explains the observed subsidence signal.

2.2 Introduction

Seismicity and interseismic strain related to the Cascadia subduction zone (Fig. 2.1) actively deforms the surrounding crust (Burgette et al., 2009; Mazzotti et al., 2002).

Further inland, volcanism born from the subducting Juan de Fuca plate causes magmatic inflation (Dzurisin et al., 2009) and creates new topography from eruptive events in the Cascade Arc (Lisowski et al., 2008) (Fig. 2.1). The Global Positioning System (GPS) is used to track active strain rates and locking of the plate interface to characterize seismic (McCaffrey et al., 2007; Schmalzle et al., 2014; Pollitz & Evans, 2017; Savage, 1983; Wang et al., 2003) and volcanic (Chang et al., 2010; De Martino et al., 2021; Dixon et al., 1997) hazards, as well as understand how geologic processes contribute to vertical crustal deformation signals today (Mazzotti et al., 2007; Mazzotti et al., 2008; Montillet et al., 2018). More generally, geodetic data can reveal spatiotemporal patterns in vertical land motion that can elucidate underlying sources of the movement occurring at different geologic time scales (Pfeffer et al., 2017). GPS time series can track loading and unloading cycles of overlapping crustal deformation signals on time scales from seasonal (e.g., Fu et al., 2015), to hundreds of years for the seismic cycle (e.g., Burgette et al., 2009), thousands of years for glacial isostatic adjustment (GIA) (e.g., Peltier et al., 2015), and millions of years for tectonic processes (e.g., Zhao et al., 2023).

Here, I attempt to document the existence and characteristics of a subsidence signal with a maximum rate of approximately –2 mm/year detected with GPS data from 648 Pacific Northwest GPS stations (Fig. 2.1) primarily from the EarthScope Network of the Americas (NOTA) and Pacific Northwest Geodetic Array (PANGA). I construct an image of vertical velocity trends in the region using the Nevada Geodetic Laboratory's (NGL) MIDAS trend estimator that locates this subsidence feature with an increased rate roughly corresponding to the longitude of the Cascade Arc and in latitudes along the entire Cascadia subduction zone.

I evaluate potential loading sources that may cause this subsidence by comparing the predictions of various models to the characteristics of the subsidence feature identified by GPS. I investigate whether plate flexure from subduction zone loading or volcanic loading are viable sources by comparing the observed subsidence signal to modeled predictions based on a range of values for flexural rigidity and other realistic mechanical properties of the lithosphere.

I also investigate the effect that postseismic relaxation from the 1700 Cascadia megathrust earthquake has on the observed vertical land motion rates and patterns. Vertical positions of postseismic motion were obtained from the Pollitz et al. (2008) model following methods by Young et al. (2023) for the estimated M9.1 earthquake. The model of postseismic vertical land motion is then interpolated into a velocity field for direct comparison with the GPS vertical velocities.

There are other contributors to the observed subsidence signal that must also be considered, however. Specifically, I examine whether climate trends from hydrological loading in the Cascade Arc and back-arc basins might explain the downward vertical motion of interest. I identify wet and dry periods with Palmer Drought Severity Index (PDSI) data and compare signals during these periods to Gravity Recovery and Climate Experiment (GRACE) and GPS spatiotemporal patterns to understand how the subsidence signal might fluctuate in different climate conditions.

Additionally, I consider possible subsidence effects from forebulge collapse associated with glacial isostatic adjustment (GIA). This occurs because of mantle flow returning the lithosphere to glacio-isostatic balance in affected areas in northern latitudes of North America after Late Pleistocene deglaciation. The process flexes the lithosphere downward in southern latitudes to compensate for uplift near the ice depocenter (Watts, 2001; Sella et al., 2007). The ICE-6G D (VM5a) GIA model (Peltier et al. 2015; Peltier et al., 2018; Argus, Peltier et al. 2014) is compared with the GPS vertical velocity field to assess whether the subsidence pattern can be explained from postglacial rebound to the north.

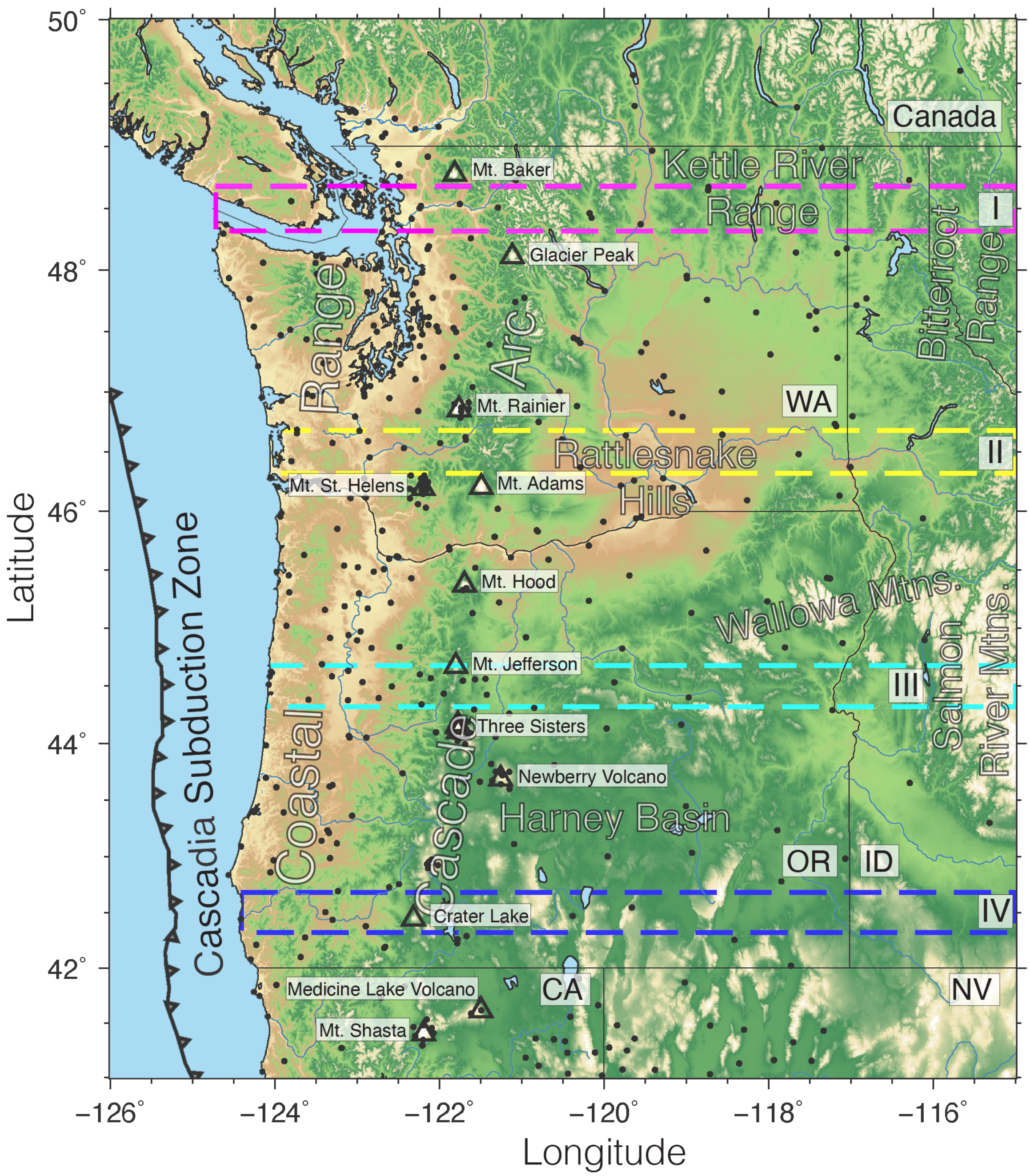

Figure 2.1. Map view of the Pacific Northwest study area. GPS stations (black circles) are displayed along with geologic and topographic features of interest, including the Cascadia subduction zone (gray triangles offshore) (Bird, 2003) and Cascade Arc volcanoes (black triangles). Constant-latitude transects used for topographic and velocity

profiles (see Analysis 2.4.3) are denoted by dashed, colored rectangles and identified by roman numerals I–IV.

2.3 Data

2.3.1 GPS Data

GPS vertical component time series with a minimum 3-year time series duration located in the Pacific Northwest United States between –126º to –115º longitude and 41º to 50º latitudes were obtained for 648 GPS stations from the NGL open access archive (Sup. Table S2.1) (Blewitt et al., 2018). The archive contains data from an amalgamation of several networks, though most GPS time series in this study were collected from the Pacific Northwest Geodetic Array (PANGA), Network of the America's (NOTA), and the United States Geological Survey (USGS) Cascades Volcano Observatory (CVO) networks. RINEX data were processed from the earliest data available from each individual station through 3 Jun. 2023. The longest running station ALBH near Victoria, British Columbia was active 9 Mar. 1994.

This study used the IGS14 reference frame, and the calculated rates are referenced to the IGS14 origin which is approximately the center of Earth mass (Altamimi et al., 2016). The processing used the Jet Propulsion Laboratory's (JPL) GipsyX 1.0 software and JPL's final orbit and clock products when calculating positioning solutions (Bertiger et al., 2020). Atmospherically-induced signal delays, which can impact estimates of vertical positions, were modeled and estimated using the Vienna Mapping Function (VMF1) with gridded a priori data taken from European Center for Medium-Range Weather Forecasts (ECMWF) models (Boehm et al., 2006). For further GPS processing details, see Kreemer et al. (2018, 2020).

2.3.2 Gravity Recovery And Climate Experiment Data

Gravity Recovery and Climate Experiment (GRACE) data measure gravity variations caused by the changing distribution of surface mass on the Earth, primarily related to the redistribution of water (Dunbar, 2013). To determine how changes in surface hydrological mass loading might affect the subsidence signal, Goddard Space Flight Center (GSFC) GRACE solutions were used to extract finer geographic resolution from gravity results. Hydrological trends illustrative of the hydrological loading component to the vertical signal were calculated from GRACE and GRACE Follow-On satellite gravity data (Loomis et al., 2019) which began 17 Apr. 2002 through 15 Nov. 2022 (Sup. Table S2.2). Best-fit trends for 76 mass concentrations (mascons) located in the Pacific Northwest study area were estimated using simple linear regression to fit a first-degree polynomial within a 95 percent confidence interval (Fig. 2.2).

Gravity trend results are subject to anisotropic spatial filtering (Han et al, 2005; Chen et al., 2005; Swenson and Wahr, 2006) and as such are only sensitive to wavelengths on par with the mascon size. Variations in spatial resolution between gravity solutions could potentially obscure details of regional gravity trends. The mascon size for the GSFC solutions is 1 x 1 arc-degrees, approximately 111 km x 79 km, but they are derived from 3 x 3 arc-degrees JPL mascons and as such are highly spatially correlated (Luthcke et al., 2013).

Hydrological loading predictions from the JPL GRACE mascon-based model (Argus et al., 2022) available through NGL station pages (e.g., the masc columns for GOBS: http://geodesy.unr.edu/gps_timeseries/tenv3_loadpredictions/GOBS.tenv3) are subtracted from the vertical positioning data. For further details on the hydrological loading models, see Argus et al. (2022). Additionally, the effects of non-tidal atmospheric and ocean loading in the GPS positioning data are corrected by subtracting the predictions of their displacement signal from the ECMWF 24-hour terrestrial water storage global hydrological model available from http://rz-vm115.gfz-potsdam.de:8080/repository (Dill and Dobslaw, 2013; Dill, 2008).

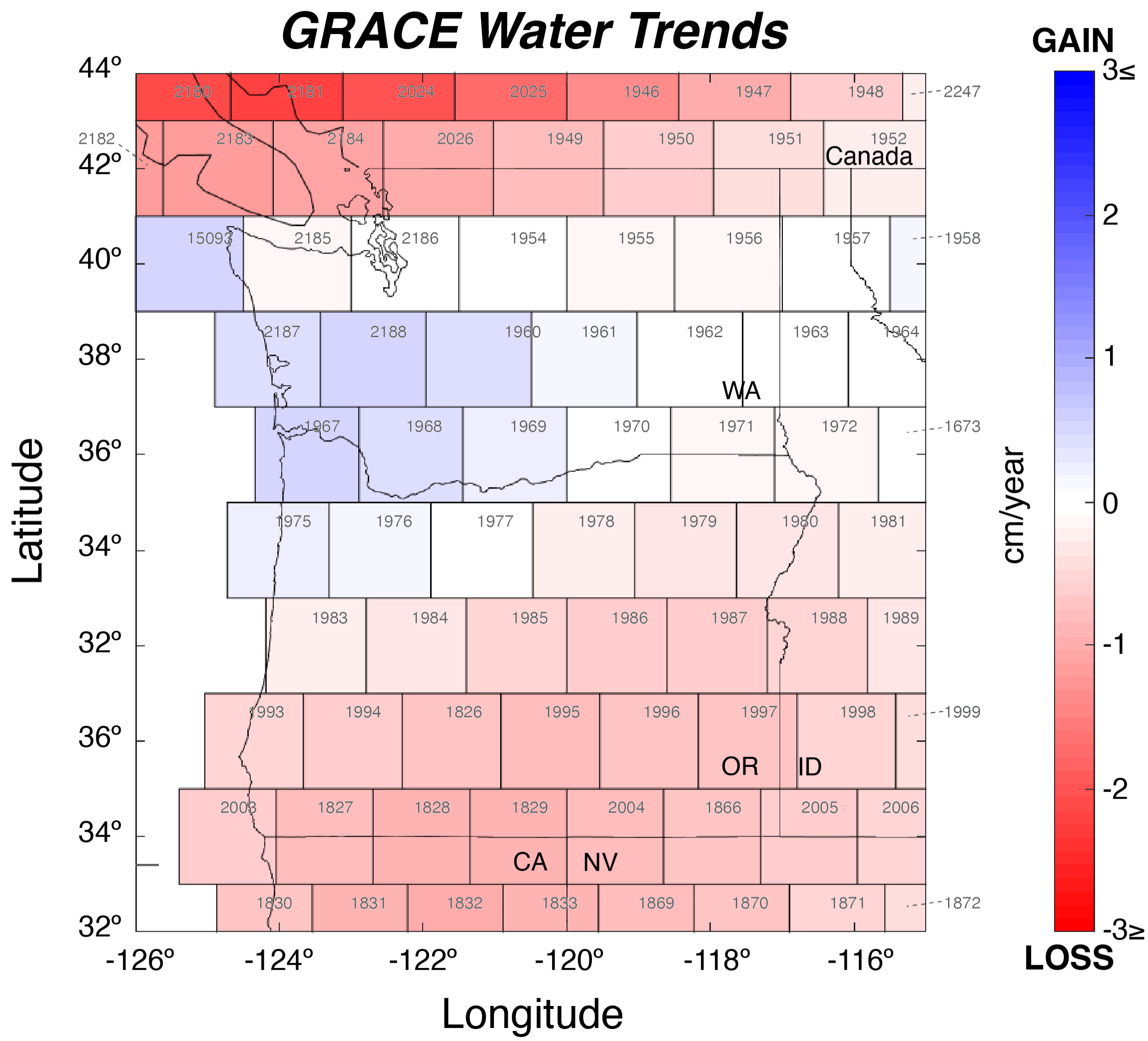

Figure 2.2. GSFC GRACE (Luthcke et al., 2013) gravity trends displaying change in equivalent water height in cm/year in 1 arc-degree mascon size, an area ~111 km x 79 km. These results are sensitive to wavelengths on par with the mascon size. Solutions show overall decreasing gravity trend for the Pacific Northwest.

2.3.3 Climatic Water Data

Vertical land motions can be impacted by groundwater extraction (Faunt et al., 2016; Larochelle et al., 2021; Overacker et al., 2022) and hydrological loading from orographic precipitation (Argus, Fu et al., 2014; Argus et al., 2017). To determine whether hydrological loading from climatic water was related to the vertical land motion trends shown by GPS data, I obtained Palmer Drought Severity Index (PDSI) data to examine them for climate patterns. PDSI time series were used to identify drought and wetness patterns (Dai et al., 2004); negative PDSI values indicate dry years and positive PDSI values indicate wet years (Dai, 2017). Extended periods of negative PDSI values indicate multi-annual drought, and extended periods of positive PDSI values indicate a trend of wetness.

Monthly PDSI data were obtained from the National Oceanographic and Atmospheric Administration (NOAA) Gridded Climate Divisional Dataset (CLIMDIV) (Vose et al. 2014) for 12 combined Washington and Oregon climate divisions (Fig. 2.3). Six climate divisions from each state were chosen because they approximately intersect or contain the subsidence signal of interest. These average monthly PDSI time series run from 17 Apr. 2002 through 15 Nov. 2022 to match the GRACE data timespan (see Data 2.3.2).

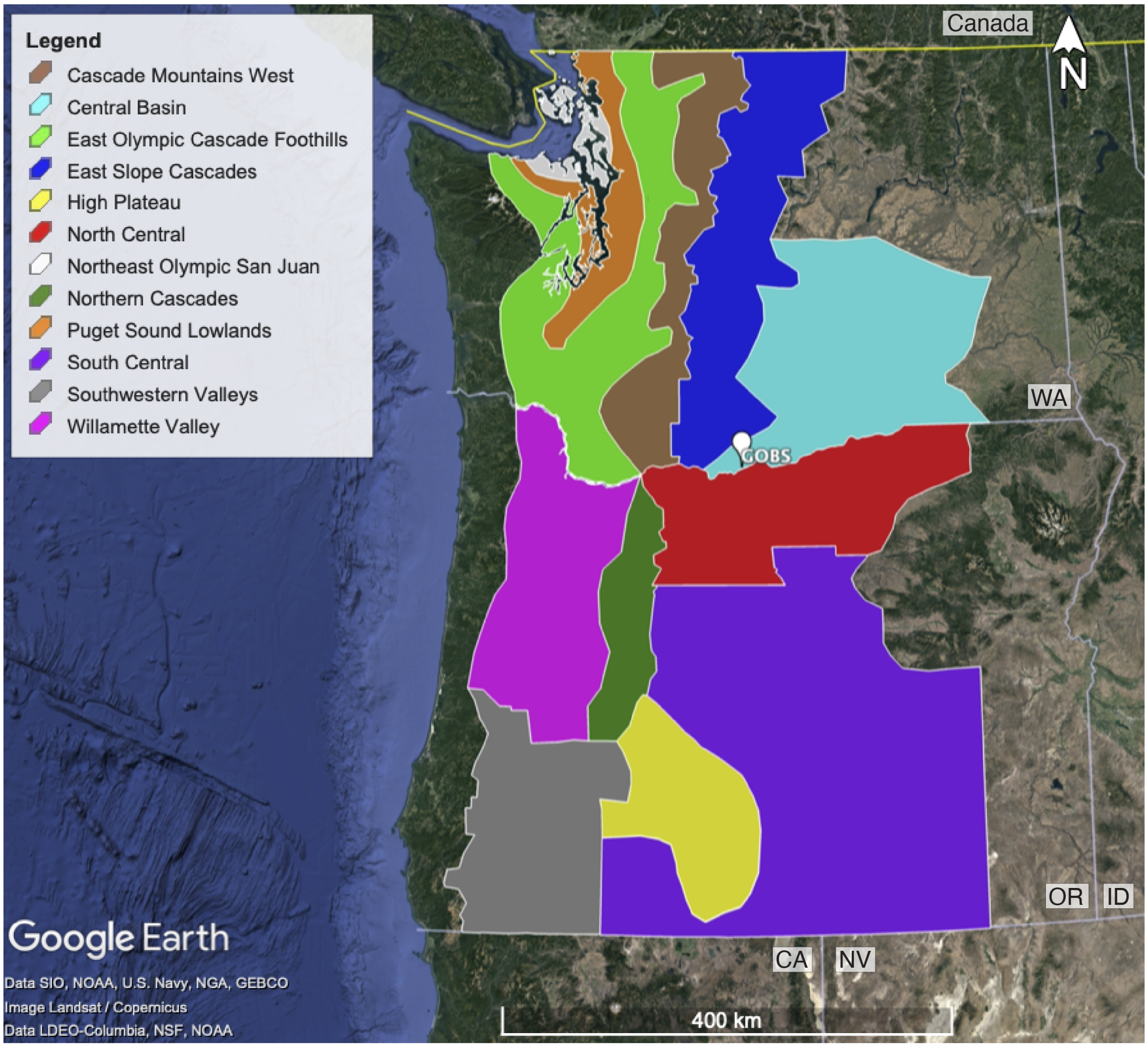

Figure 2.3. Map-view of 6 Washington and 6 Oregon NOAA Climatological Divisions used to understand whether the subsidence signal is related to hydrological loading, with locations approximately based on Cascade Arc and associated drainage basins.

2.4 Analysis

2.4.1 GPS Imaging

GPS Imaging is a robust interpolation technique that highlights spatially coherent signals that are present in multiple stations of a geodetic network. It can be used to discover and characterize the pattern of signals as well as investigate the cause of motion. In this study, I use GPS Imaging to construct a gridded vertical velocity field that reveals rates and patterns of vertical motions that would otherwise be difficult to detect. Trends in position times series are calculated using the MIDAS robust trend estimator which calculates unbiased vertical rates that are insensitive to the effects of outliers, seasonality, and undocumented discontinuities in the data (Fig. 2.4A) (Blewitt et al., 2016).

The GPS Imaging algorithm incorporates weighted median spatial filtering of vertical rates on a Delaunay triangulation of the network to obtain a vertical velocity field with speckle noise removed for improved resolution of geographically coherent signals (Fig. 2.4B) (Hammond et al., 2016). GPS Imaging interpolates values at randomly distributed stations to points on a regular grid to create a vertical velocity field (Fig. 2.4C). Signals that are similar between stations are enhanced by GPS Imaging and may be ascribed to the spatially coherent movement of the solid Earth while outliers, i.e., station velocities that differ substantially from their neighbors, are suppressed.

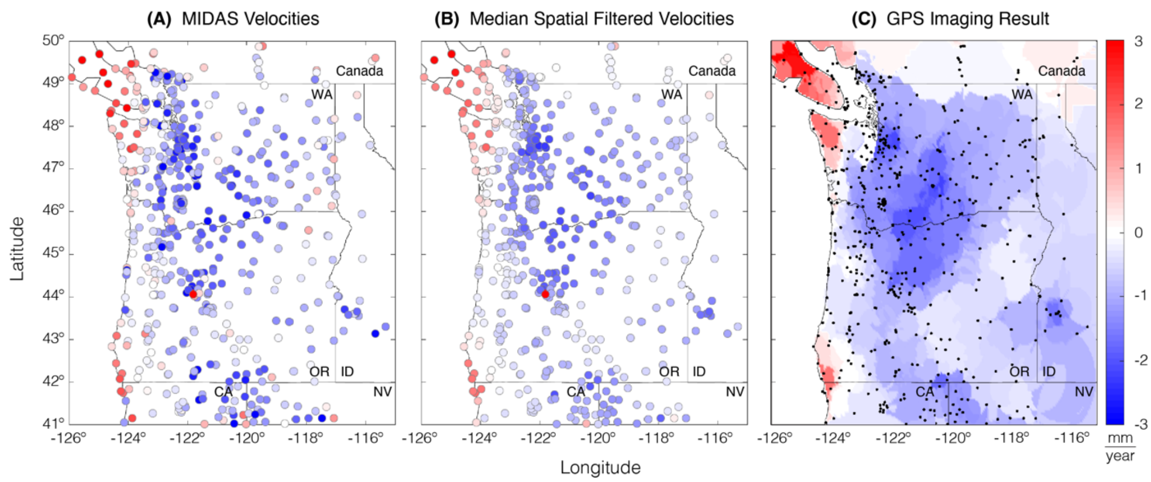

Figure 2.4. GPS Imaging of vertical motions in the Pacific Northwest. **(A)** MIDAS estimates at GPS station locations (circles with face color indicating rate of vertical land motion). **(B)** Median spatial filtered velocities. Speckle noise is removed for improved resolution of geographically coherent signals and removal of outlier rates. **(C)** GPS Imaging before artifact reduction. Small scale artifacts that appear as erratic domain boundaries, wiggles, shards, or fingers of different rates in the vertical rate field are attributable to non-homogeneous GPS station distribution.

To address small scale artifacts attributable to noise and/or short spatial wavelength structure in the GPS vertical rate field and non-homogeneous GPS station distribution, I use a bootstrapping statistical analysis of the GPS Imaging result. GPS Imaging is rerun for multiple iterations, removing a subset of the data each time. The median value of vertical rate for each gridded pixel was used to produce the resulting velocity fields. Values of percent retention were tested (Fig. 2.5), as well as the number of iterations (Fig. 2.6). The goal of this iteration was to reduce artifacts and to refine the interpolation of the vertical velocities. Results of several runs with varied parameters were compared to the initial GPS Imaging result (Fig. 2.4C), and preference was given to the test results that retained the pattern and rate of the subsidence feature of interest where station density is higher. Percent retention values were tested where a randomly selected 50, 65, and 80 percent of the stations were retained in each iteration. For low percent retention in each iteration, the contours around the signals became smoother, but vertical rates were also noticeably decreased, such as an increased rate of subsidence located near the Boise, Idaho metropolitan area. When percent retention was higher, the results were closer to the original GPS Imaging result to the point where the domain boundaries, wiggles, shards, or fingers were not substantially reduced. The moderate value of percent retention was therefore chosen because it balanced artifact reduction while retaining the signals of interest.

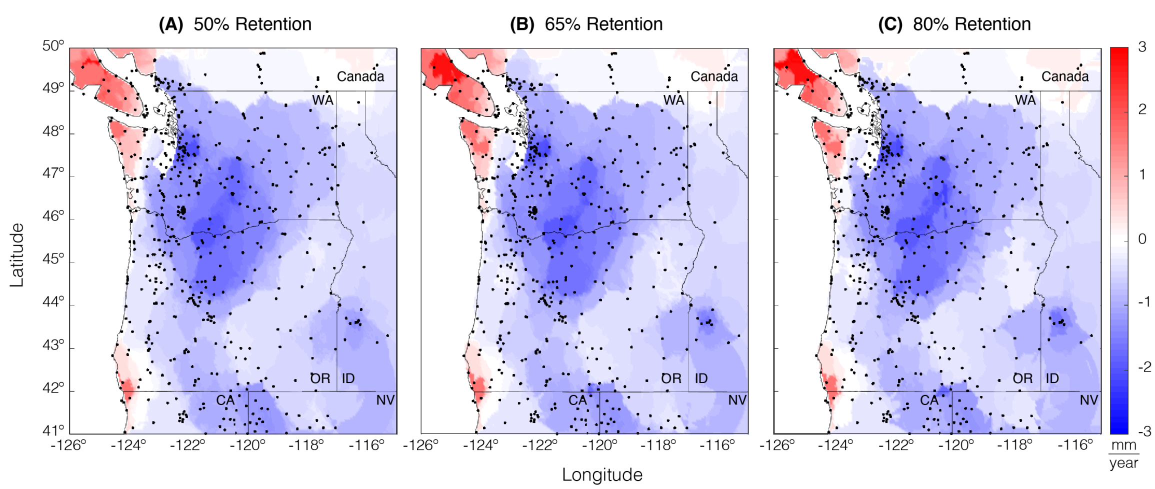

Figure 2.5. GPS Imaging bootstrap analysis tests using **(A)** 50, **(B)** 65, and **(C)** 80 percent retention of stations in each iteration.

Next, I tested 10, 20, and 40 for the number of iterations (Fig. 2.6). The results of 10 iterations showed rougher domain boundaries, and the wiggles, shards, or fingers were hardly affected. 40 iterations feature similar crescent shaped artifacts, but 20 iterations seemed to provide a balance of artifact reduction, faster processing time, and good adherence to the overall pattern calculated in the initial interpolated velocity field (Fig. 2.4C). I chose values of 65 percent retention and 20 iterations as the final bootstrapping statistical analysis parameters.

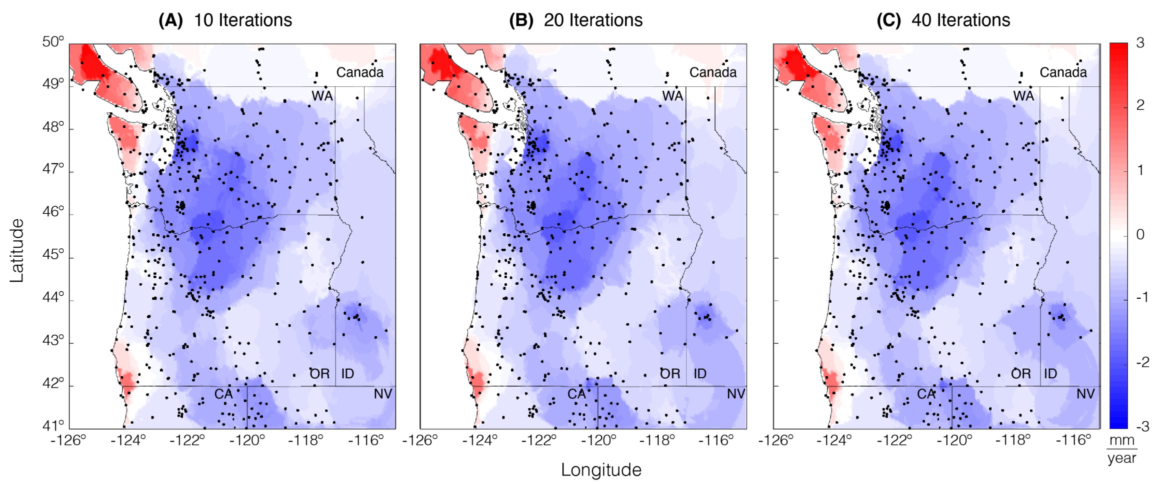

Figure 2.6. GPS Imaging bootstrap analysis tests using **(A)** 10, **(B)** 20, and **(C)** 40 iterations.

2.4.2 Resolution Tests

To check the GPS Imaging resolution, I performed a reconstruction test using a synthetic checkerboard vertical velocity field. Synthetic velocity values between 3 mm/year and –3 mm/year, with pixel borders between the checkerboards of 0 mm/year, were applied to the 648 stations used in this study. Velocities were based on station location within the checkerboard and were assigned uncertainties based on real station vertical uncertainty values. The synthetic velocities then underwent all steps of the GPS Imaging process previously described in the last section.

The synthetic velocity field interpolated from GPS station locations show adequate spatial resolution down to 2 x 2 arc-degree squares with 0.05 degrees of resolution, i.e., zero values at the boundaries of each square (Fig. 2.7). Squares with a greater number of stations were better reconstructed into their checkerboard appearance, and squares with a high amount of station density and a greater number of stations were best reconstructed to the point that the squares had visible white space defined between blocks (e.g., the blue block southeast of Vancouver Island). Squares that had a concentration of stations but low station distribution (e.g., southwest Idaho) had poorer resolution and limited reconstruction. Longitudes of, and west of, the Cascade Range where the GPS station density is greatest had greater spatial resolution than the easternmost edge of the study area where there are fewer stations and lower station density. The tests showed that spatial resolution in the Cascade Arc is sufficient for identifying signals of interest, and verifies that the resolution of the feature of interest is not biased by station spacing.

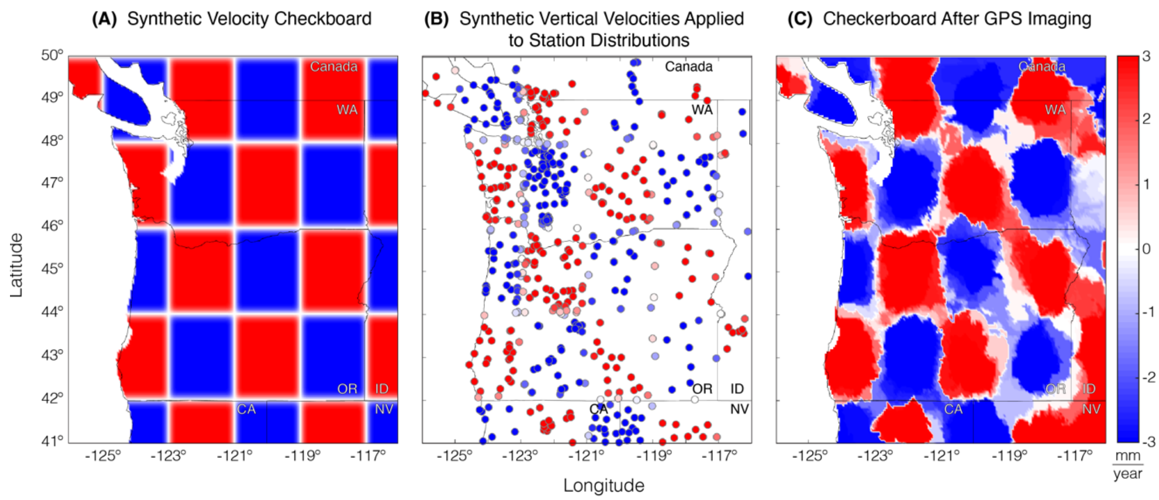

Figure 2.7. Resolution reconstruction test of GPS Imaging performed to check the quality of the reconstruction of the checkerboard pattern by the GPS network. **(A)** Synthetic velocity checkerboard applied to Pacific Northwest region to test for spatial resolution. Checkerboard is designed with 2 x 2 arc-degree intervals (blue and white rectangles) and 0.05 degree of resolution (white space between rectangles). **(B)** Station distribution with synthetic vertical velocities applied. **(C)** Reconstructed checkerboard after GPS Imaging.

2.4.3 Topographic Profiles

I investigated any possible correlation between signals and specific geographic or tectonic sources for vertical land motion revealed by the topography (Serpelloni et al., 2013; Pfeffer et al., 2017). Four topographic profiles were compared to vertical profiles that transect the subsidence feature of interest. These profiles, located along latitudes 42.5º, 44.5º, 46.5º, and 48.5º were chosen to determine whether there are any topographic commonalities from north to south that might be related to the subsidence signal (Fig. 2.1). Though each transect includes the Cascade Arc, there are latitude dependent variations in geographical features that might help indicate the potential source of subsidence as well.

I compare constant-latitude topographic profiles with GPS Imaging velocity trends and MIDAS velocities from stations located within the transect (Fig. 2.8). To illustrate a wide range of topographic and vertical velocity trends, 20 km of padding was included on both sides of the main transect latitudes, with five profile lines of topography and velocities located at 4 km intervals to the north of each main transect line, and five profile lines in 4 km intervals to the south respectively. The mean of each velocity and topographic profile was plotted with MIDAS GPS velocities and uncertainties to get the average trends per transect. Prominent geographic features like basins and mountain ranges were denoted for each transect.

These profiles indicate that there is a subsidence feature consistently focused around the approximate longitude of the Cascade Arc. Though the width of subsidence is not tightly concentrated around the topographic peaks for the Cascade Arc, it does generally include features of the arc which may include drainage basins.

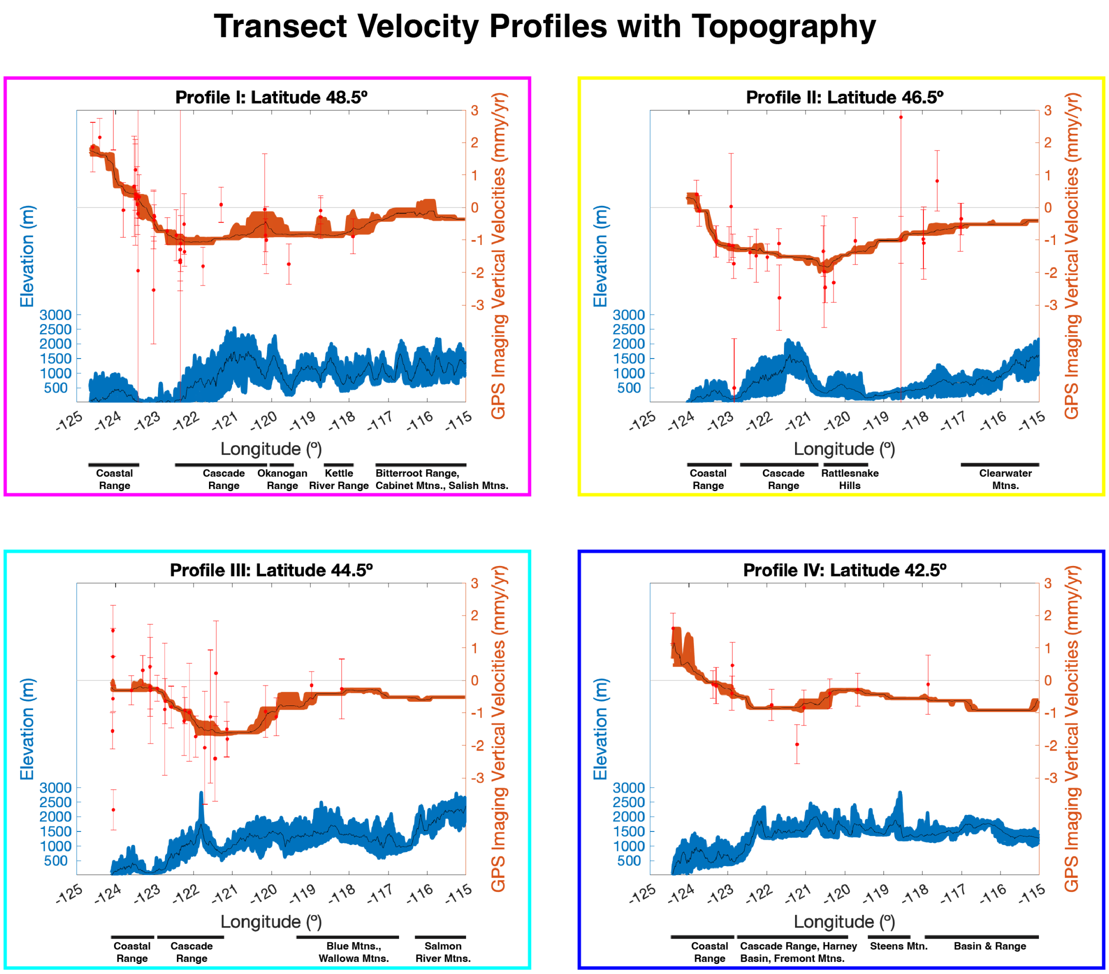

Figure 2.8. Transect velocity profiles with topography and colored boxes corresponding to colored, dashed boxes in Figure 2.1. Mean (black) of topographic (blue) and GPS Imaging vertical velocities (orange) accompany MIDAS GPS velocities with error bars (red) for each transect. The 40 km padding around the center latitude illustrates the cross-profile variability of topography and vertical velocity. Irregular coastline changes length of transect, and prominent geographic features are denoted for each transect below the longitude.

2.4.4 Examining Possible Climatological Influence in Hydrological Loading

Since the Cascade Arc and back-arc basins are regions where hydrological vertical land motion signals could occur both from orographic precipitation and water storage (Borsa et al., 2014; Fu et al., 2015), I investigated climate patterns for a connection with the subsidence signal. PDSI time series for each climate division represent changes in climate conditions, with negative PDSI values indicating dry years and positive PDSI values indicating wet years (Dai, 2017). PDSI time series were plotted against GRACE time series to better distinguish between wet and dry climate patterns and understand their relation to hydrological loading (Fig. 2.9). GPS positions for station GOBS, representative of vertical land motion in the subsidence feature of interest, is also plotted with and without atmospheric non-tidal loading, non-tidal ocean loading, and GRACE-based mascon hydrological loading corrections for comparison.

For hydrological loading from climate variations to be the principal source of the subsidence shown in the GPS Imaging result, one would expect to see a gravity trend of increasing water mass occurring during extended periods of positive PDSI values indicating multi-annual increase in wetness. This would correspond with an increase in the subsidence rate shown by GPS time series.

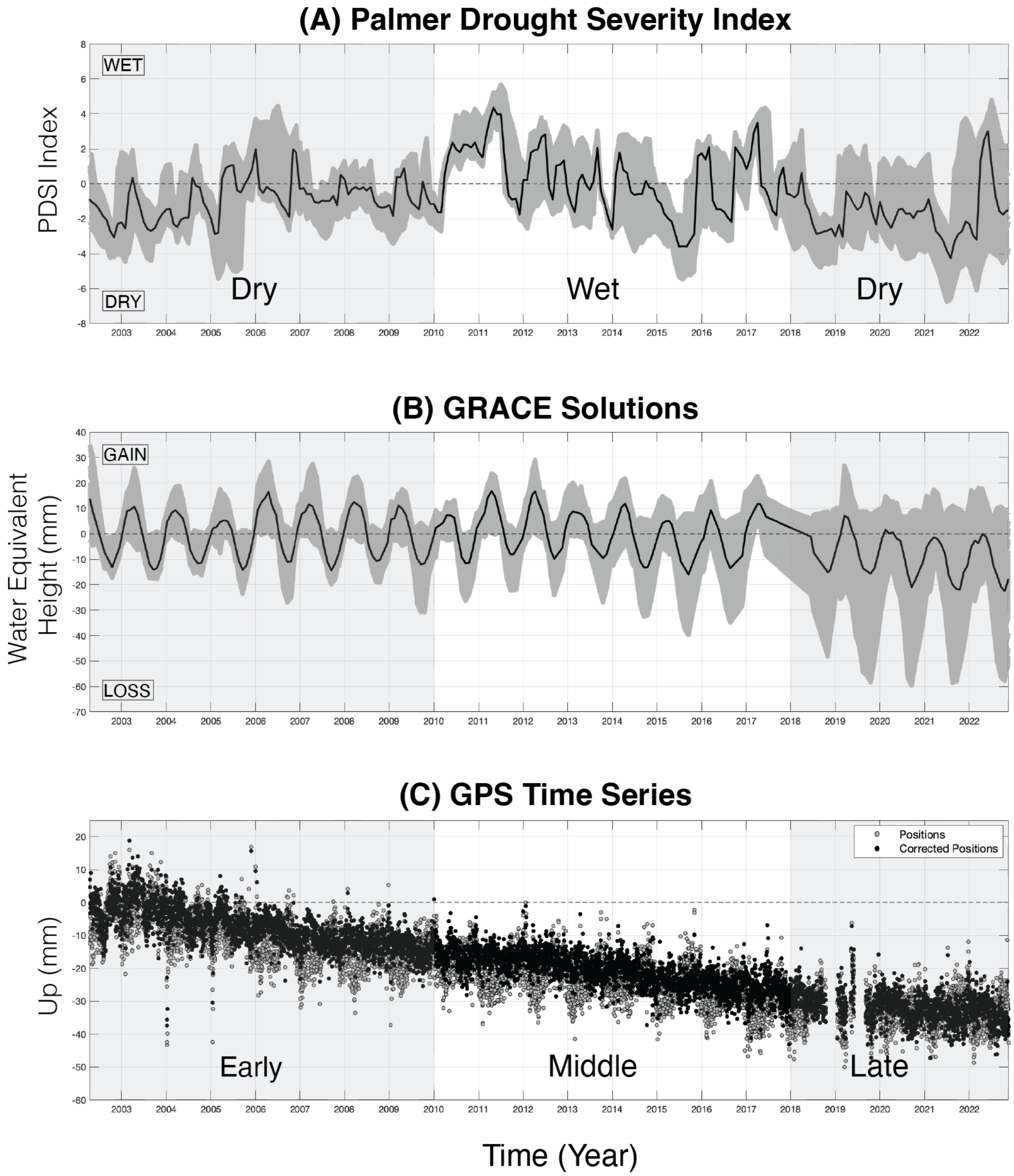

Figure 2.9. (A) 12 Climatological Division Palmer Drought Severity Index time series (locations noted on Fig. 2.3). Negative PDSI values indicate dry years; positive PDSI values indicate wet years (Dai, 2017), and dry periods are marked by gray boxes. Extended periods of PDSI values ≤–3 indicate severe drought. **(B)** 76 GRACE gravity

solutions (mascons indicated on Fig. 2.2 and Sup. Table S2.2). **(C)** GPS time series trend for station GOBS (see Fig. 2.3 for location). Median values for PDSI and GRACE shown by black lines. GPS time series has original positions (gray) and positions corrected for non-tidal atmospheric loading, non-tidal ocean loading, and mascon-based GRACE hydrological loading predictions (Argus et al., 2022). GOBS times series is representative of GPS trends in the Pacific Northwest interior near location of greatest subsidence, with early, middle, and late periods denoted (Fig. 2.10).

PDSI data collected from NOAA (Fig. 2.9A) were compared to GSFC GRACE time series data (Fig. 2.9B), and GPS time series from representative station GOBS (Fig. 2.9C). All climate division data followed similar PDSI trends, with moderate drought of median PDSI of –1 for the majority of the 2002–2009 time frame, but only would be considered severe (≤–3 PDSI) in 2003 and 2005. Conversely, a period of increasing wetness with a median value of +1.7 began in 2010 with extreme wetness (≥+3 PDSI) affecting all climate divisions in 2011. Heightened PDSI values gradually tapered off, oscillating between ±2 until mid-2015 for a short severe drought of –3.6 median for all climate divisions. This climate trend shown in median PDSI rebounded to an extreme wetness peak in winter 2017 with a value of +3.5 before another, less extreme drought period dominated from 2018 through the end of 2021 with a –2 average PDSI. The data indicate a short spike of wetness in early 2022 with an average of +2 briefly before decreasing to drought values of –1.5 by the end of the time series.

GRACE time series from GSFC (Fig. 29B) indicate a seasonal signal that is slightly shifted off peak phase with PDSI, indicating that the increase in equivalent water height is related to hydrological loading from weather over the rainy season. GSFC solution amplitudes oscillate around zero until 2015, with a very marginal decreasing trend in equivalent water height that slightly recovers in 2017 before it declines 2018 through the end of 2022.

The representative vertical-component GPS time series from GOBS (Fig. 2.9C shows a relatively consistent subsidence trend for positions corrected for the effects of non-tidal atmospheric loading, non-tidal ocean loading, and hydrological loading from GRACE-based mascon solutions. Though the variations in the hydrological load by GRACE suggest a seasonal loading signal correlated with precipitation and water mass loading from climate and GRACE time series, these trends are minimized with the application of the loading corrections. Furthermore, the GPS data after 2018 does not suggest a severe change in rate of subsidence from the drying trend shown by PDSI, indicating that there is no noticeable mismatch in the hydrological unloading model corrections from climate effects. However, a single GPS station, even a representative one that runs the entirety of the comparative time series timespan, cannot fully express how the regional vertical land motion changes over the course of the expanding network, or during wet and dry periods. Subsequently, I will use the PDSI time series to divide the GPS time series into early, middle, and late periods defined by wet and dry patterns to broadly assess how rates of motion in the study area change over time and climate.

2.4.5 Early, Middle, and Late Period Testing

To determine whether vertical land motion rates are consistent over time, how the patterns changed as the network expanded, and how they were impacted by wet vs. dry climate patterns, the GPS time series were divided into early, middle, and late periods based on climate trends (see Analysis 2.4.4). The early period spans from 1 Jan. 2002 through 31 Dec. 2009 but contains the fewest number of GPS stations at 368. Though there are some stations available before 2002, I chose a timeframe that included data post GPS network expansion that also had a more stable PDSI pattern, a moderately dry average of –1. The middle and late periods occur after the majority of GPS network expansion was completed. The middle period runs from 1 Jan. 2010 through 31 Dec. 2017, and contains 2011 and 2017, particularly wet years for all climate divisions in the Pacific Northwest, but it also contains 2015, a severe drought year. Though the median PDSI during this time is only +0.15, I define it as the comparatively wet period. There are 575 GPS stations used to calculate rates of motion for this timeframe. The late period consists of 563 GPS stations and contains data from 1 Jan. 2018 through 3 Jun. 2023. This time is dominated by drought in the Pacific Northwest, characterized by a median PDSI of –1.7, and is considered another dry period.

MIDAS velocities (Sup. Table. S2.3) were computed for the truncated time series according to the time frame for each period, and GPS Imaging was performed for each time interval using the same processing strategy as previously discussed (see Analysis 2.4.1). The early period (Fig. 2.10A) has limited spatial resolution because there were fewer GPS stations before the PANGA and NOTA networks expanded. Middle and late period GPS Imaging results have better spatial resolution owing to a more complete coverage of stations.

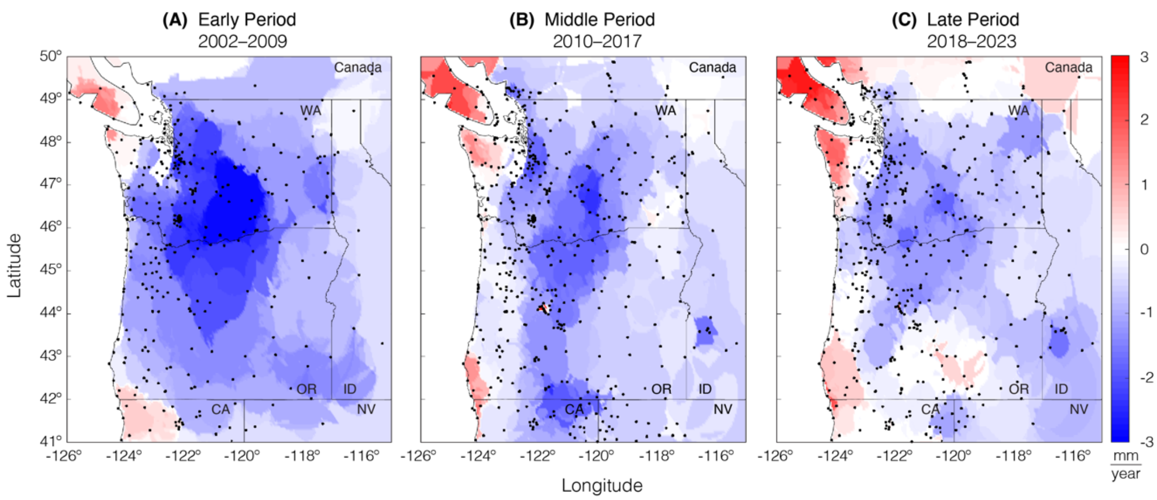

Figure 2.10. Subsidence is present in the interior Pacific Northwest throughout **(A)** early, **(B)** middle, and **(C)** late period GPS Imaging results despite different spatial resolution from station (black dots) spacing. Early period (2002–2009) has greatest swath and highest rate of subsidence. Middle period (2010–2017) rate of subsidence is decreased slightly but better concentrated around Cascade Arc. Late period (2018–2023) results show a continued decrease of subsidence rate and weaker concentration around Cascade Arc.

Early, middle, and late period results (Fig. 2.10) generally show that there is a consistent subsidence feature of greater rate than surrounding subsidence located in the interior Pacific Northwest throughout the record of GPS time series. In the early period (Fig. 2.10A) there is a broad subsidence signal in the interior with a maximum subsidence rate of –3.5 mm/year located in south-central Washington. The middle period (Fig.

2.10B) subsidence signal is slightly decreased with a maximum rate of –2.3 mm/year, but the subsidence seems more strongly concentrated around Cascade Arc longitudes. Late period (Fig. 2.10C) results show reduced concentration and decreasing rate (now a maximum of –2 mm/year) of interior subsidence as uplift is observed in previously subsiding regions of south-central Oregon. Both middle and late periods indicate there is a time variable uplift signal of 3+ mm/year in central Oregon from inflation of the Three Sisters Volcanic complex (Wicks et al., 2003; Dzurisin et al., 2009; Riddick and Schmidt, 2011). Though the early and late period timespans are defined by negative PDSI values, the dry periods are not that different from the wet middle period. The width of the subsidence is greatest in the earlier period, longest in the middle period, and is not considerably different from surrounding subsidence signals by the late period. Some of this change is attributable to station spacing, but the rate of the subsidence also decreases with time. This suggests that, though the presence of increased subsidence has been more or less consistent in this region since the beginning of the early period, it appears to be gradually dissipating both in rate and extent over time.

2.5 Results

2.5.1 Vertical Land Motion of the Pacific Northwest

GPS Imaging reveals subsidence that spans most of the study area except for the coast where there is uplift of approximately 2 mm/year (Fig. 2.11). Standing out from the surrounding areas of subsidence is a 50–250 km wide swath of approximately –2 mm/year of concentrated subsidence (Fig. 2.11). This feature extends throughout the Cascadia subduction zone latitudes and is located approximately between –123º and –120º longitudes, though it becomes more diffuse between 44º and 47º latitudes. Maximum subsidence velocity over –2.3 mm/year is observed in the interior Pacific Northwest located near the Washington-Oregon border. This is the approximate location of the Siletzia microplate accretion, and geologic contrasts could possibly be contributing to the wedge-shaped appearance as well as the greater rate of subsidence (Schmandt and Humphreys, 2011). Along the coastal regions, uplift is attributable to interseismic uplift from Cascadia locking (Mazzotti et al., 2007; Mazotti et al., 2008; Burgette et al., 2009; Montillet et al., 2018).

I compare topographic relief to vertical motions to see if there is a correlation between geographic features and vertical velocity signals. These show that the subsidence occurs along the Cascade Arc which includes drainage basins (e.g., the Columbia River Basin) along the Washington-Oregon border. This suggests the possibility that hydrological loading from orographic precipitation and storage might play a role in the subsidence. However, I correct for the effects of hydrological loading using the prediction of loading models based on GRACE data (section 2.3.2). Moreover, early, middle, and late period GPS Imaging test results suggest that the rate of the subsidence feature is not increasing during wetter periods and decreasing over dry periods. Rather, the middle period velocity field which included relatively wet years, and the early and late period velocity field that consisted of persistent droughts verified that, in general, subsidence rates in the Pacific Northwest are not strongly influenced by climatic hydrological loading.

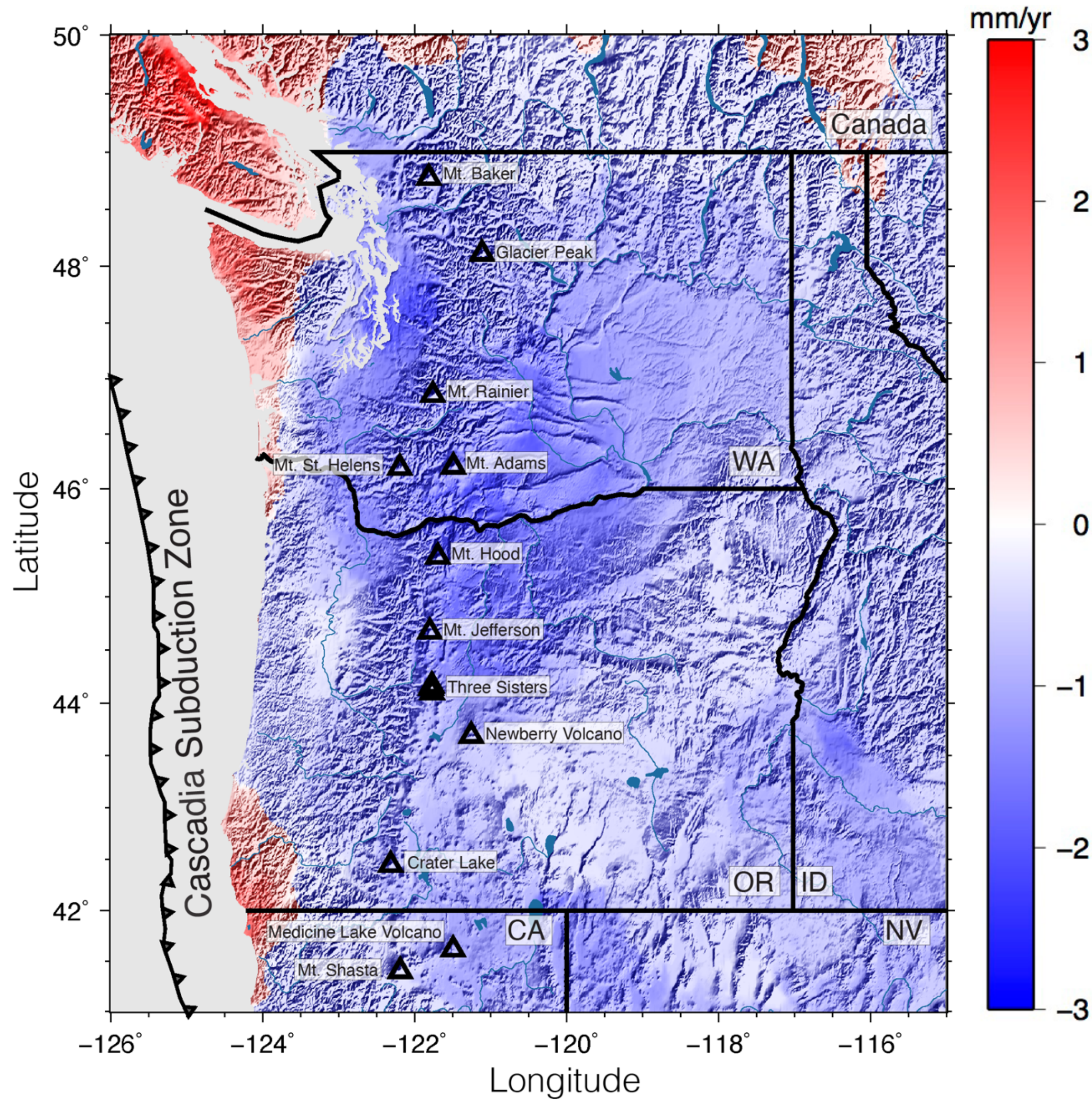

Figure 2.11. GPS Imaging results of vertical velocity field for the Pacific Northwest with topographic relief. A swath of subsidence –2 mm/year 50–250 km wide correlates with the latitudinal extent of the Cascadia subduction zone (gray triangles offshore) (Bird, 2003) and the approximate longitude of the Cascade Arc (volcanoes marked as black triangles). Maximum subsidence of over –2.3 mm/year is observed near the Washington-Oregon border between Mt. Adams and Mt. Hood.

2.6 Discussion

2.6.1 Interpretation of Subsidence

PDSI data collected from NOAA compared to GRACE data from GSFC time series and early, middle, and late period GPS Imaging results do not indicate a connection between wet and dry climate patterns and vertical land motion. Comparisons with the GPS velocity fields show a geographically centralized and consistent trend of subsidence, though the rates and spatial distribution may vary. This implies that most of the subsidence is not driven by hydrological loading related to climatological effects. GRACE gravity trends from GSFC show a very slight increasing gravity trend in the Pacific Northwest interior along the western Washington-Oregon border where there is consistent subsidence, but the majority of the Pacific Northwest is dominated by a trend of water mass loss. Furthermore, the spatial pattern away from the state line shown by GSFC trends, at least at the current resolution of approximately one hundred kilometers, did not show a geographic distribution similar to that of the GPS Imaging results further south into Oregon. This suggests the changing mass distribution of water might play a minor role in vertical land motions around the Pacific Northwest but it is probably not the main cause of the subsidence signal that is focused along the Cascade volcanic arc.

Thus, climatically driven hydrologic loading effects do not adequately explain the pattern of vertical motion. As previously stated, however, this region has a history of glaciation. Furthermore, the subsidence signal is strongly correlated with topography of the Cascade volcanic arc and extent of the subduction zone. Since these features are formed by dynamic and active geological processes related to plate tectonics, subduction, magma genesis, and volcanism in the Cascadia subduction zone, I consider large-scale plate boundary interactions, volcanic loading, and postseismic relaxation that could also potentially contribute to the subsidence feature by applying a force on the lithosphere, as well as the potential contribution from GIA.

2.6.2 Possible Effects of Glacial Isostatic Adjustment

The Pacific Northwest's history of Late Pleistocene deglaciation prompted an investigation of the possible influence that post-glacial rebound might have on the subsidence pattern shown in GPS Imaging. Glacial isostatic adjustment (GIA) unloading models were taken from the ICE-6G D (VM5a) GIA model (Peltier et al. 2015; Peltier et al., 2018; Argus, Peltier et al. 2014) and tested as a potential source for the subsidence signal. The idea is that Laurentide ice sheet loss in the North American continental interior (Sella et al., 2007) and subsequent Western Cordilleran glacial unloading in northern Washington and the west coast of Canada has caused mantle flow to return to northern latitudes and an accommodating isostatic adjustment to the south, creating a hinge effect of widespread subsidence in the area from forebulge collapse (Fig. 2.12B).

I compare the subsidence pattern in the Pacific Northwest predicted by the ICE-6G D (VM5a) GIA model to the GPS Imaging result. To do this, I downsample the GIA 0.2 x 0.2 arc-degrees latitude and longitude intervals into the same grid used by GPS Imaging (Fig. 2.12A). The GIA model contains a subsidence signal of approximately

–1 mm/year that dominates the Pacific Northwest south of the Canadian border, a lesser rate than the subsidence feature of interest at approximately –2 mm/year. Although the GIA model is also subsiding, the pattern of subsidence is not spatially concentrated along the Cascade Arc like the GPS Imaging result.

Subtracting the predictions of the GIA model from the GPS-observed vertical rate field (Fig. 2.12C) results in greater focusing of subsidence near the arc rather than less, suggesting that the subsidence feature cannot be fully explained by GIA. Furthermore, though subtracting the GIA model from the GPS Imaging result (Fig. 2.12C) reduces the rate of the subsidence feature to approximately –1 mm/year, it also extends the latitudes of subsidence north into Canada. Also, the corrections increase the homogeneity of vertical rates to the east of the Cascade Arc, and makes the uplift consistent along the entire coastline, suggesting that the gap in coastal uplift in Oregon may partly be a feature of GIA rather than only the location, depth, and distribution of locking of the subduction zone interface (Burgette et al., 2009; Schmalzle et al., 2014).

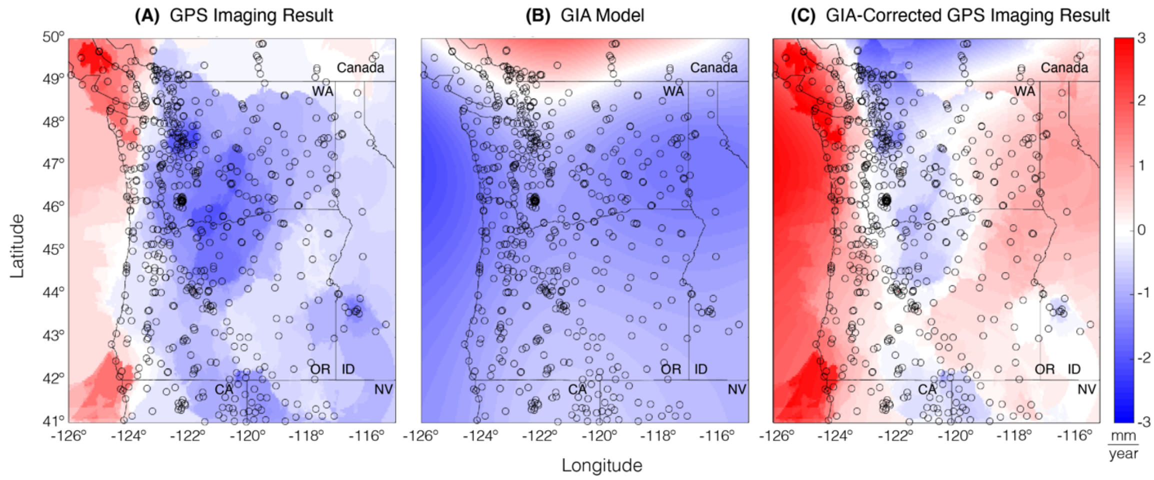

Figure 2.12. (A) GPS Imaging vertical velocity compared to the **(B**) the predictions of the ICE-6G D (VM5a) model. **(C)** Observed GPS Imaging result with the ICE-6G D (VM5a) model vertical velocity predictions subtracted. Both (A) and (B) show a downward signal along the Cascade Arc, but the pattern in the GIA model does not show a concentrated subsidence near the Arc, and (C) extends the subsidence feature further north into Canada.

GIA models predict downward vertical motions in the Pacific Northwest region, but their spatial pattern of subsidence does not match the subsidence in the GPS Imaging result. Though there may by uncertainties in the ICE-6G D (VM5a) model, e.g., it does not include the effects of lateral variations in upper mantle viscosity that likely exist, correcting for GIA in the GPS Imaging result only further focuses the subsidence signal throughout the Cascadia subduction zone latitudes and near the Cascade Arc (Fig. 2.12). It is likely that there is a GIA contribution to the widespread subsidence signal shown in the Pacific Northwest, but GIA is probably not the principal cause of the 50–250 km wide swath of subsidence.

2.6.3 Lithospheric Flexure of the North American Plate

If one considers that the subsidence is associated with ongoing crustal deformation related to plate-scale geodynamic forces, the observed subsidence can be used as a constraint for theoretical deflection models that describe elastic lithospheric flexure (Turcotte and Schubert, 2002). Lithospheric flexure can be estimated using flexural rigidity parameter *D*, which is a function of the elastic plate's Youngs modulus *E,* Poisson's ratio ν, and thickness *h*:

Eq. 2.1) $$D = \frac{Eh^3}{12(1-\nu^2)}$$

In turn, the flexural parameter α is determined by the flexural rigidity parameter, density of the mantle ρ_m and crust ρ_c, and acceleration from gravity *g*:

Eq. 2.2) $$\alpha = \left(\frac{4D}{(\rho_m-\rho_c)g}\right)^{1/4},$$

Here, I use realistic mechanical properties of the Earth's crust in this region to estimate flexural rigidity, and the flexural parameter to estimate an approximate range of plate deflection half widths for comparison with the theoretical models. The value of *D* was calculated using Eq. 2.1, assuming Young's modulus *E* = 60 GPa (Johnson and DeGraff, 1988), and a value of 0.25 is used for Poisson's ratio *v* (Turcotte and Schubert, 2002). Thickness of the plate h is tested in 2.5 km intervals from 5–50 km for the volcanic loading model on the continental plate and for the Juan de Fuca plate end loading model (Lowry and Smith, 1995). The flexural rigidities calculated in Eq. 2.1 were then used in Eq. 2.2 for an array of flexural parameter α values to give an approximate range of permissible plate deflection half widths. In Eq. 2.2, the densities of the mantle and crust are taken to be $\rho_m = 3300\ \mathrm{kg/m^3}$ (Turcotte and Schubert, 2002) and $\rho_c = 2750\ \mathrm{kg/m^3}$ from the average Cascadia crustal density (Vanyan et al., 2002).

2.6.4 Plate Deflection from Volcanic Loading

Volcanic loading occurs when magma is transported from depth and deposited on the Earth's crust by volcanic eruption, and it can cause subsidence and associated lithospheric flexural response (Moore, 1970; Watts and Cochran, 1974; McNutt and Menard, 1978; Wessel et al., 1993). To understand whether volcanic loading might be influencing the subsidence signal observed by GPS Imaging, I model a simple theoretical plate deflection profile with a line load. If the subsidence signal is caused by loading of the lithosphere with the mass of the Cascade Arc, the 50–250 km range width of the subsidence signal should be comparable with wavelengths predicted by theoretical deflection models with realistic Earth properties.

The relationship describing the bending of the elastic lithosphere under a line load is modeled using the following equation for an elastic plate floating on an inviscid asthenosphere (Turcotte and Schubert, 2002):

Eq. 2.3) $$\omega = \omega_0 e^{-x/\alpha}(\cos\frac{x}{\alpha} + \sin\frac{x}{\alpha})$$

where ω is the deflection of the plate, maximum amplitude of the deflection $\omega_0 = -1$, x is distance from the load, and α is the flexural parameter.

I calculate the deflection using a range of values for α calculated using h values from 5–50 km in 2.5 km intervals (Sup. Table S2.4). The zone in red gives permissible half width distances constrained by the subsidence feature, defined by where the model results cross zero (Fig. 2.13). Theoretical distances for volcanic load deflection give a minimum permissible half width of 62–124 km, within the range of what is observed by GPS Imaging. This suggests that volcanic loading is possibly a contributing factor to the subsidence feature of interest.

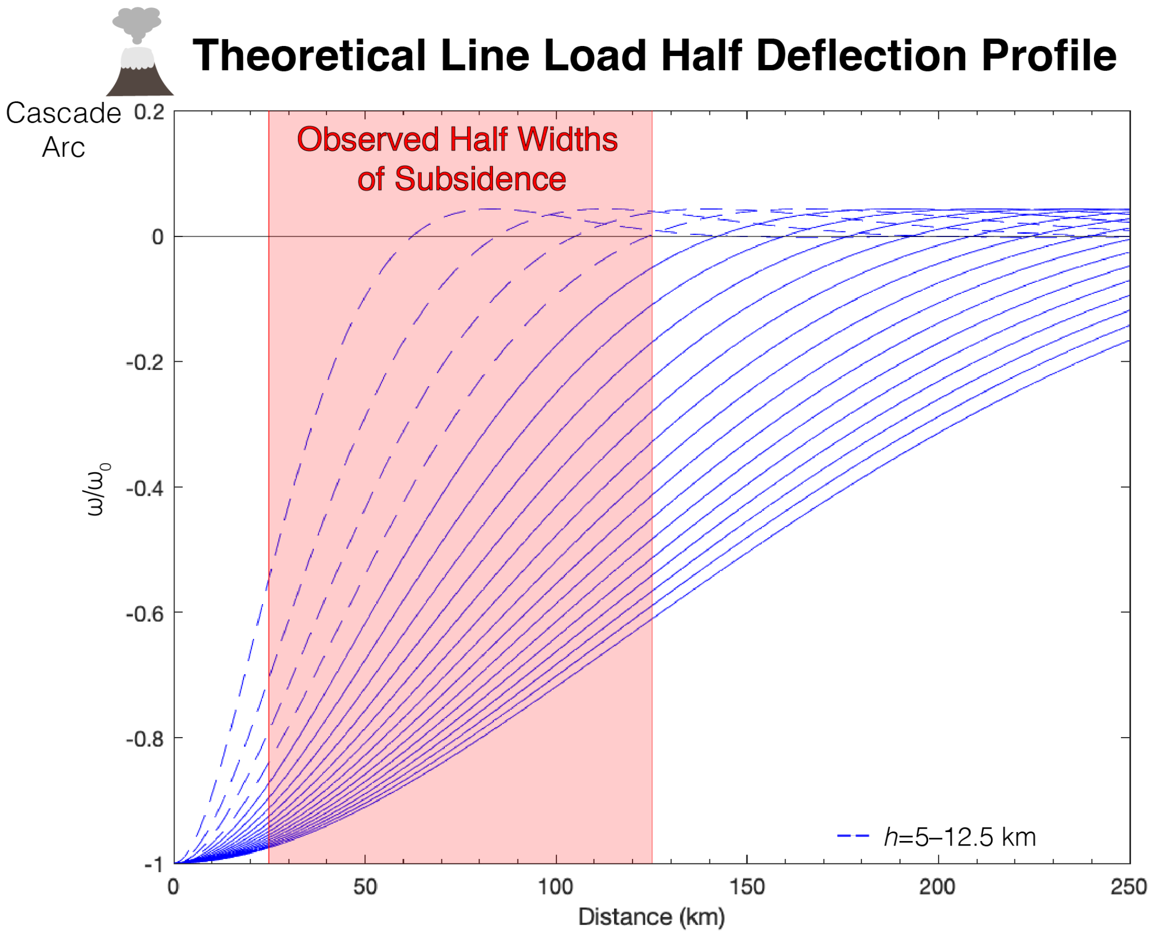

Figure 2.13. Half theoretical deflection profile (blue) calculated using Eq. 2.3 assuming a volcanic load. A range of flexural parameters α allowed by realistic geologic parameters (h from 5 to 12.5 km) are used to calculate the profiles. Curves that cross zero within the red zone (blue dashed lines) indicate half widths of the loading signal that are consistent with the observed range shown by the GPS Imaging. Model results give permissible half width distances of 62–124 km.

2.6.5 Plate Deflection from Subduction

Stresses imposed by the contraction across the contact between the North American plate and subducting Juan de Fuca plate could be another potential source of the observed subsidence (Turcotte and Schubert, 2002). Here, I model deflection profiles for the elastic lithosphere using the subducting Juan de Fuca plate as an end load on the North American lithosphere. If model results are within the 50–250 km width range of observed subsidence shown by the vertical velocity field, that subsidence could be directly related to the subducting plate.

The following equation for a floating elastic plate from Turcotte and Schubert (2002) is used to construct a model for deflection from an end load:

Eq. 2.4) $$\omega = \omega_0 e^{-x/\alpha}(\cos\frac{x}{\alpha})$$

where ω is the deflection of the plate, maximum amplitude of the deflection $\omega_0 = -1$, x is distance from the load, and α is the flexural parameter.

Theoretical deflection is tested with subducting plate thickness values of h =5–50 km with 2.5 km intervals to calculate D and α (Sup. Table S2.4). Values of α that cross zero within the red zone are permitted by the width of the observed subsidence and realistic geologic parameters (Fig. 2.14). The subducting plate end load model indicates that all end loading models produced with h values between 5–20 km can cause the observed GPS signals with theoretical lithospheric flexure half width distances of 42–117 km. This modeling adds another possible loading signal that can either contribute to, or be the primary source of the subsidence feature of interest.

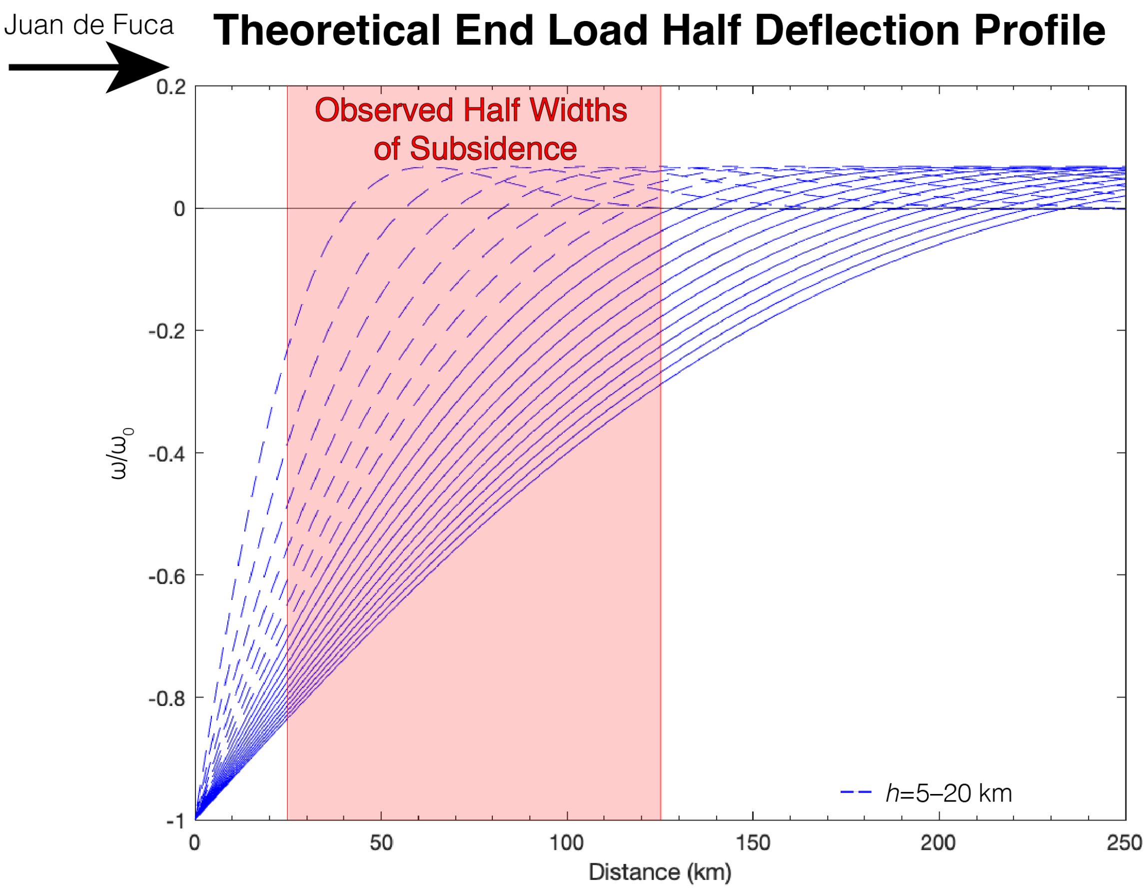

Figure 2.14. Half theoretical deflection profile (blue) calculated using Eq. 2.4 assuming a side load caused by subduction of the Juan de Fuca plate. A range of flexural parameters α (consistent with h=5 to 20 km) allowed by realistic geologic parameters that cross zero within the red zone (blue dashed lines) indicate half widths of the loading signal that are consistent with the observed range shown by the GPS Imaging. Model results give permissible half width distances of 42–117 km.

2.6.6 *Postseismic Relaxation from the 1700 M9.1 Cascadia Earthquake*

To disentangle vertical land motions caused by plate tectonic interactions between the Juan de Fuca plate subducting beneath the North American plate, I model postseismic relaxation from the 1700 M9.1 Cascadia megathrust earthquake. Cascadia postseismic models were taken from Pollitz et al. (2008) following methods by Young et al. (2023). Vertical position time series for postseismic relaxation were obtained for GPS stations used in the GPS Imaging during the study time period, and vertical velocities were estimated using least squares linear regression. Velocities were then input into the GPS Imaging analysis flow according to previous methods (see Analysis 2.4.1) to construct a vertical velocity field (Fig. 2.15A). The postseismic relaxation model from the Cascadia megathrust earthquake shows coastal uplift of 2+ mm/year and subsidence in the interior Pacific Northwest at a rate of –0.5 to –1 mm/year.

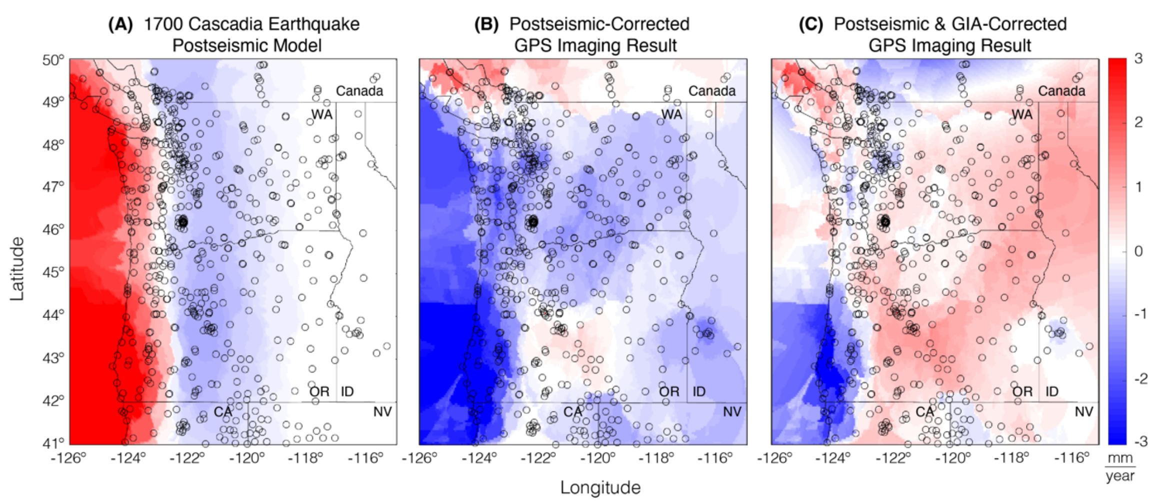

Figure 2.15. (A) GPS Imaging of vertical rate predicted from postseismic relaxation model. **(B)** The predicted signal from postseismic relaxation is removed from the GPS

Imaging result (Fig. 2.12A), and the residual field shows less subsidence in the interior Pacific Northwest. **(C)** GPS Imaging result with postseismic relaxation and GIA (Fig. 2.12) removed eliminates most of the observed Cascade Arc subsidence, indicating that this combination of processes is likely the main source contributing to subsidence signal.

To correct the vertical velocity field for postseismic effects, modeled postseismic relaxation predictions were subtracted from the GPS Imaging results (Fig. 2.15B). Along the coast, the sign of vertical motion switches from positive to negative, and the interior Pacific Northwest subsidence decreases from –2 mm/year to –1 mm/year. The decrease in subsidence rate is approximately equivalent to rates of forebulge collapse signal subsidence (Fig. 2.12B), so I next subtract GIA from the velocity field to analyze its contribution directly. Combined postseismic and GIA-corrected velocities produced by GPS Imaging show an expanse of uplift of 1–2 mm/year in the Pacific Northwest, and removes all the subsidence feature of interest, including subsidence along the central Washington-Oregon border where the rate of subsidence was consistently greatest. Remaining subsidence features appear to be related to volcanism in the Medicine Lake Volcano region, and possibly anthropogenic use of groundwater resources in the Greater Seattle and Greater Boise metropolitan areas. Regional hydrological models could focus efforts to determine the cause of remaining subsidence.

These results indicate that the dominant source of the interior Pacific Northwest subsidence feature is postseismic relaxation from the 1700 M9.1 Cascadia Earthquake. Contributions from forebulge collapse also play a key role in explaining the subsidence signal. That the subsidence feature is a combination of postseismic relaxation and GIA leads to a host of other questions however, as the corrected GPS Imaging results are now dominated by an uplift signal. Uncertainties could be introduced in the postseismic relaxation model following Young et al. (2023) from using geologic parameters designed for the Great Basin, not for Cascadia which has a higher viscosity and thicker crust. This uplift could also be a consequence of poorly resolved lateral variations in the GIA model that lead to an overestimation of the forebulge collapse signal. Additionally, the elastic and density differences of the Siletzia province, located approximately where observed subsidence is greatest, could be contributing to further uncertainties in both geologic models. It is similarly possible that the vertical velocity field uplift could be related to other loading and/or unloading sources expanded on in previous sections.

2.7 Conclusions

This study attempts to distinguish loading and other geodynamic forces that could potentially contribute to a 50–250 km wide swath of –2 mm/year subsidence shown with GPS Imaging located approximately along the Cascade Arc and spanning Cascadia subduction latitudes. Because the Cascade Arc includes back arc basins that store regional water supply, I first analyzed GRACE data for a hydrological loading signal focused along the subsidence feature of interest. Though there was a region of mass gain approximately located along the Washington-Oregon border, the majority of the study area experienced hydrological mass loss, even in areas of observed subsidence. PDSI and GRACE time series were used to define relatively wet and dry timespans, and GPS

Imaging was performed for early, middle, and late periods. The velocity results indicated that the subsidence feature was larger, subsiding at a greater rate earlier in the GPS data, and gradually diminishing in both rate and extent over time regardless of the climatic pattern of the period. Hydrological loading from climate effects was discounted as the sole source of the subsidence signal.

Next, I investigated the potential contribution of GIA to the subsidence signal caused by lithospheric flexure from Laurentide ice sheet removal and the deglaciated Western Cordilleran to the north. The ICE-6G_C (VM5a) model contains predictions for vertical land motions owing to the forebulge collapse that is widely observed in the Pacific Northwest, but the pattern and rate of subsidence in that model do not fully explain the subsidence signal observed along the Cascade Arc. Correcting the GPS Imaging result for GIA enhances the subsidence signal, extending it further north into Canada and narrowing the subsidence near the Cascades.

Recognizing that the pattern of the subsidence roughly corresponds to Cascadia subduction latitudes and Cascade Arc longitude, a theoretical plate flexure model comprised of realistic mechanical geologic properties was used to find the limits of plate flexure for volcanic and subducting plate loads. The GPS Imaging result constrained permissible plate flexure half width values at 25–125 km. Plate thickness values of 5–50 km were used to calculate flexural rigidity and the flexural parameter used in volcanic and end load models, respectively. The volcanic loading model resulted in plate deflection values of permissible half width distance range of 62–124 km. Extrapolating this full value gives a width of 124–248 km, within the greatest width range of the GPS Imaging result at 250 km. The subducting plate end load model gave permissible half width distances of 42–117 km. The full distance of 84–234 km is also within the range of the GPS Imaging result of 50–250 km. This suggests that lithospheric flexure from volcanic loading and end loading from the subducting Juan de Fuca plate could both possibly contribute to the observed subsidence feature.

I also modeled postseismic relaxation from the 1700 M9.1 Cascadia megathrust earthquake as a potential source of the subsidence. Modeled postseismic subsidence in the interior Pacific Northwest partially explained the signal of interest. When used in conjunction with the GIA model, the resultant vertical velocity field most closely matched the subsidence signal, explaining most of the subsidence. However, subtracting the predictions of these models introduced a widespread uplift signal to the area. Other potential loading and unloading sources cannot be discounted when looking at vertical land motion of the Pacific Northwest.

2.8 Data Acknowledgement

This research was supported by NASA grants NNX16AK89G under project entitled “GPS Imaging of Solid Earth’s Flex and Flow,” and 80NSSC19K1044 under project entitled “GPS Imaging of time-variable Earth deformation for multi-disciplinary science” as part of its Earth Surface and Interior program. Many thanks to the Pacific Northwest Geodetic Array and EarthScope for the operation of the PANGA and Network of the Americas GPS networks and to EarthScope for operating the data archive from which the majority of the GPS data used in this project was obtained. Additional thanks to the operators of the Federal Aviation Administration, GeoBC, Geological Survey of Canada, Leica Smartnet, Linn County, National Oceanic and Atmospheric Administration University of Washington, USGS Cascade Volcano Observatory, and US Coast Guard. GPS data from these networks were used to calculate MIDAS velocities, and current rates available through the NGL in the updated IGS14 reference frame (http://geodesy.unr.edu/velocities/midas.IGS14.vel). Models for non-tidal ocean loading, non-tidal atmospheric loading, and GRACE-based hydrological loading are documented on the NGL website (http://geodesy.unr.edu/gps_timeseries/README_tenv3load.txt) and can be found for each station under columns NTAL, NTOL, and MASC, e.g., station GOBS: http://geodesy.unr.edu/gps_timeseries/tenv3_loadpredictions/GOBS.tenv3. GSFC GRACE trends for the initial and follow-on missions were obtained from: (https://earth.gsfc.nasa.gov/geo/data/grace-mascons). Average Monthly PDSI and precipitation data from 12 climate districts in Washington and Oregon were obtained from the NOAA National Climatic Data Center (https://www.ncdc.noaa.gov/cdo-web/). Several figures herein were made with the Generic Mapping Tools software (Wessel et al., 2013).

2.9 References

Altamimi, Z., Rebischung, P., Métivier, L., & Collilieux, X. (2016). ITRF2014: A new release of the International Terrestrial Reference Frame modeling nonlinear station motions. *J. Geophys. Res. - Solid Earth*, *121*, 6109–6131, https://doi.org/10.1002/2016JB013098.

Argus, D. F., Fu, Y., & Landerer, F. W. (2014). Seasonal variation in total water storage in California inferred from GPS observations of vertical land motion. *Geophys. Res. Lett.*, *41*, 1971–1980, https://doi.org/10.1002/2014GL059570.

Argus, D. F., Landerer, F. W., Wiese, D. N., Martens, H. R., Fu, Y., Famiglietti, J. S., & Watkins, M. M. (2017). Sustained water loss in California's mountain ranges during severe drought from 2012 to 2015 inferred from GPS. *J. Geophys. Res. - Solid Earth*, *122*, 10,559–10,585, https://doi.org/10.1002/ 2017JB014424.

Argus, D. F., Martens, H. R., Borsa, A. A., Knappe, E., Wiese, D. N., Alam, S., ... & Gardiner, W. P. (2022). Subsurface water flux in California's Central Valley and its source watershed from space geodesy. *Geophys. Res. Lett.*, *49*(22), e2022GL099583.

Argus, D. F., Peltier, W. R., Drummond, R., & Moore, A. W. (2014). The Antarctica component of postglacial rebound model ICE-6G_C (VM5a) based on GPS positioning, exposure age dating of ice thicknesses, and relative sea level histories. *Geophysical Journal International*, *198*(1), 537-563.

Bird, P. (2003). An updated digital model of plate boundaries. *Geochemistry, Geophysics, Geosystems*, *4*(3).

Bertiger, W., Bar-Sever, Y., Dorsey, A., Haines, B., Harvey, N., Hemberger, D., ... & Willis, P. (2020). GipsyX/RTGx, a new tool set for space geodetic operations and research. *Advances in space research*, *66*(3), 469-489, https://doi.org/10.1016/j.asr.2020.04.015.

Blewitt, G., Kreemer, C., Hammond, W.C., & Gazeaux, J. (2016). MIDAS Robust Trend Estimator for Accurate GPS Station Velocities Without Step Detection. *J. Geophys. Res. - Solid Earth*, *121*(30), 2054-2068, https://doi.org/10.1002/2015JB012552.

Blewitt, G., Hammond, W.C., & Kreemer, C. (2018). Harnessing the GPS data explosion for interdisciplinary science. *Eos*, *99*, https://doi.org/10.1029/2018EO104623.

Boehm, J., Werl, B., & Schuh, H. (2006). Troposphere mapping functions for GPS and very long baseline interferometry from European Centre for Medium-Range Weather Forecasts operational analysis data. *J. of Geophys. Res. - Solid Earth, 111*, B02406, https://doi.org/10.1029/2005JB003629.

Borsa, A. A., Agnew, D. C., & Cayan, D. R. (2014). Ongoing drought-induced uplift in the western United States. *Science*, *345*(6204), 1587-1590.

Burgette, R. J., Weldon II, R. J., & Schmidt, D. A. (2009). Interseismic uplift rates for western Oregon and along-strike variation in locking on the Cascadia subduction zone. *J. of Geophys. Res. - Solid Earth*, *114*(B1), https://doi.org/10.1029/2008JB005679.

Chang, W. L., Smith, R. B., Farrell, J., & Puskas, C. M. (2010). An extraordinary episode of Yellowstone caldera uplift, 2004–2010, from GPS and InSAR observations. *Geophys. Res. Lett.*, *37*(23).

Chen, J. L., Wilson, C. R., Famiglietti, J. S., & Rodell, M. (2005). Spatial sensitivity of the Gravity Recovery and Climate Experiment (GRACE) time-variable gravity observations, *J. of Geophys. Res. - Solid Earth*, *110*(B8).

Dai, A., & National Center for Atmospheric Research Staff (Eds.). (2017). The Climate Data Guide: Palmer Drought Severity Index (PDSI), https://climatedataguide.ucar.edu/climate-data/palmer-drought-severity-index-pdsi.

Dai, A., Trenberth, K. E., & Qian, T. (2004). A Global Dataset of Palmer Drought Severity Index for 1870–2002: Relationship with Soil Moisture and Effects of Surface Warming. *J. Hydrometeorology*, *5*(6), 1117-1130.

De Martino, P., Dolce, M., Brandi, G., Scarpato, G., & Tammaro, U. (2021). The ground deformation history of the Neapolitan volcanic area (Campi Flegrei caldera, Somma–Vesuvius Volcano, and Ischia island) from 20 years of continuous GPS observations (2000–2019). *Remote Sensing*, *13*(14), 2725.

Dixon, T. H., Mao, A., Bursik, M., Heflin, M., Langbein, J., Stein, R., & Webb, F. (1997). Continuous monitoring of surface deformation at Long Valley Caldera, California, with GPS. *J. of Geophys. Res. - Solid Earth*, *102*(B6), 12017-12034.

Dill, R. (2008). Hydrological model LSDM for operational Earth rotation and gravity field variations. Potsdam: Deutsches GeoForschungsZentrum GFZ.

Dill, R., & Dobslaw, H. (2013). Numerical simulations of global-scale high-resolution hydrological crustal deformations. *J. Geophys. Res. - Solid Earth*, *118*(9), 5008-5017.

Dunbar, B. (2013). Mission Overview, retrieved November 29, 2017 from https://www.nasa.gov/mission_pages/Grace/overview/index.html.

Dzurisin, D., Lisowski, M., & Wicks, C. W. (2009). Continuing inflation at Three Sisters volcanic center, central Oregon Cascade Range, USA, from GPS, leveling, and InSAR observations. *Bulletin of Volcanology*, *71*, 1091-1110.

Faunt, C. C., Sneed, M., Traum, J., & Brandt, J. (2016). Water availability and land subsidence in the Central Valley, California, USA. *Hydrogeology Journal*, *24*(3), 675, https://doi.org/10.1007/s10040-015-1339-x.

Fu, Y., Argus, D. F., & Landerer, F. W. (2015). GPS as an independent measurement to estimate terrestrial water storage variations in Washington and Oregon. *J. of Geophys. Res. - Solid Earth*, *120*(1), 552-566.

Hammond, W. C., Blewitt, G., & Kreemer, C. (2016). GPS Imaging of vertical land motion in California and Nevada: Implications for Sierra Nevada uplift. *J. Geophys. Res. - Solid Earth*, *121*, 7681–7703, https://doi.org/10.1002/2016JB013458.

Han, S. C., Shum, C. K., Jekeli, C., Kuo, C. Y., Wilson, C., & Seo, K. W. (2005). Non-isotropic filtering of GRACE temporal gravity for geophysical signal enhancement. *Geophysical Journal International*, *163*(1), 18-25.

Johnson, R. B., & DeGraff, J. V. (1988). Principles of Engineering Geology. p. 138. New York, United States: Wiley.

Kreemer, C., Hammond, W.C., Blewitt, G. (2018). A robust estimation of the 3D intraplate deformation of the North American plate from GPS, *J. Geophys. Res. - Solid Earth*, *123*, *4388-4412*, https://doi.org/10.1029/2017JB015257.

Kreemer, C., Blewitt, G., & Davis, P. M. (2020). Geodetic Evidence for a Buoyant Mantle Plume Beneath the Eifel Volcanic Area, NW Europe. *Geophysical Journal International, 222*(2), 1316-1332, https://doi.org/10.1093/gji/ggaa227.

Larochelle, S., Chanard, K., Fleitout, L., Fortin, J., Gualandi, A., Longuevergne, L., ... & Avouac, J. P. (2022). Understanding the geodetic signature of large aquifer systems: Example of the Ozark Plateaus in central United States. *J. Geophys. Res. - Solid Earth*, *127*(3), e2021JB023097, https://doi.org/10.1002/essoar.10507870.1.

Lisowski, M., Dzurisin, D., Denlinger, R. P., & Iwatsubo, E. Y. (2008). *Analysis of GPS-measured deformation associated with the 2004-2006 dome-building eruption of Mount St. Helens, Washington* (No. 1750-15, pp. 301-333). US Geological Survey.

Loomis, B. D., Luthcke, S. B., & Sabaka, T. J. (2019). Regularization and error characterization of GRACE mascons. *Journal of Geodesy*, *93*, 1381–1398, https://doi.org/10.1007/s00190-019-01252-y.

Lowry, A. R, and Smith, R. B. (1995). Strength and rheology of the western U.S. Cordillera. *J. Geophys. Res. - Solid Earth*, *100*(B9), 17,947-17,963.

Luthcke, S. B., Sabaka, T. J., Loomis, B. D., Arendt, A. A., McCarthy, J. J., & Camp, J. (2013). Antarctica, Greenland and Gulf of Alaska land ice evolution from an iterated GRACE global mascon solution. *J. Glac. 59*(216), 613-631, https://doi.org/10.3189/2013JoG12J147.

Mazzotti, S., Dragert, H., Hyndman, R. D., Miller, M. M., & Henton, J. A. (2002). GPS deformation in a region of high crustal seismicity: N. Cascadia forearc. *Earth Planet. Sci. Lett.*, *198*(1-2), 41-48.

Mazzotti, S., Lambert, A., Courtier, N., Nykolaishen, L., & Dragert, H. (2007). Crustal uplift and sea level rise in northern Cascadia from GPS, absolute gravity, and tide gauge data. *Geophys. Res. Lett.*, *34*(15).

Mazzotti, S., Jones, C., & Thomson, R. E. (2008). Relative and absolute sea level rise in western Canada and northwestern United States from a combined tide gauge-GPS analysis. *J. Geophys. Res. - Oceans*, *113*(C11).

McCaffrey, R., Qamar, A. I., King, R. W., Wells, R., Khazaradze, G., Williams, C. A., ... & Zwick, P. C. (2007). Fault locking, block rotation and crustal deformation in the Pacific Northwest. *Geophysical Journal International*, *169*(3), 1315-1340.

McNutt, M., & Menard, H. W. (1978). Lithospheric flexure and uplifted atolls. *J. of Geophys. Res. - Solid Earth*, *83*(B3), 1206-1212.

Montillet, J. P., Melbourne, T. I., & Szeliga, W. M. (2018). GPS vertical land motion corrections to sea-level rise estimates in the Pacific Northwest. *J. Geophys. Res. - Oceans*, *123*(2), 1196-1212.

Moore, J. G. (1970). Relationship between subsidence and volcanic load, Hawaii. *Bulletin Volcanologique*, *34*, 562-576.

Orr, W. N., & Orr, E. L. (2006). *Geology of the Pacific Northwest*, p. 2-18. Waveland Press.

Overacker, J., Hammond, W. C., Blewitt, G., & Kreemer, C. (2022). Vertical Land Motion of the High Plains Aquifer Region of the United States: Effect of Aquifer Confinement Style, Climate Variability, and Anthropogenic Activity. *Water Resources Research*, *58*(6), e2021WR031635, https://doi.org/10.1029/2021WR031635.

Peltier, W. R., Argus, D. F., & Drummond, R. (2015). Space geodesy constrains ice age terminal deglaciation: The global ICE-6G_C (VM5a) model. *J. Geophys. Res. - Solid Earth*, *120*, 450–487, https://doi.org/10.1002/2014JB011176.

Peltier, W.R., Argus, D. F., & Drummond, R. (2018). Comment on “An assessment of the ICE-6G_C (VM5a) glacial isostatic adjustment model” by Purcell et al. *J. Geophys. Res. - Solid Earth*, *123*(2), 2019-2028.

Pfeffer, J., Spada, G., Mémin, A., Boy, J.P., & Allemand, P. (2017). Decoding the origins of vertical land motions observed today at coasts, *Geophysical Journal International*, *210*(1), 148–165, https://doi.org/10.1093/gji/ggx142.

Pollitz, F. F., & Evans, E. L. (2017). Implications of the earthquake cycle for inferring fault locking on the Cascadia megathrust. *Geophysical Journal International*, *209*(1), 167-185.

Pollitz, F. F., McCrory, P., Svarc, J., & Murray, J. (2008). Dislocation models of interseismic deformation in the western United States. *J. of Geophys. Res. - Solid Earth*, *113*(B4), B04413-n/a, https://doi.org/10.1029/2007JB005174.

Riddick, S. N., & Schmidt, D. A. (2011). Time-dependent changes in volcanic inflation rate near Three Sisters, Oregon, revealed by InSAR. *Geochemistry, Geophysics, Geosystems*, 12, Q12005. https://doi.org/10.1029/2011GC003826.

Savage, J. C. (1983). A dislocation model of strain accumulation and release at a subduction zone. *J. of Geophys. Res. - Solid Earth*, *88*(B6), 4984-4996.

Schmalzle, G. M., McCaffrey, R., & Creager, K. C. (2014). Central Cascadia subduction zone creep. *Geochemistry, Geophysics, Geosystems*, *15*(4), 1515-1532.

Schmandt, B., & Humphreys, E. (2011). Seismically imaged relict slab from the 55 Ma Siletzia accretion to the northwest United States. *Geology*, *39*(2), 175-178. https://doi.org/10.1130/G31558.1.

Sella, G. F., Stein, S., Dixon, T. H., Craymer, M., James, T. S., Mazzotti, S., & Dokka, R. K. (2007). Observation of glacial isostatic adjustment in “stable” North America with GPS. *Geophys. Res. Lett., 34*(2).

Serpelloni, E., Faccenna, C., Spada, G., Dong, D. & Williams, S. D. (2013). Vertical GPS ground motion rates in the Euro-Mediterranean region: New evidence of velocity gradients at different spatial scales along the Nubia-Eurasia plate boundary. *J. Geophys. Res. - Solid Earth*, *118*(11), 6003-6024.

Swenson, S., & Wahr, J. (2006). Post-processing removal of correlated errors in GRACE data. *Geophys. Res. Lett.*, *33*(8).

Turcotte, D. L., & Schubert, G. (2002). Geodynamics, p. 123-129. Cambridge, United Kingdom: Cambridge University Press.

Vanyan, L. L., Berdichevsky, M. N., Pushkarev, P. Y., & Romanyuk, T. V. (2002). A geoelectric model of the Cascadia subduction zone. *Izvestiia Physics of The Solid Earth C/C Of Fizika Zemli-Rossiiskaia Akademiia Nauk*, *38*(10), 816-845.

Vose, R.S., Applequist, S., Durre, I., Menne, M. J., Williams, C. N., Fenimore, C., Gleason, K, Arndt, D. (2014). Improved historical temperature and precipitation time series for U.S. climate divisions. *Journal of Applied Meteorology and Climatology*, *53*(5), 1232-1251, https://doi.org/10.1175/JAMC-D-13-0248.1.

Wang, K., Wells, R., Mazzotti, S., Hyndman, R. D., & Sagiya, T. (2003). A revised dislocation model of interseismic deformation of the Cascadia subduction zone. *J. of Geophys. Res. - Solid Earth*, *108*(B1).

Watts, A. B. (2001). *Isostasy and Flexure of the Lithosphere*, p. 114-121. Cambridge, United Kingdom: Cambridge University Press.

Watts, A. B., & Cochran, J. R. (1974). Gravity anomalies and flexure of the lithosphere along the Hawaiian-Emperor seamount chain. *Geophysical Journal International*, *38*(1), 119-141.

Wessel, P. (1993). A reexamination of the flexural deformation beneath the Hawaiian Islands. *J. of Geophys. Res. - Solid Earth*, *98*(B7), 12177-12190.

Wessel, P., Smith, W. H. F., Scharroo, R., Luis, J., & Wobbe, F. (2013). Generic Mapping Tools: Improved version released. *Eos, Trans. Am. Geophys. Union*, *94*, 409–410. https://doi.org/10.1002/2013EO450001.

Wicks, C. W., Dzurisin, D., Ingebritsen, S., Thatcher, W., Lu, Z., & Iverson, J. (2002). Magmatic activity beneath the quiescent Three Sisters volcanic center, central Oregon Cascade Range, USA. *Geophys. Res. Lett.*, 29(7), https://doi.org/10.1029/2001GL014205.

Young, Z. M., Kreemer, C., Hammond, W. C., & Blewitt, G. (2023). Interseismic Strain Accumulation between the Colorado Plateau and the Eastern California Shear Zone: Implications for the Seismic Hazard near Las Vegas, Nevada. *Bulletin of the Seismological Society of America*, *113*(2), 856-876, https://doi-org.unr.idm.oclc.org/10.1785/0120220136.

Zhao, Q., Chen, Q., van Dam, T., She, Y., & Wu, W. (2023). The vertical velocity field of the Tibetan Plateau and its surrounding areas derived from GPS and surface mass loading models. *Earth Planet. Sci. Lett.*, *609*, 118107.

2.10 Supplemental Tables

Table S2.1. Pacific Northwest GPS Stations and Vertical Velocity Data.

Station	Latitude (°N)	Longitude (°)	Vertical Velocity (mm/year)	Vertical Uncertainty (mm/year)	Agency or Company	Approximate Location
ABBY	49.0721	-122.1978	-3.188	0.835	GeoBC	Abbotsford, BC, Canada
ABOT	49.0294	-122.2666	-1.710	1.119	GeoBC	Abbotsford, BC, Canada
ABRN	42.7607	-120.1003	-0.026	0.405	NGL	Lakeview, OR
ADLL	42.1964	-120.0067	-1.760	1.336	NGL	Adel, OR
AL2H	48.3898	-123.4875	1.161	0.925	GSC	Metchosin, BC, Canada
ALB4	48.3897	-123.4877	0.403	1.560	GeoBC	Metchosin, BC, Canada
ALBH	48.3898	-123.4875	0.287	0.378	PANGA	Metchosin, BC, Canada
ANAT	46.1329	-117.1354	0.629	0.926	PANGA	Anatone, WA
ARLI	48.1741	-122.1419	-1.033	0.469	PANGA	Arlington, WA
ARLN	45.7082	-120.1833	-1.937	0.531	PANGA	Arlington, OR
ASBU	43.8206	-121.3685	-0.994	0.792	USGS CVO Network	Three Rivers, OR
ASHL	42.1807	-122.6702	0.134	0.694	PANGA	Ashland, OR
BAMF	48.8353	-125.1351	1.618	0.628	PANGA	Bamfield, BC, Canada
BASQ	42.4116	-117.8630	-0.132	0.911	PANGA	Basque, OR
BBUT	41.4388	-118.2950	-0.848	2.616	NGL	Happy Creek Station, NV
BCAB	49.0522	-122.3295	-1.498	1.051	Leica SmartNet	Abbotsford, BC, Canada
BCBU	49.2514	-123.0002	0.755	0.839	Leica SmartNet	Burnaby, BC, Canada
BCCG	49.3119	-117.6530	0.854	0.532	PANGA	Castlegar, BC, Canada
BCCH	49.1466	-122.0026	-4.810	0.803	Leica SmartNet	Chilliwack, BC, Canada
BCCQ	49.2786	-122.7911	0.698	1.299	Leica SmartNet	Coquitlam, BC, Canada
BCCY	49.7001	-124.9837	3.954	0.962	Leica SmartNet	Courtenay, BC, Canada
BCDT	49.0322	-123.0693	0.125	0.837	GeoBC	Delta, BC, Canada
BCES	48.4293	-123.4287	-0.188	0.638	PANGA	Esquimalt, BC, Canada

BCHO	49.3787	-121.4407	0.635	0.942	GeoBC	Hope, BC, Canada
BCKW	49.8848	-119.4954	-2.194	1.240	Leica SmartNet	Kelowna, BC, Canada
BCLC	49.1038	-122.6574	0.175	1.404	GeoBC	Langley, BC, Canada
BCLG	48.4429	-123.5226	0.650	1.545	TopNet	Victoria, BC, Canada
BCLI	49.1151	-123.1471	-2.275	0.609	PANGA	Richmond, BC, Canada
BCMR	49.2212	-122.5385	-1.571	0.696	PANGA	Maple Ridge, BC, Canada
BCNA	49.1839	-123.9532	2.674	2.686	Leica SmartNet	Nanaimo, BC, Canada
BCNS	48.6485	-123.4510	0.354	0.903	GeoBC	North Saanich, BC, Canada
BCPI	49.4993	-119.5922	-0.178	0.995	GeoBC	Penticton, BC, Canada
BCSC	49.4722	-123.7631	1.624	0.846	Leica SmartNet	Sechelt, BC, Canada
BCSF	49.1921	-122.8601	-0.609	0.592	PANGA	Surrey, BC, Canada
BCSL	49.5654	-119.6442	-0.436	0.552	PANGA	Summerland, BC, Canada
BCSM	48.5595	-123.7995	-0.080	0.848	GeoBC	Capital, BC, Canada
BCSQ	49.6992	-123.1540	1.724	1.198	Leica SmartNet	Squamish, BC, Canada
BCSU	49.6022	-119.6817	-0.702	1.235	Leica SmartNet	Summerland, BC, Canada
BCTS	49.0060	-123.0828	-0.307	2.082	Leica SmartNet	Delta, BC, Canada
BCVC	49.2758	-123.0893	-0.566	0.594	PANGA	Vancouver, BC, Canada
BCVI	48.4807	-123.3916	0.328	0.668	GeoBC	Sannich, BC, Canada
BDRY	48.9867	-117.3499	-0.054	0.686	PANGA	Metaline Falls, WA
BELI	48.7553	-122.4790	0.260	0.601	PANGA	Bellingham, WA
BEND	44.0572	-121.3152	-0.973	0.457	PANGA	Bend, OR
BFIR	47.6174	-122.1255	-3.934	0.560	PANGA	Bellevue, WA
BIGD	47.9333	-118.9888	-1.072	0.533	PANGA	Grand Coulee, WA
BILS	47.5393	-124.2525	-0.162	1.006	PANGA	Quinault Reservation, WA
BLDG	46.3170	-117.9753	-1.089	1.115	PANGA	Dayton, WA
BLNP	44.2458	-121.8498	-2.566	1.999	USGS CVO Network	Three Sisters, OR
BLVU	47.5992	-122.1832	-3.768	1.859	PANGA	Bellevue, WA
BLY1	42.4068	-121.0491	-0.840	0.544	PANGA	Bly, OR

BLYN	48.0161	-122.9275	-3.934	2.559	PANGA	Gardiner, WA
BNDM	44.0894	-121.3075	-1.301	0.779	PANGA	Bend, OR
BPKT	46.8832	-120.3271	-2.365	1.121	PANGA	Edgemont, WA
BRBR	41.2303	-120.1091	1.722	1.071	NGL	Surprise Valley, CA
BREW	48.1315	-119.6826	-0.985	0.384	PANGA	Brewster, WA
BRN3	49.2699	-123.0156	-1.830	1.885	PANGA	Burnaby, BC, Canada
BRNB	49.2751	-123.0218	-1.258	0.950	PANGA	Burnaby, BC, Canada
BRNT	44.4402	-118.1913	-0.265	0.925	PANGA	Unity, OR
BSUM	47.5542	-122.1323	-1.868	0.926	PANGA	Bellevue, WA
BTON	45.4858	-122.7974	-1.612	1.050	PANGA	Beaverton, OR
BURN	42.7795	-117.8435	-1.136	0.395	PANGA	Rome, OR
BUTT	41.4789	-119.8407	-1.117	0.615	NGL	Vya, NV
CABL	42.8361	-124.5633	0.467	0.355	PANGA	Sixes, OR
CACC	41.7456	-124.1843	1.798	0.687	NOAA	Crescent City, CA
CAFM	41.0179	-121.4311	0.931	0.823	Leica SmartNet	Fall River Mills, CA
CAMS	41.3142	-122.3144	0.080	1.104	Leica SmartNet	Mt. Shasta, CA
CATH	46.1973	-123.3673	-0.828	0.634	PANGA	East Cathlamet, WA
CBLV	47.6142	-122.1915	-1.421	0.567	PANGA	Bellevue, WA
CCPW	46.3212	-117.9786	-0.977	0.897	PANGA	Dayton, WA
CHCM	48.0106	-122.7759	-0.177	0.650	PANGA	Chimacum, WA
CHEL	47.8316	-119.9899	-1.493	0.665	PANGA	Chelan, WA
CHEM	43.2244	-121.7858	-0.549	0.500	PANGA	Chemult, OR
CHLW	49.1435	-121.9952	1.653	1.454	PANGA	Chilliwack, BC, Canada
CHST	46.6122	-122.9096	0.031	1.639	PANGA	Chehalis, WA
CHW2	49.1529	-121.9538	0.120	1.104	GeoBC	Chilliwack, BC, Canada
CHWK	49.1566	-122.0084	0.247	0.548	PANGA	Chilliwack, BC, Canada
CHZZ	45.4865	-123.9781	0.119	0.548	PANGA	Oceanside, OR
CIHL	43.7509	-121.1487	-0.762	0.669	USGS CVO Network	Bend, OR

CLCV	42.9760	-122.0894	-0.770	0.914	USGS CVO Network	Crater Lake, OR
CLHQ	42.8959	-122.1360	-1.054	1.686	USGS CVO Network	Crater Lake, OR
CLMS	42.9229	-122.0163	0.213	0.977	USGS CVO Network	Crater Lake, OR
CLRS	48.8203	-124.1309	1.572	0.525	PANGA	Cowichan Valley, BC, Canada
CLWZ	42.9343	-122.1492	-1.520	1.180	USGS CVO Network	Crater Lake, OR
CNCR	48.5387	-121.7493	-1.817	0.587	PANGA	Concrete, WA
COLV	48.5448	-117.9033	-0.891	0.534	PANGA	Colville, WA
COND	45.2379	-120.1814	-1.437	0.489	PANGA	Condon, OR
CORV	44.5855	-123.3046	0.306	0.455	PANGA	Corvallis, OR
COTT	41.5907	-119.3418	-1.404	0.772	NGL	Cottonwood Creek, NV
COU2	49.6895	-124.9956	2.778	1.332	GeoBC	Courtenay, BC, Canada
COUG	46.0592	-122.2608	-2.028	1.557	PANGA	Yale Lake, Washington
COUP	48.2173	-122.6856	-0.026	0.531	PANGA	Coupeville, WA
COUR	49.6896	-124.9956	3.680	0.967	GeoBC	Courtenay, BC, Canada
CPCO	43.7221	-121.2332	0.582	1.767	USGS CVO Network	La Pine, OR
CPUD	47.4302	-120.3142	-2.728	1.003	PANGA	Wenatchee, WA
CPXF	46.8401	-122.2565	-1.322	0.610	PANGA	Eatonville, WA
CPXX	46.8401	-122.2565	-1.457	0.475	PANGA	Eatonville, WA
CRA4	49.5221	-115.7689	0.211	0.669	GeoBC	Cranbrook, BC, Canada
CRA5	43.4158	-118.5749	-1.454	1.047	GeoBC	Crane, OR
CRNB	49.6002	-115.6695	1.277	4.252	GSC	East Kootenay, BC, Canada
CROK	46.2746	-122.9125	-2.436	0.576	PANGA	Castle Rock, WA
CSHQ	46.8707	-121.7324	-0.271	0.900	PANGA	Ashford, WA
CSHR	46.8707	-121.7324	-0.504	1.153	USGS CVO Network	Mt. Rainier, WA
CSKI	47.3806	-122.2358	-1.795	0.702	PANGA	Kent, WA
CST1	49.2582	-117.6575	-0.139	0.689	GeoBC	Castlegar, BC, Canada
CTPT	42.3767	-122.8940	-0.401	0.525	PANGA	Central Point, OR
CULM	47.9754	-121.6869	-0.335	1.543	PANGA	Sultan, WA

CUSH	47.4233	-123.2199	-0.293	0.702	PANGA	Lake Cushman, WA
CVO1	45.6109	-122.4961	-2.020	0.587	USGS CVO Network	Vancouver, WA
DANP	46.2800	-119.2763	-0.886	1.066	PANGA	Richland, WA
DBLO	42.7905	-120.4193	-0.148	0.789	NGL	Paisley, OR
DCSO	43.2110	-123.3415	-0.589	0.522	PANGA	Roseburg, OR
DDSN	43.1188	-123.2442	-0.570	0.425	PANGA	Roseburg, OR
DEA2	48.7527	-122.4800	-1.050	1.100	PANGA	Bellingham, WA
DEEJ	47.4688	-123.9261	2.368	0.785	PANGA	Amanda Park, WA
DLTA	49.1335	-123.0153	-1.081	0.793	GeoBC	Delta, BC, Canada
DMND	48.1368	-117.1637	-0.777	0.749	PANGA	Diamond Lake, WA
DR2O	49.3226	-119.6250	0.011	0.722	GeoBC	Okanagan-Similkameen, BC, Canada
DRA3	49.3224	-119.6248	0.542	0.866	GeoBC	Okanagan-Similkameen, BC, Canada
DRA4	49.3227	-119.6245	-0.294	0.729	GeoBC	Okanagan-Similkameen, BC, Canada
DRAO	49.3226	-119.6250	-0.200	0.360	PANGA	Okanagan-Similkameen, BC, Canada
DVPT	47.6561	-118.1478	-1.243	0.558	PANGA	Davenport, WA
DWH1	47.7741	-122.0802	-2.339	1.423	PANGA	Woodinville, WA
EGLI	43.0309	-120.7868	-0.747	2.105	NGL	Summerl Lake, OR
ELGN	45.5649	-117.9284	1.009	0.800	PANGA	Elgin, OR
ELSR	47.4976	-122.7606	-1.960	0.515	PANGA	Boise, ID
EM01	43.5591	-116.2283	-0.980	0.802	GeoBC	Boise, ID
ENTR	45.4313	-117.2881	-0.643	0.528	PANGA	Enterprise, OR
ENUM	47.2062	-121.9556	-1.399	0.637	PANGA	Enumclaw, WA
EPHR	47.3293	-119.5447	-1.214	0.514	PANGA	Ephrata, WA
EVER	41.8646	-120.5827	-0.859	2.405	NGL	Mulkey Place, CA
FAND	43.1470	-120.5804	0.435	3.560	NGL	Christmas Valley, OR
FITZ	42.0221	-120.5892	-1.945	1.238	PANGA	Lakeview, OR
FOST	41.1089	-120.7920	0.477	0.989	NGL	Big Valley, CA
FOUR	43.3643	-120.6881	-0.054	1.172	NGL	Christmas Valley, OR

FRFX	47.0077	-121.9599	-2.546	0.892	PANGA	Fairfax, WA
FRID	48.5352	-123.0181	-0.387	0.892	PANGA	Friday Harbor, WA
FSRH	49.1380	-122.2877	-0.458	1.497	GSC	Mission, BC, Canada
FTS5	46.2049	-123.9561	0.849	0.453	USCG	Fort Stevens, OR
FTS6	46.2052	-123.9560	0.625	0.492	USCG	Fort Stevens, OR
FWBD	44.2919	-117.2216	-0.276	0.519	PANGA	Huntington, OR
GBN1	44.5646	-121.4393	-2.414	1.306	USGS CVO Network	Grandview, OR
GBN2	44.5592	-121.5653	-1.116	2.053	USGS CVO Network	Grandview, OR
GBN3	44.5484	-121.7126	-2.076	1.740	USGS CVO Network	Marion Forks, OR
GBN4	44.5680	-122.1021	-0.984	1.503	USGS CVO Network	Marion Forks, OR
GBN5	44.6021	-122.2360	-1.259	1.061	USGS CVO Network	Detroit, OR
GBN6	44.4249	-121.4229	0.220	1.601	USGS CVO Network	Geneva, OR
GHCL	46.9525	-123.8019	1.147	1.185	PANGA	Aberdeen, WA
GLNW	46.0199	-121.2887	-2.065	1.516	PANGA	Glenwood, WA
GLWD	46.0198	-121.2886	-2.062	1.160	PANGA	Glenwood, WA
GOBS	45.8388	-120.8147	-1.589	0.364	PANGA	Goldendale, WA
GOLY	45.8287	-120.8025	-2.184	0.558	PANGA	Goldendale, WA
GRAV	41.3499	-120.6052	-0.266	1.165	PANGA	Bormister, CA
GRCK	48.1436	-117.6646	-0.901	0.588	PANGA	Valley, WA
GRMD	46.7955	-123.0226	-1.879	0.756	PANGA	Grand Mound, WA
GRP4	48.1947	-122.1273	-1.107	0.728	PANGA	Arlington, WA
GRSV	45.3644	-120.7874	-1.696	0.516	PANGA	Grass Valley, OR
GTPS	42.4345	-123.2974	-0.168	0.559	PANGA	Grants Pass, OR
GUAN	42.0157	-119.4830	-0.892	1.519	NGL	Adel, OR
GWN5	45.7826	-121.3276	-2.062	0.559	USCG	Lyle, WA
GWN6	45.7826	-121.3273	-2.811	0.646	USCG	Lyle, WA
HAHD	47.2908	-121.7881	-2.470	0.688	PANGA	Page, WA
HALF	44.8724	-117.0998	-0.638	0.566	PANGA	Pine, OR

HGP1	47.0193	-122.9211	-2.098	2.941	PANGA	Tumwater, WA
HLSY	44.3776	-123.1091	0.423	1.311	PANGA	Halsey, OR
HOTS	41.1544	-117.4742	-3.122	2.205	NGL	Golconda, NV
HRPR	43.8659	-117.6079	-0.809	0.759	PANGA	Harper, OR
HRTM	42.2470	-119.5642	-1.825	2.979	NGL	Adel, OR
HTCH	47.1917	-120.9659	0.253	2.581	PANGA	South Cle Elum, WA
HUSB	44.1195	-121.8494	7.104	0.844	PANGA	Three Sisters, OR
HWKV	42.1182	-119.1484	0.854	1.120	NGL	Hawk Valley, OR
IDBO	43.6117	-116.3186	-1.937	0.645	TURN	Boise, ID
IDCA	47.7416	-116.7965	-0.266	0.769	TURN	Coeur d'Alene, ID
IDFL	44.0092	-116.9161	-1.660	0.670	TURN	Fruitland, ID
IDHD	43.9086	-116.2020	-0.606	0.825	TURN	Horseshoe Bend, ID
IDLW	46.4089	-117.0262	-0.609	0.741	TURN	Lewiston, ID
IDM1	43.6060	-116.3865	-0.424	1.266	TURN	Meridian, ID
IDMH	43.1376	-115.6697	-2.814	0.659	TURN	Mountain Home, ID
IDMN	43.7057	-116.7012	-2.330	0.952	TURN	Caldwell, ID
IDNA	43.5823	-116.5700	-1.604	0.692	TURN	Nampa, ID
IDNP	45.9397	-116.1213	-0.517	0.424	PANGA	Grangeville, ID
IDNR	43.2054	-116.7501	-0.923	0.915	TURN	Reynolds, ID
IDTD	43.6529	-116.2834	-1.788	0.486	PANGA	Boise, ID
INW1	47.7144	-116.9298	-0.390	0.852	PANGA	Post Falls, ID
IWAC	46.3059	-124.0394	0.152	0.985	PANGA	Ilwaco, WA
JAKE	41.1520	-117.0634	1.294	1.408	NGL	Jakes Creek, NV
JIME	45.5231	-122.9905	-1.057	0.574	PANGA	Hillsboro, OR
JKPR	46.5350	-122.8379	-5.562	1.526	PANGA	Chehalis, WA
JOBO	48.5624	-122.4373	-0.862	0.784	PANGA	Edison, WA
JORD	48.4331	-124.0539	4.112	2.338	PANGA	River Jordan, BC, Canada
JRO1	46.2751	-122.2176	-0.984	0.522	PANGA	Mt. St. Helens, WA

JUN1	43.7438	-118.0785	-0.910	0.826	OR DOT	Juntura, OR
KAHL	46.6411	-118.5573	2.787	34.464	PANGA	Kahlotus, WA
KEL1	49.8762	-119.4572	-1.333	1.133	GeoBC	Kelowna, BC, Canada
KELS	46.1182	-122.8961	-1.502	0.829	PANGA	Kelso, WA
KENI	46.1979	-119.1586	-1.231	0.639	PANGA	Kennewick, WA
KFRC	42.2242	-121.7839	-1.100	0.767	PANGA	Klamath Falls, OR
KLO3	49.8774	-119.4576	1.532	1.200	GeoBC	Kelowna, BC, Canada
KLTS	46.6432	-118.5582	-0.998	0.725	PANGA	Kahlotus, WA
KLWN	49.8696	-119.5811	0.289	1.117	GeoBC	West Kelowna, BC, Canada
KOOT	47.7707	-116.8096	-0.755	0.506	PANGA	Coeur d'Alene, ID
KRMT	47.8029	-122.3210	-0.992	1.031	PANGA	Mountlake Terrace, WA
KTBW	47.5473	-122.7954	-0.939	0.396	PANGA	Bremerton, WA
KWBU	43.7524	-121.3120	-2.189	0.919	USGS CVO Network	La Pine, OR
LAPN	43.6646	-121.5060	-0.923	0.661	PANGA	La Pine, OR
LCR1	46.8196	-117.8786	-0.765	0.777	PANGA	LaCrosse, WA
LCSO	44.6344	-123.1067	-0.315	1.631	PANGA	Albany, OR
LFLO	43.9836	-124.1077	-1.166	0.557	PANGA	Florence, OR
LIKE	41.2278	-120.4432	-2.201	1.435	NGL	Likely, CA
LINH	47.0003	-120.5385	-2.102	0.540	PANGA	Ellensburg, WA
LINL	44.1786	-121.9027	-2.750	1.834	USGS CVO Network	Belknap Springs, OR
LKCP	47.9444	-121.8309	-2.115	0.500	PANGA	Everett, WA
LKVW	42.1721	-120.3467	-2.149	0.646	PANGA	Lakeview, OR
LMID	46.3694	-120.2847	-2.313	0.613	PANGA	Toppenish, WA
LNG2	49.0581	-122.7033	-1.824	0.639	GeoBC	Surrey, BC, Canada
LNGB	47.2188	-122.7583	-0.624	0.454	PANGA	Longbranch, WA
LNGV	41.7852	-119.7524	-1.211	0.504	NGL	Long Valley, NV
LNRD	41.4766	-118.7101	-0.551	1.310	NGL	Quinn River Crossing, NV
LOST	41.0739	-119.7738	-1.074	0.448	NGL	Gerlach, NV

LPSB	44.0512	-123.0901	-0.251	0.442	PANGA	Eugene, OR
LSIG	47.6952	-121.6896	-2.262	0.514	PANGA	South Fork Tolt Reservoir, WA
LTAH	47.2824	-117.1639	-0.805	0.470	PANGA	Latah, WA
LVIL	41.0704	-119.3776	-1.201	1.249	NGL	Gerlach, NV
LWCK	46.2781	-124.0538	0.022	1.087	PANGA	Ilwaco, WA
LWST	46.3732	-117.0023	-0.356	0.481	PANGA	Lewiston, ID
MADE	41.0352	-120.4356	-2.969	2.646	NGL	Madeline, CA
MASC	41.6051	-119.5480	-1.236	0.422	NGL	Massacre Range, NV
MCSO	44.9738	-122.9557	0.041	0.457	PANGA	Salem, OR
MDMT	42.4183	-121.2216	-1.965	0.605	PANGA	Beatty, OR
MDRS	44.6640	-121.1304	-1.818	0.550	PANGA	Madras, OR
MECR	44.0853	-121.8252	6.414	1.657	USGS CVO Network	Three Sisters, OR
MGRB	48.9997	-124.6971	3.234	3.141	PANGA	Alberni-Clayoquot, BC, Canada
MHTL	45.3287	-121.7112	-0.986	0.912	PANGA	Mt. Hood, OR
MIS1	49.1592	-122.2876	-0.597	0.720	GeoBC	Mission, BC, Canada
MKAH	48.3707	-124.5892	1.857	0.765	PANGA	Sekiu, WA
MLKE	47.1309	-119.2741	-0.992	0.725	PANGA	Moses Lake, WA
MODB	41.9023	-120.3028	-0.607	0.576	PANGA	Willow Ranch, CA
MON3	46.9829	-123.6036	0.153	0.701	PANGA	Montesano, WA
MRIB	49.4670	-123.9141	2.549	0.798	PANGA	Merry Island, BC, Canada
MRSD	46.7853	-121.7420	-0.496	0.848	PANGA	Mt. Rainier, WA
MSLK	47.1306	-119.2738	-1.834	0.936	PANGA	Moses Lake, WA
MTCL	44.5652	-120.1466	-0.962	0.799	PANGA	Mitchell, OR
MUIR	46.8356	-121.7332	-2.946	0.693	PANGA	Mt. Rainier, WA
MYRA	49.5510	-125.5707	4.365	1.273	PANGA	Strathcona, BC, Canada
NANA	49.1638	-123.9381	1.022	0.599	GeoBC	Nanaimo, BC, Canada
NANI	49.1072	-123.8968	0.346	0.744	GeoBC	Nanaimo, BC, Canada
NANO	49.2948	-124.0865	1.176	0.372	PANGA	Winchelsea Islands, BC, Canada

NCOW	48.8239	-123.7199	0.787	0.701	GeoBC	Duncan, BC, Canada
NEAH	48.2979	-124.6249	2.679	0.625	PANGA	Sekiu, WA
NEWP	44.5850	-124.0619	1.528	0.791	PANGA	Newport, OR
NGWN	42.3063	-119.4047	-1.967	1.998	NGL	Lone Grave Butte, OR
NINT	47.4951	-121.7971	-1.529	0.947	PANGA	North Bend, WA
NORM	43.7389	-121.2527	-0.613	0.766	USGS CVO Network	La Pine, OR
NVAN	49.3223	-123.1069	-0.067	0.855	GeoBC	North Vancouver, BC, Canada
NWBG	45.3001	-122.9755	-1.014	0.636	PANGA	Newberg, OR
NWE3	49.2002	-122.9417	-0.922	0.601	GeoBC	New Westminster, BC, Canada
NWPT	48.1777	-117.0481	0.408	0.778	PANGA	Newport, WA
OAKR	43.7383	-122.4446	-1.810	0.539	PANGA	Oakridge, OR
OBEC	44.0660	-123.0981	-0.767	0.623	PANGA	Eugene, OR
OBSR	46.8998	-121.8154	-0.562	0.546	PANGA	Mt. Rainier, WA
OCEN	46.9524	-124.1597	0.689	0.571	PANGA	Ocean Shores, WA
ODOT	44.8967	-123.0008	-0.362	0.547	PANGA	Salem, OR
ODSA	47.3290	-118.7126	-1.385	0.826	PANGA	Odessa, WA
OKNG	48.3734	-119.5515	-1.747	0.622	PANGA	Okanogan, WA
OLAR	46.9612	-122.9085	-1.279	0.582	PANGA	Tumwater, WA
OLI1	49.1795	-119.5454	-0.869	0.587	GeoBC	Oliver, BC, Canada
OLMP	47.0448	-122.8952	-3.021	0.621	PANGA	Olympia, WA
ONAB	44.5145	-124.0745	-1.559	0.555	PANGA	Seal Rock, OR
ONT1	44.0232	-116.9380	-0.854	0.671	OR DOT	Ontario, OR
ORAL	45.7186	-120.2025	-1.303	0.687	Leica SmartNet	Arlington, OR
ORBN	44.0943	-121.3019	-1.275	1.184	Leica SmartNet	Bend, OR
ORCD	45.2270	-120.1806	-1.668	0.699	Leica SmartNet	Condon, OR
ORDO	45.2341	-122.8159	-1.036	0.753	Leica SmartNet	Aurora, OR
OREU	44.0450	-123.1619	0.016	0.680	Leica SmartNet	Eugene, OR
ORFL	43.9864	-124.1113	-0.224	0.748	Leica SmartNet	Florence, OR

ORGR	45.4976	-122.4159	-1.280	0.731	Leica SmartNet	Gresham, OR
ORHA	44.2898	-123.1544	0.088	0.766	Leica SmartNet	Harrisburg, OR
ORHI	45.5191	-123.0253	-0.915	0.736	Leica SmartNet	Cornelius, OR
ORHM	45.8052	-119.3211	-2.213	0.834	Leica SmartNet	Hermiston, OR
ORHP	45.3607	-119.5652	-1.209	0.752	Leica SmartNet	Heppner, OR
ORK5	42.2888	-121.6693	-2.699	0.750	USCG	Klamath Falls, OR
ORK6	42.2888	-121.6697	-3.376	0.756	USCG	Klamath Falls, OR
ORKF	42.1434	-121.8086	-2.547	0.838	Leica SmartNet	Klamath Falls, OR
ORM1	44.6016	-121.1410	-1.510	0.842	Leica SmartNet	Madras, OR
ORMF	42.3799	-122.8845	0.464	0.707	Leica SmartNet	Central Point, OR
ORMO	45.1545	-122.6020	-1.100	0.760	Leica SmartNet	Molalla, OR
ORMV	45.1879	-123.2091	-0.798	0.729	Leica SmartNet	McMinnville, OR
ORNW	44.6748	-124.0612	0.726	0.873	Leica SmartNet	Newport, OR
OROR	43.7464	-122.4853	-0.859	0.810	Leica SmartNet	Oakridge, OR
ORPE	45.6709	-118.8502	-0.710	0.762	Leica SmartNet	Pendleton, OR
ORPO	45.5070	-122.6728	-1.222	0.569	Leica SmartNet	Portland, OR
ORRB	43.2984	-123.3492	-0.110	0.718	Leica SmartNet	Roseburg, OR
ORS1	44.1642	-119.0588	-0.416	0.605	PANGA	Seneca, OR
ORS2	44.1641	-119.0584	-0.388	0.673	USCG	Seneca, OR
ORSB	44.6253	-124.0488	-3.992	0.620	PANGA	Newport, OR
ORSH	44.3977	-122.7276	-0.639	0.699	Leica SmartNet	Sweet Home, OR
ORSL	44.9730	-122.9553	-0.373	0.762	Leica SmartNet	Salem, OR
ORTA	44.5583	-123.1111	-0.210	0.904	Leica SmartNet	Tangent, OR
ORTI	45.4856	-123.8462	-0.309	0.753	Leica SmartNet	Tillamook, OR
ORWA	45.5864	-120.6866	-1.357	0.724	Leica SmartNet	Wasco, OR
OTHL	46.8226	-119.1679	-1.093	0.986	PANGA	Othello, WA
OTIS	48.4178	-122.3366	-1.295	21.530	PANGA	Mount Vernon, WA
OYLR	47.4746	-122.2048	-2.983	1.034	PANGA	Renton, WA

P013	41.4287	-117.3300	0.315	0.402	NOTA	Paradise Valley, NV
P017	41.2759	-119.9355	-0.471	0.448	NOTA	Hays Canyon Peak, NV
P018	42.9817	-117.0646	-1.049	0.375	NOTA	Jordan Valley, OR
P019	43.3002	-115.3117	-1.396	0.395	NOTA	Castle Rocks, ID
P020	47.0022	-118.5658	-0.833	0.348	NOTA	Lind, WA
P021	48.6747	-118.7303	-0.105	0.405	NOTA	Republic, WA
P022	45.2318	-118.0138	-0.197	0.458	NOTA	La Grande, OR
P023	44.8984	-116.1030	-0.165	0.441	NOTA	McCall, ID
P024	47.5622	-115.8424	-0.365	0.447	NOTA	Wallace, ID
P025	48.7310	-116.2875	0.515	0.445	NOTA	Bonners Ferry, ID
P061	42.9674	-124.0140	-0.224	0.605	NOTA	Myrtle Point, OR
P062	43.1124	-121.0907	-0.311	0.445	NOTA	Silver Lake, OR
P063	44.9227	-120.9462	-1.605	0.410	NOTA	Shaniko, OR
P064	47.9698	-123.4877	0.559	0.673	NOTA	Port Angeles, WA
P065	46.8440	-120.9331	-1.427	0.464	NOTA	Nile, WA
P145	41.3577	-119.6243	-0.680	0.403	NOTA	Vya, NV
P154	41.8071	-123.3601	0.205	0.507	NOTA	Happy Camp, CA
P155	41.2724	-123.1888	-0.343	0.491	NOTA	Sawyers Bar, CA
P179	42.0990	-123.6856	0.046	0.527	NOTA	O'Brien, OR
P191	42.2754	-123.6323	-0.062	0.495	NOTA	Selma, OR
P316	41.5591	-124.0861	-1.242	0.660	NOTA	Requa, CA
P325	41.1517	-123.8826	2.144	0.398	NOTA	Martins Ferry, CA
P347	41.1833	-120.9485	-1.026	0.446	NOTA	Adin, CA
P362	42.2091	-124.2258	1.688	0.436	NOTA	Carpenterville, OR
P363	42.8601	-124.0540	0.280	0.573	NOTA	Powers, OR
P364	43.0903	-124.4093	1.755	0.419	NOTA	Bandon, OR
P365	43.3955	-124.2535	0.418	0.411	NOTA	Coos Bay, OR
P366	43.6143	-123.9796	-0.252	0.506	NOTA	Reedsport, OR

P367	44.5852	-124.0616	-0.558	0.405	NOTA	Newport, OR
P368	42.5035	-123.3834	-0.123	0.426	NOTA	Merlin, OR
P369	43.1401	-123.4295	-0.641	0.467	NOTA	Winston, OR
P370	42.1910	-122.6564	-0.485	0.455	NOTA	Ashland, OR
P371	43.3633	-123.0579	-0.517	0.387	NOTA	Glide, OR
P372	45.4281	-117.2517	-0.408	0.407	NOTA	Enterprise, OR
P373	43.6225	-123.3333	-0.484	0.405	NOTA	Drain, OR
P374	44.3819	-123.5906	-0.308	0.448	NOTA	Alsea, OR
P375	44.6893	-123.4270	0.234	0.452	NOTA	Kings Valley, OR
P376	44.9412	-123.1023	-0.106	0.394	NOTA	Salem, OR
P377	44.0521	-122.8871	-0.612	0.410	NOTA	Springfield, OR
P378	44.5350	-122.9309	-0.248	0.395	NOTA	Lebanon, OR
P379	44.4965	-122.5770	-0.823	0.645	NOTA	Sweet Home, OR
P380	42.2597	-121.7797	-0.855	0.375	NOTA	Klamath Falls, OR
P381	43.0018	-119.9518	-0.311	0.400	NOTA	Wagontire, OR
P382	43.1771	-121.7696	-0.613	0.609	NOTA	Chemult, OR
P383	44.3422	-122.2172	-0.928	0.403	NOTA	Cascadia, OR
P384	44.8411	-122.4828	-0.650	0.484	NOTA	Mill City, OR
P385	44.4348	-121.9458	-1.733	0.639	NOTA	Santiam Junction, OR
P386	44.4028	-118.9678	-0.156	0.424	NOTA	John Day, OR
P387	44.2968	-121.5745	-1.882	0.550	NOTA	Sisters, OR
P388	42.4688	-120.3776	-0.407	0.459	NOTA	Valley Falls, OR
P389	43.8120	-120.6034	-0.331	0.384	NOTA	Brothers, OR
P390	43.0340	-118.9285	-0.124	0.387	NOTA	Narrows, OR
P391	42.2546	-118.4125	-0.557	0.401	NOTA	Fields, OR
P392	43.4468	-119.0010	-1.309	0.366	NOTA	Burns, OR
P393	43.2345	-117.8920	-0.629	0.384	NOTA	Crowley, OR
P394	44.8349	-117.7996	-0.273	0.405	NOTA	Baker City, OR

P395	45.0223	-123.8575	0.027	0.502	NOTA	Otis, OR
P396	45.3095	-123.8229	-0.381	0.600	NOTA	Cloverdale, OR
P397	46.4216	-123.7992	0.402	0.437	NOTA	Naselle, WA
P398	46.9258	-123.9161	0.709	0.459	NOTA	Aberdeen, WA
P399	47.4339	-123.6130	0.575	0.563	NOTA	Quinault, WA
P400	47.5133	-123.8125	1.860	1.120	NOTA	Quinault, WA
P401	47.9372	-124.5570	0.491	0.389	NOTA	Mora, WA
P402	47.7662	-124.3059	1.661	0.415	NOTA	Forks, WA
P403	48.0623	-124.1409	1.916	0.557	NOTA	Sappho, WA
P404	45.1585	-123.3903	-0.683	0.419	NOTA	Bellevue, OR
P405	45.6293	-123.6438	-0.720	0.453	NOTA	Jordan Creek, OR
P406	45.1904	-123.1523	-0.606	0.397	NOTA	McMinnville, OR
P407	45.9546	-123.9310	0.352	0.562	NOTA	Seaside, OR
P408	46.2005	-123.3766	-0.750	0.464	NOTA	Cathlamet, WA
P409	45.8513	-123.2395	-0.558	0.418	NOTA	Vernonia, OR
P410	46.1111	-123.0786	-1.543	0.469	NOTA	Ranier, OR
P411	45.5380	-123.1574	-0.386	0.492	NOTA	Forest Grove, OR
P412	45.2211	-122.5891	-1.196	0.389	NOTA	Mulino, OR
P413	48.4265	-120.1496	-0.857	0.499	NOTA	Winthrop, WA
P414	45.8349	-122.6928	-1.317	0.406	NOTA	Ridgefield, WA
P415	46.6560	-123.7299	-0.108	0.468	NOTA	Raymond, WA
P416	47.0399	-121.5969	-1.191	0.475	NOTA	Mt. Rainier, WA
P417	46.5747	-123.2979	-1.047	0.483	NOTA	Pe Ell, WA
P418	47.2366	-123.4078	-0.580	0.441	NOTA	Matlock, WA
P419	47.4093	-123.3665	-0.343	0.555	NOTA	Lake Cushman, WA
P420	46.5886	-122.8663	-1.180	0.369	NOTA	Forest, WA
P421	46.5319	-122.4292	-1.385	0.490	NOTA	Ajlune, WA
P422	46.7979	-116.9797	-0.610	0.394	NOTA	Viola, ID

P423	47.2879	-122.9412	-0.804	0.454	NOTA	Grant, WA
P424	47.8232	-122.8747	-0.096	0.554	NOTA	Quilcene, WA
P425	46.4527	-122.8454	-1.729	0.461	NOTA	Toledo, WA
P426	47.8027	-122.5146	-1.757	0.552	NOTA	Kingston, WA
P427	45.4302	-122.3406	-1.841	0.397	NOTA	Boring, OR
P429	45.6761	-121.8774	-1.915	0.478	NOTA	Cascade Locks, OR
P430	47.0038	-123.4362	-0.528	0.604	NOTA	Elma, WA
P431	46.5721	-121.9885	-1.536	0.418	NOTA	Randle, WA
P432	46.6229	-121.6832	-1.110	0.457	NOTA	Packwood, WA
P433	44.5325	-119.8720	-1.125	0.584	NOTA	Antone, OR
P434	47.7402	-121.0756	-0.958	0.424	NOTA	Wellington, WA
P435	48.0595	-123.5033	-0.255	0.606	NOTA	Elwha, WA
P436	48.0453	-123.1343	0.058	0.515	NOTA	Sequim, WA
P437	48.0018	-122.4592	-1.408	0.449	NOTA	South Whidbey, WA
P438	48.4191	-122.6703	-0.729	0.410	NOTA	Northwest Island, Washington
P439	48.7082	-122.9093	-0.566	0.405	NOTA	Eastsound, WA
P440	48.8562	-122.4933	-0.966	0.425	NOTA	Bellingham, WA
P441	48.9160	-122.1396	-0.453	0.537	NOTA	Kendall, WA
P442	48.2605	-121.6155	-1.321	0.611	PANGA	Darrington, WA
P443	48.5096	-121.2856	0.084	0.547	NOTA	Concrete, WA
P444	48.7302	-121.0675	-0.888	0.714	PANGA	Ruby Mountain, WA
P445	45.5901	-120.6722	-1.525	0.419	NOTA	Wasco, OR
P446	46.1157	-122.8928	-1.307	0.458	NOTA	Kelso, WA
P447	45.4528	-119.6901	-1.377	0.393	NOTA	Lexington, OR
P448	45.9106	-120.0052	-2.764	0.410	NOTA	Alderdale, WA
P449	46.2598	-119.6310	-1.697	0.402	NOTA	Chaffee, WA
P450	45.9533	-119.5442	-1.683	0.369	NOTA	Paterson, WA
P451	46.7928	-119.0414	-1.016	0.374	NOTA	Bruce, WA

P452	47.4035	-119.4873	-1.111	0.454	NOTA	Soap Lake, WA
P453	47.7591	-118.7455	-0.930	0.414	NOTA	Wilbur, WA
P454	47.9538	-118.9926	-0.791	0.380	NOTA	Grand Coulee, WA
P655	41.2945	-122.2063	-0.485	0.861	NOTA	Mt. Shasta, CA
P656	41.3448	-122.1958	0.155	7.537	NOTA	Mt. Shasta, CA
P657	41.3812	-122.2938	-0.376	0.652	NOTA	Mt. Shasta, CA
P658	41.4792	-122.1909	-0.363	0.658	NOTA	Mt. Shasta, CA
P659	41.4537	-122.0927	-0.138	1.139	NOTA	Mt. Shasta, CA
P660	41.4096	-122.0677	-1.052	1.269	NOTA	Mt. Shasta, CA
P661	41.4636	-122.3127	-0.423	0.545	NOTA	Mt. Shasta, CA
P663	41.5319	-122.1529	-0.285	0.719	NOTA	Mt. Shasta, CA
P672	41.7116	-121.5069	-0.988	0.457	NOTA	Lava Beds NM, CA
P673	41.5858	-121.6130	-4.141	0.804	NOTA	Mt. Hoffman, CA
P674	41.6163	-121.4900	-1.852	0.584	NOTA	Mt. Hoffman, CA
P687	46.1096	-122.3546	-1.456	0.713	NOTA	Cougar, WA
P688	46.0301	-122.1642	-0.887	0.802	NOTA	Cougar, WA
P689	46.1896	-122.3606	-1.138	0.398	NOTA	Mt. St. Helens, WA
P690	46.1800	-122.1899	-2.426	0.888	NOTA	Mt. St. Helens, WA
P691	46.2315	-122.2270	-0.382	0.484	NOTA	Mt. St. Helens, WA
P692	46.2245	-122.1842	-0.706	0.556	NOTA	Mt. St. Helens, WA
P693	46.2103	-122.2023	-2.604	0.870	NOTA	Mt. St. Helens, WA
P694	46.2996	-122.1819	-0.280	0.524	NOTA	Mt. St. Helens, WA
P695	46.1990	-122.1642	-1.966	0.658	NOTA	Mt. St. Helens, WA
P696	46.1969	-122.1516	-1.644	0.545	NOTA	Mt. St. Helens, WA
P697	46.1876	-122.1766	-4.019	1.073	NOTA	Mt. St. Helens, WA
P698	46.1735	-122.1606	-1.515	0.526	NOTA	Mt. St. Helens, WA
P699	46.1898	-122.2032	-3.995	1.953	NOTA	Mt. St. Helens, WA
P700	46.1781	-122.2174	-0.823	0.514	NOTA	Mt. St. Helens, WA

P701	46.1946	-122.1334	-0.514	0.585	NOTA	Mt. St. Helens, WA
P702	46.3002	-122.3456	-1.286	0.417	NOTA	Mt. St. Helens, WA
P703	46.1453	-122.1962	-1.021	0.872	NOTA	Mt. St. Helens, WA
P705	46.1730	-122.3106	-1.085	0.728	NOTA	Mt. St. Helens, WA
P730	41.3592	-120.8282	-0.767	0.526	NOTA	Canby, CA
P731	41.3325	-120.4728	-0.917	0.469	NOTA	McArthur, CA
P732	43.3925	-123.8914	-0.216	0.481	NOTA	Allegany, OR
P733	42.4420	-124.4133	1.596	0.463	NOTA	Wedderburn, OR
P734	42.0766	-124.2933	2.080	0.472	NOTA	Brookings, OR
P735	42.6916	-123.2310	0.063	0.489	NOTA	Golden, OR
P736	42.5798	-121.8801	-0.759	0.488	NOTA	Chiloquin, OR
P737	42.7271	-122.6096	-1.122	0.561	NOTA	Prospect, OR
P738	42.5461	-119.6587	-0.285	0.510	NOTA	Plush, OR
P739	42.0202	-117.7254	-0.289	0.443	NOTA	McDermitt, NV
P784	41.8308	-122.4205	-0.316	0.491	NOTA	Ager, CA
P786	41.8455	-123.9808	0.886	0.591	NOTA	Gasquet, CA
P791	45.3445	-121.6727	-1.214	0.834	NOTA	Mt. Hood, OR
P792	46.2446	-122.1369	-1.078	2.178	NOTA	Mt. St. Helens, WA
P813	47.7592	-118.7455	-1.657	0.739	NOTA	Wilbur, WA
P814	47.7592	-118.7454	-1.689	0.704	NOTA	Wilbur, WA
P815	47.9372	-124.5572	0.782	0.554	NOTA	Quillayute, WA
P816	47.9371	-124.5571	0.658	0.577	NOTA	Quillayute, WA
P820	42.8619	-124.0539	0.912	0.852	NOTA	Powers, OR
P821	43.1446	-123.4290	1.520	1.006	NOTA	Winston, OR
PABH	47.2128	-124.2046	-0.227	0.338	PANGA	Pacific Beach, WA
PARP	41.3242	-117.6980	-0.621	1.929	NGL	Paradise Valley, NV
PCOL	47.1721	-122.5708	-1.204	0.479	PANGA	Lakewood, WA
PCS2	44.9191	-123.3278	-1.702	0.852	PANGA	Dallas, OR

PDTN	45.6659	-118.7569	-1.034	0.735	PANGA	Pendleton, OR
PDXA	45.5969	-122.6092	-1.503	0.668	PANGA	Portland, OR
PER1	47.9817	-122.2081	-4.227	1.497	PANGA	Everett, WA
PFLD	47.8985	-122.2822	-1.472	0.445	PANGA	Everett, WA
PGC5	48.6485	-123.4511	0.104	0.424	PANGA	North Saanich, BC, Canada
PKDL	45.5183	-121.5637	-1.902	0.780	PANGA	Mt. Hood, OR
PKWD	46.5998	-121.6770	-2.779	1.008	PANGA	Randle, WA
PLMN	46.7339	-117.1931	-1.024	0.469	PANGA	Pullman, WA
PLNA	44.1321	-119.9668	-0.856	0.558	PANGA	Paulina, OR
PMAR	43.9907	-121.6867	-1.296	0.710	PANGA	Mt. Bachelor, OR
PNCL	48.1015	-123.4153	-1.940	4.139	PANGA	Port Angeles, WA
PNDL	45.6696	-118.7915	-1.441	1.035	PANGA	Pendleton, OR
PNHG	46.8591	-121.6426	-8.309	5.086	PANGA	Mt. Rainier, WA
PNHR	46.8590	-121.6426	-17.103	6.196	PANGA	Mt. Rainier, WA
PNTC	49.5008	-119.5939	-0.077	0.602	GeoBC	Penticton, BC, Canada
PNVL	44.3121	-120.8446	-1.851	0.500	PANGA	Prineville, OR
POME	46.4799	-117.6317	0.823	0.939	PANGA	Pomeroy, WA
PORC	41.5995	-120.7432	-2.038	0.641	NGL	Porcupine Rim, CA
POTH	44.0969	-122.0398	-3.663	1.749	USGS CVO Network	Belknap Springs, OR
POUL	47.7547	-122.6672	-4.813	2.586	PANGA	Poulsbo, WA
PRDY	47.3914	-122.6095	-0.995	0.462	PANGA	Purdy, WA
PRSR	46.2157	-119.7908	-1.385	0.697	PANGA	Prosser, WA
PSEA	47.4514	-122.3202	-2.253	0.732	PANGA	SeaTac, WA
PSPT	42.7548	-122.4895	-0.986	0.588	PANGA	Prospect, OR
PTAA	48.1168	-123.4944	0.398	0.661	PANGA	Port Angeles, WA
PTAL	49.2563	-124.8610	2.932	0.384	PANGA	Alberni-Clayoquot, BC, Canada
PTRF	48.5443	-124.4131	2.154	0.586	PANGA	Port Renfrew, BC, Canada
PTSG	41.7827	-124.2552	2.124	0.381	PANGA	Crescent City, CA

PTSN	45.9392	-119.6098	-0.044	0.866	PANGA	Paterson, WA
PUPU	47.4996	-122.0081	-0.996	1.052	PANGA	Issaquah, WA
QMAR	47.7751	-120.9656	0.341	1.127	PANGA	Berne, WA
QUL2	49.3459	-124.4430	1.079	0.689	GeoBC	Qualicum Beach, BV, Canada
RDL2	42.9545	-123.3622	-0.206	1.449	PANGA	Riddle, OR
REDM	44.2598	-121.1479	-1.323	0.367	PANGA	Redmond, OR
REED	43.7010	-124.1078	-1.982	0.600	PANGA	Reedsport, OR
RIC2	46.2774	-119.2777	-0.978	0.671	PANGA	Richland, WA
RKD1	48.9644	-119.4130	0.033	0.577	PANGA	Oroville, WA
RMDB	44.2598	-121.1479	-1.889	0.465	PANGA	Redmond, OR
RMRK	46.7495	-120.7923	-1.518	0.721	PANGA	Naches, WA
ROKY	47.0196	-122.3462	-1.347	1.423	PANGA	Elk Plain, WA
RPT5	47.3875	-122.3748	-2.327	0.515	USCG	Vashon, WA
RPT6	47.3872	-122.3750	-2.666	0.498	USCG	Puget Sound, Washington
RPUB	48.6494	-118.7341	-0.299	0.658	PANGA	Republic, WA
RSBG	43.2350	-123.3594	-0.487	0.721	PANGA	Roseburg, OR
RYA1	48.2175	-116.2620	-1.083	0.924	PANGA	Hope, ID
RYMD	46.6841	-123.7304	-1.258	0.533	PANGA	Raymond, WA
SAC4	48.5667	-123.4207	-1.941	53.096	GeoBC	Saanichton, BC, Canada
SAMM	47.5399	-122.0332	-1.920	0.798	PANGA	Issaquah, WA
SATS	46.9657	-123.5412	-1.676	2.725	PANGA	Montesano, WA
SC00	46.9509	-120.7246	-1.519	0.469	PANGA	Ellensburg, WA
SC02	48.5462	-123.0076	-0.280	0.365	PANGA	Friday Harbor, WA
SC03	47.8166	-123.7057	1.984	1.227	PANGA	Olympic National Park, WA
SC04	48.9232	-123.7041	0.666	0.424	PANGA	Chemainus, BC, Canada
SCHO	41.1297	-118.3554	-1.790	1.371	NGL	Winnemucca, NV
SCMV	48.4179	-122.3372	-1.624	0.636	PANGA	Mount Vernon, WA
SEAI	47.6870	-122.2563	-1.852	0.612	NOAA	Seattle, WA

SEAS	45.9842	-123.9224	0.635	0.567	PANGA	Seaside, OR
SEAT	47.6540	-122.3095	-1.817	0.365	PANGA	Seattle, WA
SEDK	48.5042	-122.2389	-0.510	0.930	PANGA	Sedro-Woolley, WA
SEDR	48.5216	-122.2238	-1.358	0.449	PANGA	Sedro-Woolley, WA
SEPR	46.2003	-122.1910	-20.172	1.939	PANGA	Mt. St. Helens, WA
SEQM	48.0914	-123.1135	0.354	0.734	PANGA	Sequim, WA
SHLD	41.8684	-119.0157	-0.430	0.372	PANGA	Denio, NV
SHRK	45.4643	-121.5288	-1.884	0.934	PANGA	Mt. Hood, OR
SKCO	45.6942	-121.8840	-3.470	1.281	PANGA	Stevenson, WA
SKGT	48.4334	-122.3425	-1.693	0.881	PANGA	Mt. Vernon, WA
SKMA	45.6942	-121.8840	-1.259	1.123	PANGA	Stevenson, WA
SKND	41.0316	-118.7082	0.014	3.486	NGL	Sulphur, NV
SLUM	41.1602	-117.9314	-1.844	2.034	NGL	Winnemucca, NV
SMAI	47.5236	-122.3451	-1.957	0.436	PANGA	Seattle, WA
SNDR	43.0033	-120.2510	-0.268	0.535	NGL	Saunders Rim, OR
SNOQ	47.3913	-121.3883	-0.895	0.752	PANGA	Snoqualmie Pass, WA
SNRS	46.9146	-121.6436	-0.839	2.089	PANGA	Ashford, WA
SPKN	47.6277	-117.5026	-0.683	0.567	PANGA	Spokane, WA
SPKV	47.6774	-117.2715	-0.025	1.440	PANGA	Spokane, WA
SPN5	47.5184	-117.4237	-0.966	0.515	USCG	Spokane, WA
SPN6	47.5184	-117.4234	-1.518	0.531	USCG	Spokane, WA
SPRA	44.8267	-119.7763	-1.185	0.534	PANGA	Spray, OR
SPRG	47.3099	-117.9753	-0.504	0.443	PANGA	Sprague, WA
SQAW	44.1924	-121.6505	-0.952	1.487	USGS CVO Network	Three Sisters, OR
SQIM	48.0824	-123.1020	-0.957	0.914	PANGA	Sequim, WA
SQMS	49.7252	-123.1417	0.640	0.864	GeoBC	Squamish, BC, Canada
SSHO	47.6823	-122.3152	-2.256	0.537	PANGA	Seattle, WA
STAY	44.8307	-122.8209	-0.156	0.466	PANGA	Sublimity, OR

STHM	44.3962	-122.7342	-0.893	2.036	PANGA	Sweet Home, OR
SUHS	42.9869	-123.3288	-0.342	0.779	PANGA	Tri-City, OR
SUPR	41.6618	-120.0690	-2.198	0.628	NGL	Surprise Valley, CA
SUR6	49.0742	-122.6919	-1.331	3.737	GSC	Surrey, BC, Canada
SURR	49.1746	-122.6951	-3.636	0.595	GeoBC	Surrey, BC, Canada
SVI2	43.6431	-121.2533	-0.538	0.673	USGS CVO Network	La Pine, OR
SWNB	43.6727	-121.3554	-0.765	0.566	USGS CVO Network	La Pine, OR
SWRN	42.0489	-120.0458	-2.692	1.680	NGL	Adel, OR
SYNC	44.0239	-121.7767	0.992	3.121	USGS CVO Network	Three Sisters, OR
TACO	47.2289	-122.4715	-2.410	0.511	PANGA	Tacoma, WA
TAY1	46.7146	-117.1762	-0.901	1.159	PANGA	Pullman, WA
TDLS	45.6077	-121.1295	-2.032	0.695	PANGA	The Dalles, OR
TFNO	49.1541	-125.9078	1.989	0.571	PANGA	Tofino, BC, Canada
TGAU	46.2192	-122.1923	-1.172	2.137	USGS CVO Network	Mt. St. Helens, WA
TGUA	46.2192	-122.1923	-2.488	0.738	PANGA	Mt. St. Helens, WA
THAR	46.2753	-122.1740	-0.936	0.655	PANGA	Mt. St. Helens, WA
THRM	44.0898	-121.6196	0.597	2.167	USGS CVO Network	Three Sisters, OR
THUN	47.1058	-122.2885	-1.276	0.406	PANGA	Puyallup, WA
TILL	45.4551	-123.8308	-0.431	0.571	PANGA	Tillamook, OR
TMBU	43.6018	-121.1446	-0.535	0.780	USGS CVO Network	Sunriver, OR
TPW2	46.2074	-123.7684	-0.229	0.407	PANGA	Navy Heights, OR
TRAI	49.0981	-117.7100	-1.441	0.894	PANGA	Trail, BC, Canada
TRND	41.0539	-124.1509	-1.179	0.432	PANGA	Trinidad, CA
TSEP	46.2000	-122.1907	-35.245	42.398	USGS CVO Network	Mt. St. Helens, WA
TSTU	46.2369	-122.2241	-3.848	0.625	PANGA	Mt. St. Helens, WA
TULE	41.0178	-120.0230	1.087	1.169	NGL	Tuledad Canyon, CA
TUMW	46.9843	-122.9122	-1.315	0.836	PANGA	Tumwater, WA
TWHL	47.0159	-122.9229	-1.005	0.416	PANGA	Tumwater, WA

TWIW	46.2129	-122.1587	-0.721	0.665	PANGA	Mt. St. Helens, WA
TWRI	46.1979	-122.2119	-2.499	1.377	PANGA	Mt. St. Helens, WA
TWSP	48.3655	-120.1217	-1.004	1.040	PANGA	Twisp, WA
UCLU	48.9256	-125.5416	1.216	0.422	PANGA	Ucluelet, BC, Canada
UFDA	47.7550	-122.6674	-0.458	0.557	PANGA	Poulsbo, WA
UKIA	45.1328	-118.9366	-0.699	0.494	PANGA	Ukiah, OR
VCWA	45.6176	-122.5161	-1.783	0.652	PANGA	Vancouver, WA
VNCR	49.2660	-123.0985	-3.957	3.001	PANGA	Mattawa, WA
VRNT	46.6369	-119.7320	-1.032	0.725	PANGA	Brewster, WA
WABR	48.1004	-119.7803	-0.868	0.806	PANGA	Brewster, WA
WACC	47.6115	-119.2934	-0.700	0.655	PANGA	Coulee City, WA
WACS	46.6754	-122.9700	-1.143	0.556	PANGA	Chehalis, WA
WACX	46.9545	-117.3324	-0.817	0.766	Leica SmartNet	Colfax, WA
WACY	47.5637	-117.5947	0.162	0.670	Leica SmartNet	Cheney, WA
WAEL	46.9835	-120.5470	-1.777	0.693	Leica SmartNet	Ellensburg, WA
WAEN	47.2033	-121.9854	-1.502	0.691	Leica SmartNet	Enumclaw, WA
WAEV	47.9815	-122.2081	-1.641	0.553	PANGA	Everett, WA
WAFD	48.8284	-122.5551	-1.013	0.632	Leica SmartNet	Ferndale, WA
WAFH	48.5327	-123.0186	-0.247	0.787	Leica SmartNet	Friday Harbor, WA
WAFR	48.5306	-123.0272	-2.548	1.647	Leica SmartNet	Friday Harbor, WA
WAGO	41.2916	-119.5140	-1.621	0.436	NGL	Wagontire Spring, NV
WAKI	47.7088	-122.1875	-1.667	0.572	Leica SmartNet	Kirkland, WA
WAKL	46.1135	-122.8895	-1.709	0.786	Leica SmartNet	Kelso, WA
WALA	46.0915	-118.2581	0.460	0.845	PANGA	Walla Walla, WA
WALL	41.2485	-119.7188	-3.191	1.201	NGL	Wall Canyon, NV
WAMC	45.2238	-121.2736	-1.649	0.607	PANGA	Wamic, OR
WAMO	46.5547	-122.2737	-1.491	0.815	Leica SmartNet	Morton, WA
WAMS	46.9776	-123.6024	-0.087	0.732	Leica SmartNet	Montesano, WA

WAMV	48.3845	-122.3331	-1.108	0.868	Leica SmartNet	Mt. Vernon, WA
WAMW	46.7618	-119.9324	-1.377	0.901	Leica SmartNet	Mattawa, WA
WAOL	47.0465	-122.8438	-0.815	0.773	Leica SmartNet	Olympia, WA
WAOT	46.8104	-119.1737	-1.213	0.653	Leica SmartNet	Othello, WA
WAOY	47.0479	-122.8389	-4.064	1.065	Leica SmartNet	Olympia, WA
WAPA	46.2491	-119.0803	-0.926	0.718	Leica SmartNet	Pasco, WA
WAPO	47.8035	-122.5692	-1.138	0.498	Leica SmartNet	Poulsbo, WA
WAPS	47.4512	-122.3208	-1.870	0.520	PANGA	SeaTac, WA
WAQU	47.2351	-119.8379	-1.196	0.684	Leica SmartNet	Quincy, WA
WARM	47.6807	-122.1367	-2.045	0.716	Leica SmartNet	Redmond, WA
WARZ	47.1211	-118.3832	-1.247	0.724	Leica SmartNet	Ritzville, WA
WASK	47.6657	-117.4206	-0.412	0.473	Leica SmartNet	Spokane, WA
WASN	46.3038	-120.0214	-1.472	0.731	Leica SmartNet	Sunnyside, WA
WASQ	47.5266	-121.8262	-2.685	0.583	PANGA	Snoqualmie, WA
WATK	47.2279	-117.0676	0.943	0.755	Leica SmartNet	Tekoa, WA
WAWE	47.4044	-120.2850	-1.716	0.615	Leica SmartNet	East Wenatchee, WA
WAWL	46.0818	-118.2822	-0.754	0.682	Leica SmartNet	Walla Walla, WA
WAYA	46.6167	-120.5511	-1.348	0.781	Leica SmartNet	Yakima, WA
WDBN	45.1709	-122.8701	-4.010	0.547	PANGA	Woodburn, OR
WEBG	45.7796	-122.5628	0.723	0.938	PANGA	Battle Ground, WA
WHBR	44.1632	-121.9786	-2.116	1.729	USGS CVO Network	Belknap Springs, OR
WHD5	48.3127	-122.6961	-1.559	0.566	USCG	Oak Harbor, WA
WHD6	48.3124	-122.6961	-2.562	0.627	USCG	Oak Harbor, WA
WIF3	44.0596	-121.8176	4.612	2.548	USGS CVO Network	Three Sisters, OR
WIFC	44.0596	-121.8176	-3.374	4.098	PANGA	Three Sisters, OR
WIFR	44.0597	-121.8176	3.592	1.610	PANGA	Three Sisters, OR
WMSG	45.1313	-121.5973	-1.191	0.628	PANGA	Maupin, OR
WNTH	48.4632	-120.1730	-0.054	1.701	PANGA	Winthrop, WA

WRNR	41.5571	-120.4047	-0.461	0.827	NGL	Surprise Station, CA
WVN3	49.3517	-123.2511	0.348	3.374	GSC	West Vancouver, BC, Canada
XANE	47.4449	-120.3662	-0.642	0.932	PANGA	West Wenatchee, WA
YAKI	46.6050	-120.5051	-2.461	0.482	PANGA	Yakima, WA
YAKS	46.5845	-120.5299	-1.976	1.715	PANGA	Yakima, WA
YBHB	41.7317	-122.7107	-0.449	0.550	PANGA	Yreka, CA
YELM	46.9487	-122.6057	-0.978	0.462	PANGA	Yelm, WA
YONC	43.6341	-123.2983	-0.534	0.568	PANGA	Yoncalla, OR
ZSE1	47.2870	-122.1884	-1.655	0.507	FAA	Auburn, WA

FAA: Federal Aviation Administration
GSC: Geological Survey of Canada
NGL: Nevada Geodetic Laboratory
NOAA: National Oceanic and Atmospheric Administration
NOTA: Network Of The Americas
PANGA: Pacific Northwest Geodetic Array
TURN: The Utah Reference Network
USCG: United States Coast Guard
USGS CVO: United States Geological Survey Cascades Volcano Observatory

Table S2.2. GSFC GRACE mascon IDs for the Pacific Northwest.

Mascon ID	Equivalent Water Height Trend (cm/year)
1826	-0.7184
1827	-0.7895
1828	-0.8837
1829	-0.8894
1830	-0.6757
1831	-0.8684
1832	-0.9448
1833	-0.9083
1866	-0.7122
1869	-0.7898
1870	-0.6595
1871	-0.5380
1872	-0.4474
1946	-1.3535
1947	-0.9750
1948	-0.5951
1949	-0.7951
1950	-0.6393
1951	-0.4409
1952	-0.1993
1954	-0.0654
1955	-0.1074

1956	-0.1281
1957	-0.0465
1958	0.1202
1960	0.3790
1961	0.1820
1962	0.0194
1963	-0.0294
1964	0.0471
1967	0.5325
1968	0.4552
1969	0.2436
1970	0.0066
1971	-0.1451
1972	-0.1430
1973	-0.0185
1975	0.2123
1976	0.1468
1977	-0.0221
1978	-0.2304
1979	-0.3526
1980	-0.3502
1981	-0.2319
1983	-0.2420
1984	-0.3476
1985	-0.4755
1986	-0.5669
1987	-0.5763
1988	-0.4858
1989	-0.3349
1993	-0.5199
1994	-0.6380
1995	-0.7542
1996	-0.7410
1997	-0.6650
1998	-0.5364
1999	-0.3956
2003	-0.6095
2004	-0.8229
2005	-0.5959
2006	-0.4750
2024	-2.0273
2025	-1.7196
2026	-0.9637
2180	-2.1348
2181	-2.1789
2182	-1.1780
2183	-1.1750
2184	-1.0875
2185	-0.1303
2186	-0.0585
2187	0.4326
2188	0.4719
2247	-0.2284
15093	0.5216

Table S2.3. Early, Middle, and Late Period Velocity Data.

Station	Early		Middle		Late	
	Vertical Velocity (mm/year)	Vertical Uncertainty (mm/year)	Vertical Velocity (mm/year)	Vertical Uncertainty (mm/year)	Vertical Velocity (mm/year)	Vertical Uncertainty (mm/year)
ABBY					-2.809	0.978
ABOT					-2.012	1.111
ADLL			-3.448	2.723	0.669	1.898
AL2H					1.571	0.888
ALB4					0.215	1.540
ALBH	-0.922	0.817	1.182	0.792	1.237	0.869
ANAT	2.604	3.051	0.066	1.398	-1.788	10.077
ARLI	-1.628	1.054	-1.804	0.773	-0.475	0.913
ARLN	-5.264	1.688	-2.036	0.799	-1.176	1.070
ASBU			-2.231	1.127	-0.291	1.209
ASHL	0.973	1.511	0.038	1.183	-0.234	1.331
BAMF	1.533	1.389	0.554	1.114	2.312	1.234
BASQ					-0.252	0.908
BBUT			-0.790	2.619		
BCAB			2.029	4.653	-0.452	0.823
BCBU			-10.258	4.838	1.257	0.911
BCCG			0.723	0.679	0.920	0.994
BCCH			-4.767	4.036	-2.849	1.037
BCCQ			-4.514	4.039	-0.018	1.179
BCCY					3.802	0.956
BCDT					-0.003	0.833
BCES			-1.047	0.880	1.091	1.017
BCHO			-4.442	6.819	0.852	1.029
BCKW			-3.869	3.194	-2.441	1.561
BCLC			1.672	2.102	-4.102	3.289
BCLG					0.650	1.543
BCLI			-2.903	0.843	-1.246	0.936
BCMR			-1.989	0.920	-1.018	1.205
BCNA			-0.710	3.256	3.253	4.404
BCNS			-0.176	0.850	1.175	0.914
BCPI					-0.313	0.989
BCSC			-2.519	4.530	1.034	0.903
BCSF			-0.965	0.791	0.326	0.968
BCSL			-0.496	0.761	0.080	0.889
BCSM			-0.177	1.144	0.265	1.365
BCSQ					1.783	1.174
BCSU			-0.380	3.384	-0.240	1.723
BCTS			0.693	3.126		
BCVC			-0.932	0.833	-0.065	0.914
BCVI			-3.125	3.826	0.624	0.740
BDRY	0.859	2.747	-0.054	1.043	-1.214	1.416
BELI	2.506	2.780	-0.560	0.829	2.036	1.183
BEND	-0.835	1.064	-1.706	0.686	0.262	0.911
BFIR	-3.994	2.084	-3.731	0.861	-5.314	1.033
BIGD	-0.888	1.252	-1.057	0.806	-2.166	1.143
BILS			-1.181	1.333	0.705	1.796
BLDG					-1.394	1.084
BLNP			-3.222	2.435	2.830	3.411
BLVU	-3.768	1.859				
BLY1			-1.454	0.789	-0.281	0.824
BLYN	-1.858	1.629	-3.207	8.722	41.946	19.525
BNDM			-3.262	2.410	-0.965	0.899
BPKT			-2.431	0.953	-5.677	2.007
BRBR						
BREW	-0.955	0.738	-1.489	0.687	-0.623	0.827

BRN3			-2.356	2.872	2.833	2.656
BRNB	-1.677	1.545	0.361	1.179		
BRNT					-0.338	0.919
BSUM	-3.578	2.049	-0.774	1.358	-4.746	1.188
BTON	-1.576	1.311	-5.089	1.807	2.831	2.470
BURN	-1.550	0.983	-1.743	0.752	-0.864	0.778
BUTT			-2.355	1.771	-0.928	0.822
CABL	-0.238	0.829	1.237	0.638	0.748	0.703
CACC			1.803	0.926	2.413	1.220
CAFM					0.374	0.918
CAMS					-0.116	1.110
CATH	-3.381	1.730	0.610	1.042	-2.597	1.070
CBLV	-3.536	5.647	-1.775	0.940	-0.896	0.835
CCPW			-0.898	1.266	-0.372	1.561
CHCM	-3.951	2.688	-1.716	0.931	2.747	1.258
CHEL	-3.035	1.194	-1.848	1.302	0.016	1.065
CHEM			-1.439	0.684	0.581	0.866
CHLW					2.244	1.527
CHST			1.219	4.056	2.329	2.861
CHW2			0.137	1.104		
CHWK	0.470	1.075	0.400	0.933	-0.143	1.376
CHZZ	-0.564	1.054	-0.755	0.915	-1.096	1.271
CIHL			-1.521	0.878	0.338	1.004
CLCV			-1.195	1.311	-0.516	1.540
CLHQ			-1.748	2.206	0.073	2.561
CLMS			0.047	1.395	0.005	1.108
CLRS	4.408	2.236	1.535	0.793	1.617	0.872
CLWZ			-2.988	1.709	-1.433	1.518
CNCR	-2.533	1.893	-1.928	0.805	-1.654	1.168
COLV	-0.811	1.787	-0.579	0.771	-1.854	0.936
COND			-1.808	0.714	-0.871	0.710
CORV	-1.063	0.846	0.470	0.752	-0.840	1.922
COTT			0.105	0.824	-7.379	1.499
COU2					3.229	1.311
COUG	-1.640	2.655	1.370	2.751	-3.343	1.830
COUP	-0.773	1.095	0.595	0.876	-0.330	0.896
COUR			2.149	0.802	10.299	3.331
CPCO			-1.932	2.495	2.470	2.314
CPUD	-1.371	1.369	-5.004	1.817	-0.675	3.837
CPXF	-0.153	1.289	-1.777	1.020	-1.387	1.387
CPXX	-0.820	1.075	-1.369	0.653	-3.728	6.252
CRA4			-0.166	1.098	0.786	1.210
CRA5					-1.591	1.055
CRNB	-5.015	6.229				
CROK	-2.921	1.271	-1.060	0.809	-4.337	1.113
CSHQ			-0.957	1.552	0.272	1.255
CSHR	-0.375	1.802	-0.021	1.756		
CSKI	-6.003	1.745	-1.886	1.235	-0.842	1.286
CST1			-0.574	1.126	0.751	1.168
CTPT	-0.483	1.652	-0.645	0.685	-0.940	1.139
CULM					-0.310	1.570
CUSH	-2.103	3.892	0.506	0.933	0.016	1.227
CVO1	-2.333	0.843	-0.293	0.894	-0.576	1.279
DANP					-1.081	1.057
DBLO					2.283	5.032
DCSO	-0.886	0.878	-0.336	0.714		
DDSN	-0.693	0.741	-0.054	0.610	-1.227	1.178
DEA2	-1.007	1.169				
DEEJ			1.807	1.060	3.688	0.993
DLTA					-0.263	0.953
DMND			-0.268	0.761	-1.867	2.196
DR2O			0.516	2.991	0.299	0.781

DRA3			3.149	1.916	0.066	0.949
DRA4			-0.725	1.225	0.400	0.974
DRAO	-0.006	0.669	-0.532	0.738	0.088	0.786
DVPT	0.750	1.508	-1.196	0.817	-1.675	0.879
DWH1	-1.120	1.478				
EGLI					9.093	4.176
ELGN			2.062	1.324	0.269	1.119
ELSR	-2.183	1.052	-1.352	0.883	-1.547	0.869
EM01			-1.639	1.174	-0.777	1.518
ENTR			-0.581	0.689	-0.931	1.063
ENUM	-1.987	1.131	-1.691	1.082	1.152	2.013
EPHR	-0.260	1.379	-1.291	0.789	-1.638	0.813
EVER			-7.608	1.329	0.445	1.391
FAND					7.292	4.821
FITZ			-4.283	1.531	-0.481	1.233
FOST			3.514	1.051	1.164	0.659
FOUR					-6.724	5.794
FRFX			-2.546	0.890		
FRID	-0.498	1.399	1.220	14.029		
FSRH	0.050	2.155				
FTS5	1.420	0.872	0.396	0.623	1.529	1.616
FTS6	-0.499	0.910	0.520	0.621	1.401	1.920
FWBD			-0.551	0.761	-0.326	0.760
GBN1			-1.789	1.521	-4.613	3.495
GBN2			-0.511	2.442	-6.901	6.360
GBN3			-0.638	2.099	-4.001	3.682
GBN4			0.388	1.834	-1.801	3.178
GBN5			-0.593	1.326	-4.715	2.812
GBN6			0.504	2.008	1.001	8.269
GHCL					1.077	1.142
GLNW	-3.831	2.522	-0.880	2.647		
GLWD			1.317	1.320	-6.036	1.413
GOBS	-1.811	0.640	-1.598	0.609	-1.541	0.875
GOLY	-3.748	1.895	-1.832	0.790	-1.870	0.919
GRAV			-0.929	1.220	2.601	1.067
GRCK	1.908	1.936	-0.097	0.817	-2.491	0.867
GRMD	-4.198	1.535	-2.035	0.953	2.983	1.665
GRP4	-1.375	1.046	-0.533	1.293		
GRSV			-2.098	0.678	-0.682	0.874
GTPS	0.420	1.866	0.023	0.745	-1.001	1.283
GUAN			-3.493	2.090	3.082	1.210
GWN5	-2.981	1.109	-2.510	0.719	-0.840	2.261
GWN6	-5.420	1.241	-2.239	0.764	-1.242	2.408
HAHD			-1.278	0.960	-3.185	1.082
HALF			-0.768	0.820	-0.425	0.835
HGP1	-2.098	1.454	-268.879	17.659		
HLSY	-3.355	1.875	-0.353	2.401	3.262	2.535
HOTS			-3.136	2.188		
HRPR					-0.397	0.962
HRTM			-3.093	3.398	-7.264	1.623
HTCH	7.503	9.214	-2.379	3.177		
HUSB	7.765	1.571	4.926	1.214	7.918	1.702
HWKV			-0.700	2.526	1.126	1.591
IDBO			-1.597	1.727	-1.770	0.761
IDCA			1.040	2.633	-0.334	0.909
IDFL			0.217	1.597	-2.085	0.818
IDHD			465.554	118.339	-0.779	0.756
IDLW			0.332	2.364	-0.402	0.838
IDM1					-0.804	1.267
IDMH			-2.182	1.504	-3.337	0.811
IDMN					-2.907	1.049
IDNA			0.056	1.642	-1.699	0.808

IDNP	-0.365	0.857	-0.620	0.601	0.110	1.166
IDNR			-1.372	2.472	-1.681	1.072
IDTD	-1.375	0.845	-3.006	0.905	-0.959	1.004
INW1	-0.648	1.152	-1.117	1.570		
IWAC	-2.034	1.483	2.005	1.669		
JAKE			3.189	1.521		
JIME	-1.240	0.813	-0.569	0.960	-1.580	1.179
JKPR					-5.648	1.470
JOBO			-1.869	1.243	-0.076	1.070
JORD					1.548	2.618
JRO1	-4.433	1.034	1.029	0.848	0.085	0.773
JUN1			-1.472	2.532	-0.808	0.982
KAHL	0.320	42.732	-2.132	240.550		
KEL1			-1.318	1.135		
KELS	-1.699	0.956				
KENI	13.108	1.694	-1.265	0.788	-1.566	1.009
KFRC			-2.355	0.942	1.209	1.570
KLO3					0.498	1.025
KLTS			-0.027	1.096	-1.277	1.081
KLWN					0.287	1.117
KOOT	-1.733	1.278	-0.248	0.835	-1.226	0.894
KRMT	-0.811	1.724	-2.978	1.417		
KTBW	-1.151	0.669	-1.057	0.658	-0.724	0.889
KWBU			-2.838	1.323	-1.242	1.390
LAPN	2.405	1.369	-0.217	1.029	-5.322	1.120
LCR1					-0.938	0.773
LCSO	-1.280	6.105	0.283	3.127	-0.040	1.379
LFLO	-1.211	1.147	-0.619	0.851	-2.129	1.148
LIKE			-4.813	2.271	-11.798	9.008
LINH	-2.871	0.848	-2.162	0.897	-0.967	1.035
LINL			-2.271	2.481	-2.077	3.954
LKCP	-2.587	0.794	-1.725	0.810	-2.199	1.161
LKVW			-1.845	1.103	-1.712	0.855
LMID			-2.417	0.889	-2.737	0.943
LNG2			-2.281	1.075	-0.917	0.784
LNGB	-0.288	1.119	-1.165	0.663	0.009	0.878
LNGV			-0.221	0.708	-3.719	1.496
LNRD			-0.566	1.314		
LOST			1.145	1.926		
LPSB	-0.526	0.828	-0.278	0.647	-0.284	1.105
LSIG	-1.730	1.160	-2.050	0.887	-2.730	0.888
LTAH	0.602	1.108	-1.291	0.753	-1.657	0.853
LVIL			-1.721	1.357		
LWCK			0.819	1.024	0.306	9.205
LWST	-4.005	2.139	-0.651	0.659	0.242	0.872
MADE	-0.442	1.960	2.471	3.109	-8.069	3.530
MASC			-2.062	0.624	-0.878	1.379
MCSO	-0.013	0.880	-0.098	0.699	0.914	1.081
MDMT	-2.321	1.158	-2.525	0.941	0.299	1.452
MDRS			-2.297	0.747	-1.041	0.909
MECR			5.767	1.702		
MGRB					3.224	3.042
MHTL	-1.535	2.086	-2.956	1.357	1.196	1.737
MIS1			-0.855	0.808	-1.591	0.989
MKAH	2.102	4.220	3.525	1.227	1.323	1.153
MLKE			-3.862	1.345	0.131	0.867
MODB	-0.114	0.990	-1.390	1.060	-0.033	1.230
MON3			-0.105	0.830	0.164	3.844
MRIB					2.456	0.788
MRSD	-7.035	5.033	0.206	1.285	-0.022	1.242
MSLK	-3.730	1.660	-1.660	1.270		
MTCL			-4.414	4.409	-0.638	0.880

MUIR	-3.445	2.088	-3.228	0.964	-1.491	1.403
MYRA			7.835	3.546	2.699	1.394
NANA			0.235	0.780	2.709	0.984
NANI			0.268	1.215	1.291	1.257
NANO	0.211	0.690	1.463	0.603	2.157	0.702
NCOW			-0.345	0.913	0.930	0.988
NEAH	2.214	0.976	3.473	1.406	1.738	1.816
NEWP	0.530	1.092				
NGWN			-2.909	3.365	2.974	1.475
NINT	-5.799	1.621	0.479	1.825	-0.457	1.285
NORM			-1.599	1.123	-0.836	1.123
NVAN					0.776	1.041
NWBG	-0.719	0.872	-0.178	0.940	5.243	2.546
NWE3			-1.672	0.986	-0.566	0.826
NWPT	-0.103	1.251	0.098	1.229		
OAKR			-1.790	0.725	-2.161	0.885
OBEC	-1.809	1.161	-1.015	1.335	0.315	1.322
OBSR	-1.229	2.933	-0.604	0.734	0.228	1.025
OCEN			-0.182	0.761	2.495	0.998
ODOT			-0.362	0.731	0.010	0.943
ODSA					-1.180	0.835
OKNG			-1.763	0.813	-1.607	0.995
OLAR			-1.261	0.936	-1.373	0.826
OLI1			-0.883	0.849	-0.533	0.894
OLMP			-2.335	0.829	-4.059	0.990
ONAB	-0.750	3.221	-1.084	0.698	-4.784	1.021
ONT1					-0.845	0.693
ORAL			-2.254	3.967	-1.135	0.754
ORBN			-1.071	2.493	-2.603	2.084
ORCD			-3.694	2.987	-1.455	0.782
ORDO			1.321	3.273	-0.933	0.834
OREU			1.739	3.121	-0.088	0.754
ORFL			-0.745	3.093	0.214	0.860
ORGR			-0.150	2.531	-1.146	0.836
ORHA			0.639	3.084	0.124	0.863
ORHI			2.031	2.620	-1.607	0.845
ORHM			0.072	2.849	-2.178	0.950
ORHP					-1.419	0.815
ORK5	3.277	15.847	-3.167	0.888		
ORK6	2.445	16.441	-3.910	0.887		
ORKF					-2.699	0.921
ORM1					-1.401	0.931
ORMF					0.708	0.770
ORMO					-0.684	0.790
ORMV			0.555	2.835	-0.756	0.803
ORNW			3.581	3.291	0.324	0.980
OROR			-1.570	3.289	-1.092	0.911
ORPE			0.164	3.471	-0.642	0.825
ORPO	-2.314	1.409	-0.122	1.022	-1.313	0.867
ORRB					-0.229	0.766
ORS1	-0.627	0.843	-0.318	0.967		
ORS2	-0.564	0.975	-0.467	1.030		
ORSB			-4.100	1.032	-4.228	1.377
ORSH			-2.651	3.671	-0.550	0.768
ORSL			0.975	2.892	-0.117	0.800
ORTA			2.064	3.135	-0.124	1.029
ORTI			-4.651	3.007	-0.373	0.815
ORWA			-2.635	3.120	-1.148	0.802
OTHL	-2.840	1.329	-1.141	1.687	0.818	1.280
OTIS	-1.322	22.726				
OYLR	-3.376	1.739	-3.219	1.883	-1.756	1.594
P013	-0.060	1.143	0.106	0.584	1.173	0.791

P017	-0.470	1.139	-0.439	0.695	-0.590	0.835
P018	-2.296	1.582	-0.682	0.503	-1.612	0.738
P019	-0.251	1.152	-1.701	0.571	-1.014	0.709
P020	-1.126	0.764	-0.835	0.551	-0.410	0.653
P021	-0.788	0.832	0.182	0.683	-0.160	0.825
P022	-0.483	0.941	-0.223	0.716	-0.169	0.937
P023	-0.395	1.207	-0.017	0.667	-0.467	0.812
P024	0.353	3.048	-0.246	0.571	-0.029	0.761
P025	0.260	1.356	0.668	0.677	0.640	0.764
P061	-0.150	1.215	-0.505	0.770		
P062	-1.299	1.471	-0.824	0.652	0.272	0.802
P063	-2.117	0.919	-1.454	0.640	-1.311	0.794
P064	-0.081	3.160	0.824	0.805	1.679	6.642
P065	-2.169	1.144	-1.607	0.713	-0.912	0.843
P145	-0.395	0.994	-0.721	0.588	-0.538	0.853
P154	0.630	1.411	-0.369	0.763	0.674	0.972
P155	0.578	1.421	-0.344	0.700	-0.696	1.013
P179	-0.838	1.609	-0.539	0.779	0.877	0.932
P191	-0.619	1.516	-0.158	0.735	0.032	0.931
P316	-2.093	1.085	-1.087	1.160	-1.192	1.370
P325	2.007	0.975	1.795	0.633	2.748	0.736
P347	-0.841	1.378	-1.013	0.648	-1.497	0.898
P362	0.842	1.145	2.110	0.599	0.601	0.995
P363	-0.578	1.377	0.417	0.682		
P364	0.687	1.363	1.764	0.619	2.142	0.737
P365	-0.352	1.193	0.186	0.617	1.132	0.727
P366	-2.515	2.051	-0.731	0.710	0.652	0.918
P367	-1.488	1.038	-0.577	0.604	-0.353	0.799
P368	-1.094	1.021	-0.354	0.675	0.708	0.757
P369	-0.901	0.951	-0.752	0.645	-0.039	1.478
P370	-0.828	0.972	-0.796	0.706	-0.369	0.891
P371	-1.528	0.788	-0.254	0.576	-0.393	0.862
P372	-1.009	1.173	-0.211	0.611	-0.363	0.717
P373	-1.073	0.832	-0.115	0.637	-0.627	0.826
P374	-0.826	1.022	-0.311	0.708	-0.076	0.828
P375	-0.455	1.925	0.022	0.636	0.542	0.837
P376	-1.377	0.775	0.017	0.633	1.120	0.759
P377	-1.394	0.962	-0.268	0.605	-0.908	0.853
P378	-1.338	1.186	-0.225	0.570	0.010	0.753
P379	-1.810	0.969	-0.274	0.898		
P380	-1.594	0.745	-1.303	0.598	0.513	0.742
P381	-2.398	1.266	-0.745	0.580	0.760	0.677
P382	-1.333	3.712	-1.269	0.862	-0.030	1.092
P383	-0.377	1.303	-1.129	0.594	-0.895	0.745
P384	-2.295	3.359	-0.766	0.686	-0.433	0.793
P385	-1.334	1.924	-1.839	0.800	-2.522	1.575
P386	-0.813	1.195	0.041	0.647	-0.298	0.740
P387	-4.146	1.434	-2.077	0.844	-1.344	0.972
P388	-1.384	0.966	-0.435	0.742	0.193	0.842
P389	-1.938	1.154	-0.554	0.574	0.534	0.684
P390	-1.123	1.232	-0.259	0.551	0.475	0.723
P391	-3.322	2.121	-0.610	0.565	-0.204	0.667
P392	-1.659	1.117	-1.393	0.550	-1.157	0.669
P393	-1.831	1.280	-0.361	0.560	-0.687	0.698
P394	-0.561	1.135	-0.005	0.623	-0.347	0.722
P395	-1.484	1.162	-0.156	0.748	0.736	0.965
P396	-2.387	1.641	0.027	0.852	-0.727	1.184
P397	-2.771	1.173	0.592	0.649	0.925	0.773
P398	0.047	0.986	0.332	0.612	2.339	1.178
P399	0.577	3.203	1.005	0.710	0.732	1.184
P400	3.822	4.619	1.324	1.439	2.536	2.732
P401	0.057	0.769	0.797	0.585	0.377	0.867

P402	1.535	1.109	1.708	0.621	1.787	0.772
P403	0.168	1.054	2.633	0.838	2.965	1.202
P404	-1.958	0.943	-0.344	0.644	-0.619	0.827
P405	-0.130	1.750	-0.555	0.670	-1.613	0.736
P406	-1.427	0.891	-0.489	0.609	-0.349	0.823
P407	-0.385	1.317	0.771	0.859	-0.805	1.099
P408	-2.131	0.956	-0.903	0.738	-0.570	0.895
P409	-1.183	0.817	-0.765	0.653	0.081	0.885
P410	0.219	2.005	-1.528	0.683	-1.651	0.839
P411	-0.844	1.278	-0.164	0.745	-0.350	0.947
P412	-1.670	0.993	-0.921	0.598	-1.007	0.701
P413	-3.452	2.360	-0.470	0.716	-0.717	0.902
P414	-2.011	1.000	-0.813	0.628	-0.983	0.728
P415	-1.430	0.821	0.084	0.690	0.388	1.407
P416	-3.122	2.236	-1.047	0.663	-0.965	0.860
P417	-1.755	0.981	-1.402	0.716	-0.717	1.085
P418	-0.610	1.083	0.116	0.645	-1.048	0.855
P419	-1.346	2.586	0.349	0.798	-0.526	1.088
P420	-1.600	0.748	-1.195	0.582	-0.880	0.695
P421	0.636	1.688	-1.149	0.670	-2.299	0.939
P422	-1.207	1.190	-0.436	0.591	-0.645	0.699
P423	-1.300	0.912	-0.817	0.708	0.222	0.904
P424	-2.763	3.659	0.040	0.803	0.069	0.908
P425	-6.049	2.660	-1.299	0.610	-1.535	0.882
P426	-2.854	0.991	-1.549	0.766	-1.047	1.557
P427	-2.946	0.921	-1.633	0.600	-1.717	0.757
P429	-2.487	1.205	-1.840	0.718	-1.840	0.889
P430	-0.494	0.876	-0.464	0.990		
P431	-3.302	1.574	-1.418	0.585	-0.975	0.776
P432	-2.334	0.843	-0.853	0.711	-0.500	1.061
P433	-2.234	1.919	-1.066	0.696	-1.249	1.756
P434	-2.405	1.944	-0.852	0.623	-0.441	0.731
P435	1.263	1.266	-0.398	0.925	-0.586	1.212
P436	-0.721	1.184	-0.332	0.769	1.060	1.042
P437	-1.864	1.363	-1.229	0.660	-1.071	0.830
P438	-1.226	0.949	-1.382	0.587	0.450	0.904
P439	-0.784	0.870	-0.481	0.621	-0.468	0.825
P440	-1.134	1.106	-1.475	0.611	0.045	0.718
P441	-2.754	3.326	-0.008	0.791	-0.325	0.875
P442	-2.245	1.234	-0.483	0.868	-2.508	1.870
P443	-2.734	2.460	0.050	0.795	0.169	0.977
P444	-2.889	1.474	0.420	0.995	-1.689	1.988
P445	-2.329	0.909	-1.269	0.661	-1.193	0.769
P446	-2.331	1.363	-0.782	0.675	-1.397	0.839
P447	-2.610	1.323	-1.302	0.561	-1.188	0.717
P448	-3.189	0.935	-2.525	0.637	-2.871	0.755
P449	-2.823	0.924	-1.550	0.601	-0.989	0.821
P450	-2.281	0.781	-1.476	0.586	-1.445	0.690
P451	-0.932	0.853	-0.870	0.591	-0.886	0.705
P452	-1.377	0.950	-1.236	0.721	-0.615	0.916
P453	-1.227	0.793	-0.925	0.647	-0.425	0.974
P454	-1.349	0.813	-0.681	0.601	-0.146	0.715
P655	0.088	1.626	-1.320	1.065	3.439	2.839
P656	1.890	1.611	-2.323	13.408	2.316	17.839
P657	1.189	1.725	-1.461	0.984	0.651	1.271
P658	0.378	1.600	-0.782	0.920	0.270	1.735
P659	-1.263	2.733	-1.397	1.578	2.265	2.195
P660	-4.434	3.514	-1.375	1.817	4.772	3.671
P661	0.175	1.385	-0.924	0.832	0.051	1.143
P663	1.908	2.047	-0.757	1.037	-0.340	1.431
P672	-0.992	0.943	-1.932	0.754	-0.197	0.886
P673	-3.992	1.578	-5.381	1.367	-1.941	1.422

P674	-0.871	1.251	-3.031	0.893	0.004	1.236
P687	-2.166	1.481	-1.426	1.044	-1.415	1.649
P688	-3.044	3.927	-1.173	1.236	-0.011	1.547
P689	-1.753	0.860	-0.684	0.597	-1.104	0.860
P690	-3.709	1.621	-1.200	1.413	-1.923	1.309
P691	1.277	1.146	-0.773	0.696	-0.688	0.938
P692	0.055	1.589	-0.172	0.792	-1.032	0.995
P693	-3.569	1.339	-1.528	1.615	-2.914	1.677
P694	-0.664	1.401	0.644	0.862	-0.733	0.793
P695	-1.967	1.293	-1.824	1.064	-2.201	1.089
P696	-2.722	1.096	-1.353	0.857	-0.727	1.212
P697	-4.586	1.698	-2.804	1.770	-2.885	2.180
P698	-2.789	1.119	-0.956	0.843	-1.377	1.006
P699	-5.821	2.386	-2.164	3.845		
P700	0.289	1.395	-1.066	0.757	-0.971	1.010
P701	0.261	1.497	-0.672	0.898	-0.841	1.079
P702	-2.455	0.781	-0.843	0.662	-0.338	1.014
P703	-1.343	2.413	-1.087	1.161	-2.116	1.975
P705	-1.977	4.648	-0.955	0.910	-0.719	1.749
P730	-0.962	1.500	-0.673	0.798	-1.293	0.999
P731	0.422	1.344	-0.696	0.685	-2.396	0.904
P732	-5.294	1.892	-0.217	0.658	0.348	0.896
P733	3.047	4.470	1.266	0.637	2.185	0.837
P734	1.180	1.350	2.101	0.744	1.987	0.838
P735	-2.434	2.737	0.005	0.688	0.596	0.846
P736	-3.315	1.904	-1.635	0.758	-0.080	0.784
P737	-2.426	2.433	-0.819	0.751	-1.954	1.198
P738	-1.047	2.059	-0.154	0.752	-0.030	0.891
P739	-1.646	1.871	-0.183	0.650	-0.324	0.738
P784	0.006	3.069	-0.520	0.715	-0.173	0.826
P786	1.176	3.945	0.869	0.787	0.043	1.113
P791			-2.694	1.445	-1.208	1.315
P792	-2.226	4.400	-0.777	2.707	-0.951	7.945
P813			-1.857	0.930	-1.150	1.080
P814			-1.708	0.879	-3.679	12.651
P815			0.085	0.865	1.414	0.733
P816			0.556	0.885	1.037	0.870
P820					0.607	0.876
P821					1.610	0.988
PABH	-1.404	0.639	-0.031	0.590	0.787	0.691
PARP			-0.621	1.912		
PCOL	-1.310	0.860	-0.120	0.866	-1.731	0.992
PCS2	-2.310	1.600	-0.358	1.743	-4.551	1.875
PDTN			-1.111	0.777	-1.187	1.732
PDXA	1.063	2.557	-1.233	0.944	-0.970	1.050
PER1	-2.498	1.659	-5.715	3.562		
PFLD	-2.020	0.856	-1.134	0.731	-0.546	0.889
PGC5	-1.150	0.889	0.158	0.637	1.046	0.748
PKDL	9.031	48.025	-1.697	1.006	-3.340	1.608
PKWD	-3.282	2.141	-3.688	1.770	-2.048	2.011
PLMN	-2.684	1.465	-0.032	0.742	-1.874	0.766
PLNA			-0.642	0.881	-0.984	0.818
PMAR	-2.733	1.200	-0.292	1.077	-1.273	1.690
PNCL	-0.488	1.308	-69.465	4.234		
PNDL	-1.938	1.209	-57.369	7.750		
PNHG	1.073	6.429	-17.180	16.634	-10.724	2.989
PNHR			-17.196	6.209		
PNTC			-1.024	0.833	-0.002	0.886
PNVL			-1.043	0.668	-3.059	0.821
POME	3.470	3.590	0.797	1.762	-0.832	6.820
PORC			-3.374	1.003	-2.139	0.815
POTH			-3.316	2.042		

POUL	-4.809	2.570				
PRDY	-0.002	1.021	-1.487	0.691	-0.549	0.975
PRSR	-2.071	1.645	-1.379	0.883	-1.854	1.843
PSEA	-3.134	1.136	-1.615	1.132		
PSPT	-1.245	1.517	-0.868	0.822	-1.928	1.196
PTAA			0.080	0.875	-0.469	1.111
PTAL	2.979	0.710	2.693	0.648	3.486	0.728
PTRF	1.547	1.907	2.911	0.931	1.793	0.944
PTSG	1.261	0.849	1.669	0.584	2.303	0.730
PTSN	2.104	2.734	-0.141	1.297	-1.295	1.094
PUPU	0.333	1.690	-2.431	1.663	-1.662	3.400
QMAR	1.090	2.806	-0.886	1.522	-0.142	2.099
QUL2			1.368	1.178	2.437	0.921
RDL2					-0.453	1.410
REDM	-2.104	0.681	-1.711	0.575	-1.283	1.128
REED			-1.287	0.687	-4.794	1.385
RIC2	-5.143	2.521	-0.788	0.842	0.163	2.158
RKD1			-0.530	0.763	0.808	1.036
RMDB	-1.850	0.850	-1.619	0.584	-13.250	1.919
RMRK	-3.086	4.403	-1.734	0.996	-0.730	1.107
ROKY					-1.671	1.392
RPT5	-1.324	0.969	-2.036	0.606		
RPT6	-2.376	0.844	-2.672	0.659		
RPUB			-0.801	0.952	-0.103	0.984
RSBG			-0.481	0.958	-0.396	1.340
RYA1			0.388	1.286	-2.489	1.442
RYMD	-3.744	1.820	-0.458	0.687	-3.275	1.029
SAC4			-1.225	2.330	-666.342	170.056
SAMM	0.152	5.327	-2.186	1.043	-0.801	1.562
SATS	2.899	7.424				
SC00	-0.707	0.781	-2.765	0.931	-1.610	0.848
SC02	-0.671	0.666	-0.226	0.592	0.303	0.774
SC03	1.967	1.227				
SC04	-0.073	0.772	0.805	0.727	1.210	0.821
SCHO			0.830	2.170		
SCMV	-2.461	1.669	-1.264	0.737		
SEAI	-2.021	1.040	-1.806	0.967		
SEAS	2.760	2.759	0.399	0.643	-1.311	3.073
SEAT	-1.841	0.661	-1.946	0.616	-2.882	0.967
SEDK	-1.672	1.393	0.971	1.664		
SEDR	-1.962	0.874	-0.935	0.780	-0.823	0.863
SEPR					-20.690	1.998
SEQM			-0.473	1.264	0.701	1.034
SHLD	-0.981	0.755	-0.312	0.603	-0.391	0.796
SHRK			-1.226	2.180	-1.338	1.127
SKCO					-3.693	1.239
SKGT					-1.816	0.867
SKMA	3.768	2.840	-1.998	1.161		
SKND			-0.158	3.492		
SLUM			-1.893	2.014		
SMAI	-3.121	0.803	-1.231	0.750	-1.441	0.855
SNDR					1.318	4.069
SNOQ	-2.390	2.185	0.033	3.181	-1.248	0.949
SNRS	-6.675	6.920	0.846	2.599	-1.621	4.099
SPKN	0.179	1.193	-1.296	0.850	-0.153	1.062
SPKV	-1.394	1.883				
SPN5	-1.573	0.864	-0.576	0.645		
SPN6	-2.986	0.953	-0.725	0.656		
SPRA			-1.527	0.767	-0.682	0.784
SPRG	-2.025	1.598	-0.208	0.670	-0.225	0.757
SQAW			-0.147	1.823	-2.730	3.449
SQIM	-3.546	1.590	0.301	1.274		

SQMS			-0.578	1.153	0.196	1.152
SSHO	-0.512	0.984	-3.154	0.846	-1.660	0.948
STAY	0.719	0.943	-0.282	0.727	-0.436	0.932
STHM	-1.517	1.785	-1.833	3.388	2.521	1.888
SUHS			-0.503	0.796		
SUPR			0.790	1.619	-2.806	0.772
SUR6	-3.931	2.360				
SURR			-3.727	0.888	-2.374	1.035
SVI2			-1.755	0.988	1.520	0.827
SWNB			-1.563	0.822	-0.133	0.846
SWRN			-4.698	2.948		
SYNC			3.871	3.691	-9.434	7.028
TACO	-3.698	2.245	-2.269	0.748	-1.875	0.829
TAY1	-2.709	1.408	4.352	2.606		
TDLS	-2.878	1.581	-1.579	0.828	-3.049	20.583
TFNO	4.110	4.666	0.818	0.822	2.953	0.928
TGAU			5.425	6.316		
TGUA	-4.738	1.231	-0.183	1.500	-0.946	1.249
THAR	-0.099	1.537	0.047	1.244	-1.197	1.185
THRM			1.122	2.378		
THUN	0.168	1.139	-1.283	0.613	-1.095	0.692
TILL	1.121	2.917	-0.788	0.732	-1.017	1.258
TMBU			-0.821	1.137	-0.152	1.185
TPW2	-0.812	0.770	0.062	0.682	-0.252	0.847
TRAI			-3.133	1.424	-0.706	1.185
TRND	-1.357	0.787	-1.303	0.825	-1.176	0.850
TSEP			-35.242	42.435		
TSTU	-2.634	1.357	-3.921	1.227	-3.993	1.023
TULE			-0.848	1.690		
TUMW	-1.456	1.720	-1.543	1.317	-0.606	1.467
TWHL	-1.215	0.682	-0.436	0.691	-0.787	0.897
TWIW	-1.065	1.256	0.064	1.102	-1.373	1.289
TWRI	-4.300	2.392	-0.251	3.838	-1.714	1.807
TWSP			-2.735	2.231	-0.207	1.198
UCLU	1.178	0.837	1.242	0.746	1.508	0.785
UFDA	-0.815	1.818	-0.671	0.806	-0.983	0.986
UKIA			-0.543	0.722	-0.884	0.731
VCWA	-1.107	1.868	-0.818	1.092	-1.689	0.950
VNCR			-3.976	3.003		
VRNT	-3.327	1.387	0.124	1.050	-2.306	1.382
WABR			-0.536	1.312	-1.119	0.801
WACC			-0.632	2.729	-0.623	0.739
WACS			-1.493	0.889	-0.563	0.766
WACX			-0.406	2.864	-0.546	0.875
WACY			2.171	2.081	0.313	0.754
WAEL			-0.652	2.806	-1.743	0.763
WAEN			-3.001	3.027	-1.427	0.737
WAEV			-2.044	0.874	-1.171	0.771
WAFD			-1.070	1.832	-0.691	0.730
WAFH					-0.362	0.788
WAFR			-2.549	1.647		
WAGO			-1.802	1.018		
WAKI	-1.257	1.047	-1.677	0.680		
WAKL			-0.719	2.747	-1.293	0.848
WALA	-1.743	1.284	0.231	1.074	0.524	1.558
WALL			3.136	0.729		
WAMC			-2.128	0.938	-1.198	0.910
WAMO					-1.360	0.860
WAMS			-2.181	2.740	0.413	0.830
WAMV			-0.651	2.460	-0.813	0.993
WAMW			-5.371	4.420	-0.941	1.002
WAOL			4.315	2.502	-0.839	0.820

WAOT			-1.907	2.877	-0.734	0.723
WAOY			-4.064	1.066		
WAPA			-0.402	3.020	-0.642	0.806
WAPO	-2.462	1.285	-1.993	0.834	0.226	0.768
WAPS			-2.514	0.904	-1.324	0.684
WAQU			0.364	2.362	-1.164	0.764
WARM			-0.730	2.846	-2.062	0.794
WARZ			-2.734	2.929	-0.732	0.805
WASK	-0.645	0.963	-0.949	0.681	0.336	0.880
WASN			-2.784	3.451	-1.203	0.807
WASQ	-5.068	1.597	-2.971	1.107	-1.266	0.915
WATK			0.746	2.831	0.689	0.838
WAWE	8.915	5.977	-1.340	1.914	-1.344	0.874
WAWL			-0.370	2.284	-0.576	0.780
WAYA			-1.271	2.798	-1.248	0.858
WDBN	-3.825	0.991	-3.505	0.817	-4.265	1.312
WEBG			-0.613	1.844	2.389	1.018
WHBR			-1.972	2.302	-2.952	4.391
WHD5	-2.597	2.043	-1.194	0.688	-0.845	2.154
WHD6	-4.844	1.508	-1.616	0.680	-0.750	2.157
WIF3					4.618	2.560
WIFC	-3.380	4.103				
WIFR	6.375	7.857	3.175	1.383		
WMSG			-1.347	0.823	-0.835	1.111
WNTH	-2.570	2.567	2.007	2.764		
WRNR			-3.768	1.386	-1.074	0.921
WVN3	0.715	3.294				
XANE			-1.174	1.033	1.531	2.241
YAKI	-3.727	0.838	-2.285	0.897	-2.017	0.888
YAKS					-2.614	1.732
YBHB	-1.079	1.066	-1.017	0.966	0.301	1.373
YELM	-0.680	0.955	-1.436	0.645	0.818	1.022
YONC			-0.645	0.659	-0.240	1.359
ZSE1	-2.082	1.464	-1.830	0.726	-1.252	0.802

*Station ABRN excluded due to insufficient data per period.

Table S2.4 Plate flexure modeling parameters.

North American Elastic Plate Thickness, *h* (km)	Flexural Rigidity, *D* (GPa/m³)	Flexural Parameter, α (km)
5	6.67E+10	26.51
7.5	2.25E+11	35.94
10	5.33E+11	44.59
12.5	1.04E+12	52.72
15	1.80E+12	60.44
17.5	2.86E+12	67.85
20	4.27E+12	74.99
22.5	6.08E+12	81.92
25	8.33E+12	88.66
27.5	1.11E+13	95.23
30	1.44E+13	101.65
32.5	1.83E+13	107.94
35	2.29E+13	114.11
37.5	2.81E+13	120.17
40	3.41E+13	126.13
42.5	4.09E+13	131.99
45	4.86E+13	137.77
47.5	5.72E+13	143.48
50	6.67E+13	149.10

3

Vertical Land Motion of the High Plains Aquifer Region of the United States: Effect of Aquifer Confinement Style, Climate Variability, and Anthropogenic Activity

3.1 Publication Status

This section contains published material from: Overacker, J., Hammond, W. C., Blewitt, G., & Kreemer, C. (2022). Vertical Land Motion of the High Plains Aquifer Region of the United States: Effect of Aquifer Confinement Style, Climate Variability, and Anthropogenic Activity. *Water Resources Research*, *58*(6), e2021WR031635, https://doi.org/10.1029/2021WR031635.

3.2 Key Points

- A GPS vertical velocity field with GIA removed reveals ~2 mm/year of uplift spatially correlated with the southern High Plains aquifer.
- Uplift is consistent with seasonal and anthropogenic-driven hydrological unloading further aggravated by climate change.
- The sign of vertical land motion from aquifer depletion depends on aquifer confinement style and land does not necessarily subside.

3.3 Abstract

We use GPS data to image vertical crustal velocities in the vicinity of the Great Plains physiographic province of the United States. In the southern Great Plains, we find

crustal uplift of up to 2 mm/year in an area ~670 km x 280 km. This signal is spatially correlated with the area of greatest groundwater decline in the southern High Plains aquifer. To determine the uplift mechanism and its possible relation to aquifer depletion, we investigate changes in aquifer water content. Gravity data coupled with an elastic model show the uplift rate is consistent with hydrological unloading from anthropogenic aquifer depletion exacerbated by severe drought. Our model that encompasses two regions of greatest groundwater decline indicates a water volume loss of -5.1 km^3/year is sufficient to match the observed signal. In other large aquifers, vertical crustal motions associated with groundwater depletion are often dominated by near-field subsidence. Our results challenge the perception that vertical motions driven by aquifer depletion necessarily equate to near-field subsidence. In the High Plains system, depletion causes near-field uplift because of the combination of mass removal and the style of geologic reservoir. As current climate change models predict aggravated drought conditions in the southern Great Plains in the coming decades, we expect to see an increasing rate of uplift caused by groundwater depletion unless there is offsetting recharge or changes in water resource management.

3.4 Plain Language Summary

We use high-precision data from hundreds of GPS stations in the Great Plains region of the United States to create a map of vertical land motion in the area. In the southern portion of the map, the land is moving up at a rate of almost 2 mm/year, which

contrasts the downward motion of the surrounding area. The location of the uplift appears related to the southern portion of the High Plains aquifer. We study climate, water, and GPS trends over time to understand if the upward movement is connected to dropping aquifer levels. The data show that uplift is in response to water level declines caused by increased human reliance on groundwater from drought and drying climate patterns. Though groundwater pumping over time typically suggests land subsidence, the water in the aquifer is at atmospheric pressure, and does not experience the pressure differential within an aquifer reservoir that causes the ground to go down. Our results challenge the perception that vertical land motions driven by aquifer depletion necessarily equate to land subsidence.

3.5 Introduction

Vertical land motion is a response of the solid Earth to underlying geologic, tectonic, and geodynamic processes, as well as surface loading forces. Relevant processes work on a range of spatial and temporal scales, with timing ranging from annual seasonality to millions of years, and spatial extent ranging from basin to continental scales. Multiple processes may be simultaneously present in a region. Vertical crustal motion trends detected in Global Positioning System (GPS) time series can identify geologic processes such as tectonic uplift (e.g., Bürgmann et al., 2006; Beavan et al., 2010), magmatic injection (e.g., Dzurisin et al., 2009), mantle upwelling (e.g., Kreemer et al., 2020), interseismic buckling at plate interfaces (e.g., Burgette et al., 2009), glacial isostatic adjustment (e.g., Peltier et al., 2015), and aquifer depletion (e.g., Amos et al., 2014; Sneed et al., 2013; Young et al., 2021). Each of these processes give different geodetic signatures (Pfeffer et al., 2017), and thus, measuring the timing and extent of vertical land motion patterns can illuminate which processes are at work.

Previous geodetic studies have shown that hydrological effects in ground and surface water systems can impact the vertical crustal motions of a region, both seasonally (Amos et al., 2014; Argus, Fu, et al. 2014) and over decades (Hammond et al., 2016). These studies have shown aquifer depletion to cause subsidence through compaction of drained sediments (Faunt et al., 2016; Galloway et al., 1999) in addition to minor far-field uplift attributable to surface mass unloading (Amos et al., 2014; Argus, Fu, et al. 2014, 2017; Borsa et al., 2014; Martens et al., 2016; Chanard et al., 2018). In this study, we use GPS Imaging, a technique that creates a vertical velocity field from GPS positioning time series, to detect and characterize an anomalous signal of crustal uplift in the southern Great Plains. This signal contrasts with the forebulge collapse signal (i.e., subsidence) that dominates a large portion of the northern United States (Peltier et al., 2015; Kreemer et al., 2018; Argus et al., 2021; Sella et al., 2007; Karegar et al., 2016). The distribution of uplift in the southern Great Plains approximately corresponds to the southern extent of the High Plains aquifer.

The High Plains aquifer, also known as the Ogallala aquifer, is the largest groundwater system in the United States. Predominantly located within the Ogallala Formation, water-bearing geologic units in this unconfined aquifer system consist of unconsolidated clays, silts, sands, and gravels from ancient interbraided streams and dunes (Weeks et al., 1988). Though saturated sediments are not evenly distributed, ranging from sparse to overlapping aqueous units, previous studies have concluded that there is sufficient hydraulic interconnection to consider the High Plains aquifer a continuous water table (Weeks et al., 1988). The High Plains aquifer comprises an area of roughly 450,000 km^2 beneath eight states; South Dakota (SD), Wyoming (WY), Nebraska (NE), Colorado (CO), Kansas (KS), Oklahoma (OK), New Mexico (NM), and Texas (TX) (Weeks et al., 1988). These states rely on agriculture for a large component of their economy (Shafer et al., 2014), and the High Plains aquifer is a major source of groundwater for crop irrigation (Weeks et al., 1988; Whittemore et al., 2016). Since the beginning of the 20th century, groundwater withdrawal rates indicate that aquifer water levels are in decline and, in some southern portions of the aquifer, water levels declined by over 45 m between 1900 and 2015 (Konikow, 2013; McGuire, 2017; Whittemore et al., 2016; Scanlon et al., 2012). Between 1950 through 2007, an estimated 330 km^3 of groundwater has been lost in the southern part of the High Plains aquifer (Scanlon et al. 2012).

We investigate the connection between the GPS uplift signal and hydrological conditions inside and intersecting with the High Plains aquifer boundaries, as identified by Willet et al. (2018), to determine the mechanism driving uplift and whether a relationship exists between uplift and anthropogenic groundwater withdrawal. First, we examine the temporal and spatial pattern of vertical land motion in the Great Plains, which we consider to be within the longitude bounds of −96º to −106º and latitude bounds of 31ºN to 34.5ºN for the purposes of our study. We use vertical component time series from 379 continuously operating GPS stations in the Great Plains region. To prevent over sensitivity to seasonality or outlying data, velocity trends in the GPS time series were solved using the Nevada Geodetic Laboratory's (NGL) MIDAS robust trend estimator (Blewitt et al., 2016), which calculates vertical velocities for over 19,000 stations globally (Blewitt et al., 2018). These vertical velocities were then used in GPS Imaging to build an interpolated spatial pattern of vertical motion. Resolution tests were performed to determine whether the velocity field was adversely affected by spatially inhomogeneous GPS station distribution. Since continental-scale crustal flexure can also impact vertical motion in the mid-continent, the ICE-6G D (VM5a) glacial isostatic adjustment model (Peltier et al., 2015; Peltier et al., 2018; Argus, Peltier, et al. 2014) was used to correct for the regional uplift signal. We incorporate climatic and groundwater data into our study to examine what roles surficial and subsurface hydrological signals might play in the regional uplift. Spatiotemporal signals from the Palmer Drought Severity Index (PDSI), Gravity Recovery and Climate Experiment (GRACE), and groundwater well time series are compared with GPS time series within the High Plains aquifer bounds and GPS Imaging results. Seasonal GPS time series signals were also examined for short-term hydrological impacts.

The data when used in conjunction show that aquifer depletion is the underlying source of uplift in the High Plains aquifer. These results have ramifications for studies of vertical land motion outside the Great Plains that are important to consider as GPS data usage for the purpose of constraining terrestrial water storage continues to grow. In particular, vertical land motion signals will need to be clearly attributed to the correct mechanical sources before they can be used for interpretations or projections. Changes in hydrological conditions in aquifers, especially those that are regionally extensive and heavily exploited, may be capable of causing regional vertical land motion whose sign depends on the geologic properties of the reservoir, climate conditions, and cultural impact on the resource.

3.6 Data

3.6.1 GPS Data

We use vertical component GPS data with a minimum 3-year time series duration from the NGL open access archive from 379 stations from various networks (Sup. Table S3.1) (Blewitt et al., 2018). Positioning data used in this study span from the beginning of each respective GPS time series through 31 Dec. 2019. The data were recently reprocessed to improve precision and accuracy using the Jet Propulsion Laboratory's (JPL) GipsyX 1.0 software, and JPL's final orbit and clock products (Bertiger et al., 2020). Signal delays attributable to the atmosphere were modeled and estimated using the Vienna Mapping Function (VMF1) with gridded a priori data taken from European Center for Medium-Range Weather Forecasts (ECMWF) models (Boehm et al., 2006). These models improve GPS estimates of crustal motion and, when used in conjunction with the updated IGS14 reference frame, provide more precise solutions in vertical-component GPS time series (Martens et al., 2020). All GPS vertical component time series and rates were calculated with IGS14-consistent models and standards, which aligns the IGS14 origin with the center of mass of the Earth system (Altamimi et al., 2016). Additional details about processing of the GPS observations into vertical component time series including treatment of metadata, data editing, ambiguity resolution, antenna phase center calibrations, and estimation strategy are provided in Kreemer et al. (2018, 2020).

3.6.2 GPS Time Series of the High Plains Aquifer

We compare vertical component GPS time series directly with climate and hydrological data from the High Plains aquifer. Using the locations of 379 GPS stations described in the previous section, we determined whether the station locations fell within the bounds of the High Plains aquifer as defined by Willett et al. (2018). Of the 379 GPS stations in the survey area, 77 GPS sites are inside the High Plains aquifer (Fig. 3.1 and Sup. Table S3.2) while the rest are outside the aquifer and provide a reference against which to measure High Plains aquifer movement. The stations are divided into subsets belonging to the northern and southern High Plains aquifer which have very different vertical land motion patterns, as we will show. Within the Willett et al. (2018) bounds, we define 38ºN latitude as the dividing line between north and south portions of the aquifer system; 28 and 49 stations are located north and south of 38ºN, respectively (Sup. Table S3.2).

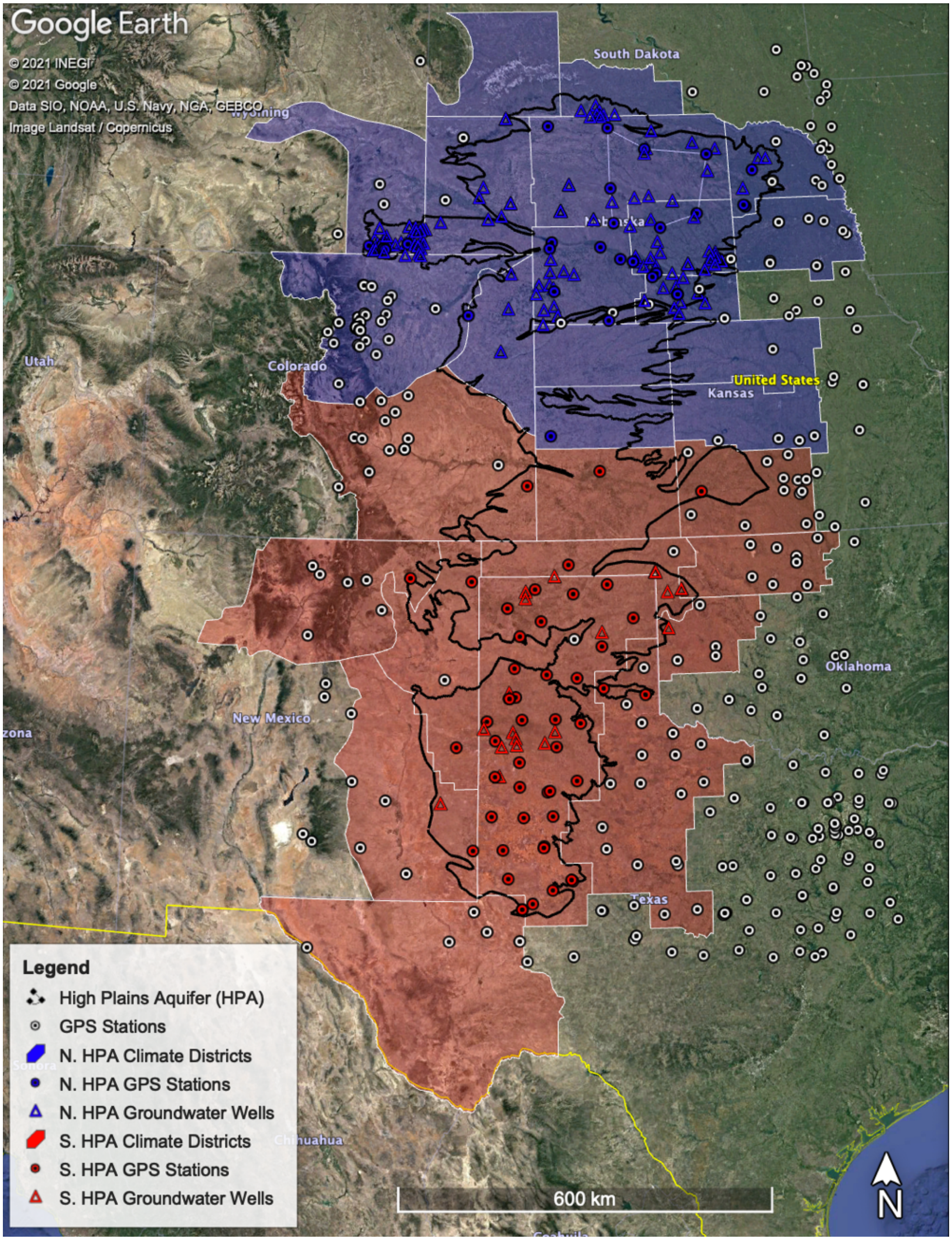

Figure 3.1. The High Plains aquifer (outlined in black) (Willett et al., 2018) encompasses parts of 28 climate districts (Vose et al., 2014), divided here by northern

(blue polygons) and southern (red polygons) portions of the aquifer system (Sup. Table S3.4). GPS stations used by GPS Imaging are overlain (circles) (Sup. Table S3.1). We classify 28 GPS stations as part of the northern part of the aquifer (blue circles) and 49 GPS stations in the southern part of the aquifer system (red circles) (Sup. Table S3.2). 121 groundwater wells sites are within our northern bounds (blue triangles), and 21 groundwater wells are in the southern bounds (red triangles) (Sup. Table S3.5).

The duration of these position time series range from the minimum 3 years to over two decades, and we consider 1 Jan. 2005 through 31 Dec. 2019 as the time period for our study. In general, the time series are continuous, though a few gaps exist which can range from days to several months in duration but do not have a significant adverse effect on individual trend estimates. Regional trends in vertical positions will be compared to GRACE, climate, and groundwater data discussed below.

3.6.3 Gravity Recovery and Climate Experiment

To investigate the spatial distribution of long-term hydrological trends in the High Plains aquifer region, we consider Gravity Recovery and Climate Experiment (GRACE) satellite data. GRACE measures the changing distribution of mass, primarily water, on the Earth's surface, including gravity perturbations caused by groundwater extraction (Tapley et al., 2004; Dunbar, 2013). Because GRACE does not distinguish between different styles of containment within aqueous units, we consider GRACE data to be representative of mass variation in the High Plains aquifer water content as a whole

(Brookfield et al., 2018). In this study, we use Goddard Space Flight Center (GSFC) GRACE time series solutions defined by 1 arc-degree (~100 km) mass concentrations (mascons) of gravitational pull to examine finer-scale regional gravity trends near the High Plains aquifer (Fig. 3.2) (Loomis et al., 2019). The fundamental spatial resolution of GRACE is ~300 km, and therefore each GSFC mascon is strongly correlated to their nearest neighbor mascons (Luthcke et al., 2013).

GSFC GRACE trends, including data from the GRACE Follow-On mission, were calculated from the GSFC solutions (Loomis et al., 2019). Continuous GRACE time series run from the start of the mission through present day, but mascon trends for the Great Plains were calculated through the last available data point in 2019, spanning 17 Mar. 2002–16 Dec. 2019 (Fig. 3.3). Fifty-eight mascons whose locations cover the geographical area of the High Plains aquifer system were divided into north and south parts of the aquifer based on their proximity to 38ºN latitude (Fig. 3.2 and Table S3.3). The northern High Plains aquifer has 28 GRACE time series, the southern High Plains aquifer has 30 (Sup. Table S3.3).

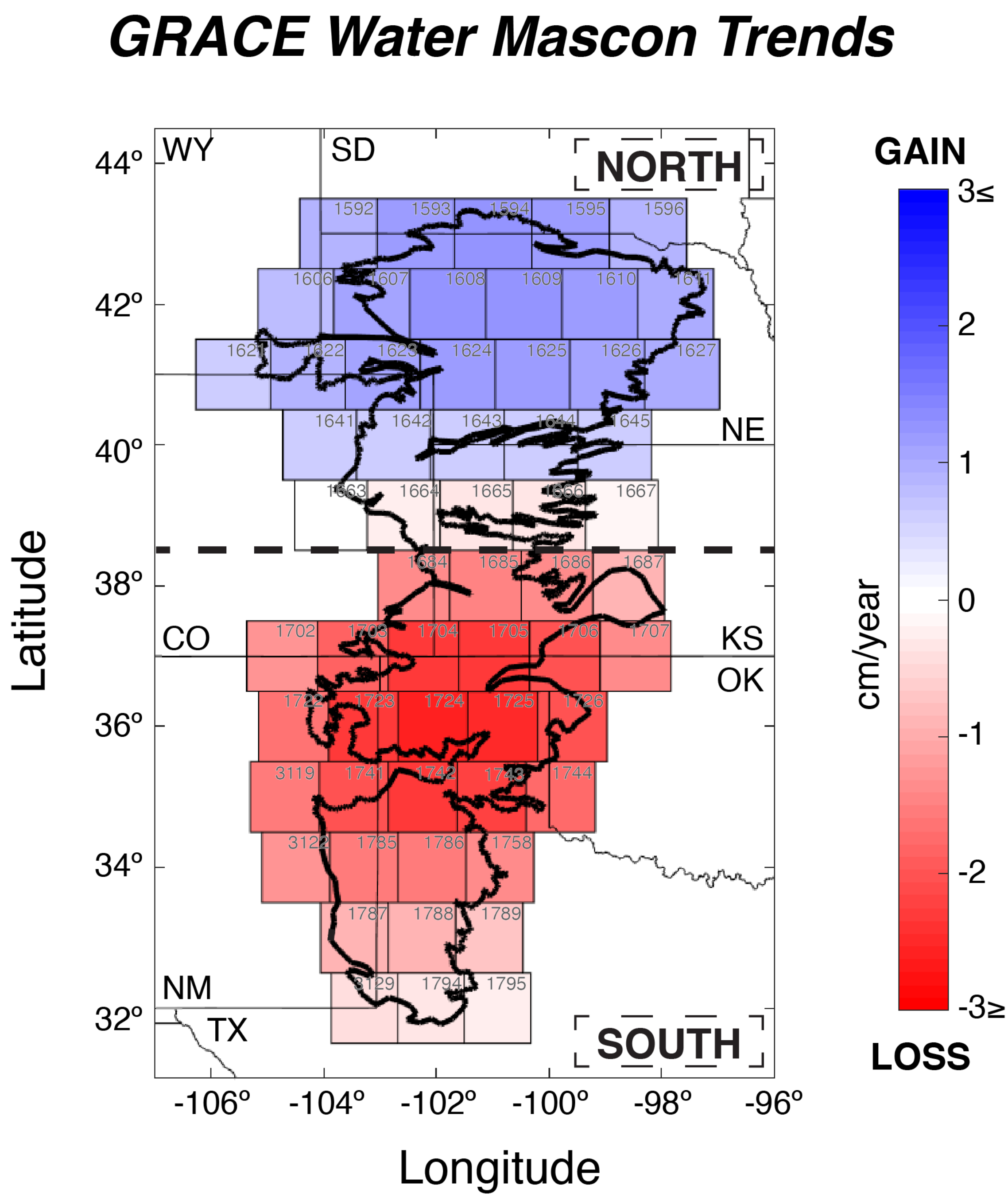

Figure 3.2. GSFC GRACE trends shown for the High Plains aquifer (outlined in black) divided into north and south sections (heavy dashed line). Gravity time series derived from 1° x 1° mascons (black squares) with GSFC mascon ID noted.

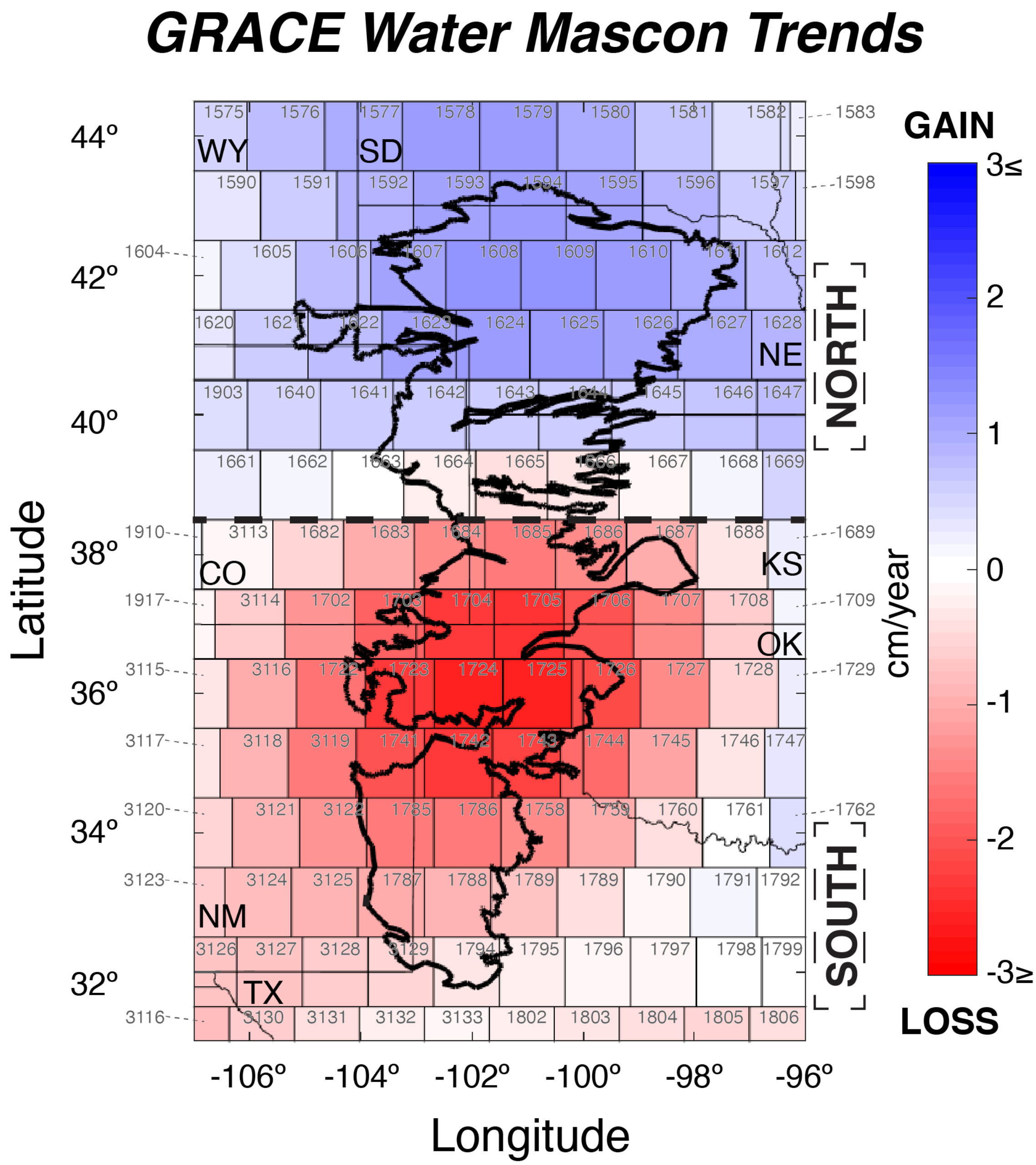

Figure 3.3. GSFC GRACE trends shown for the Great Plains study area divided into north and south sections (heavy dashed line). Gravity time series derived from 1° x 1° mascons (black squares) with GSFC mascon ID noted. High Plains aquifer outlined in black.

3.6.4 Climatic Water

To understand the role that climate change plays in the context of the High Plains aquifer and groundwater pumping, we gathered data from 28 climate divisions that overlap the aquifer region (Fig. 3.1) (Vose et al., 2014; Willett et al., 2018). Periods of drought or wet periods are indicated by Palmer Drought Severity Index (PDSI) data, which uses precipitation, atmospheric moisture supply, and surficial moisture demand to represent hydrological variations in the climate (Dai et al., 2004). Positive PDSI values indicate relatively wet periods and negative PDSI values indicate dry conditions. We acquired monthly PDSI data from the National Oceanic and Atmospheric Administration (NOAA) National Climatic Data Center for 16 climate divisions in the northern and 12 climate divisions in the southern part of the High Plains aquifer system. The dataset is continuous over our study's timespan (Sup. Table S3.4).

3.6.5 Groundwater Well Monitoring

We use groundwater well data obtained for the High Plains aquifer system as an indicator for anthropogenic and climatic impacts on the aquifer. We examine decadal trends in water levels and how they relate to GPS, GRACE, and PDSI trends. The well data were retrieved from the United States Geologic Survey (USGS) Groundwater Daily database using the High Plains aquifer as search criteria for all data available between 1900 through the end of 2019. Multiple and interconnected well sites were culled so that only one wellhead per site was included in the study, since water level change was essentially equivalent among sites on a single well. Only groundwater wells within the High Plains aquifer bounds were included to be consistent with the GRACE, PDSI, and GPS data bounds, and sites were required to have a minimum of two data points. The wells were then classified as northern or southern by their spatial relation to 38ºN latitude.

Of the 142 wells that fit these criteria, 121 belonged in the northern High Plains aquifer and only 21 were in the southern High Plains aquifer due to the limited availability of public groundwater monitoring (Fig. 3.3 and Sup. Table S3.5). In total, there is consistent regional well data in the northern High Plains aquifer ranging from 1934–2019 and 1930–2019 in the southern High Plains aquifer. The lengths of these time series range from days to many decades depending on the well. Older time series generally have large gaps in data collection, sometimes spanning decades, while water levels in younger time series are typically measured more frequently, from days to months. No individual well time series comprises the entirety of the historical timespan but, when used in conjunction, they demonstrate the overall trends of groundwater levels in the High Plains aquifer (Fig. 3.4).

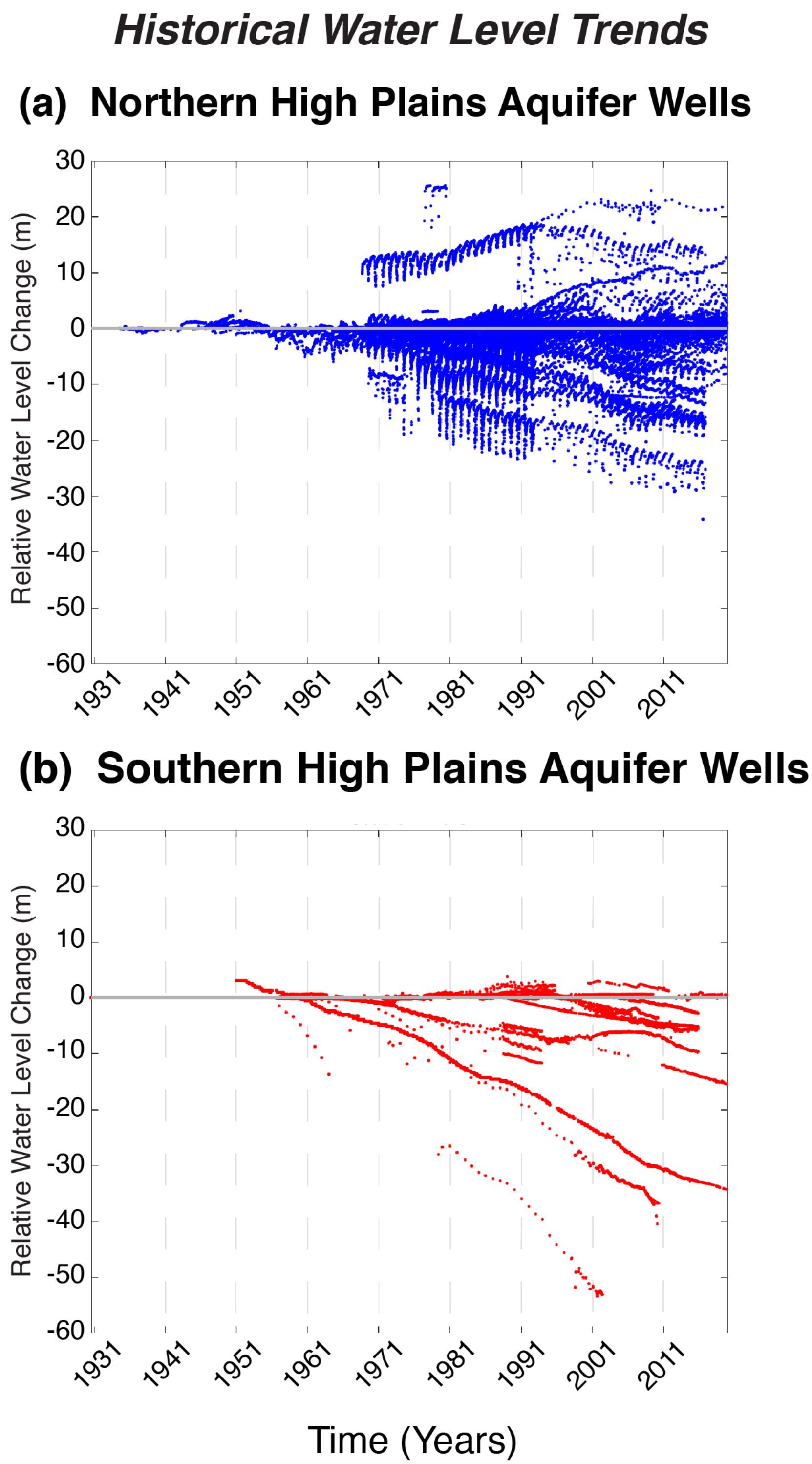

Figure 3.4. Historical water level trends from well data in **(a)** the northern High Plains aquifer and **(b)** the southern High Plains aquifer.

Water level changes were centered at zero for a given well's first measurement for each of the 142 wells in the dataset. The change relative to zero was then plotted against time. Groundwater levels ≥5 m in the positive or negative direction between the first data point and the last measurement are considered to be significant increases or declines in the groundwater level. Changes <5 m are not considered significant since groundwater measurements under 5 m typically returned back to the starting point over the lifespan of the well measurements. This helped to identify long-term trends in groundwater use that might reveal a clearer picture of hydrological fluctuations in the High Plains aquifer, and potential anthropogenic contributions to the water levels.

3.7 Analysis

3.7.1 GPS Imaging Processing Flow

Estimating vertical motions from GPS positioning data has traditionally been difficult owing to greater uncertainty in solutions for vertical positions and a diversity of processes contributing to the signals with low signal-to-noise ratios (Bennett and Hreinsdóttir, 2007; Mazzotti et al., 2007; Beavan et al., 2010). While technical advances in GPS data reduction have improved accuracy of GPS positions (Argus, 2012; Schmidt et al., 2016; Sibthorpe et al., 2011), vertical velocities can still be sensitive to unmodeled effects (e.g., undocumented equipment changes, atmospheric loading, or other transient motions) or bias introduced in imperfect modeling of refractivity of the atmosphere (Tregoning and Watson, 2009). Our processing practice addresses some of these concerns by using the MIDAS trend estimator, which calculates trends in the GPS times series that are robust and insensitive to the effects of outliers, seasonality, and undocumented steps in the data (Blewitt et al., 2016). We obtained 379 vertical MIDAS velocities from the GPS time series through 31 Dec. 2019 (Sup. Table S3.1) (Blewitt et al., 2018).

To better constrain the spatial distribution of the uplift signal, we construct an interpolated GPS velocity field using the GPS Imaging technique modified from Hammond et al. (2016) to show vertical motions in the Great Plains region of the United States (Fig. 3.5a). To obtain a vertical rate field of the Great Plains region, the GPS Imaging algorithm incorporates weighted median spatial filtering on a Delaunay triangulation of the 379 GPS station velocities (Fig. 3.5b) to diminish the influence of outlier vertical rates (Fig. 3.5c). An outlier vertical rate is defined as one uncorroborated by the nearest stations, often caused by deficiencies in station or monument design, very local deformation effects, equipment problems, or geophysical signal impacting only a single station. GPS Imaging thus enhances the signals that are similar between stations that may be ascribed to the spatially coherent movement of the solid Earth rather than individual outliers that could potentially bias the velocity field.

As a part of our GPS Imaging vertical rate field estimation, we apply an artifact reduction technique. Small scale artifacts in the vertical rate field can sometimes appear as domain boundaries that are attributable to inhomogeneous GPS station distribution. We iterate the GPS Imaging process for the Great Plains 20 times, each iteration removing a random 35% of velocities to reduce the effects of these artifacts. Testing of the number of iterations showed that fewer than 20 iterations only partially removed the artifacts, and removing more than 35% of velocities per iteration affected the rate and breadth of the vertical land motion field. Similar to the statistical bootstrapping method, we identify the median model by taking the median value of the vertical rate at each pixel of the vertical field to create the new velocity field (Fig. 3.5d).

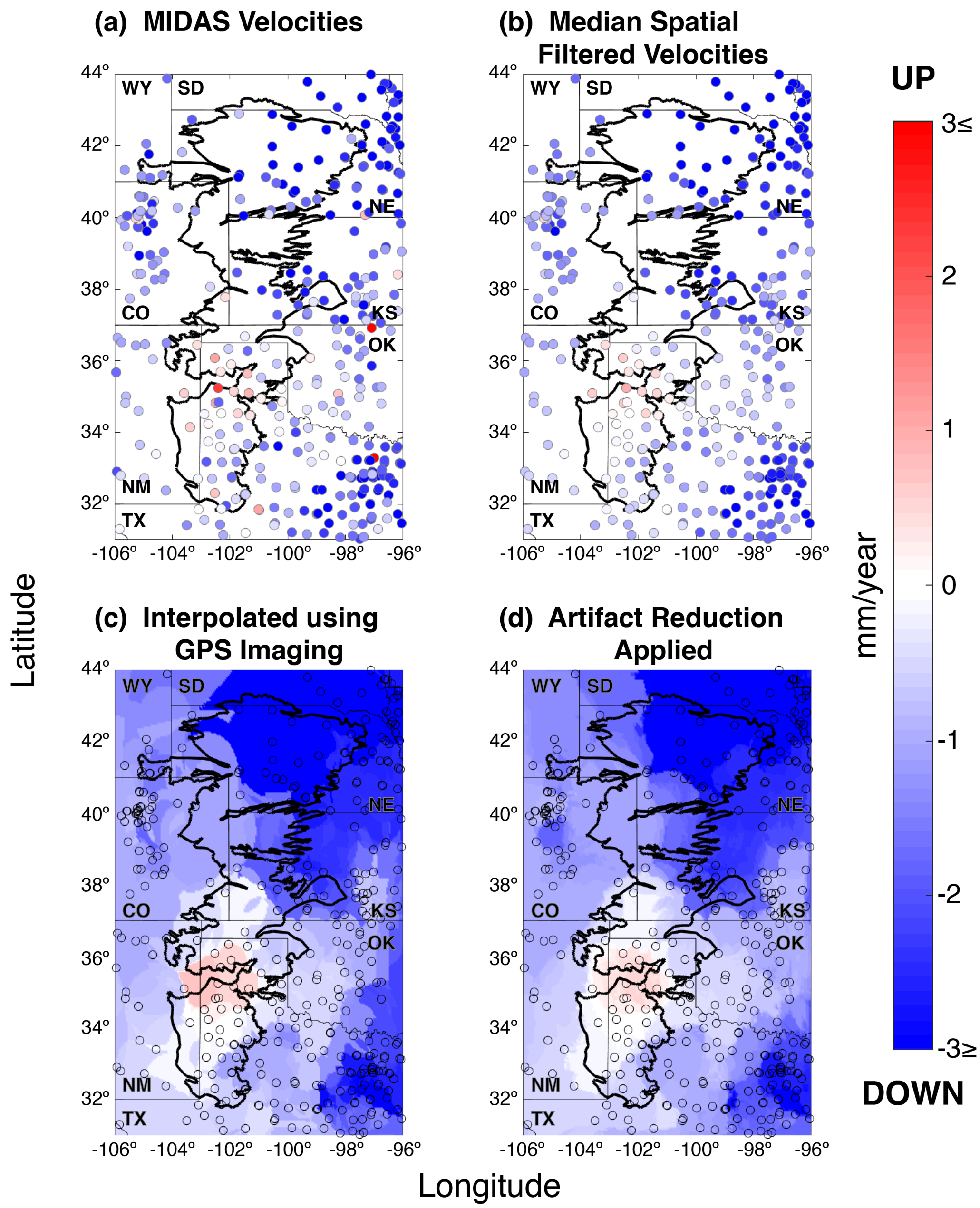

Figure 3.5. High Plains aquifer is shown with black outline. **(a)** MIDAS velocities before GIA corrections are applied. **(b)** Median spatial filtered velocities with speckle noise removed before GIA corrections are applied. **(c)** Vertical velocity field from GPS Imaging before artifact reduction and GIA corrections are applied. **(d)** Vertical velocity

field from GPS Imaging after bootstrapping statistical analysis but before GIA corrections are applied.

We next correct the vertical velocity field produced by GPS Imaging for the effects of glacial isostatic adjustment (GIA) which greatly influences vertical motions across North America following Late Pleistocene deglaciation (Peltier et al., 2015). As the northern part of the continent experiences post-glacial uplift, the lithosphere flexes to accommodate unloading and drives subsidence in the far field via forebulge collapse (Watts, 2001). We use the ICE-6G D (VM5a) glacial isostatic adjustment model (Fig. 3.6) (Peltier et al. 2015; Peltier et al., 2018; Argus, Peltier, et al. 2014) which fits vertical GPS rates and GRACE measurements in the Canadian interior (Argus et al., 2021). The glacial isostatic adjustment model was interpolated from 0.2º x 0.2º latitude and longitude intervals to match the GPS Imaging grid size of 0.0083º x 0.0083º latitude and longitude. We then remove the effect of the forebulge collapse estimated by subtracting glacial isostatic adjustment model predictions from the GPS Imaging results. All GPS Imaging figures where vertical land motion is presented are corrected for the effects of glacial isostatic adjustment unless otherwise noted.

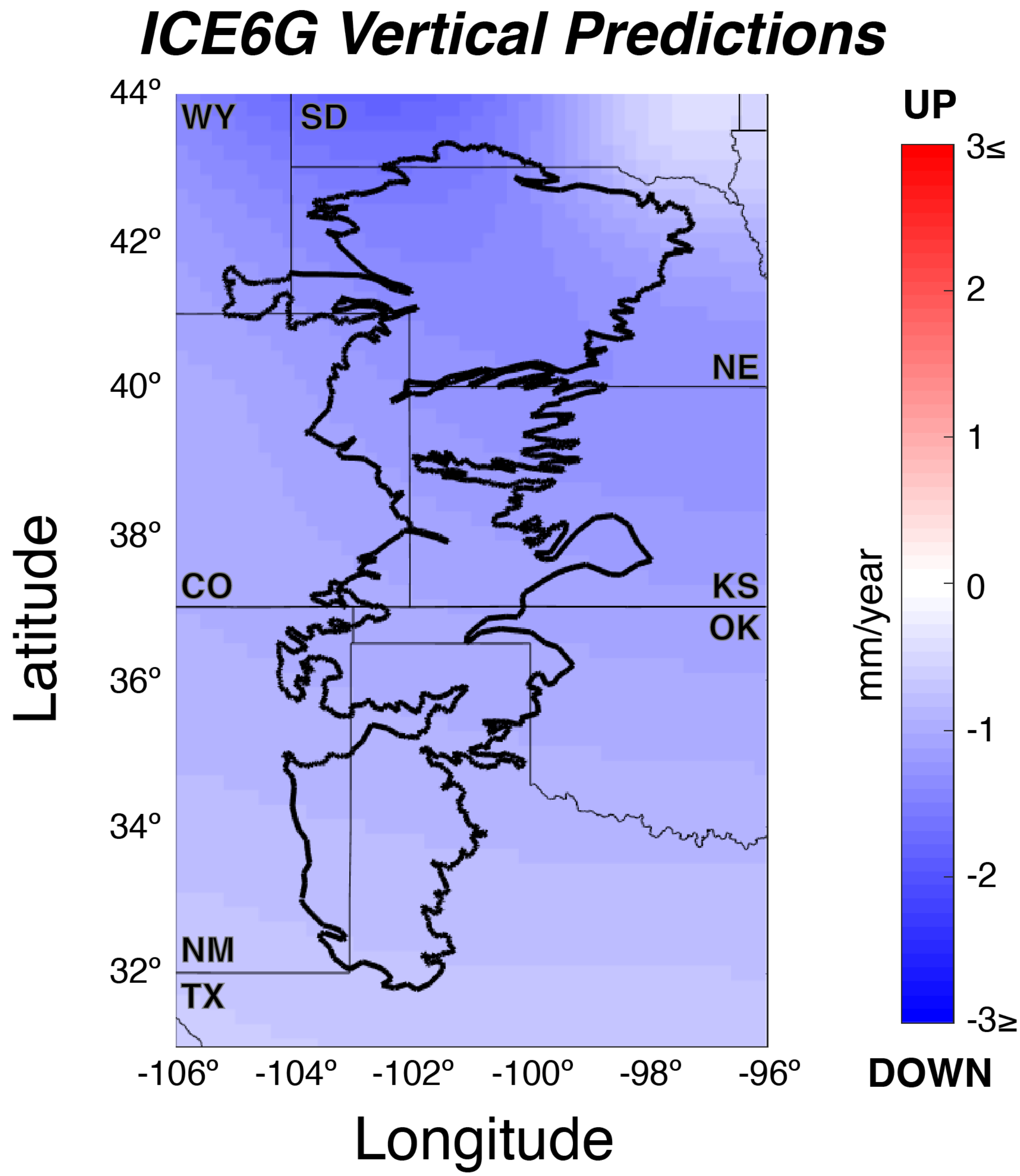

Figure 3.6. Interpolated vertical velocity field of Great Plains forebulge collapse signal caused by North American Late Pleistocene deglaciation according to the ICE 6G D (VM5a) glacial isostatic adjustment model by Peltier et al. (2015; 2018) and Argus et al.

(2014). Median value of post-glacial rebound is -0.50 mm/year. High Plains aquifer outlined in black.

3.7.2 Resolution Tests

To verify that the location of the anomaly is not biased by station spacing, we performed resolution reconstruction tests using a synthetic checkerboard model. The overall resolution of imaging of the Great Plains vertical land motion is adequate for a checkerboard model with 4º x 4º blocks of alternating positive and negative vertical land motion. There are minor distortions occurring in areas with fewest GPS stations, such as eastern Colorado, but these are improved by applying the bootstrapping statistical technique (Fig. 3.7). The Texas Panhandle and surrounding areas of greatest uplift had better resolution with adequate reconstruction of 2º x 2º alternating blocks due to greater GPS station density (Fig. 3.8). Because of the reduction of artifacts, we are confident that the velocity field created by GPS Imaging reflects accurate spatial distribution of the uplift anomaly in the southern High Plains aquifer.

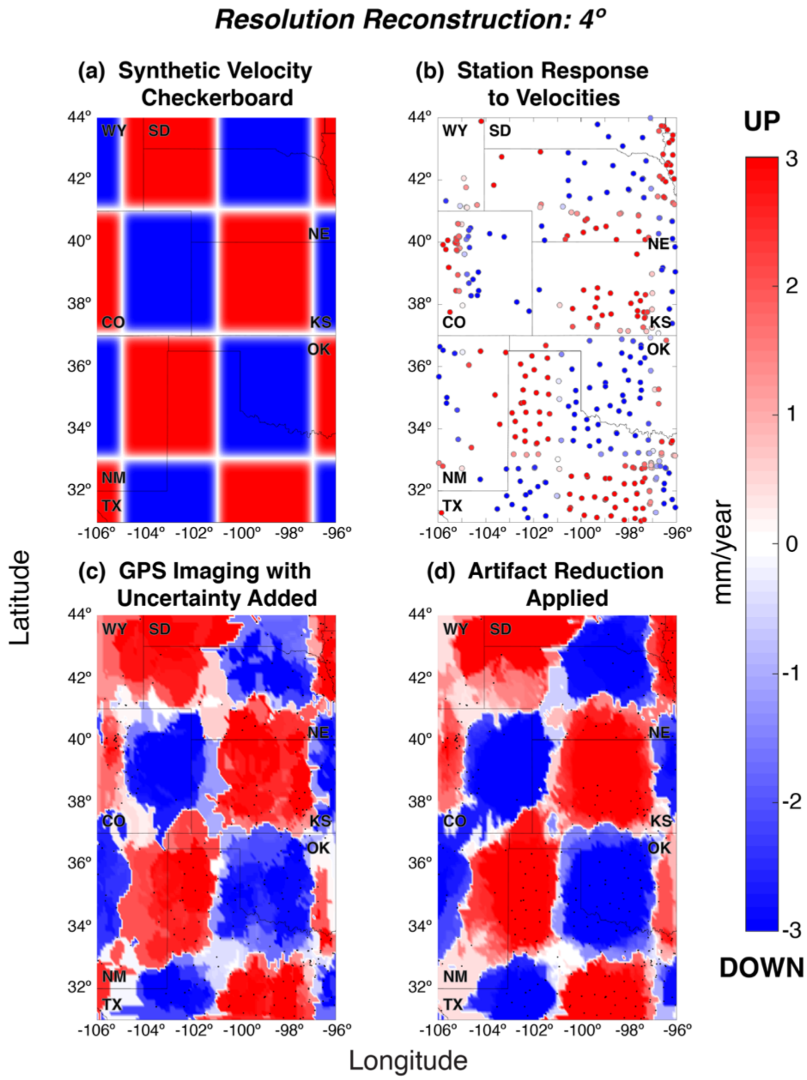

Figure 3.7. Checkerboard resolution test with 4° intervals and 0.1° of resolution. Resolution testing using synthetic checkerboard velocity input of ±3 mm/year from station locations (dots). **(a)** Synthetic velocity checkerboard applied to the Great Plains region to test for spatial resolution. **(b)** Station distribution with synthetic vertical velocities applied. **(c)** Resultant checkerboard after GPS Imaging with present current uncertainty added. **(d)** Final resultant checkerboard of GPS Imaging result after bootstrapping technique applied. Only stations inside the study area were used in the artifact reduction process.

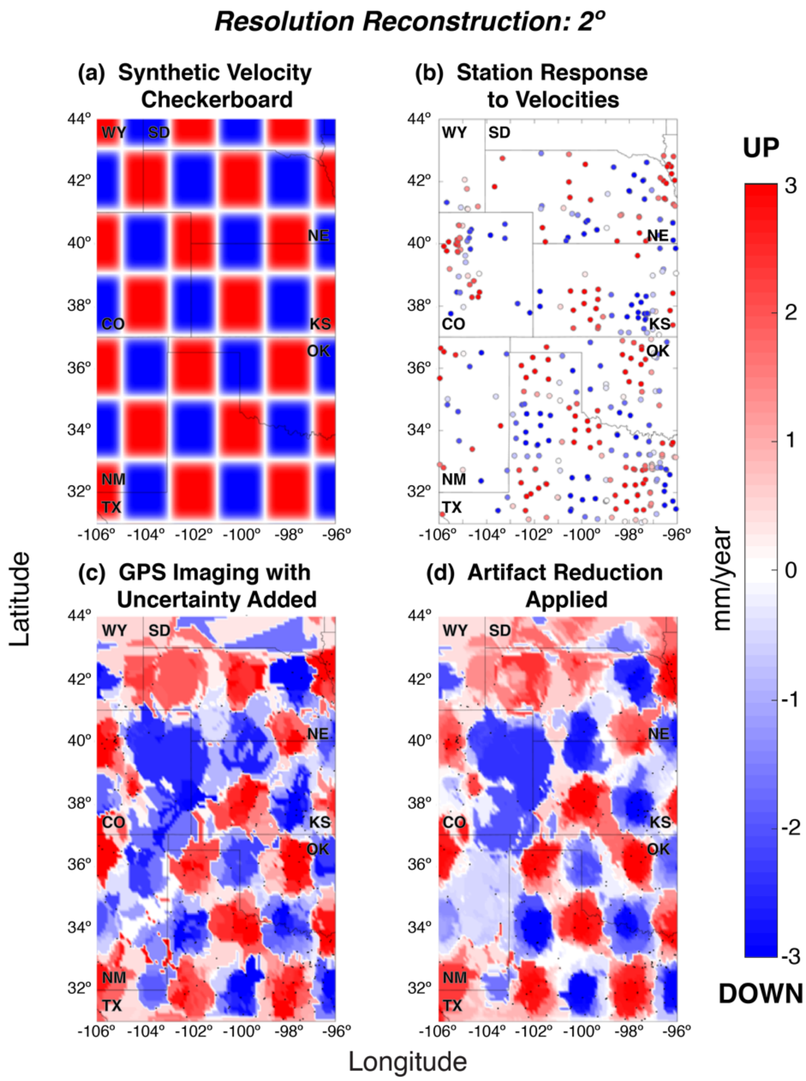

Figure 3.8. Checkerboard resolution test with 2° intervals and 0.1° of resolution. Resolution testing using synthetic checkerboard velocity input of mm/year from station locations (dots). **(a)** Synthetic velocity checkerboard applied to the Great Plains region to test for spatial resolution. **(b)** Station distribution with synthetic vertical velocities applied. **(c)** Resultant checkerboard after GPS Imaging with present current uncertainty added. **(d)** Final resultant checkerboard of GPS Imaging result after bootstrapping technique applied. Only stations inside the study area were used in the artifact reduction process.

3.7.3 Topographic Profiles

Vertical GPS signals can sometimes be attributable to topographic changes driven by underlying geodynamic processes (Serpelloni et al., 2013; Pfeffer et al., 2017). Though the lithosphere in the vicinity of the Great Plains is tectonically stable compared to tectonic plate boundaries, and our study area is located away from continental margins, we investigated whether the uplift might be related to topographical changes in the landscape of the region. Specifically, we wanted to determine whether the uplift pattern is correlated with topography of the study area.

Two main transects, one centered around 35.25ºN latitude and the other at −102º longitude, were taken with 0.5º padding on either side to illustrate the trend pattern (Fig. 3.9a). Eleven GPS Imaging velocities and elevation profiles, centered around each latitude and longitude and spaced ~1 km apart formed each corresponding transect to avoid redundancy. The mean GPS Imaging velocity and mean topography were calculated along each profile and plotted for comparison (Fig. 3.9b and 3.9c). The MIDAS GPS velocities for stations that fell within the transect bounds were also plotted (Fig. 3.9b and 3.9c), but GPS Imaging results within those bounds were constrained by velocities both inside and outside the bounds. The result shows that the GPS vertical land motion signal is not correlated with topography, and therefore the signal is likely not associated with the processes that built the topography.

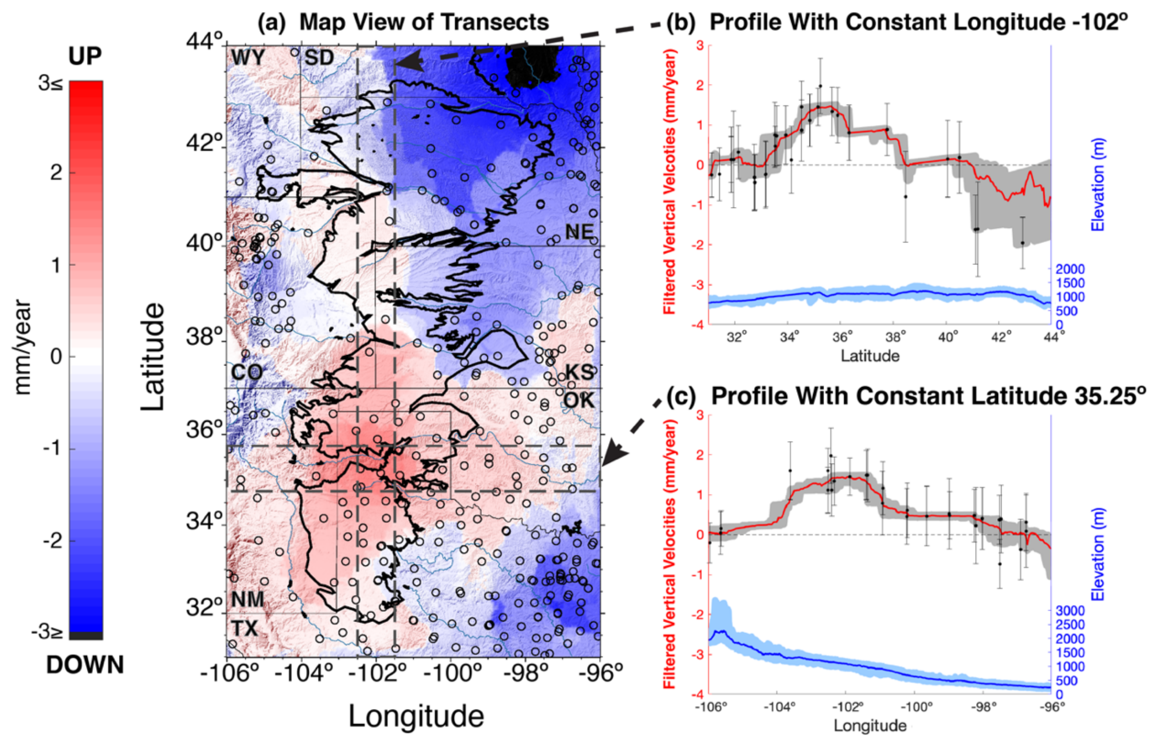

Figure 3.9. **(a)** Map view of GPS vertical land motion with model for GIA removed (see Fig. 3.10 for uncertainties). Gray dashed lines indicate the location of transects centered on the region of greatest uplift. GPS station locations shown with black circles. High Plains aquifer outlined with bold black. Profiles with **(b)** constant longitude and **(c)** constant latitude display the vertical velocity corrected for GIA, and topographic changes across the region of greatest uplift. Transects include 0.5º of padding around center line for GPS Imaging vertical velocities and topographic data. The set of velocity transects (gray) was averaged and the mean (red) is plotted across the profiles. Filtered GPS velocities for each transect are plotted (black dots) with accompanying 2σ error bars. While we show velocities from stations within the profile bounds, GPS Imaging results are often constrained by velocities outside those bounds. The interpolated velocity is constrained by the set of topographic transects (light blue) and its mean average (blue) is

plotted across the profiles. Uplift at the KS-OK eastern edge is likely related to the Ozark Plateaus aquifer system (Larochelle et al., 2021).

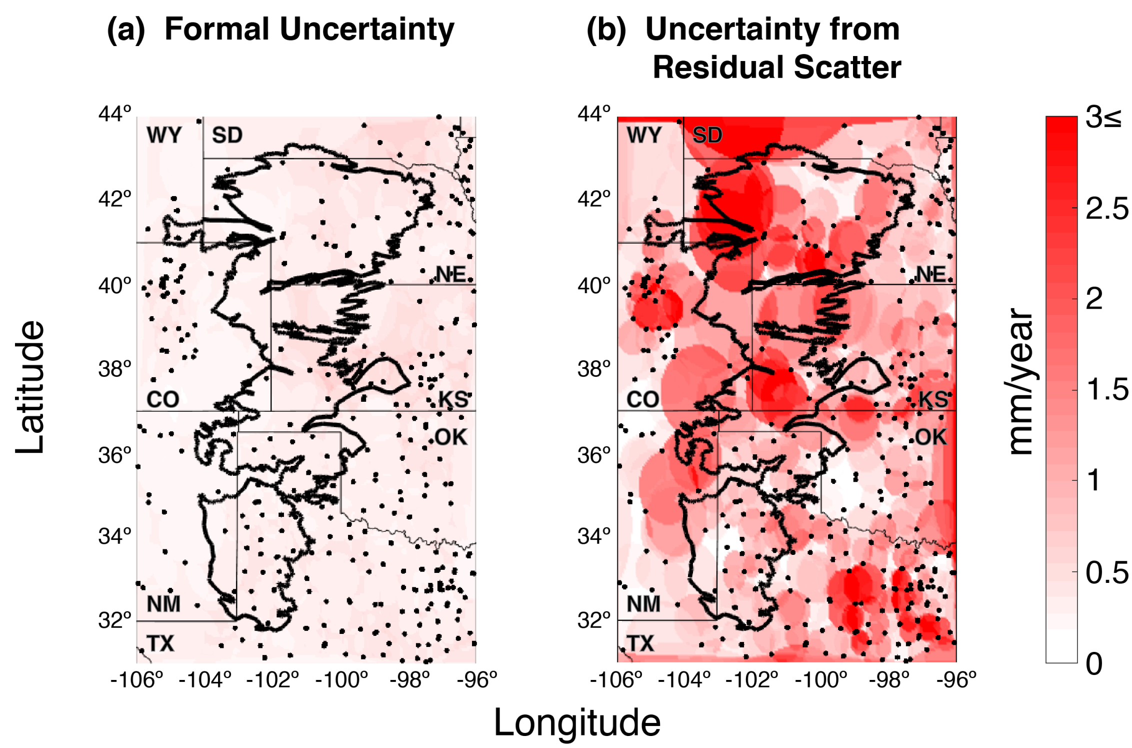

Figure 3.10. Vertical velocity uncertainty for the GPS Imaging result. **(a)** Formal uncertainties calculated from the weighted mean of contributing velocities. **(b)** Uncertainties computed from root-mean-square of residual scatter from contributing velocities.

3.7.4 Seasonality

Most vertical GPS position time series in our dataset show seasonal oscillations caused primarily by the effects of hydrological loading. We consider short-term variations because they illustrate the link between short-term hydrological forcing and the spatiotemporal vertical land motion response, which is presumed to be elastic. To infer the seasonality of hydrological loading, we calculated the amplitude and peak phase of the vertical time series used in our GPS Imaging.

Before solving for seasonality terms, however, we correct each time series for offsets. Offsets, or steps, present as sharp, immediate discontinuities in position time series that can occur because of changes in GPS station equipment or site conditions, or from earthquakes that move the station. NGL currently maintains a list of step events for all GPS stations in its holdings. The records in this file are flagged as “potential steps” because the time series may not have significant offsets at these times, e.g., if a logged equipment change resulted in no discernible effect or the station is sufficiently distant from the earthquake hypocenter. Potential equipment steps are derived from station IGS log files, and earthquake events are derived from earthquake source parameter information available from the USGS National Earthquake Information Center. Unfortunately, our set of station log files is incomplete and/or site logs are incomplete, and thus we also manually examined each individual time series for undocumented offsets. Of the 379 stations in our dataset, 101 undocumented offsets were discovered, and the missing step times were tabulated and added to the master list of documented offsets for correction. For time series with offsets from either earthquake events or equipment changes, we used position data from five days before the step and three days after each step to estimate the step size. The difference of the median positions before and after the offset time was subtracted from the subsequent positions.

With the offsets corrected, annual terms can be estimated using the following equation:

$$\text{Eq. 3.1)} \qquad u(t) = b + S_1 \sin(\omega\, t) + C_1 cos\,(\omega\, t)$$

Where u are vertical GPS positions given at time t detrended with MIDAS velocities, b is the intercept, and $\omega = 2\pi$ is angular frequency in radians per year. S_1 and C_1 are sine and cosine annual terms. We performed a weighted linear inversion for intercept and amplitudes of the cosine and sine annual terms and the position time series to calculate b, S_1, and C_1 terms in Eq. 3.1. The annual sine and cosine terms were then converted into amplitude (*A)* and peak phase (ϕ):

$$\text{Eq. 3.2)} \qquad A = \sqrt{{C_1}^2 + {S_1}^2} \qquad\qquad \text{Eq. 3.3)} \qquad \phi = \mathrm{atan2}(S_1, C_1)$$

Where atan2 is the 4-quadrant arctangent function. The peak phase ϕ can be converted into day of the year (DOY) for a more intuitive way of representing the timing of the maximum in seasonal vertical component height.

$$\text{Eq. 3.4)} \qquad \text{Day of Year} = \frac{365\phi}{2\pi}$$

We apply the GPS Imaging algorithm to the amplitude and phase values at each station to see the spatial variation in patterns of amplitude and timing of vertical seasonal motion. GPS Imaging was performed according to the previously described standard procedure (see Analysis 3.7.1) except corrections for GIA which are not applied. The resultant images show the spatial variability of vertical land motion seasonality for the Great Plains region (Fig. 3.11). Phase resolution is typically not well resolved in areas of very low amplitude, e.g., in northern Texas the distinction between winter and spring peak time is not well resolved, but the peak in winter in Nebraska is well resolved.

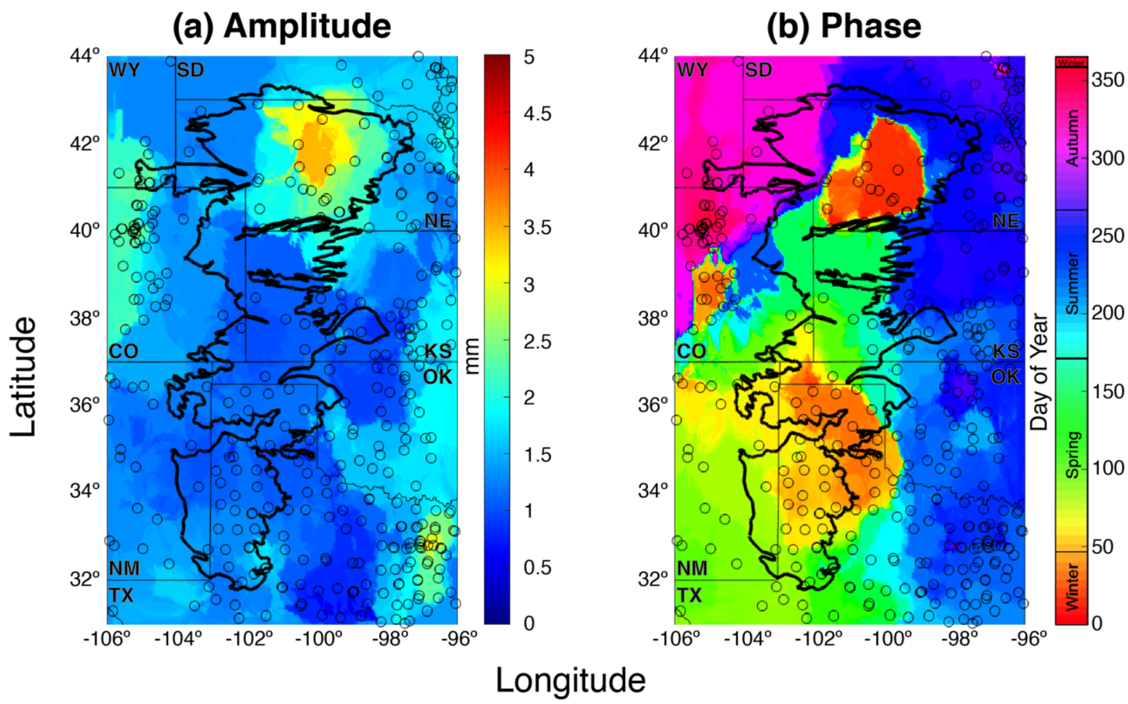

Figure 3.11. Outline of the High Plains aquifer bounds is in black. **(a)** GPS Imaging of seasonal amplitudes (see Fig. 3.12 for uncertainties). **(b)** GPS Imaging results for day of year vertical height is a maximum (see Fig. 3.13 for uncertainties). Color scheme indicates the day of the year the vertical positions are at their highest.

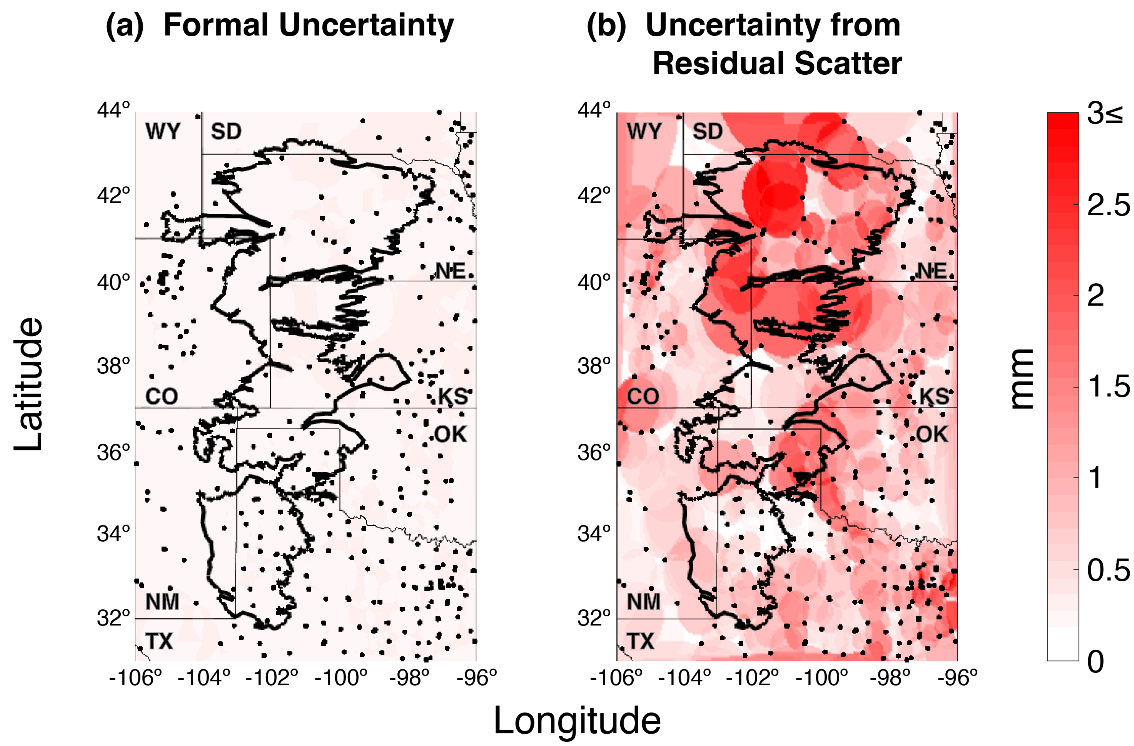

Figure 3.12. Amplitude uncertainty for the GPS Imaging result of seasonality. **(a)** Formal uncertainties calculated from the weighted mean of contributing amplitudes. **(b)** Uncertainties computed from root-mean-square of residual scatter from contributing amplitudes.

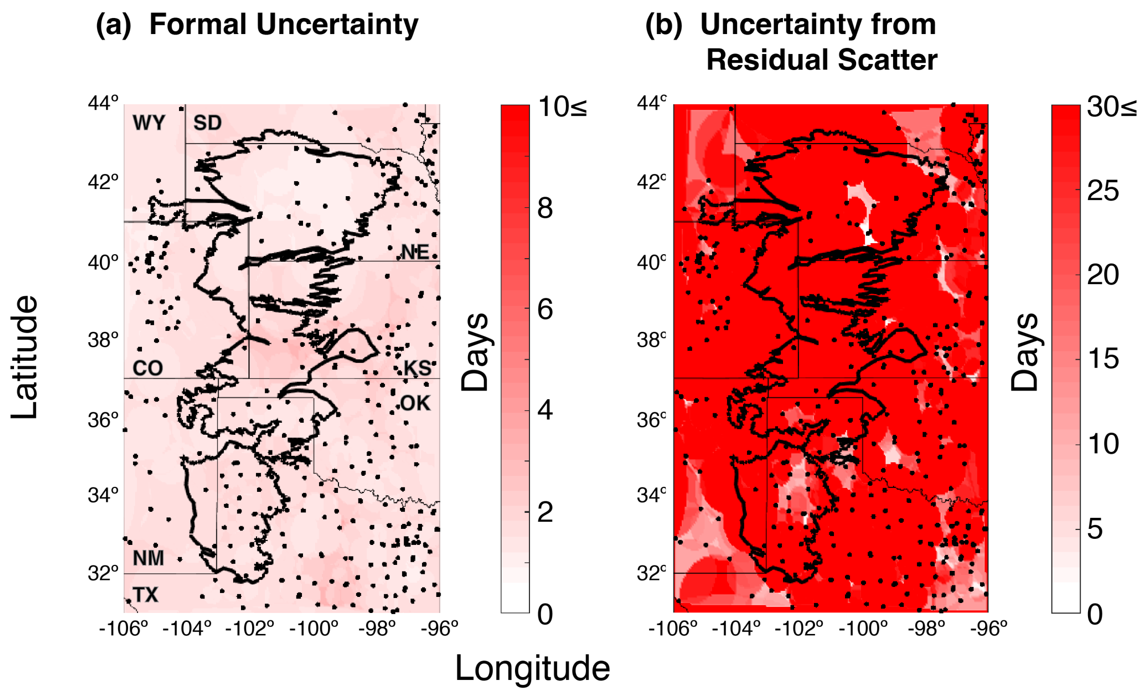

Figure 3.13. Phase uncertainty for the GPS Imaging result of seasonality. **(a)** Formal uncertainties calculated from the weighted mean of contributing phases. **(b)** Uncertainties computed from root-mean-square of residual scatter from contributing phases.

3.7.5 High Plains Aquifer Time Series

Times series of GPS, GRACE, and PDSI between 1 Jan. 2005 and 31 Dec. 2019 exhibit correlations in time between these datasets that support the importance of hydrological influences on High Plains aquifer vertical motion. To reduce scatter, we combined the daily positions for each time series to obtain monthly medians. From the monthly data for each regional dataset, we then calculated median lines to compare and discern overarching regional trends (Fig. 3.14g). The standard deviation (σ) for each month was computed and a zone of $\pm 2\sigma$ is plotted with the median (Fig. 3.14g). The time series trends were adjusted to remove the effects of GIA.

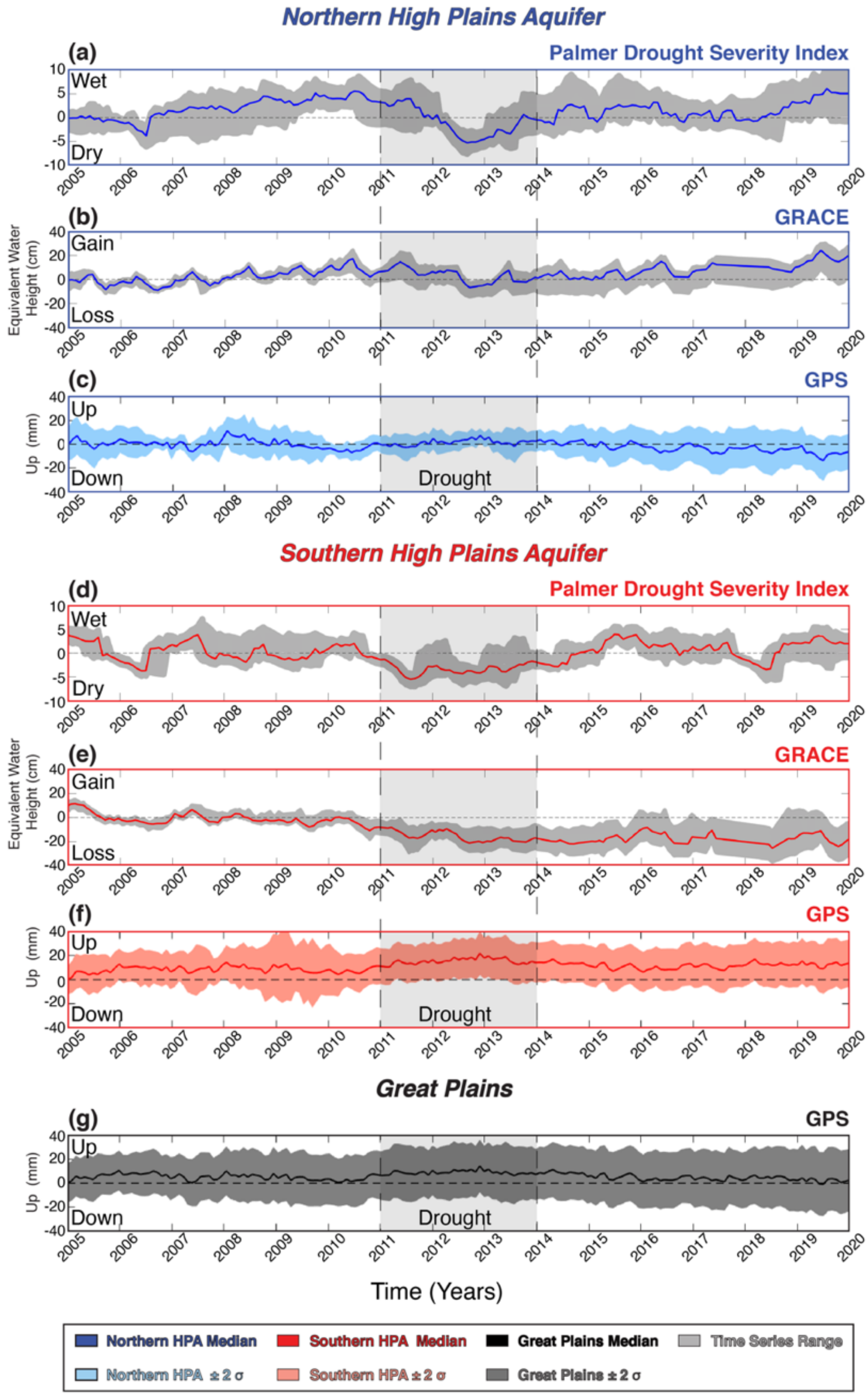

Figure 3.14. Time series comparisons for the Northern **(a–c)** and Southern **(d–f)** High Plains aquifer, and Great Plains **(g)**. Time series comparison of PDSI **(a & d)**, GRACE

(**b & e)**, and GPS time series **(c, f, & g)**. The median (solid color line) was calculated from the overlapping time series range (light gray). Light background colors show $\pm 2\sigma$, the standard deviation of the GPS time series vertical positioning data.

The PDSI time series were used to define early and late periods to distinguish these intervals from the long-term climatic trends in the High Plains aquifer. Drying patterns between the northern and southern parts of the High Plains aquifer differ within these time frames, so the overall PDSI was used to define the periods. Extended duration positive (>2) or negative (<−2) PDSI values indicate long-term wet or drought periods respectively (Dai, 2019). We define the early/dry period range from 1 Jan. 2005 through 31 Dec. 2013. The early/dry period includes the three-year period of severe drought from 2011–2013, with 2011 notably the most intense one-year drought in the history of Texas centralized in the Texas Panhandle (Nielsen-Gammon, 2011). The entire High Plains aquifer has a mean PDSI of −0.13 during this time. We define the late/wet period as 1 Jan. 2014 through 31 Dec. 2019, and this timespan has an overall High Plains aquifer PDSI mean value of 1.18. The early/dry and late/wet periods are not divided evenly in time due to the relatively short duration of drought events, and partly based on considerations regarding the number of GPS time series available in each period. Though the climate trends are not consistent over the entire time frame, and though there are climatic differences between the northern and southern High Plains aquifer, we are confident that the designated early and late periods of observation show a general trend of drying or moisture that is representative of the High Plains aquifer climate.

GRACE trends for individual mascon time series were also calculated to plot the spatial distribution of gravity signals in the High Plains aquifer (Fig. 3.2) to compare with the GPS Imaging results. To further illustrate the difference in water input between the southern and northern parts of the aquifer, best-fit trends for each mascon were calculated using a simple linear regression to fit a first-degree polynomial within a 95 percent confidence interval (Sup. Table S3.3).

3.8 Results

The monthly median of all vertical GPS time series within the study area shows an overall uplift trend in the Great Plains region (Fig. 3.14g). This time series is used as a baseline against which to compare signals from the northern and southern regions, and early and late periods. The overall trend for the entirety of the Great Plains study area indicates a near zero velocity (after adjusting for GIA) of approximately −0.13 mm/year between 2005 and the end of 2019. Between 2005–2007, the trend for the Great Plains shows a moderate rise in vertical land motion to +6 mm, then subsidence through the latter half of 2010 down to +2 mm. Through the 2011–2013 drought, the time series shows sharp uplift gains from approximately +8.5 mm to as high as +14 mm for the entirety of the Great Plains. This finding is consistent with Borsa et al.'s (2014) California vertical land motion study that showed a very long wavelength response to drought which stands as a background to the more local drought signals. Post-drought subsidence shows the time series trend declining from +14 mm to +2 mm from 2013 through the end of 2019.

3.8.1 Uplift of the High Plains Aquifer

The GPS Imaging result shows an uplift trend in the southern portion of the High Plains aquifer with the greatest rate of uplift centered around the Texas Panhandle (Fig. 3.9a). The uplift rate is ~1.5–1.7 mm/year and extends throughout the southern High Plains aquifer region. The area with positive uplift is approximately 670 km long from north to south and 280 km wide from east to west, though this is latitude dependent (for GPS Imaging uncertainties, see Fig. 3.10). The area of greatest uplift extends from the southwest corner of Kansas into the Texas Panhandle. Topographic profiles demonstrate no correlation between the anomalous uplift pattern and topography in either latitude or longitude. Instead, uplift is spatially correlated to areas of greatest groundwater withdrawal in the High Plains aquifer system since 1900 (McGuire, 2017: Fig. 3.15).

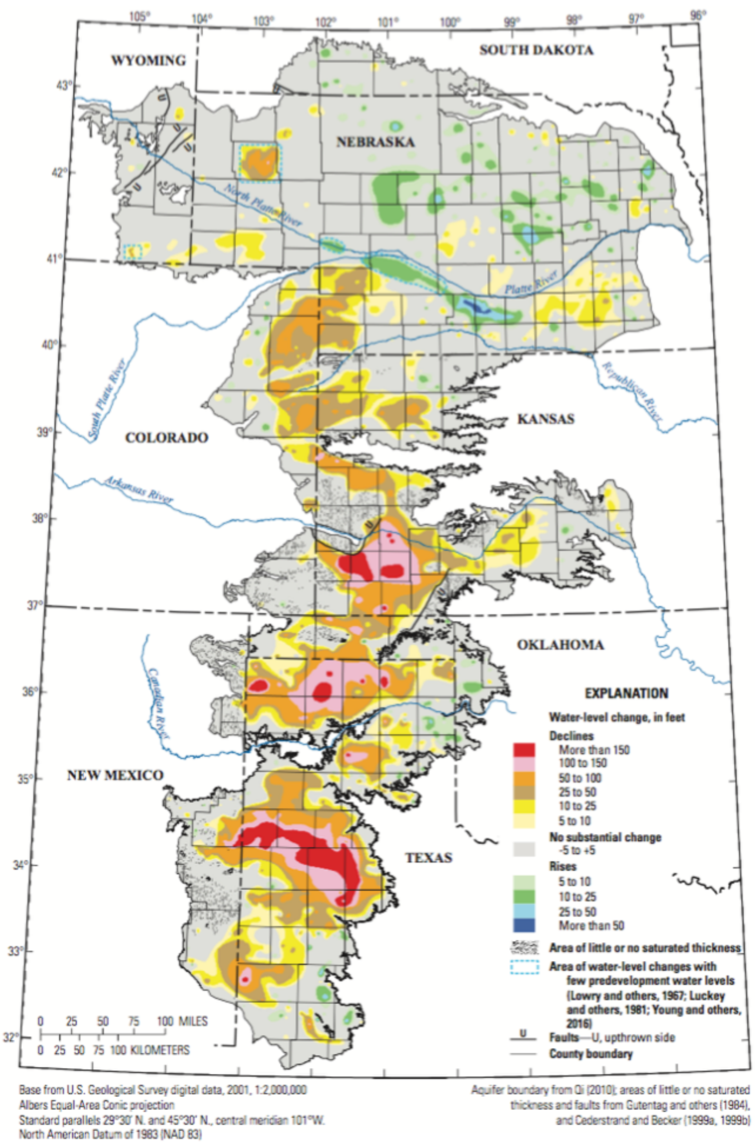

Figure 3.15. From McGuire (2017). Water level changes from pre-development era (circa 1950) through 2015. High Plains aquifer shows prominent water-level declines throughout the Texas panhandle region north into Kansas. Areas of greatest water level decline are shown in warm colors, with red representing >46 m of decline, pink from 30–46 m, orange from 15–30 m, and brown and yellow between 1.5–15 m. Cool colors represent areas of water-level increase, generally less than 15 m with most increases occurring in the northernmost section of the aquifer.

According to trends monitored by the USGS, High Plains aquifer groundwater levels have changed by as much as −53 m between 1956 and 2002 (Sup. Table S3.5) within the area of greatest uplift, and most of the southern portion of the aquifer shows declines of at least 7 m (Fig. 3.15). Total volume of water removed in the High Plains aquifer is estimated at 330 km^3 as of 2007 (Scanlon et al., 2012). By comparison, cumulative oil production in the nearby Anadarko Basin is estimated at more than 0.8 km^3 (Davis et al., 1988) while the Permian Basin to the south has produced over 5.25 km^3 (US Energy Information Administration, 2018), meaning widespread uplift due to oil production and associated byproducts is highly unlikely. There are no geologic indicators of recent large magnitude (>M6) tectonic activity or magmatic activity (Gutentag et al., 1984) near the center of uplift that can impact vertical motions (e.g., post-seismic relaxation (Gourmelen and Amelung, 2005; Hammond et al., 2012)) or mantle upwelling (Kreemer et al., 2020). Spatial distribution of the uplift encompasses nearly the entirety of the southern High Plains aquifer, so we investigate the possibility that long-term hydrological unloading is the primary source of uplift.

3.8.2 Connecting Vertical Land Motion to Climate

To illustrate the effect that climate variability has on the Great Plains vertical velocity field, we examine how vertical uplift rates respond to climatic trends spanning multiple water seasons. Increasing uplift during periods of drought is expected when hydrological loading effects (as opposed to poroelastic effects) drive vertical motions on a regional scale. During the drought years, groundwater withdrawal from the High Plains aquifer was more intense as precipitation and surface water resources became exacerbated. During the span of our time series comparison, the Great Plains underwent several periods of drought, including continuous drought from 2011–2013, with 2011 being the most intense one-year drought in Texas history (Nielsen-Gammon, 2011). Employing the definition of early/dry versus late/wet periods using PDSI data (see Analysis 3.7.5) we divided all GPS time series into their early and late periods and calculated MIDAS rates. GPS Imaging was performed for each period (Fig. 3.16).

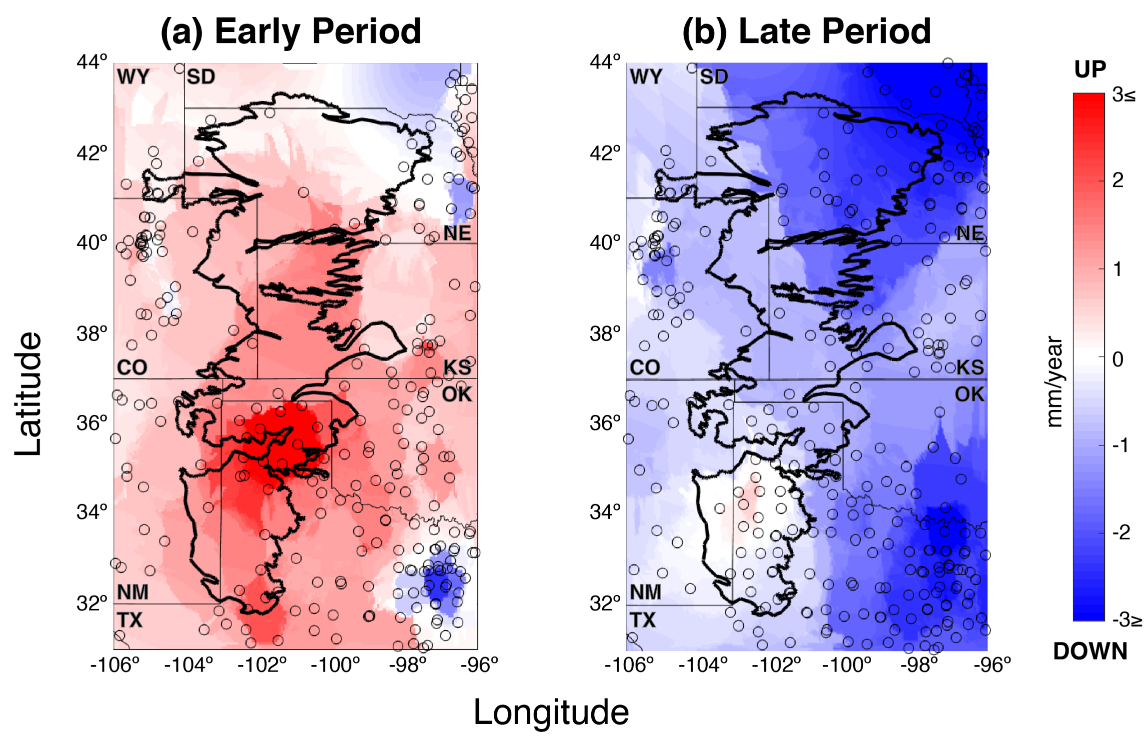

Figure 3.16. High Plains aquifer outlined in black. Circles represent GPS station locations. **(a)** Vertical velocity during early/dry period from 2005–2013. **(b)** Vertical velocity during late/wet period ranging from 2014–2019.

The early/dry period (2005–2013) is dominated by uplift across the entire High Plains aquifer region, with a rate of nearly 4 mm/year centered around the Texas Panhandle (over double the maximum rate for the entire period of observation). In the late/wet period (2014–2019), most of the study region is dominated by subsidence, although the southwestern Texas Panhandle experiences a more subdued uplift of 0.5 mm/year (less than one third the rate for the entire period). In general, the southern portion of the aquifer appears to be subsiding at a lesser rate than the surrounding areas. That the GPS stations move upward during drying and downward during wet periods corroborates their source, and the primary anomaly in the southern High Plains aquifer over the entire period is a response to hydrological unloading.

The monthly median GPS time series data from the southern and northern regions show a similar story (Fig. 3.14). Preceding the drought years, the vertical position data largely oscillated around +0.5 mm in the northern High Plains aquifer until 2009, when there was a short subsiding trend from 2009–2011 of about −1 mm. In the southern High Plains aquifer, the position time series increased slightly but oscillated around +8 mm before the drought. During the drought years of 2011–2013, both northern and southern regions moved upwards rapidly. The northern region moved from −1 mm up to +7 mm, and the southern region moved further upwards from +8 mm to +22 mm. Post-drought, both time series shift to downward trends again, with the southern High Plains aquifer position time series higher than its pre-drought position at approximately +12 mm, and the northern High Plains aquifer further subsiding to as low as −14 mm, but generally oscillating around −3 mm.

The difference between the northern and southern High Plains aquifer vertical land motion responses is likely tied to geographical differences in climate. PDSI time series indicate that the northern High Plains aquifer has greater amounts of time spent with positive PDSI values, which indicates it experienced more times with wetter than average climate during the observation period (Fig. 3.14a and 3.14d). The exception of the time series is during the 2011–2013 drought, which exhibits negative PDSI values, with the median PDSI being greater than −5 in 2012. Unlike to the north, the southern High Plains aquifer PDSI time series median crosses into negative PDSI range outside of the severe drought timespan, generally hovering between ±3. This indicates the southern High Plains aquifer has spent more time in a state of drier than average conditions and experiences greater climate variability than the northern High Plains aquifer.

3.8.3 Effect of Seasonality on Vertical Land Motion

Previous studies have illustrated that seasonal changes in precipitation, snowpack, lake loading, and surface water can be similar to climate variations, detected using GPS on regional (Fu and Freymueller, 2012; Argus, Fu, et al. 2014) to global (Blewitt et al., 2001) scales. While our study is most interested in vertical land motion trends spanning more than one calendar year, seasonality can provide insight into spatial variations in seasonal amplitude and peak phase that affect long term loading patterns.

The GPS Imaging of seasonal vertical oscillation shows three regions with amplitude of more than 2 mm (Fig. 3.11a). The first region is located along the western boundary of the study area in the Rocky Mountains. The second region is located in the southeastern portion of the study area and is centered around the Dallas/Ft. Worth metropolitan area with an amplitude of ~3 mm. The final region is within the northeastern portion of the High Plains aquifer in central Nebraska. There, seasonal amplitudes fluctuate the most, up to 3.5 mm. It is notable that the zone of greatest seasonality is within the northern High Plains aquifer, rather than in the south which experiences the fastest uplift. We speculate that the source of high amplitude vertical land motion seasonality is related to higher rates of precipitation accounting for greater water mass changes in the northern High Plains aquifer groundwater system.

The phase of the GPS vertical position time series shows which time of year the vertical land motion reaches its highest point in its annual cycle, and hence can reveal when hydrological loading is at a minimum. The results from GPS Imaging of annual phase indicate that the High Plains aquifer lies in a point of intersection between three different domains of seasonal motion (Fig. 3.11b). To the southwest of the High Plains aquifer the peak phase is in the late winter to early spring; to the east the peak is at the end of summer to early fall; to the northwest the motion peaks in late autumn. These three areas respond to loads applied at different times, with their peak position up to 60 days out of phase.

That the High Plains aquifer lies at the exact intersection of these distinct domains of seasonal hydrological load timing is consistent with its being located between the American Southwest, eastern United States, and the Rocky Mountains. The southwest Great Plains has a more arid climate and is driest during early springtime, before it experiences monsoonal rain patterns in summer. Alternating reds and greens are adjacent in time and are likely due to poorly resolved phase occurring when amplitude is very low.

The eastern Great Plains, though also receiving precipitation during the summer months, is more greatly influenced by its proximity between the Gulf of Mexico and the mid-continent, meaning the effects of winter polar vortices could be enough to postpone peak unloading until late in the summer. The minimum hydrological load in the northwestern region of the Great Plains is in autumn, when the previous winter's snowpack in the Rocky Mountains is depleted but the new snowy season has yet to begin in force. These patterns fit with the broader timing of hydrological loading domains across the continental United States (Hammond et al., 2021) and further support the seasonal deformation being explained with hydrological loading.

3.8.4 Water Mass Loss in the High Plains Aquifer

Previous studies that used GRACE to study groundwater depletion in the Texas Panhandle found that GRACE is a valuable tool to monitor terrestrial water storage changes through drought periods (Long et al., 2013) and throughout the High Plains aquifer over longer monitoring periods (Rateb et al., 2020). Here we show GRACE trends for a broader area and compare them to trends in PDSI and GPS-measured vertical land motion. The GRACE data indicate trends in surface mass change are also consistent with hydrological loading driving the observed High Plains aquifer uplift.

According to GSFC solutions, the northern portion of the aquifer has a gravity trend associated with an increasing mass load at an average rate of 0.7 cm/year equivalent water height, and the southern portion shows a trend of decreasing mass with a mean rate of −1.5 cm/year equivalent water height (Fig. 3.2). The region with greatest mass loss in the High Plains aquifer is located in the Texas Panhandle, where equivalent water height decreased at a rate of approximately −2.6 cm/year. This spatial pattern corroborates the groundwater decline map (Fig. 3.15) (Konikow, 2013; McGuire, 2017), and the area of greatest uplift shown in the GPS Imaging result (Fig. 3.9a). GSFC solutions for the northern Great Plains do not vary significantly, also giving an equivalent water height average of 0.7 cm/year, but the southern Great Plains have a mean equivalent water height of −0.8 cm/year (Fig. 3.3; Sup. Table S3.3).

GRACE median monthly solution time series (Fig. 3.14) corroborate these overall trends (Fig. 3.9a). The northern portion of the High Plains aquifer shows an overall equivalent water height increase of approximately 20 cm until the 2011–2013 severe drought began. With the drought fully underway, nearly 15 cm of equivalent water height is lost, and only begins to recover starting in 2013 through the end of the time series. Data from the southern region of the High Plains aquifer give the opposite trend. Pre-drought, there was an overall decline of approximately 15 cm equivalent water height. With the drought, further losses of 15 cm equivalent water height occurred with only modest recovery after the severe drought ended. By the end of the time series, GRACE trends show total losses between 2005 through 2019 of approximately 25 cm equivalent water height in the southern High Plains aquifer, consistent with unloading-driven uplift.

We can also calculate approximate water volume changes in the High Plains aquifer (Fig. 3.2) and for the entirety of the Great Plains (Fig. 3.3) during the study interval. Using the pre-defined dividing line between north and south to sum volume trends according to 1° x 1° area mascon blocks, the northern High Plains aquifer has an increasing water volume trend of 2.0 km^3/year and the southern High Plains aquifer decreases at a rate of 4.7 km^3/year, giving a net change of −2.7 km^3/year for the entire High Plains aquifer. Because GRACE mascons are dependent on their nearest neighbor mascons, however, we also expand our estimations to include mascons in the entire Great Plains study area, keeping the north/south dividing line. For the northern Great Plains, 3.5 km^3/year of water volume is added, and the southern Great Plains sees a decline of 6.7 km^3/year. The Great Plains has a total net water volume trend of −3.2 km^3/year according to our GRACE mascon estimations.

3.8.5 Groundwater Fluctuations in the High Plains Aquifer

Previous studies have shown that groundwater levels since 1900 have been holding consistent in the northern High Plains aquifer but are on the decline in the southern High Plains aquifer, which has been especially aggravated in the Texas Panhandle because of historic drought (McGuire, 2017). Our results, focused within the Willett et al. (2018) defined boundary of the High Plains aquifer, confirm these spatial patterns and overall trends. Of the 21 wells located in the southern High Plains aquifer, 11 show significant groundwater declines since the first data point collected in 1930, with the remaining 10 indicating a net zero effect over the duration of the water level data (Sup. Table S3.5). The greatest water level change in the entire dataset was well ID 342356102572501, where the water level dropped over 53 m since its first measurement in 1956 through its last measurement in 2002. Seasonal fluctuations in water levels are minimal throughout the well time series, indicating little precipitation effect on the groundwater usage, and consistent anthropogenic reliance on groundwater resources.

The 121 groundwater wells in the northern High Plains aquifer show a different pattern of usage and recharge than the southern High Plains aquifer. A total of 18 wells show declines of over 5 m, 7 wells show significant increases over 5 m, and the remaining wells show water levels experiencing cyclical recharge and loss of about the same rate, indicating an approximately net zero effect (Sup. Table S3.5). The greatest water level change was a decline of 25.3 m, but the second greatest change was an increase of 24.7 m. Unlike the southern High Plains aquifer, the northern High Plains aquifer also shows clear seasonal swings in water level changes, indicating the effect of precipitation on water usage and recharge. We suggest that these seasonal swings are due to two factors: the northern aquifer has a greater frequency of groundwater measurements, and the northern wells are, in general, far shallower in depth to water level than they are in the south. The median depth to water level in the northern aquifer is approximately 14 m compared to the median depth of 43 m in the south (Sup. Table S3.5). This would mean recharge from the wetter climate in the northern portion of the High Plains aquifer would occur at a faster rate compared to the southern High Plains aquifer.

3.9 Discussion

3.9.1 Interpretation of Uplift

To summarize the observations, the northern High Plains aquifer has greater periods of extreme moisture, cyclic water mass loss and recovery, and GPS time series show an overall trend of subsidence and the greatest amplitudes of seasonality. In the southern High Plains aquifer, there are more periods of extreme drought, greater water mass lost with little to no recovery, and GPS time series show an uplift trend through 2014 before gradually leveling. Uplift correlates with periods of drought, including increased GPS uplift and GRACE mass lost during extreme droughts. The GPS Imaging, GRACE, PDSI, GPS time series, and groundwater well data trends agree: the uplift signal is consistent with seasonal and climate-driven hydrological unloading.

Annual seasonality calculated from GPS time series provides spatiotemporal patterns of seasonal amplitude and timing of peak height that indicates seasonal uplift is largely dominated by hydrological loading (Fig. 3.11). The results show the intersection of three different weather domains in our Great Plains study area that hydrologically impact the High Plains aquifer and help explain the differences between northern and southern High Plains aquifer climates. We postulate that most of the High Plains aquifer bounds are dominated by the arid southwestern style of climate, with the annual peak phase preceding the wet season that occurs from monsoonal rain patterns in summer. The northernmost part of the aquifer experiences a mix of annual peak phase times of year, generally between autumn and spring, likely because it is the junction of the three weather domains.

This seasonal response is consistent with the evidence of multi-annual hydrological unloading. The timing of the peak in annual motion throughout the High Plains aquifer points to hydrological loading of the seasonal vertical land motion, suggesting that the system will have similar responses to trends and trend changes in multi-annual changes in hydrological loads. Climatological trends from PDSI and gravity trends from GRACE each have an inverse relation with the vertical land motion, providing further evidence for control by hydrological loading.

Our results indicate that the velocity of crustal uplift accelerates in regions experiencing multi-year periods of severe drought where there is increased reliance on groundwater resources. In wetter periods, when groundwater is abundant, the uplift velocity slows or even reverts to subsidence. The southern High Plains aquifer, which has experienced greater duration and severity of drought and less recharge, has sustained an uplift trend in the Texas Panhandle and surrounding region. Furthermore, there is evidence of greatest aquifer declines in this area as shown by historical groundwater well data. The velocity trends in the southern portion of the High Plains aquifer are consistent with hydrological unloading from aquifer depletion, perhaps driving uplift for several decades before high-precision continuous GPS measurements were available.

Aquifer-controlled uplift suggests an anthropogenic source, and previous studies have demonstrated that anthropogenic depletion of a groundwater reservoir can accelerate uplift (Argus, Fu, et al. 2014; Argus et al., 2017; Hammond et al., 2016; Young et al., 2021). In some previous studies, aquifer depletion in unconsolidated sediments is associated with regional subsidence around areas of greatest drawdown (e.g., Carbognin et al., 2005; Sneed et al., 2013), and uplift, if observed, is spatially associated with the flanks of the unloading (Amos et al., 2014). Our results indicate that areas of the High Plains aquifer that experienced the greatest amount of groundwater decline experience broad uplift only, suggesting that unloading is the dominant driving mechanism of vertical land motion. This challenges the common perception that vertical motions in unconsolidated sediments driven by aquifer depletion cause subsidence.

The difference between subsidence shown in previous aquifer-based vertical land motion studies and the uplift response in the High Plains aquifer is likely attributable to distinctions in aquifer mechanics. In confined systems comprised of unconsolidated sediments, where impermeable layers bound the aquifer above and below (e.g., California's Great Valley, Las Vegas Basin, etc.), groundwater pumping causes a pressure differential within the reservoir that leads to sediment compaction (Alley et al., 1999). Although the High Plains aquifer is similarly located in unconsolidated sediments and alluvium, it is an unconfined system, meaning that groundwater is at atmospheric pressure (Weeks and Gutentag, 1981). In this case there is no pressure differential to trigger a regional-scale poroelastic response, so the effects of hydrological mass unloading from groundwater withdrawal cause only uplift. The hydrologically induced fluctuations we are observing with GPS Imaging in the High Plains aquifer behave more similarly to unconfined karstic aquifer systems, where recharge shows crustal subsidence and depletion shows uplift (Silverii et al., 2019), despite the High Plains aquifer reservoir being composed of unconsolidated material. Thus, regional vertical motions caused by hydrological unloading within an aquifer are dependent not only on where observations are made with respect to the loading mass, but also on the type of aquifer system. This understanding could have wider implications when investigating anomalous vertical land motion. In addition to interpretations of other potential vertical land motion sources like post-seismic rebound, deglaciation, erosion, or magmatic intrusion, hydrological unloading could also potentially influence vertical land motion in a region experiencing uplift and would need to be considered as a possibility.

3.9.2 Modeling the Load

To understand the hydrological changes required to drive the observed uplift, we estimate the rate of groundwater mass unloading needed to recreate the uplift signal seen with GPS. We build a simple unloading model using the LoadDef software (Martens et al., 2019) and based on the preliminary reference Earth model (PREM) (Dziewonski and Anderson, 1981) to predict a vertical velocity field of the southern High Plains aquifer for comparison with the observed vertical velocity field. We located the center of mass unloading in the Texas Panhandle since that is where the GPS Imaging uplift is greatest. This is also the approximate location of two of the largest drawdowns of groundwater since the early 1900’s (Scanlon et al., 2012; McGuire, 2017: Fig. 3.15). There is no indication of an anomalous horizontal signal near the uplift, therefore the size of the freshwater load was constrained only by the region of greatest uplift shown by GPS Imaging. The unloading model shape was approximated by contouring uplift values 1 mm/year or greater from the GPS Imaging result to define a perimeter of a mass change. The perimeter was then simplified by culling points of the polygon to lessen minor effects from the bootstrapping statistical analysis, and the geometry of the unloading mass was congruent with the polygon based on uplift response (Fig. 3.17). We solved for the water load thickness that minimizes the misfit between the observed uplift rate and that predicted by the model.

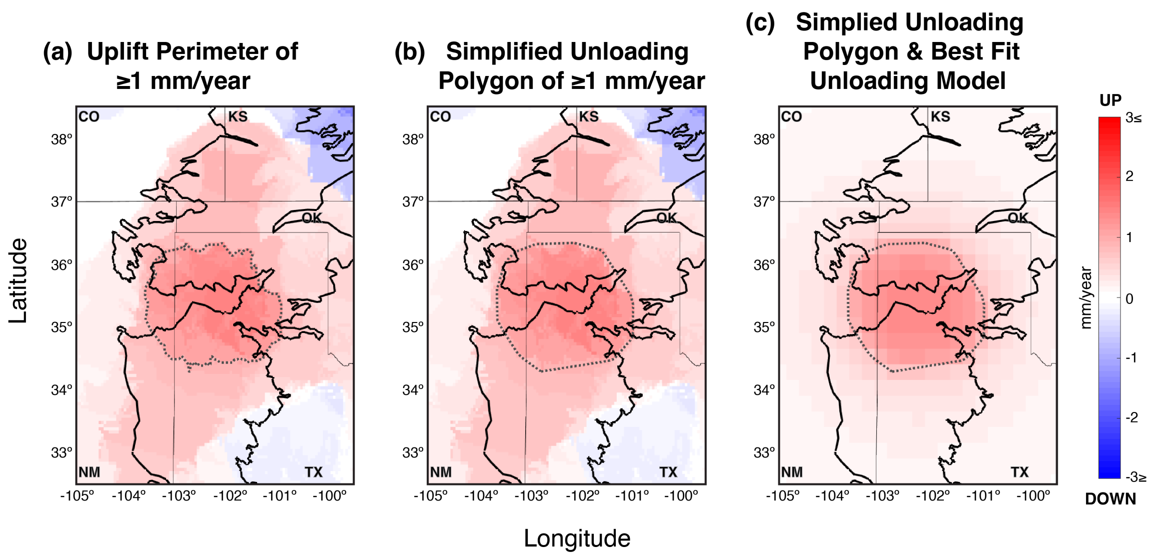

Figure 3.17. Comparison between polygons (gray dots) of uplift perimeter and simplified unloading in the southern High Plains aquifer (outlined in black). (**a**) A zoomed-in view of the southern High Plains aquifer from Figure 3.9 centered around the anomalous uplift feature located near the Texas Panhandle with perimeter of uplift ≥1 mm/year. **(b)** Observed vertical land motion with simplified unloading polygon overlain. **(c)** Predictions from our hydrological unloading model centered around the Texas Panhandle with simplified unloading polygon. The location, dimension and yearly rate of water mass loss were optimized to best predict the uplift observed using GPS Imaging.

Our vertical displacement results indicate that an equivalent water height loss of −11.36 cm/year is needed to generate the observed vertical land motion shown by our GPS Imaging result (Fig. 3.18). According to our simple unloading model, this is equivalent to a water volume of approximately −5.1 km^3/year removed from an area centered approximately on the Texas Panhandle since the first GPS measurements. Sources of uncertainty in this estimate include GPS spatial resolution, simplistic dimensions of the load, assumption of geographic uniformity across the mass change area, and time variability not included in the model. Uncertainty for the elastic constants (e.g., Poisson's ratio and Young's modulus in PREM) also contributes to the uncertainty in the inferred water mass load. Considering that some studies find seismic velocities in the upper 0.5 km that are much lower (e.g., 0.3−2.1 km/s, Paine, 1994) than are found in the shallowest layer of PREM (6.2 km/s), less water may be needed to cause the observed deformation, suggesting that our equivalent water height loss estimate is an upper bound on the unloading center of mass.

The unloading model maximum equivalent water height result of −11.36 cm/year is more than quadruple the rate of the maximum estimated GRACE trend of −2.6 cm/year and over seven times the mean rate in the entire southern High Plains aquifer of −1.5 cm/year (Fig. 3.2 and Table S3.3). Our model rate may be higher than the GRACE rates because GPS Imaging is detecting crustal unloading for changes in groundwater storage levels that occurred before the GRACE timeframe (2002–2020). Also, remembering that spatial resolution differs between GRACE and GPS, and that the real mass changes are likely more concentrated than is resolvable by the GRACE data, we compare our unloading results to changes in groundwater loss estimates. Our GRACE water volume loss estimates are 4.7 km^3/year for the southern High Plains aquifer and 6.7 km^3/year for the southern Great Plains (Fig. 3.3). Considering that our simplistic unloading model assumes total water loss for the High Plains aquifer is centered over the Texas Panhandle region, our inferred water volume loss of 5.1 km^3/year is on the lower end of reasonable estimates. Furthermore, estimates for groundwater depletion in the High Plains aquifer by Scanlon et al. (2012) give a depletion rate of 5.7 km^3/year for the entirety of the High Plains aquifer system to total approximately 330 km^3 of total volume loss from the 1950s through 2007 (Scanlon et al., 2012). This rate is nearly double our net GRACE volume estimate for the Great Plains of −2.6. km^3/year. Thus our GRACE-estimated volume loss likely underestimates the water mass removed. Scanlon et al. (2012) additionally state that the depletion rate increased to approximately 7 km^3/year from 1987–2007, which overlaps with the early period of our study. We therefore consider our GPS-modeled rate of −5.1 km^3/year an adequate lower bound of average water loss in the region, and consistent with GRACE and groundwater estimates.

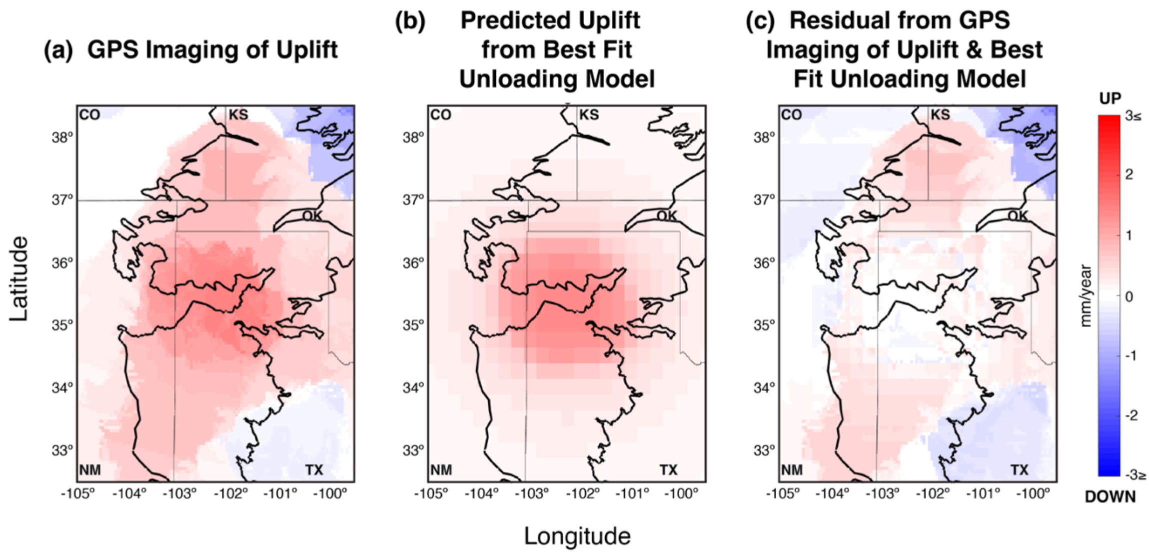

Figure 3.18. Comparison between observed vertical land motion and prediction of a simple hydrological unloading model of the southern High Plains aquifer outlined in black. **(a)** A zoomed-in view of the southern High Plains aquifer from Figure 3.9 centered around the anomalous uplift feature located near the Texas Panhandle. **(b)** Predictions from our hydrological unloading model centered around the Texas Panhandle. The location, dimension and yearly rate of water mass loss were optimized to best predict the uplift observed using GPS Imaging. **(c)** Difference between observed uplift and unloading model.

This model illustrates the relationship between crustal uplift, climate variability, and anthropogenic groundwater withdrawal in the High Plains aquifer region in the area where there is likely to be multi-annual vertical land motion impacts. Current climate change models predict increasingly aggravated drought conditions in the coming decades that would further reduce groundwater recharge (Crosbie et al., 2013; Cook et al., 2015). This could accelerate uplift velocities resulting from a feedback cycle of reduced surface water and recharge that causes further anthropogenic reliance on groundwater resources which increases the rate of hydrological unloading. Understanding future effects of climate change on the High Plains aquifer will ultimately depend on the development of an effective long-term water management policy that combines monitoring of water withdrawal rates, climatic trends, groundwater recharge, and vertical land motion (Whittemore et al., 2016).

3.10 Conclusions

Our study suggests that there is a relationship between crustal uplift and mass unloading from groundwater depletion in the southern High Plains aquifer. Climatic, GPS, and hydrological data indicate that uplift correlates with periods of drought, including an increased rate of uplift during extreme droughts, likely exacerbated by increased anthropogenic depletion of aquifer resources caused by climate variability. Historical water level declines and climate drying trends in the southern High Plains aquifer intimate that aquifer related vertical land motion was perhaps active for decades before GPS instrumentation was in place. Our simple elastic unloading model constrained by results from GPS Imaging suggests that groundwater depleted approximately 5.1 km^3/year in the Texas Panhandle portion of the High Plains aquifer is sufficient to create the observed uplift signal. As climate change continues to increase reliance on groundwater extraction in the southern High Plains aquifer, GPS can monitor the rate of aquifer depletion induced vertical crustal deformation and estimate the volume of mass unloaded from the region.

In contrast to other vertical land motion studies involving aquifer depletion, our results show that aquifer depletion is not universally tied to subsidence but that its sign depends on whether groundwater is in a confined or unconfined aquifer system. Hydrological unloading from an aquifer can have signals dominated by subsidence or uplift depending on the regional subsurface geology, which should be considered as a potential control on anomalous uplift.

This case study of the Great Plains presents a methodology to synthesize geophysical, geodetic, and hydrological datasets to resolve the dynamic, and potentially anthropogenically-influenced nature of uplift. These techniques can be applied in other regions experiencing anomalous vertical land motion.

3.11 Acknowledgements

NASA supported this research with grant NNX16AK89G under project entitled "GPS Imaging of Solid Earth's Flex and Flow," and grant 80NSSC19K1044 under project entitled "GPS Imaging of time-variable Earth deformation for multi-disciplinary science" as part of its Earth Surface and Interior program. We thank UNAVCO and National Geodetic Survey CORS networks for the operation of the GPS archive from which we obtained most GPS data used in this project. We also thank the operators of numerous GPS networks, including Leica Smartnet, TopNET, the Bureau of Land

Management, University Corporation for Atmospheric Research, University of Colorado, University of Wyoming, University of Texas, University of Oklahoma, King Surveyors, Inc., Colorado Department of Transportation, Iowa Department of Transportation, Minnesota Department of Transportation, New Mexico Department of Transportation, Oklahoma Department of Transportation, Texas Department of Transportation, NOAA, Sedgwick County, US Coast Guard, NASA, Seiler Instruments, City of Grand Island Utility Department, Central Nebraska Public Power and Irrigation District, and the National Institute of Standards and Technology. We used GPS time series data from these networks to estimate MIDAS trends, with current rates available through the NGL (http://geodesy.unr.edu/velocities/midas.IGS14.vel). GSFC GRACE trends, including data from the GRACE Follow-On mission, were obtained from: (https://earth.gsfc.nasa.gov/geo/data/grace-mascons). Monthly PDSI data from 28 climate districts were obtained from the NOAA National Climatic Data Center (https://www.ncdc.noaa.gov/cdo-web/). Well water level depth data was obtained from the USGS Groundwater Daily database (https://waterdata.usgs.gov/nwis/dv/). The list of step events for all GPS stations used in this study is provided by the Nevada Geodetic Laboratory (http://geodesy.unr.edu/NGLStationPages/steps.txt). This manuscript was improved by considering the careful and thorough comments from Manoo Shirzaei, Don Argus, an anonymous reviewer, and the Associate Editor.

3.12 References

Alley, W. M., Reilly, T. E., & Franke, O. L. (1999). Sustainability of Ground-Water Resources: U.S. Geological Survey Circular 1186, p. 12-14, https://pubs.usgs.gov/circ/circ1186/pdf/circ1186.pdf.

Altamimi, Z., Rebischung, P., Métivier, L., & Collilieux, X. (2016). ITRF2014: A new release of the International Terrestrial Reference Frame modeling nonlinear station motions. *J. Geophys. Res. - Solid Earth*, *121*(8), 6109-6131.

Amos, C. B., Audet, P., Hammond, W. C., Bürgmann, R., Johanson, I. A., & Blewitt, G. (2014). Uplift and seismicity driven by groundwater depletion in central California. *Nature*, *509*(7501), 483–486, https://doi.org/10.1038/nature13275.

Argus, D. F. (2012). Uncertainty in the velocity between the mass center and surface of Earth. *J. of Geophys. Res. - Solid Earth*, *117*(B10).

Argus, D. F., Fu, Y., & Landerer, F. W. (2014). Seasonal variation in total water storage in California inferred from GPS observations of vertical land motion. *Geophys. Res. Lett., 41*, 1971–1980, https://doi.org/10.1002/2014GL059570.

Argus, D. F., Landerer, F. W., Wiese, D. N., Martens, H. R., Fu, Y., Famiglietti, J. S., & Watkins, M. M. (2017). Sustained water loss in California's mountain ranges during severe drought from 2012 to 2015 inferred from GPS. *J. Geophys. Res. - Solid Earth, 122*, 10,559–10,585, https://doi.org/10.1002/ 2017JB014424.

Argus, D. F., Peltier, W. R., Blewitt, G., & Kreemer, C. (2021). The Viscosity of the Top Third of the Lower Mantle Estimated Using GPS, GRACE, and Relative Sea Level Measurements of Glacial Isostatic Adjustment. *J. Geophys. Res. - Solid Earth*, *126*(5), e2020JB021537.

Argus, D. F., Peltier, W. R., Drummond, R., & Moore, A. W. (2014). The Antarctica component of postglacial rebound model ICE-6G_C (VM5a) based on GPS positioning, exposure age dating of ice thicknesses, and relative sea level histories. *Geophysical Journal International*, *198*(1), 537-563.

Beavan, J., Denys, P., Denham, M., Hager, B., Herring, T., & Molnar, P. (2010). Distribution of present-day vertical deformation across the Southern Alps, New Zealand, from 10 years of GPS data. *Geophys. Res. Lett.*, *37*, L16305, https://doi.org/10.1029/2010GL044165.

Bennett, R., & Hreinsdóttir, S. (2007). Constraints on vertical crustal motion for long baselines in the central Mediterranean region using continuous GPS. *Earth Planet. Sci. Lett., 257*, 419–434.

Bertiger, W., Bar-Sever, Y., Dorsey, A., Haines, B., Harvey, N., Hemberger, D., et al. (2020). GipsyX/RTGx, a new tool set for space geodetic operations and research. *Advances in Space Research*, *66*(3), 469–489, https://doi.org/10.1016/j.asr.2020.04.015.

Blewitt, G., Kreemer, C., Hammond, W.C., & Gazeaux, J. (2016). MIDAS Robust Trend Estimator for Accurate GPS Station Velocities Without Step Detection. *J. Geophys. Res. - Solid Earth*, *121*(30), 2054-2068, https://doi.org/10.1002/2015JB012552.

Blewitt, G., Lavallée, D., Clarke, P., & Nurudinov, K. (2001). A new global model of Earth deformation: Seasonal cycle detected. *Science*, *294*, 2342–2345, https://doi.org/10.1126/science.1065328.

Blewitt, G., Hammond, W.C., & Kreemer, C. (2018). Harnessing the GPS data explosion for interdisciplinary science. *Eos, 99*, https://doi.org/10.1029/2018EO104623.

Boehm, J., Werl, B., & Schuh, H. (2006). Troposphere mapping functions for GPS and very long baseline interferometry from European Centre for Medium-Range Weather Forecasts operational analysis data. *J. of Geophys. Res. - Solid Earth*, *111*, B02406, https://doi.org/10.1029/2005JB003629.

Borsa, A. A., Agnew, D. C., & Cayan, D. R. (2014). Ongoing drought-induced uplift in the western United States. *Science*, *345*(6204), 1587-1590.

Brookfield, A. E., Hill, M. C., Rodell, M., Loomis, B. D., Stotler, R. L., Porter, M. E., & Bohling, G. C. (2018). In situ and GRACE-based groundwater observations: Similarities, discrepancies, and evaluation in the High Plains aquifer in Kansas. *Water Resources Research*, *54*(10), 8034-8044, https://doi.org/10.1029/2018WR023836.

Burgette, R. J., Weldon II, R. J., & Schmidt, D. A. (2009). Interseismic uplift rates for western Oregon and along-strike variation in locking on the Cascadia subduction zone. *J. of Geophys. Res. - Solid Earth, 114*, B01408, https://doi.org/10.1029/2008JB005679.

Bürgmann, R., Hilly, G., Ferretti, A., & Novali, F. (2006). Resolving vertical tectonics in the San Francisco Bay Area from permanent scatterer InSAR and GPS analysis. *Geology*, *34*(3), 221–224, https://doi.org/10.1130/G22064.1.

Carbognin, L., Pietro, T., & Luigi, T. (2005). Land Subsidence in the Venetian area: Known and recent aspects. *Giornale di Geologia Applicata*, *1,* 5 –11, https://doi.org/10.1474/GGA.2005-01.0-01.0001.

Chanard, K., Fleitout, L., Calais, E., Rebischung, P., & Avouac, J. P. (2018). Toward a global horizontal and vertical elastic load deformation model derived from GRACE and GNSS station position time series. *J. of Geophys. Res. - Solid Earth*, *123*(4), 3225-3237.

Cook, B. I., Ault, T. R., & Smerdon, J. E. (2015). Unprecedented 21st century drought risk in the American Southwest and Central Plains. *Science Advances*, *1*(1). e1400082.

Crosbie, R. S., Scanlon, B. R., Mpelasoka, F. S., Reedy, R. C., Gates, J. B., & Zhang, L. (2013). Potential climate change effects on groundwater recharge in the High Plains aquifer, USA. *Water Resources Research, 49*, 3936–3951. https://doi.org/10.1002/wrcr.20292.

Dai, A., & National Center for Atmospheric Research Staff (Eds.). (2019). The Climate Data Guide: Palmer Drought Severity Index (PDSI), https://climatedataguide.ucar.edu/climate-data/palmer-drought-severity-index-pdsi.

Dai, A., Trenberth, K. E., & Qian, T. (2004). A Global Dataset of Palmer Drought Severity Index for 1870–2002: Relationship with Soil Moisture and Effects of Surface Warming. *J. Hydrometeorology, 5*(6), 1117-1130.

Davis, H. G., Northcutt, R. A., & Johnson, K. S. (1988). The greater Anadarko basin: an overview of petroleum exploration and development. In *Anadarko basin symposium* (p. 13-24).

Dunbar, B. (2013). Mission Overview, retrieved November 29, 2017 from https://www.nasa.gov/mission_pages/Grace/overview/index.html.

Dziewonski, A. M., & Anderson, D. L. (1981). Preliminary reference Earth model. *Physics of the earth and planetary interiors*, *25*(4), 297-356.

Dzurisin, D., Lisowski, M., & Wicks, C. W. (2009). Continuing inflation at Three Sisters volcanic center, central Oregon Cascade range, USA, from GPS, leveling, and InSAR observations. *Bulletin of Volcanology*, 71(10), 1091-1110. https://doi.org/10.1007/s00445-009-0296-4.

Faunt, C. C., Sneed, M., Traum, J., & Brandt, J. (2016). Water availability and land subsidence in the Central Valley, California, USA. *Hydrogeology Journal*, *24*(3), 675, https://doi.org/10.1007/s10040-015-1339-x.

Fu, Y., & Freymueller, J. T. (2012). Seasonal and long-term vertical deformation in the Nepal Himalaya constrained by GPS and GRACE measurements. *J. of Geophys. Res. - Solid Earth, 117*, B03407, https://doi.org/10.1029/2011JB008925.

Galloway, D. L., Jones, D. R., & Ingebritsen, S. E. (Eds.). (1999). *Land subsidence in the United States* (Vol. 1182). US Geological Survey.

Gourmelen, N., & Amelung, F. (2005). Postseismic mantle relaxation in the central Nevada seismic belt. *Science, 310*(5753), 1473-1476.

Gutentag, E. D., Heimes, F. J., Krother, N. C., Luckey, R. R., & Weeks, J. B. (1984). Geohydrology of the High Plains Aquifer in Parts of Colorado, Kansas, Nebraska, New Mexico, Oklahoma, South Dakota, Texas, and Wyoming: U.S. Geological Survey Professional Paper 1400–B, p. 7–17.

Hammond, W. C., Blewitt, G., & Kreemer, C. (2016). GPS Imaging of vertical land motion in California and Nevada: Implications for Sierra Nevada uplift. *J. Geophys. Res. - Solid Earth*, *121*, 7681–7703, https://doi.org/10.1002/2016JB013458.

Hammond, W. C., Blewitt, G., Li, Z., Plag, H. P., & Kreemer, C. (2012). Contemporary uplift of the Sierra Nevada, western United States, from GPS and InSAR measurements. *Geology, 40*(7), 667-670.

Hammond, W. C., Blewitt, G., Kreemer, C., & Nerem, R. S. (2021). GPS imaging of global vertical land motion for studies of sea level rise. *J. Geophys. Res. - Solid Earth*, *126*(7), e2021JB022355, https://doi.org/10.1029/2021JB022355.

Karegar, M. A., Dixon, T. H., & Engelhart, S. E. (2016). Subsidence along the Atlantic Coast of North America: Insights from GPS and late Holocene relative sea level data. *Geophys. Res. Lett.*, *43*, 3126–3133, https://doi.org/10.1002/2016GL068015.

Kreemer, C., Blewitt, G., & Davis, P. M. (2020). Geodetic Evidence for a Buoyant Mantle Plume Beneath the Eifel Volcanic Area, NW Europe. *Geophysical Journal International*, *222*(2), 1316-1332, https://doi.org/10.1093/gji/ggaa227.

Kreemer, C., Hammond, W.C., Blewitt, G. (2018). A robust estimation of the 3D intraplate deformation of the North American plate from GPS, *J. Geophys. Res. - Solid Earth*, *123, 4388-4412,* https://doi.org/10.1029/2017JB015257.

Konikow, L. F. (2013). Groundwater Depletion in the United States (1900-2008). *U.S. Geological Survey Scientific Investigations Report, 53*(1). 63. https://doi.org/10.1111/gwat.12306.

Larochelle, S., Chanard, K., Fleitout, L., Fortin, J., Gualandi, A., Longuevergne, L., ... & Avouac, J. P. (2022). Understanding the geodetic signature of large aquifer systems: Example of the Ozark Plateaus in central United States. *J. Geophys. Res. - Solid Earth*, *127*(3), e2021JB023097, https://doi.org/10.1002/essoar.10507870.1.

Loomis, B. D., Luthcke, S. B., & Sabaka, T. J. (2019). Regularization and error characterization of GRACE mascons. *Journal of Geodesy*, *93*, 1381–1398, https://doi.org/10.1007/s00190-019-01252-y.

Long, D., Scanlon, B. R., Longuevergne, L., Sun, A. Y., Fernando, D. N., & Save, H. (2013). GRACE satellite monitoring of large depletion in water storage in response to the 2011 drought in Texas. *Geophys. Res. Lett., 40*(13). 3395-3401. https://doi.org/10.1002/grl.50655.

Luthcke, S. B., Sabaka, T. J., Loomis, B. D., Arendt, A. A., McCarthy, J. J., & Camp, J. (2013). Antarctica, Greenland and Gulf of Alaska land ice evolution from an iterated GRACE global mascon solution. *J. Glac.*, *59*(216), 613-631, https://doi.org/10.3189/2013JoG12J147.

Martens, H. R., Argus, D. F., Norberg, C., Blewitt, G., Herring, T. A., Moore, A. W… & Kreemer, C. (2020). Atmospheric pressure loading in GPS positions: dependency on GPS processing methods and effect on assessment of seasonal deformation in the contiguous USA and Alaska. *Journal of Geodesy*, *94*(12), 1-22.

Martens, H. R., Rivera, L., & Simons, M. (2019). LoadDef: A Python-based toolkit to model elastic deformation caused by surface mass loading on spherically symmetric bodies. *Earth and Space Science*, *6*(2), 311-323.

Martens, H. R., Rivera, L., Simons, M., & Ito, T. (2016). The sensitivity of surface mass loading displacement response to perturbations in the elastic structure of the crust and mantle. *J. Geophys. Res. - Solid Earth*, *121*, 3911–3938, https://doi.org/10.1002/2015JB012456.

Mazzotti, S., Lambert, A., Courtier, N., Nykolaishen, L., & Dragert, H. (2007). Crustal uplift and sea level rise in northern Cascadia from GPS, absolute gravity, and tide gauge data. *Geophys. Res. Lett., 34*, L15306, https://doi.org/10.1029/2007GL030283.

McGuire, V. L. (2017). Water-level and recoverable water in storage changes, High Plains aquifer, predevelopment to 2015 and 2013–15. *Scientific Investigations Report*, https://doi.org/10.3133/sir20175040.

Nielsen-Gammon, J. W. (2011). The 2011 Texas drought: a briefing packet for the Texas Legislature. College Station, TX: Office of the State Climatologist, College of Geosciences, Texas A and M University. Retrieved February 24, 2019, from http://www.senate.state.tx.us/cmtes/82/c510/0110BI-JohnNielsen-Gammon.pdf.

Paine, J. G., (1994). Subsidence beneath a playa basin on the Southern High Plains, U.S.A.: Evidence from shallow seismic data. *GSA Bulletin, 106*(2), 233-242.

Peltier, W. R., Argus, D. F., & Drummond, R. (2015). Space geodesy constrains ice age terminal deglaciation: The global ICE-6G_C (VM5a) model. *J. Geophys. Res. - Solid Earth*, *120*, 450–487, https://doi.org/10.1002/2014JB011176.

Peltier, W.R., Argus, D. F., & Drummond, R. (2018). Comment on "An assessment of the ICE-6G_C (VM5a) glacial isostatic adjustment model" by Purcell et al. *J. Geophys. Res. - Solid Earth*, *123*(2), 2019-2028.

Pfeffer, J., Spada, G., Mémin, A., Boy, J.P., & Allemand, P. (2017). Decoding the origins of vertical land motions observed today at coasts. *Geophysical Journal International*, *210*(1), 148–165, https://doi.org/10.1093/gji/ggx142.

Rateb, A., Scanlon, B. R., Pool, D. R., Sun, A., Zhang, Z., Chen, J., et al. (2020). Comparison of groundwater storage changes from GRACE satellites with monitoring and modeling of major U.S. aquifers. *Water Resources Research, 56*, e2020WR027556, https://doi.org/10.1029/2020WR027556.

Scanlon, B. R., Faunt, C. C., Longuevergne, L., Reedy, R. C., Alley, W. M., McGuire, V. L., & McMahon, P. B. (2012). Groundwater depletion and sustainability of irrigation in the US High Plains and Central Valley. *Proceedings of the national academy of sciences*, *109*(24), 9320-9325.

Schmid, R., Dach, R., Collilieux, X., Jäggi, A., Schmitz, M., & Dilssner, F. (2016). Absolute IGS antenna phase center model igs08. atx: status and potential improvements. *Journal of Geodesy*, *90*(4), 343-364.

Sella, G. F., S. Stein, T. H. Dixon, M. Craymer, T. S. James, S. Mazzotti, and R. K. Dokka (2007). Observation of glacial isostatic adjustment in "stable" North America with GPS. *Geophys. Res. Lett.*, *34*, L02306, https://doi.org/10.1029/2006GL027081.

Serpelloni, E., Faccenna, C., Spada, G., Dong, D. & Williams, S. D. (2013). Vertical GPS ground motion rates in the Euro-Mediterranean region: New evidence of velocity gradients at different spatial scales along the Nubia-Eurasia plate boundary *J. Geophys. Res. - Solid Earth*, *118*(11), 6003-6024.

Shafer, M., Ojima, D., Antle, J. M., Melillo, J., Richmond, T., & Yohe, G. (2014). Climate change impacts in the United States: the third national climate assessment. Washington, DC: *U.S. Global Change Research Program*, 441–461. Chapter 19, http://nca2014.globalchange.gov/report/regions/great-plains.

Sibthorpe, A., Bertiger, W., Desai, S. D., Haines, B., Harvey, N., & Weiss, J. P. (2011). An evaluation of solar radiation pressure strategies for the GPS constellation. *Journal of Geodesy*, *85*(8), 505-517.

Silverii, F., D'Agostino, N., Borsa, A. A., Calcaterra, S., Gambino, P., Giuliani, R., & Mattone, M. (2019). Transient crustal deformation from karst aquifers hydrology in the Apennines (Italy). *Earth Planet. Sci. Lett.*, *506*, 23-37.

Sneed, M., Brandt, J., & Solt, M. (2013). Land subsidence along the Delta-Mendota Canal in the northern part of the San Joaquin Valley, California, 2003–10: U.S. Geological Survey Scientific Investigations Report 2013–5142, 87 p., https://doi.org/10.3133/sir20135142.

Tapley, B. D., Bettadpur, S., Ries, J. C., Thompson, P. F. & Watkins, M. M. (2004). GRACE measurements of mass variability in the Earth system. *Science, 305*(5683), 503–505, https://doi.org/10.1126/science.1099192.

Tregoning, P., & Watson, C. (2009). Atmospheric effects and spurious signals in GPS analyses. *J. of Geophys. Res. - Solid Earth, 114*, B09403, https://doi.org/10.1029/2009JB006344.

US Energy Information Administration. (2018). Permian Basin Wolfcamp Shale Play Geology review.

Vose, R.S., Applequist, S., Durre, I., Menne, M. J., Williams, C. N., Fenimore, C., Gleason, K, Arndt, D. (2014). Improved historical temperature and precipitation time series for U.S. climate divisions. *Journal of Applied Meteorology and Climatology*, *53*(5), 1232-1251, https://doi.org/10.1175/JAMC-D-13-0248.1.

Watts, A. B. (2001). *Isostasy and Flexure of the Lithosphere*, p. 114-121. Cambridge, United Kingdom: Cambridge University Press.

Weeks, J. B., Gutentag, E. D., Heimes, F. J., & Luckey, R. R. (1988). Summary of the High Plains regional aquifer-system analysis in parts of Colorado, Kansas, Nebraska, New Mexico, Oklahoma, South Dakota, Texas, and Wyoming: *U.S. Geological Survey Professional Paper* 1400–A, p. 30.

Weeks, J. B., & Gutentag, E. D. (1981). Bedrock geology, altitude of base, and 1980 saturated thickness of the High Plains aquifer in parts of Colorado, Kansas, Nebraska, New Mexico, Oklahoma, South Dakota, Texas, and Wyoming: *U.S. Geological Survey Hydrologic Investigations Atlas* HA–648, 2 sheets, scale 1:2,500,000, http://pubs.er.usgs.gov/publication/ha648.

Whittemore, D. O., Butler, Jr., J. J., & Wilson, B. B. (2016). Assessing the major drivers of water-level declines: New insights into the future of heavily stressed aquifers. *Hydrological Sciences Journal, 61*(1), 134–145, https://doi.org/10.1080/02626667.2014.959958.

Willett, S. D., McCoy, S. W., & Beeson, H. W. (2018). Transience of the North American High Plains landscape and its impact on surface water. *Nature*, *561*(7724), 528-532.

Young, Z. M., Kreemer, C., & Blewitt, G. (2021). GPS Constraints on Drought-Induced Groundwater Loss Around Great Salt Lake, Utah, With Implications for Seismicity Modulation. *J. Geophys. Res. - Solid Earth*, *126*(10), e2021JB022020.

3.13 Supplemental Tables

Table S3.1. Great Plains GPS Station and Vertical Velocity Data

Station	Latitude (°N)	Longitude (°)	Vertical Velocity (mm/year)	Vertical Uncertainty (mm/year)	GIA-Corrected Vertical Velocity (mm/year)	Agency or Company	Approximate Location
ABL1	32.4537	-99.7305	-0.690	0.859	-0.084	Leica SmartNet	Abilene, TX
AMC2	38.8031	-104.5246	-0.947	0.449	-0.196	USNO	Schriever AFB, CO
ARVA	39.8032	-105.0878	-3.918	0.903	-1.403	Leica SmartNet	Arvada, CO
BONH	33.5514	-96.2109	-2.128	0.304	-1.356	TopNET	Bonham, TX
BOSQ	31.9233	-97.6574	-2.158	1.052	-1.426	Leica SmartNet	Meridian, TX
BUR5	41.1880	-104.3532	-1.268	0.759	-0.074	Leica SmartNet	Burns, WY
CCTY	38.4383	-105.2448	-0.607	0.768	0.385	Leica SmartNet	Cañon City, CO
CHEY	41.1176	-104.8101	-2.607	0.898	-1.457	Leica SmartNet	Cheyenne, WY
CHLL	40.4466	-104.6379	-0.393	0.806	0.270	UCAR	Greeley, CO
CHUG	41.7622	-104.8209	-3.293	0.756	-0.406	Leica SmartNet	Chugwater, WY
COBD	40.0639	-105.2032	-3.257	1.069	0.130	Leica SmartNet	Boulder, CO
COCA	39.0384	-104.2977	-1.438	0.743	-0.398	Leica SmartNet	Calhan, CO
CODN	39.8251	-104.6681	-2.423	0.649	-1.164	Leica SmartNet	Denver, CO
CODV	38.9411	-105.1615	-3.970	1.112	-0.844	Leica SmartNet	Divide, CO
COFC	40.5934	-105.1604	-0.943	0.619	0.133	King Surveyors, Inc.	Fort Collins, CO
COFG	40.2678	-103.8254	-0.826	0.800	0.311	Leica SmartNet	Log Lane Village, CO
COGR	40.3780	-104.7043	-2.608	0.877	-0.426	Leica SmartNet	Evans, CO
COGW	39.6101	-104.8869	-5.930	0.887	-2.947	Leica SmartNet	Greenwood Village, CO
COPU	38.2717	-104.6142	-1.364	0.712	-0.359	Leica SmartNet	Pueblo, CO
COSG	38.9601	-104.7809	-1.845	1.056	-0.831	Leica SmartNet	Colorado Springs, CO
COWI	39.9172	-105.7861	-0.686	0.911	0.054	Leica SmartNet	Winter Park, CO
CTMC	39.7215	-105.1929	-1.811	0.712	-0.977	CO DOT	Golden, CO

DEAC	39.7401	-105.2212	-1.987	1.111	-0.799	Leica SmartNet	Golden, CO
DSRC	39.9914	-105.2610	-1.408	0.561	0.198	NOAA	Boulder, CO
ECSD	43.7337	-96.6140	-2.677	0.553	-2.209	NOTA	Edison Township, SD
FBYN	40.0769	-97.3128	0.881	0.744	-1.012	NOAA	Buckley, NE
FLA2	40.1654	-105.1033	-0.898	0.804	0.142	Leica SmartNet	Longmont, CO
FNT1	38.6825	-104.7001	-1.220	0.718	-0.351	Leica SmartNet	Fountain, CO
GDAC	37.7755	-102.1800	0.509	0.656	0.886	NOAA	Holly, CO
GEOS	40.0827	-104.8108	-2.215	1.110	-1.160	Leica SmartNet	Fort Lupton, CO
GILC	41.1585	-105.0763	-1.164	0.739	-0.030	Leica SmartNet	Cheyenne, WY
GPRY	32.7451	-97.0054	-4.318	0.406	-1.971	TopNET	Grand Prairie, TX
HBRK	38.3046	-97.2935	-0.587	0.568	0.323	NOAA	Menno, KS
HIX1	40.5751	-105.0042	-1.513	0.760	-0.428	Leica SmartNet	Fort Collins, CO
HVLK	37.6515	-99.1068	-0.324	0.690	-0.365	NOAA	Haviland, KS
IAAK	42.8227	-96.5635	-3.329	1.010	-2.639	Leica SmartNet	Akron, IA
IAD2	43.2855	-96.1816	-3.837	1.038	-2.625	Leica SmartNet	Garfield Township, IA
IALM	42.7981	-96.1487	-3.180	0.839	-2.491	Iowa DOT	Le Mars, IA
IALW	42.4771	-96.2425	-3.835	1.154	-2.385	Leica SmartNet	Lawton, IA
IAOA	42.0276	-96.1080	-3.019	0.821	-1.969	Iowa DOT	Onawa, IA
IAON	42.0287	-96.0953	-2.918	1.112	-1.969	Leica SmartNet	Onawa, IA
IARR	43.4335	-96.1488	-3.016	0.874	-2.483	Iowa DOT	Rock Rapids, IA
IARV	43.1978	-96.3141	-2.323	0.927	-2.443	Iowa DOT	Rock Valley, IA
IASN	42.2390	-96.2311	-2.803	0.771	-1.919	Iowa DOT	Sloan, IA
IASX	42.5500	-96.3485	-3.668	0.784	-2.550	Iowa DOT	Sioux City, IA
ICT1	37.5877	-97.3089	-0.719	0.710	0.422	Sedgwick County	Wichita, KS
ICT2	37.7518	-97.3681	-0.122	0.824	0.435	Sedgwick County	Wichita, KS
ICT3	37.7526	-97.2162	-0.524	0.665	0.568	Sedgwick County	Payne, KS
ICT4	37.6190	-97.6325	-1.050	0.835	-0.728	Sedgwick County	Afton, KS
ICT5	37.7867	-97.6258	-0.554	0.630	0.105	Sedgwick County	Andale, KS

JTNT	33.0172	-100.9771	-0.754	0.658	-0.211	NOAA	Justiceburg, TX
KSAY	37.1445	-98.0304	-3.526	1.438	-1.041	Leica SmartNet	Anthony, KS
KSBK	37.5511	-99.6351	-2.050	1.267	-0.725	Leica SmartNet	Bucklin, KS
KSCM	37.8601	-100.3547	-2.075	1.421	-0.962	Leica SmartNet	Foote, KS
KSCO	39.6105	-97.6623	-2.312	1.389	-1.020	Leica SmartNet	Concordia, KS
KSCP	38.9713	-97.0200	-1.654	1.334	-0.396	Leica SmartNet	Chapman, KS
KSCW	37.2736	-99.3276	-1.805	1.342	-0.720	Leica SmartNet	Coldwater, KS
KSEM	38.4041	-96.1784	0.522	1.084	0.312	Leica SmartNet	Emporia, KS
KSEU	37.8517	-96.2899	-1.669	1.433	-0.499	Leica SmartNet	Eureka, KS
KSGB	38.3547	-98.7648	-2.595	1.283	-1.216	Leica SmartNet	Great Bend, KS
KSGC	37.9691	-100.8964	-2.440	1.254	-0.968	Leica SmartNet	Garden City, KS
KSHA	37.5586	-97.3449	-3.128	1.460	-0.798	Leica SmartNet	Haysville, KS
KSHU	38.0313	-97.9024	-1.865	1.287	-0.691	Leica SmartNet	Hutchinson, KS
KSKY	37.9112	-99.4061	-2.779	1.363	-0.937	Leica SmartNet	Kinsley, KS
KSLC	38.5320	-99.3055	-2.641	1.374	-1.444	Leica SmartNet	La Crosse, KS
KSMA	38.3599	-97.0119	-1.930	1.362	-0.459	Leica SmartNet	Marion, KS
KSMD	37.2851	-100.3586	-1.828	1.305	-0.758	Leica SmartNet	Meade, KS
KSMH	39.1790	-96.5737	-2.326	1.580	-0.736	Leica SmartNet	Manhattan, KS
KSMP	38.3464	-97.6699	-2.101	1.389	-0.897	Leica SmartNet	King City, KS
KSNC	38.4533	-99.8947	-2.908	1.305	-1.466	Leica SmartNet	Ness City, KS
KSPR	37.6907	-98.7410	-2.405	1.523	-1.273	Leica SmartNet	Pratt, KS
KSSN	39.8419	-96.0554	-2.011	1.320	-0.736	Leica SmartNet	Richmond, KS
KST5	39.0446	-96.0391	-1.204	0.684	-0.715	USCG	Maple Hill, KS
KST6	39.0444	-96.0391	-0.906	0.693	0.362	USCG	Maple Hill, KS
KSTB	38.4681	-101.7522	-1.918	1.139	-0.800	Leica SmartNet	Tribune, KS
KSU1	39.1008	-96.6095	-1.113	0.594	0.156	NOTA	Manhattan, KS
KSWF	37.2407	-97.0244	-1.934	1.549	-0.822	Leica SmartNet	Winfield, KS
KSWN	37.2656	-97.3971	-2.135	1.359	-1.026	Leica SmartNet	Wellington, KS

LMNO	36.6854	-97.4807	-0.378	0.643	0.629	NOAA	Lamont, KS
MFLE	39.9476	-105.1944	-0.713	1.275	0.309	UCAR	Boulder, CO
MFP0	39.9496	-105.1944	2.555	0.900	0.309	NASA	Boulder, CO
MFTC	39.9493	-105.1943	-0.035	0.769	-0.125	NASA	Boulder, CO
MFTN	39.9493	-105.1943	-1.147	0.688	-0.125	NASA	Boulder, CO
MFTS	39.9493	-105.1943	-1.034	0.606	-0.012	NASA	Boulder, CO
MFTW	39.9493	-105.1943	-1.242	0.663	-0.125	NASA	Boulder, CO
MNBV	43.6083	-96.3782	-2.160	0.662	-1.826	Minnesota DOT	Beaver Creek Township, MN
MRRN	42.9043	-101.6964	-0.641	0.648	-1.955	NOAA	Merriman, NE
NEA2	41.6751	-97.9806	-3.306	0.915	-1.338	Seiler Instruments	Albion, NE
NEAL	41.6985	-98.0117	-2.495	0.753	-1.338	Leica SmartNet	Albion, NE
NEAN	42.5503	-99.8526	-3.710	0.839	-2.426	Seiler Instruments	Ainsworth, NE
NEAP	40.3059	-99.9054	-1.126	0.688	-0.450	Seiler Instruments	Arapahoe, NE
NEB2	41.2637	-96.1442	-2.514	0.930	-1.347	Leica SmartNet	Omaha, NE
NEBA	42.0164	-96.5731	-3.536	0.983	-2.542	Leica SmartNet	Bancroft, NE
NEBB	41.4023	-99.6260	-3.342	0.778	-2.134	Leica SmartNet	Broken Bow, NE
NEBE	40.2661	-96.7449	-2.032	0.847	-0.791	Leica SmartNet	Beatrice, NE
NEBK	40.0614	-101.5310	-3.275	0.963	0.153	Leica SmartNet	Benkelman, NE
NEBU	40.3354	-97.5750	-3.200	0.764	-1.203	Leica SmartNet	Bruning, NE
NEC1	41.4298	-97.3638	-3.021	0.836	-1.855	Leica SmartNet	Columbus, NE
NECL	41.7131	-97.0617	-3.537	1.410	-2.074	Leica SmartNet	Clarkson, NE
NECO	41.4280	-97.3695	-2.018	0.681	-1.855	Leica SmartNet	Columbus, NE
NEDR	40.7726	-96.7003	-2.082	0.547	-1.117	Seiler Instruments	Lincoln, NE
NEF1	41.4192	-96.4917	-2.473	1.195	-1.331	Leica SmartNet	Platte, NE
NEFM	41.4509	-96.5376	-4.040	1.426	-1.446	Leica SmartNet	Platte, NE
NEFR	40.1482	-97.1707	-2.501	0.810	-1.204	Seiler Instruments	Fairbury, NE
NEGI	40.9223	-98.3282	-2.289	0.766	-1.206	City of Grand Island Utility Department	Grand Island, NE
NEGN	40.9103	-98.3810	-2.509	0.816	-1.218	Leica SmartNet	Grand Island, NE

NEGO	40.9201	-100.1659	-3.899	1.102	-2.561	Seiler Instruments	Gothenburg, NE
NEHA	42.6122	-97.2774	-4.364	0.867	-2.727	Leica SmartNet	Hartington, NE
NEHD	40.4392	-99.3696	-2.567	1.091	-1.247	Seiler Instruments	Holdrege, NE
NEHO	40.4383	-99.3620	-1.763	0.671	-0.443	CNPPID	Holdrege, NE
NEIM	40.5085	-101.6439	-1.092	0.897	0.187	Seiler Instruments	Imperial, NE
NEJ1	40.6951	-99.8174	-4.744	1.070	-2.570	CNPPID	Bethel, NE
NEJM	40.9591	-100.3992	-1.695	1.821	-0.568	CNPPID	Brady, NE
NEKO	41.2099	-101.6704	-3.500	1.182	-1.611	CNPPID	Ogallala, NE
NELI	40.7763	-96.7122	-2.371	0.836	-1.122	Leica SmartNet	Lincoln, NE
NELX	40.7445	-99.7395	-3.458	0.745	-2.128	Seiler Instruments	Lexington, NE
NELY	41.9383	-96.4593	-1.786	0.700	-1.482	Seiler Instruments	Logan, NE
NEMC	40.1994	-100.5782	-1.509	0.664	-0.214	Seiler Instruments	Willow Grove, NE
NEMI	40.5024	-98.9570	-1.516	0.692	-1.192	Seiler Instruments	Minden, NE
NENB	41.4621	-96.7798	-2.578	0.770	-1.438	Seiler Instruments	North Bend, NE
NENF	42.0370	-97.4109	-3.040	0.687	-2.156	Seiler Instruments	Norfolk, NE
NENO	42.0218	-97.4259	-3.165	0.792	-2.011	Leica SmartNet	Norfolk, NE
NENP	41.1361	-100.7654	-1.910	0.609	-0.556	Seiler Instruments	North Platte, NE
NEOG	41.1226	-101.7133	-2.959	0.868	-1.621	Seiler Instruments	Ogallala, NE
NEOM	41.2156	-96.0804	-1.983	0.646	-0.835	Seiler Instruments	Ralston, NE
NEON	42.4583	-98.6584	-3.687	0.897	-2.641	Seiler Instruments	O'Neill, NE
NEOR	41.5952	-98.9169	-3.623	0.774	-2.371	Seiler Instruments	Ord, NE
NEPC	40.1116	-96.1592	-2.660	0.947	-1.366	Seiler Instruments	Pawnee City, NE
NEPR	42.1072	-96.7064	-3.520	1.269	-2.568	Leica SmartNet	Pender, NE
NERC	40.0756	-98.5181	-3.998	0.728	-1.892	Seiler Instruments	Red Cloud, NE
NESC	41.8272	-103.6610	-0.718	0.611	0.205	Scotts Bluff County	Gering, NE
NESE	40.6782	-96.1819	-3.173	1.310	-1.260	Leica SmartNet	Syracuse, NE
NEST	41.4800	-100.5015	-2.914	1.102	-1.549	Seiler Instruments	Gandy, NE
NESY	40.6685	-96.1733	-2.869	1.493	-1.401	Leica SmartNet	Syracuse, NE

NETH	41.9844	-100.5360	-4.262	0.929	-2.132	Seiler Instruments	Thedford, NE
NEVN	42.8725	-100.5437	-3.514	0.867	-2.297	Seiler Instruments	Valentine, NE
NEY1	40.8702	-97.5915	-2.944	0.948	-1.677	Leica SmartNet	York, NE
NEYK	40.8432	-97.5940	-1.668	0.671	-1.104	Seiler Instruments	York, NE
NISA	39.9948	-105.2629	-0.518	1.086	0.229	NIST	Boulder, CO
NIST	39.9951	-105.2626	-0.824	0.647	0.198	NIST	Boulder, CO
NISU	39.9954	-105.2623	-0.836	1.024	0.198	NIST	Boulder, CO
NLGN	42.2067	-97.7953	-0.975	1.117	-1.561	NOAA	Willow Creek, NE
NMAL	32.9011	-105.9531	-2.055	0.903	0.022	Leica SmartNet	Alamogordo, NM
NMCA	32.3759	-104.2280	-0.938	1.322	0.215	Leica SmartNet	Carlsbad, NM
NMHB	32.7048	-103.1269	-0.115	0.678	0.646	Leica SmartNet	Hobbs, NM
NMRO	33.3950	-104.5891	-0.068	0.487	0.667	NM DOT	Roswell, NM
NMSF	35.6738	-105.9586	-1.738	0.500	-0.208	NM DOT	Santa Fe, NM
NWOT	40.0554	-105.5905	-0.021	0.961	0.326	University of CO	Ward, CO
OASS	42.4735	-96.4143	-2.748	0.766	-2.704	Seiler Instruments	South Sioux City, NE
OKAD	34.8003	-96.7383	-0.614	0.715	0.315	OK DOT	Ada, OK
OKAL	34.6323	-99.3294	-0.243	0.601	0.425	OK DOT	Altus, OK
OKAO	35.0764	-98.2459	0.748	0.658	0.479	OK DOT	Anadarko, OK
OKAR	34.1685	-97.1692	-1.256	0.734	-0.371	OK DOT	Ardmore, OK
OKBF	36.8280	-99.6414	-0.732	0.608	0.317	OK DOT	Morrison, OK
OKCL	35.4832	-98.9715	-0.898	0.595	0.480	OK DOT	Clinton, OK
OKDN	34.4793	-97.9666	-0.702	0.663	0.203	OK DOT	Duncan, OK
OKDT	35.4901	-97.5077	-1.707	0.610	-0.733	OK DOT	Oklahoma City, OK
OKGM	36.6746	-101.4794	-0.174	0.531	0.831	OK DOT	Guymon, OK
OKLW	34.5728	-98.4099	-0.322	0.712	0.204	OK DOT	Bishop, OK
OKPR	36.2762	-97.3217	-1.005	0.606	0.028	OK DOT	Perry, OK
OKSY	35.3150	-99.6377	-0.482	0.746	0.463	OK DOT	Sayre, OK
OKTE	35.2602	-96.8978	-1.332	0.758	-0.373	OK DOT	Tecumseh, OK

P027	32.8019	-105.8042	-0.343	0.518	0.211	NOTA	Sunspot, NM
P035	34.6014	-105.1836	-0.652	0.433	0.195	NOTA	Vaughn, NM
P036	36.4203	-105.2937	-1.092	0.479	-0.077	NOTA	Angel Fire, NM
P037	38.4218	-105.1047	-0.884	0.489	-0.068	NOTA	Penrose, CO
P038	34.1473	-103.4073	0.704	0.479	0.773	NOTA	Portales, NM
P039	36.4481	-103.1540	0.442	0.503	1.407	NOTA	Clayton, NM
P040	38.0715	-102.6870	-0.433	0.494	0.627	NOTA	Lamar, CO
P041	39.9495	-105.1943	-0.869	0.550	0.124	NOTA	Boulder, CO
P042	42.0515	-104.9106	-1.401	0.492	-0.150	NOTA	Chugcreek, WY
P043	43.8811	-104.1857	-1.757	0.512	-0.082	NOTA	Newcastle, WY
P044	40.1718	-103.2225	-1.099	0.492	0.074	NOTA	Akron, CO
P070	36.0448	-104.6980	-0.524	0.530	0.269	NOTA	Wagon Mound, NM
P120	35.0075	-105.6261	-0.803	0.445	0.152	NOTA	Clines Corners, NM
P123	36.6352	-105.9108	-0.947	0.457	-0.020	NOTA	Tres Piedras, NM
PLTC	40.1816	-104.7259	-0.697	0.493	0.169	NOAA	Platteville, CO
PRCO	34.9799	-97.5192	-0.462	0.614	0.369	NOAA	Washington, OK
PRX5	39.9495	-105.1943	0.487	1.274	0.153	NOTA	Boulder, CO
PSRS	38.4345	-104.2849	-1.563	0.756	-0.343	Leica SmartNet	Pueblo, CO
PUB5	38.2868	-104.3455	-1.224	0.537	-0.209	USCG	Pueblo, CO
PUB6	38.2871	-104.3455	-1.096	0.529	-0.209	USCG	Pueblo, CO
RG03	33.6547	-105.1542	-0.646	0.558	0.141	University of CO	Arabela, NM
RG04	34.8244	-105.6442	-0.704	0.532	0.042	University of CO	Clines Corners, NM
RG08	32.7284	-104.9941	-0.512	0.475	0.224	University of CO	Hope, NM
RG11	36.5232	-105.7791	-1.004	0.459	-0.081	University of CO	Arroyo Hondo, NM
RG12	36.4586	-104.9683	-0.974	0.556	-0.040	University of CO	Cimarron, NM
RG13	36.4913	-104.2115	-1.300	0.471	-0.025	University of CO	Springer, NM
RG17	39.7618	-105.6696	-1.261	0.842	-0.263	University of CO	Empire, CO
RG19	39.1901	-105.5520	-0.451	0.791	0.214	University of CO	Tarryall, CO

RG23	37.7439	-105.4985	-0.777	0.611	0.023	University of CO	Great Sand Dunes NP, CO
RG24	37.9635	-104.9668	-1.062	0.570	-0.075	University of CO	Rye, CO
RICE	32.2436	-96.4998	-3.777	0.966	-2.222	Leica SmartNet	Rice, TX
RWDN	40.0867	-100.6535	-0.416	0.967	0.161	NOAA	McCook, NE
SA00	40.0352	-105.2433	-0.793	0.838	0.232	UCAR	Boulder, CO
SA11	41.3204	-105.6678	-1.108	0.587	0.003	University of WY	Laramie, WY
SA17	31.7160	-98.9867	-0.498	0.783	0.086	University of TX	Brownwood, TX
SA19	33.8738	-98.5199	0.474	0.855	0.799	University of TX-Austin	Wichita Falls, TX
SA60	39.9782	-105.2754	0.566	1.325	1.586	UCAR	Boulder, CO
SA62	40.5878	-105.1476	-1.256	0.765	-0.180	UCAR	Fort Collins, CO
SDCL	43.7851	-99.3119	-5.264	1.344	-3.448	Leica SmartNet	Chamberlain, SD
SDFR	43.3592	-97.4216	-3.930	1.276	-3.417	Leica SmartNet	Freeman, SD
SDGA	43.7193	-96.5137	-4.185	1.359	-2.812	Leica SmartNet	Garretson, SD
SDMA	43.9880	-97.0926	-4.477	1.191	-3.755	Leica SmartNet	Madison, SD
SDP1	43.3853	-98.8439	-4.514	1.261	-3.069	Leica SmartNet	Platte, SD
SDSF	43.7338	-96.6218	-2.439	0.827	-2.823	USGS	Edison Township, SD
SDWG	43.0823	-98.2559	-2.556	1.321	-2.957	Leica SmartNet	Wagner, SD
SFSD	43.5721	-96.7285	-3.291	0.713	-2.812	Minnesota DOT	Sioux Falls, SD
SG01	36.6041	-97.4848	-0.925	0.633	0.048	University of OK	Lamont, OK
SG04	37.1319	-97.2661	-0.433	0.600	0.669	University of OK	Greene, KS
SG08	36.8413	-96.4280	-0.871	0.618	0.210	University of OK	Pawhuska, OK
SG09	36.4308	-98.2844	-0.649	0.626	0.172	University of OK	Ringwood, OK
SG10	36.8814	-98.2864	-0.863	0.640	0.207	University of OK	Burlington, OK
SG11	37.3316	-99.3089	-1.277	0.846	-0.711	University of OK	Coldwater Township, KS
SG12	38.2020	-99.3169	-1.487	0.920	-1.429	University of OK	Morton, KS
SG13	38.1146	-97.5152	-1.672	0.897	0.596	University of OK	Alta Mills, KS
SG14	37.8430	-97.0206	-0.880	1.001	0.285	University of OK	Towanda, KS
SG16	37.3842	-96.1807	-0.442	0.733	0.259	University of OK	Elk Falls, KS

SG18	34.8835	-98.2039	-1.142	0.958	0.227	University of OK	Cyril, OK
SG19	35.3555	-98.9779	-0.430	0.882	0.522	University of OK	Bessie, OK
SG20	35.5568	-98.0158	-0.333	0.777	0.404	University of CO	El Reno, OK
SG24	40.0542	-105.5889	-1.990	0.938	0.219	University of CO	Ward, CO
SG34	35.2691	-96.7402	-0.864	0.906	0.089	University of OK	Pleasant Grove, OK
SG41	37.1510	-98.3621	-2.045	1.120	-0.955	UCAR	Hazelton, KS
SG42	36.8193	-97.8199	-1.399	1.257	-0.331	UCAR	Medford, OK
SG43	36.9255	-97.0818	3.544	1.507	0.652	UCAR	Newkirk, OK
SG44	37.0697	-96.7606	-1.974	1.188	-0.838	UCAR	Spring Creek, KS
SG45	35.8617	-97.0697	-2.654	2.917	-0.197	UCAR	Tryon, OK
SG46	36.1171	-97.5110	-1.197	1.179	-0.181	UCAR	Douglas, OK
SG47	36.3106	-97.9275	-1.584	1.575	-0.170	UCAR	Waukomis, OK
SG48	35.8800	-98.1731	-0.884	1.317	0.112	UCAR	Lomega, OK
SG72	35.2365	-97.4652	-0.570	0.847	0.386	University of OK	Norman, OK
SGPO	36.6042	-97.4848	-1.821	0.402	0.128	GFZ	Lamont, OK
SMSW	32.4746	-100.3994	-1.008	0.747	-0.243	Leica SmartNet	Sweetwater, TX
SUM5	34.8251	-102.5118	0.226	0.575	1.116	USCG	Westway, TX
SUM6	34.8251	-102.5121	1.059	0.568	1.598	USCG	Westway, TX
TCUN	35.0850	-103.6091	0.708	0.725	1.598	NOAA	Tucumcari, NM
TMGO	40.1309	-105.2327	0.022	0.496	0.134	NOAA	Altona, CO
TMS3	40.1300	-105.2328	-3.122	2.567	-0.958	GFZ	Altona, CO
TWG1	32.7947	-96.8241	-3.446	1.177	-1.968	Leica SmartNet	Dallas, TX
TX90	32.9114	-97.0595	-2.852	0.906	-1.962	Leica SmartNet	Dallas, TX
TXAB	32.5033	-99.7568	-0.683	0.562	0.081	TX DOT	Abilene, TX
TXAD	32.3080	-102.5436	0.761	0.629	0.326	TX DOT	Andrews, TX
TXAM	35.1536	-101.8785	0.540	0.463	1.453	TX DOT	Amarillo, TX
TXAR	32.7590	-97.0603	-2.477	0.696	-1.687	TX DOT	Arlington, TX
TXB3	31.1495	-99.3361	-1.160	0.907	-0.481	TX DOT	Brady, TX

TXB4	34.5088	-102.8935	-0.117	0.883	1.094	TX DOT	Bovina, TX
TXB5	31.4722	-96.0461	-3.352	1.144	-2.256	TX DOT	Buffalo, TX
TXB8	32.2854	-101.4982	-1.334	1.145	-0.337	TX DOT	Big Spring, TX
TXBD	31.7375	-98.9667	-1.085	0.897	-0.365	TX DOT	Brownwood, TX
TXBF	33.1653	-102.2828	-1.037	0.842	-0.241	TX DOT	Brownfield, TX
TXBG	32.2676	-101.4758	-0.586	0.757	0.162	TX DOT	Big Spring, TX
TXBI	31.7607	-99.9681	-0.851	0.685	-0.288	TX DOT	Ballinger, TX
TXBL	31.1927	-101.4737	0.127	0.695	0.292	TX DOT	Reagan, TX
TXBN	33.6067	-96.1753	-2.202	0.711	-1.279	TX DOT	Bonham, TX
TXBR	35.6403	-101.3979	0.812	0.613	1.487	TX DOT	Borger, TX
TXBT	31.0326	-97.4790	-2.243	0.717	-1.132	TX DOT	Belton, TX
TXBW	31.7376	-98.9668	-0.631	1.045	-0.365	TX DOT	Brownwood, TX
TXC0	32.3983	-98.9829	-2.859	1.297	-2.081	Leica SmartNet	Cisco, TX
TXC3	31.8098	-99.4221	-2.341	0.844	-0.437	TX DOT	Coleman, TX
TXC4	31.9104	-98.5972	-3.744	1.108	-2.528	TX DOT	Comanche, TX
TXCB	32.2882	-97.4121	-5.203	1.030	-2.715	Leica SmartNet	Cleburne, TX
TXCD	35.1016	-101.3626	0.996	0.662	1.486	TX DOT	Claude, TX
TXCE	31.4228	-102.3576	-1.348	0.655	-0.237	TX DOT	Crane, TX
TXCG	35.6881	-102.3291	0.399	0.607	1.337	TX DOT	Channing, TX
TXCH	34.4596	-100.2783	-0.304	0.560	0.584	TX DOT	Childress, TX
TXCI	35.9203	-100.3783	-0.699	0.756	0.328	TX DOT	Canadian, TX
TXCL	34.9512	-100.9134	0.250	0.665	1.162	TX DOT	Clarendon, TX
TXCO	33.1653	-96.6279	-2.302	0.563	-1.290	TX DOT	McKinney, TX
TXCW	33.9972	-99.7239	-2.163	0.793	-0.532	TX DOT	Crowell, TX
TXD2	33.2815	-96.9867	97.893	0.866	-1.261	TopNET	Krugerville, TX
TXDA	32.8000	-96.6729	-2.260	0.678	-1.465	TX DOT	Mesquite, TX
TXDC	33.2362	-97.6087	-1.508	0.595	-0.684	TX DOT	Decatur, TX
TXDE	33.2105	-97.1628	-2.712	0.563	-1.891	TX DOT	Denton, TX

TXDF	32.8786	-97.0422	-2.762	0.990	-1.962	Leica SmartNet	Euless, TX
TXDK	33.6237	-100.8302	-1.514	0.798	-0.105	TX DOT	Dickens, TX
TXDL	36.0778	-102.5387	1.159	0.781	1.664	TX DOT	Dalhart, TX
TXDM	34.5301	-102.3031	-0.013	0.770	0.862	TX DOT	Dimmitt, TX
TXDN	33.2150	-97.1255	-4.143	0.950	-1.891	Leica SmartNet	Denton, TX
TXDT	33.2349	-97.5879	-2.794	0.880	-1.870	Leica SmartNet	Decatur, TX
TXDU	35.8937	-101.9639	0.293	0.693	1.247	TX DOT	Dumas, TX
TXEA	32.4028	-98.8089	-2.845	0.888	-2.080	TX DOT	Eastland, TX
TXEN	31.2175	-99.8600	-1.874	0.709	-1.191	TX DOT	Eden, TX
TXES	32.3697	-96.8628	-3.373	0.618	-2.610	TX DOT	Waxahachie, TX
TXEY	31.7432	-98.9451	-3.258	1.173	-2.139	Leica SmartNet	Early, TX
TXFA	31.2959	-105.8496	-0.127	0.665	0.114	TX DOT	Fort Hancock
TXFD	31.7231	-96.1709	-2.981	0.877	-2.250	TX DOT	Fairfield, TX
TXFN	32.7213	-96.4433	-2.793	0.381	-1.793	TopNET	Forney, TX
TXFT	32.7199	-97.4510	-8.090	0.593	-3.515	TopNET	Fort Worth, TX
TXFW	32.7431	-97.3285	-4.301	0.883	-3.512	Leica SmartNet	Fort Worth, TX
TXFY	32.7484	-96.4719	-2.405	0.992	-1.614	Leica SmartNet	Forney, TX
TXG3	33.1385	-96.1077	-2.107	0.477	-1.483	TopNET	Greenville, TX
TXGE	33.1320	-96.0555	-2.454	0.694	-1.635	TX DOT	Greenville, TX
TXGH	33.6169	-100.3231	-3.273	0.867	-0.677	TX DOT	Guthrie, TX
TXGI	33.6419	-97.1765	-1.724	0.706	-0.874	TX DOT	Gainesville, TX
TXGL	31.4722	-98.5680	-2.904	0.877	-2.203	TX DOT	Goldthwaite, TX
TXGR	32.2404	-97.7544	-1.426	0.728	-0.726	TX DOT	Glen Rose, TX
TXGT	31.4326	-97.7080	-0.638	0.808	-0.920	TX DOT	Gatesville, TX
TXGU	36.2699	-101.4057	-1.680	0.782	0.421	TX DOT	Gruver, TX
TXHB	32.0114	-97.1297	-3.475	0.815	-2.734	Leica SmartNet	Hillsboro, TX
TXHI	31.9892	-97.1298	-3.783	0.780	-2.734	TX DOT	Hillsboro, TX
TXHM	31.6995	-98.1067	-1.968	0.812	-1.249	TX DOT	Hamilton, TX

TXHR	34.8457	-102.4066	-1.806	0.654	1.117	TX DOT	Hereford, TX
TXJA	33.1948	-98.1456	0.121	0.680	-0.473	TX DOT	Jacksboro, TX
TXKA	32.5718	-96.3143	-2.581	0.747	-1.804	TX DOT	Kaufman, TX
TXKE	32.4097	-97.3232	-2.387	0.705	-1.767	TX DOT	Cleburne, TX
TXKL	31.1208	-97.7322	-1.675	0.838	-0.988	Leica SmartNet	Killeen, TX
TXKM	31.8426	-103.1087	0.037	0.656	0.595	TX DOT	Kermit, TX
TXL1	33.9384	-102.3495	-0.731	0.724	0.752	TX DOT	Littlefield, TX
TXL2	32.7408	-101.9530	-1.088	0.834	-0.313	Leica SmartNet	Lamesa, TX
TXLA	32.7614	-101.9439	-1.703	0.688	-0.438	TX DOT	Lamesa, TX
TXLB	33.5204	-101.8784	1.508	0.814	0.748	Leica SmartNet	Lubbock, TX
TXLD	33.5943	-102.3458	-0.072	0.747	0.732	TX DOT	Levelland, TX
TXLS	31.0651	-98.1788	-1.625	0.922	-0.947	Leica SmartNet	Lampasas, TX
TXLU	33.5354	-101.8428	-0.358	0.496	0.465	TX DOT	Lubbock, TX
TXM1	33.7378	-102.7597	-0.089	0.835	0.737	TX DOT	Morton, TX
TXM5	31.9521	-102.1413	-2.010	1.214	0.137	Leica SmartNet	Midland, TX
TXMC	31.1321	-102.2325	-0.927	0.551	-0.252	TX DOT	McCamey, TX
TXME	34.7239	-100.5294	-1.316	0.736	0.782	TX DOT	Memphis, TX
TXMH	31.5577	-102.8940	-0.574	0.585	0.120	TX DOT	Monahans, TX
TXML	34.2398	-102.7536	0.228	0.908	0.841	TX DOT	Muleshoe, TX
TXMN	31.9101	-97.6619	-1.986	0.723	-1.254	TX DOT	Meridan, TX
TXMR	31.3059	-96.8640	-0.250	0.844	-0.499	TX DOT	Marlin, TX
TXMU	33.4493	-99.6452	-1.397	1.579	-0.565	TX DOT	Munday, TX
TXMW	32.8042	-98.1429	-3.554	0.863	-0.279	TX DOT	Mineral Wells, TX
TXMX	31.5951	-96.5244	-0.552	0.852	-0.302	TX DOT	Forest Glade, TX
TXMY	33.2235	-96.6233	-2.090	0.963	-1.287	Leica SmartNet	McKinney, TX
TXNA	32.0418	-96.5387	-1.026	0.620	-2.233	TX DOT	Corsicana, TX
TXNO	33.7757	-97.7260	-1.428	0.736	-0.567	TX DOT	Nocona, TX
TXOD	31.8739	-102.3152	-0.588	0.813	0.130	TX DOT	Odessa, TX

TXOE	31.8735	-102.3140	-0.113	0.574	0.130	TX DOT	Odessa, TX
TXOL	33.3560	-98.7497	-0.062	0.673	0.507	TX DOT	Olney, TX
TXP2	33.1822	-102.8182	-1.908	0.975	0.679	TX DOT	Plains, TX
TXPC	31.4175	-103.5157	-1.354	0.678	-0.250	TX DOT	Pecos, TX
TXPD	34.0123	-100.2896	-0.118	0.653	-0.323	TX DOT	Paducah, TX
TXPM	35.5341	-100.9287	-0.646	0.792	0.785	TX DOT	Pampa, TX
TXPW	34.1500	-101.7232	-0.832	0.836	0.128	TX DOT	Plainview, TX
TXPY	36.3934	-100.8155	-0.161	0.643	0.302	TX DOT	Perryton, TX
TXQU	34.2994	-99.7550	-1.185	0.636	0.579	TX DOT	Quanah, TX
TXR2	32.9548	-96.7175	-1.916	0.551	-1.112	TX DOT	Richardson, TX
TXRA	33.6722	-101.3873	-0.939	0.868	-0.107	TX DOT	Ralls, TX
TXRL	31.9004	-100.4694	-1.568	0.791	-0.279	TX DOT	Robert Lee, TX
TXS3	32.7118	-102.6298	-0.626	0.875	0.140	TX DOT	Seminole, TX
TXS7	31.8367	-100.9876	0.065	1.092	0.790	Leica SmartNet	Sterling City, TX
TXS8	31.4651	-100.4400	-1.353	1.001	-0.653	Leica SmartNet	San Angelo, TX
TXSA	31.4143	-100.4729	-0.390	0.576	0.306	TX DOT	San Angelo, TX
TXSB	31.1981	-98.7457	-2.240	0.908	-0.940	TX DOT	San Saba, TX
TXSC	31.8416	-101.0106	1.096	0.710	0.852	TX DOT	Sterling City, TX
TXSD	32.7097	-100.9113	-0.865	0.949	-0.087	Leica SmartNet	Snyder, TX
TXSF	36.3382	-102.0617	-0.561	0.693	0.804	TX DOT	Stratford, TX
TXSG	32.8557	-97.3442	-1.691	0.618	-1.916	TX DOT	Saginaw, TX
TXSH	35.2259	-100.2186	0.035	0.698	0.454	TX DOT	Shamrock, TX
TXSL	34.4741	-101.3141	0.356	0.801	1.130	TX DOT	Silverton, TX
TXSO	32.1412	-101.8076	-0.417	0.660	0.323	TX DOT	Stanton, TX
TXSR	33.5916	-96.6070	-2.315	0.852	-1.353	TX DOT	Sherman, TX
TXST	32.2326	-98.1822	-1.482	0.594	-1.214	TX DOT	Stephenville, TX
TXSY	33.6024	-99.2584	-0.529	0.680	0.313	TX DOT	Seymour, TX
TXTC	31.0739	-97.3519	-1.205	0.999	-1.131	Leica SmartNet	Temple, TX

TXTH	33.1790	-99.1679	-0.322	0.689	0.134	TX DOT	Throckmorton , TX
TXTO	33.1805	-101.7951	-1.213	0.810	-0.234	TX DOT	Tahoka, TX
TXTU	34.5337	-101.7394	0.570	0.640	1.451	TX DOT	Tulia, TX
TXVE	34.1329	-99.2832	-0.500	0.746	0.377	TX DOT	Vernon, TX
TXVG	35.2439	-102.4244	2.366	0.693	1.972	TX DOT	Vega, TX
TXWA	31.5777	-97.1105	-2.153	0.608	-0.765	TX DOT	Waco, TX
TXWC	31.6427	-97.0873	-1.484	0.897	-0.762	Leica SmartNet	Waco, TX
TXWD	32.7393	-97.7801	-2.694	0.940	-1.905	Leica SmartNet	Weatherford, TX
TXWE	32.7589	-97.8235	-1.072	0.644	-0.637	TX DOT	Weatherford, TX
TXWF	33.8539	-98.5056	-1.292	0.570	-0.431	TX DOT	Wichita Falls, TX
TXWL	34.8497	-100.2021	0.213	0.682	0.608	TX DOT	Wellington, TX
TXWX	32.4266	-96.8383	-2.534	0.840	-1.764	Leica SmartNet	Waxahachie, TX
UNAC	40.0612	-105.2056	-0.784	0.807	0.244	JPL	Boulder, CO
VANM	31.4393	-97.4063	-1.819	0.949	-1.110	Leica SmartNet	McGregor, TX
VCIO	36.0717	-99.2173	0.273	0.614	0.515	NOAA	Leedey, OK
WHN5	42.7393	-103.3288	-1.122	0.574	0.092	USCG	Whitney, NE
WHN6	42.7395	-103.3286	-1.939	0.621	-0.264	USCG	Whitney, NE
WMOK	34.7379	-98.7805	-0.781	0.576	0.486	NOTA	Indiahoma, OK
WYLC	41.1045	-104.7754	-1.628	0.504	-0.478	BLM	Cheyenne, WY
ZDV1	40.1873	-105.1272	-0.871	0.548	0.143	FAA	Longmont, CO
ZFW1	32.8306	-97.0665	-0.650	0.675	-1.965	FAA	Fort Worth, TX

BLM: Bureau of Land Management
CNPPID: Central Nebraska Public Power and Irrigation District
DOT: Department of Transportation (by state)
FAA: Federal Aviation Administration
GFZ: German Research Centre for Geosciences
JPL: Jet Propulsion Laboratory
NASA: National Aeronautics and Space Administration
NIST: National Institute of Standards and Technology
NOAA: National Oceanic and Atmospheric Administration
NOTA: Network Of The Americas
UCAR: University Corporation for Atmospheric Research
USCG: United States Coast Guard

USNO: United States Naval Observatory

Table S3.2. GPS Station time series classifications for the High Plains aquifer region

North	South
BUR5	GDAC
CHEY	HVLK
GILC	KSGC
KSTB	NMHB
MRRN	OKGM
NEA2	P038
NEAL	P039
NEAN	RG13
NEBB	SUM5
NEGO	SUM6
NEHD	TXAD
NEHO	TXAM
NEIM	TXB4
NEJ1	TXB8
NEJM	TXBF
NEKO	TXBG
NELX	TXCD
NENP	TXCG
NEOG	TXCI
NEON	TXCL
NEOR	TXDL
NEST	TXDM
NETH	TXDU
NEVN	TXGU
NLGN	TXHR
P044	TXL1
RWDN	TXL2
WYLC	TXLA
	TXLB
	TXLD
	TXLU
	TXM1
	TXM5
	TXML
	TXOD
	TXOE
	TXP2
	TXPM
	TXPW
	TXPY
	TXRA
	TXS3
	TXSD
	TXSL
	TXSO
	TXTO
	TXTU
	TXVG
	TXWL

Table S3.3. GSFC GRACE mascon IDs for the High Plains aquifer region

Northern High Plains Aquifer		Southern High Plains Aquifer		Surrounding Great Plains	
Mascon ID	Equivalent Water Height Trend (cm/year)	Mascon ID	Equivalent Water Height Trend (cm/year)	Mascon ID	Equivalent Water Height Trend (cm/year)
1592	0.8731	1684	-1.3663	1575	0.5260
1593	1.1049	1685	-1.5149	1576	0.7561
1594	1.1940	1686	-1.3650	1577	0.9963
1595	1.1082	1687	-0.9419	1578	1.1526
1596	0.8964	1702	-1.2428	1579	1.1630
1606	0.7567	1703	-1.8563	1580	0.9967
1607	1.0441	1704	-2.2723	1581	0.7170
1608	1.2325	1705	-2.3438	1582	0.4125
1609	1.2784	1706	-2.0217	1583	0.2018
1610	1.1840	1707	-1.3864	1590	0.3031
1611	1.0044	1722	-1.6743	1591	0.5787
1621	0.5888	1723	-2.2814	1597	0.6346
1622	0.8378	1724	-2.6116	1598	0.4297
1623	1.0326	1725	-2.5365	1604	0.1851
1624	1.1359	1726	-2.0648	1605	0.4442
1625	1.1452	1741	-2.0426	1612	0.8066
1626	1.0836	1742	-2.2839	1620	0.3303
1627	1.0020	1743	-2.1682	1628	0.9262
1641	0.6129	1744	-1.7191	1640	0.5366
1642	0.6251	1758	-1.3557	1646	0.7060
1643	0.6011	1785	-1.5549	1647	0.8277
1644	0.5864	1786	-1.5823	1661	0.2250
1645	0.6117	1787	-0.9418	1662	0.1330
1663	-0.0503	1788	-0.8755	1668	0.1706
1664	-0.2539	1789	-0.6822	1669	0.5424
1665	-0.3815	1794	-0.3644	1682	-0.5464
1666	-0.3561	1795	-0.2598	1683	-0.9928
1667	-0.1616	3119	-1.5386	1688	-0.3513
		3122	-1.3032	1689	0.2612
		3129	-0.4695	1708	-0.6034
				1709	0.1471
				1727	-1.3283
				1728	-0.4990
				1729	0.2298
				1745	-1.0517
				1746	-0.3307
				1747	0.2844
				1759	-0.9432
				1760	-0.4361
				1761	0.0599
				1762	0.4363
				1790	-0.4172
				1791	-0.1408
				1792	0.1225
				1793	0.1225
				1794	-0.3644
				1795	-0.2103
				1796	-0.1816
				1797	-0.1221
				1798	-0.0518
				1799	0.0181
				1802	-0.2103
				1803	-0.3193
				1804	-0.4393
				1805	-0.4867

				1806	-0.4323
				1903	0.3912
				1910	0.0938
				1917	-0.1146
				3113	-0.1582
				3114	-0.6099
				3115	-0.3272
				3116	-0.9590
				3117	-0.3418
				3118	-0.9121
				3120	-0.4977
				3121	-0.9118
				3123	-0.5723
				3126	-0.7044
				3127	-0.6721
				3128	-0.5778
				3130	-0.6328
				3131	-0.4230
				3132	-0.2493
				3133	-0.1784
				3166	-0.7780
				3214	-0.7562
				3215	-0.8913

Table S3.4. Climate divisions defined for the High Plains aquifer region

North	South
Kansas Drainage Basin, CO	Arkansas Drainage Basin, CO
Platte Drainage Basin, CO	South Central, KS
Central, KS	Southwest, KS
North Central, KS	Northeastern Plains, NM
Northwest, KS	Northern Mountains, NM
West Central, KS	Southeastern Plains, NM
Central, NE	North Central, OK
East Central, NE	Panhandle, OK
North Central, NE	West Central, OK
Northeast, NE	High Plains, TX
Panhandle, NE	Low Rolling Plains, TX
South Central, NE	Trans Pecos, TX
Southwest, NE	
South Central, SD	
Southwest, SD	
Lower Platte, WY	

Table S3.5. High Plains aquifer region groundwater well locations and IDs.

North				
USGS Well ID	**Latitude (°N)**	**Longitude (°)**	**Starting Depth Below Surface (m)**	**Water Level Change (m)**
391730102422000	39.2917	-102.6997	-37.9049	1.1156
393908102384100	39.6522	-102.6444	-29.1389	-10.4059
400155101521302	40.0287	-101.8712	-6.3947	0.8352
400852101352701	40.1483	-101.5958	-26.0695	-17.1328
400920099215501	40.1556	-99.3653	-26.0634	-2.6792
401401101510701	40.2336	-101.8519	-14.6487	-13.3624

401416099270601	40.2378	-99.4517	-42.2758	-3.6881
401518102295701	40.2550	-102.4992	-36.5760	-2.9230
401703101394801	40.2858	-101.6628	-14.5359	-11.2593
401735098522701	40.2931	-98.8742	-51.8952	-1.8166
401857099195201	40.3158	-99.3311	-53.9191	-0.9449
402101099595001	40.3503	-99.9972	-44.2874	4.4928
402625098594501	40.4403	-98.9958	-25.5300	1.8867
402757101591201	40.4658	-101.9867	-9.7536	-15.9288
403132099381001	40.5256	-99.6361	-68.8604	21.6835
403217099235801	40.5381	-99.3994	-5.4864	-1.6429
403235101395501	40.5447	-101.6664	-17.0688	-16.7518
403516101560601	40.5878	-101.9350	-18.8184	-16.9438
403543101443201	40.5953	-101.7422	-20.7264	-4.6543
403954099152101	40.6649	-99.2559	-2.5481	-0.3444
404343099272901	40.7284	-99.4579	-4.6025	1.3228
404516102264400	40.7544	-102.4456	-62.0359	-0.4694
404519101170301	40.7408	-101.2844	-50.0786	-7.2451
404618098504401	40.7717	-98.8456	-6.1112	1.9812
404620101433401	40.7722	-101.7261	-33.4975	-25.2588
404706101282201	40.7850	-101.4728	-42.1904	13.1704
404717099460501	40.7876	-99.7680	-1.8867	0.0914
404949099445701	40.8301	-99.7499	-4.1178	1.0211
405014099591001	40.8373	-99.9862	-2.2189	-0.4054
405040098384503	40.8444	-98.6456	-11.9024	0.9174
405118099514901	40.8551	-99.8636	-1.3137	-0.5151
405129099090201	40.8580	-99.1528	-37.6550	-1.9995
405137099085201	40.8583	-99.1530	-33.6194	-6.0899
405315098304302	40.8880	-98.5119	-7.0805	3.4168
405435098432601	40.9097	-98.7240	-21.1745	-0.2103
405445100074001	40.9122	-100.1284	-1.8136	0.3688
405503098441801	40.9174	-98.7384	-39.3771	-0.4999
405632098373501	40.9420	-98.6268	-11.8567	4.2306
405737101423201	40.9600	-101.7081	-52.1208	-5.8613
405738099504501	40.9606	-99.8458	-14.2311	4.1178
405855098383001	40.9821	-98.6417	-29.1724	-4.4196
405855100073901	40.9819	-100.1274	-17.6936	1.2162
410059104072401	41.0163	-104.1241	-4.8829	-5.8644
410102098374201	41.0172	-98.6283	-21.8328	0.9357
410111104223102	41.0164	-104.4093	-6.1570	-1.3777
410154099394701	41.0317	-99.6631	-14.2037	1.9538
410156098442601	41.0323	-98.7405	-2.0208	-0.5791
410233104093203	41.0426	-104.1589	-18.3093	1.9660
410324104481701	41.0554	-104.8066	-13.9751	1.9202
410507105003802	41.0854	-105.0106	-17.0566	5.1511
410508105003801	41.0854	-105.0105	-26.6700	2.1153
410530104574001	41.0901	-104.9609	-12.4511	-17.7820
410616104462401	41.1546	-104.7729	-12.0487	-0.4542
410703104071201	41.1175	-104.1206	-12.1920	-6.0960
410757104582302	41.1324	-104.9743	-32.5435	-4.6116
410827104501601	41.1416	-104.8390	-2.3744	-0.1433
410838104530401	41.1420	-104.8860	-2.5786	-0.4846
410900104110701	41.1500	-104.1853	-7.2116	-0.5486
410912104103801	41.1535	-104.1779	-5.7394	-3.0175
410930104524701	41.1576	-104.8806	-6.5136	-0.5669
410940104435701	41.1604	-104.7319	-43.2267	16.9774
411005104355001	41.1679	-104.5980	-48.7314	0.6248
411022104141201	41.1726	-104.2366	-6.1265	-1.6002
411034104554001	41.1754	-104.9289	-3.9624	-6.4313
411114104242501	41.1866	-104.4073	-13.9111	-2.0879
411126099422501	41.1904	-99.7070	-0.4816	-0.0671
411136104125301	41.3600	-104.2149	-60.2010	-0.2316
411210104452001	41.2030	-104.7561	-38.5237	-4.2946
411213104501401	41.2037	-104.8375	-30.0258	-3.3985

411214104293301	41.2039	-104.4925	-31.5163	-0.4389
411238104070801	41.2106	-104.1195	-9.6865	-2.7950
411531104194701	41.2587	-104.3301	-28.8219	-2.2342
411725104454601	41.2861	-104.7645	-44.1960	24.6827
412227104081401	41.3743	-104.1372	-44.2631	-1.2283
412227104081402	41.3742	-104.1372	-46.2077	-0.7894
412336104022801	41.3933	-104.0403	-74.5175	-8.1839
412343104053101	41.3951	-104.0921	-54.4068	-12.4054
412400104533901	41.4069	-104.8993	-45.6529	-0.1768
412507104133701	41.4186	-104.2269	-33.7810	1.4874
412522100121201	41.4228	-100.2034	-0.8870	0.1341
412604104203701	41.4344	-104.3435	-68.6989	-0.2042
412605104203001	41.4344	-104.3431	-68.1380	-0.2134
412944103452701	41.4953	-103.7576	-52.9346	1.4539
413038099482701	41.5106	-99.8075	-21.3970	-0.2408
413130100531201	41.5250	-100.8867	-32.3393	0.5395
413130100531202	41.5251	-100.8884	-31.7937	0.6218
413156098591201	41.5322	-98.9867	-21.1684	12.6583
413216102520201	41.5378	-102.8672	-22.7167	-0.5486
413455102370701	41.5831	-102.6174	-94.6404	-6.0655
414031101305601	41.6536	-101.5031	-4.5964	0.5974
414031101305602	41.6525	-101.5042	-5.6632	2.7219
414031101305603	41.6525	-101.5042	-4.7976	0.8809
414607102263301	41.7692	-102.4447	-1.0455	0.6797
414607102263302	41.7693	-102.4447	-0.6157	0.5060
414637099224701	41.7769	-99.3797	-2.2068	-0.1219
414643100313101	41.7786	-100.5252	-4.5324	-0.0945
414952100060301	41.8311	-100.1009	-1.0820	-0.1006
415108099493401	41.8525	-99.8269	-32.6258	0.4968
415118103020903	41.8550	-103.0358	-9.9334	8.0772
415559098005201	41.9331	-98.0144	-31.7967	2.4140
420006102561201	42.0019	-102.9561	-17.5626	-0.1768
420204101200502	42.0344	-101.3347	-1.8288	0.9083
420204101200503	42.0344	-101.3347	-0.8077	-0.2225
421210098402001	42.2028	-98.6722	-2.1641	-0.4389
422150097402401	42.3652	-97.6716	-9.4488	2.4567
422156097314301	42.3656	-97.5286	-10.1072	1.8898
422849099521503	42.4803	-99.8708	-2.0208	0.3322
423148098300601	42.5300	-98.5017	-10.8052	-0.5669
423307099494501	42.5519	-99.8292	-11.6708	1.7892
423730098560001	42.6250	-98.9333	-9.4214	1.2162
424837099425201	42.8103	-99.7144	-26.5816	1.9873
430027102311801	43.0075	-102.5217	-13.3411	0.7681
430027102311806	43.0075	-102.5217	-12.0457	-4.6878
430153100531002	43.0314	-100.8861	-6.3612	0.6066
430154100411801	43.0322	-100.6883	-3.6576	2.0361
430314100372001	43.0539	-100.6222	-14.2067	0.9449
430337100243201	43.0603	-100.4089	-10.4364	2.6396
430415100451501	43.0708	-100.7542	-6.1844	0.6675
430712100421301	43.1183	-100.7022	-14.4597	-0.0945
430726101033501	43.1239	-101.0597	-9.0830	0.4389
431158100461002	43.1994	-100.7694	-25.1917	-0.4724

South

USGS Well ID	Latitude (°N)	Longitude (°)	Starting Depth Below Surface (m)	Water Level Change (m)
332115103403301	33.3567	-103.6778	-18.8031	0.4602
333856102332401	33.6489	-102.5567	-35.0520	-11.6921
334404102414301	33.7344	-102.6953	-43.2511	-3.6210
340848102392801	34.1467	-102.6578	-39.3192	-5.5626
341010102240801	34.1695	-102.4041	-11.5824	-34.4637
341146101555701	34.1961	-101.9325	-77.4497	-7.1933

341544102251001	34.2622	-102.4194	-54.2544	-2.6182
342059102280701	34.3497	-102.4686	-47.5488	-36.8351
342116101452901	34.3544	-101.7581	-52.4256	-5.2212
342356102572501	34.3989	-102.9569	-53.3674	-53.1785
345342102313801	34.8950	-102.5272	-59.7469	-9.7048
354325100560301	35.7236	-100.9342	-98.0389	-2.8316
354527099470501	35.7575	-99.7847	-17.1298	0.3505
361209102142601	36.2025	-102.2406	-89.6112	-6.0107
361536099464601	36.2597	-99.7831	-25.5849	2.1153
361714099315101	36.2903	-99.5328	-9.0007	1.1704
361739099323301	36.2943	-99.5426	-38.2372	0.5639
361750102140501	36.2972	-102.2347	-81.3816	-9.5280
363033101440701	36.5092	-101.7353	-57.5920	-15.6698
363224099584601	36.5400	-99.9794	-12.3535	0.3871
363235099592801	36.5431	-99.9911	-9.9487	0.9571

4

Coverage, Completeness, and Resolution of Coseismic Displacements in the GPS Mega-Network Global Earthquake Catalog

4.1 Key Points

- Coverage and completeness of the GPS Mega-Network Global Earthquake Catalog increases with magnitude of event and network growth over time.
- Coseismic displacement estimates for each GPS station are improved by optimizing the duration of the time window within ±30 days around the earthquake origin time.
- Radius of influence within which coseismic displacements are potentially significant is empirically defined as $r_0 = \begin{cases} 10^{0.5M-0.79}, & 5.5 \leq M \leq 8.6 \\ 3235.94, & M > 8.6 \end{cases}$

4.2 Abstract

Earthquakes deform the Earth surface and move nearby GPS stations, causing discontinuities in their position time series. These displacements give key information about earthquake distribution, style and process. Along with InSAR, seismic, and geologic data, coseismic displacements can constrain the rupture dynamics, ambiguities in the source plane, elastic structure of Earth's interior, and stress change on nearby faults. Moreover, knowledge of coseismic displacement is needed to correct GPS position time series when focusing on other processes such as tectonics, volcanism, aquifer changes, geophysical loading, etc. that are constrained by the time series trend.

The Nevada Geodetic Laboratory produces time series for 20,000+ GPS stations which comprise the GPS Mega-Network, plus a list of times when earthquakes potentially move stations based on station locations, epicenter, and magnitude. I developed new, robust methods to estimate coseismic displacement amplitudes at all

potentially earthquake-affected times for all events M≥5.5 since 1994. Here, I evaluate the spatial and temporal degree of GPS Global Earthquake Catalog completeness with respect to the USGS NEIC Earthquake Catalog (U.S. Geological Survey, 2017). Between 1994.0 and 2022.3, 14,059 earthquakes M≥5.5 occurred of which 24.5% had coseismic displacement estimates available for 7,486 GPS stations, accounting for 63,122 estimations total. This relatively low percentage of estimated GPS coseismic displacements available per earthquake is attributable to the many earthquakes M<7 that occur along mid-oceanic ridges away from GPS instrumentation. The average percent of estimated GPS coseismic displacements available in the GPS Global Earthquake Catalog improves for earthquakes M≥7, and increased from 31% in 1994 to 89% in 2021, suggesting that the GPS Mega-Network is evolving to capture most of Earth's large seismic events.

4.3 Introduction

When an earthquake occurs the Earth's surface is rapidly and permanently deformed. Global Positioning System (GPS) stations precisely measure position and record the movement as a sharp, immediate discontinuity in ground displacement (Williams, 2003; Gazeaux et al., 2013; Metivier et al., 2014). Following earthquakes, GPS displacements provide critical information used to refine properties of the source, ambiguities in the source plane, and rapidly provide an overview for the scope, style, and direction of surface deformation. These data are complementary to other geodetic methods such as InSAR, and to seismic and geologic data which also constrain the source. They constrain the static stress changes which can encourage or suppress slip on nearby faults (Harris and Simpson, 1998; Gomberg et al., 1998; Stein, 1999; Freed, 2005). Likewise, coseismic deformation describes the starting conditions for postseismic processes such as viscous relaxation (Pollitz, 1997), afterslip (Perfettini and Avouac, 2004; Churchill et al., 2022), and poroelastic changes (Fialko, 2004), that can elucidate geodynamic and rheological properties of Earth's lithosphere and asthenosphere (Bürgmann and Dresen, 2008; Freed et al., 2007). Thus, coseismic displacements provide fundamental constraints on processes at work in the solid Earth system that drive earthquake hazards.

In addition to their direct value in earthquake research, GPS position time series are often used to study other aspects of active Earth deformation, such as mantle flow (Becker et al., 2015), glacial isostatic adjustment (Kreemer et al., 2020; Peltier et al. 2015), seasonal hydrological loading (Fu and Freymueller, 2012; Amos et al., 2014; Argus et al., 2014; Borsa et al., 2014), ocean tidal loading (Martens et al. 2016), aquifer depletion (Larochelle et al., 2021; Overacker et al., 2022), plate boundary deformation (Flesch et al., 2000; Kreemer et al., 2000), and magmatic injection (Dzurisin et al., 2009; Montgomery-Brown et al., 2015). Results from these studies can be negatively impacted if earthquake displacements in GPS position time series are not accounted for. Additionally, defining accurate reference frames requires GPS stations to be as stable as possible, which means coseismic displacements must be corrected for, or at least identified to exclude stations (Williams, 2003; Blewitt et al., 2013; Tregoning et al., 2013; Altamimi et al., 2016). Whatever the application, it is important to estimate the size of earthquake displacements objectively and accurately in GPS time series.

Since the beginning of the Nevada Geodetic Laboratory's (NGL) GPS holdings starting 1 Jan. 1994 through 20 Apr. 2022, there have been 14,059 earthquakes M5.5 or greater recorded worldwide by the United States Geological Survey National Earthquake Information Center (U.S. Geological Survey, 20177). Most, but not all, of these earthquakes occurred along tectonic plate boundary zones (Fig. 4.1A). Not coincidentally, the majority of the 20,224 GPS stations processed as part of the GPS Mega-Network by NGL are also located in these tectonically active areas (Fig. 4.1B).

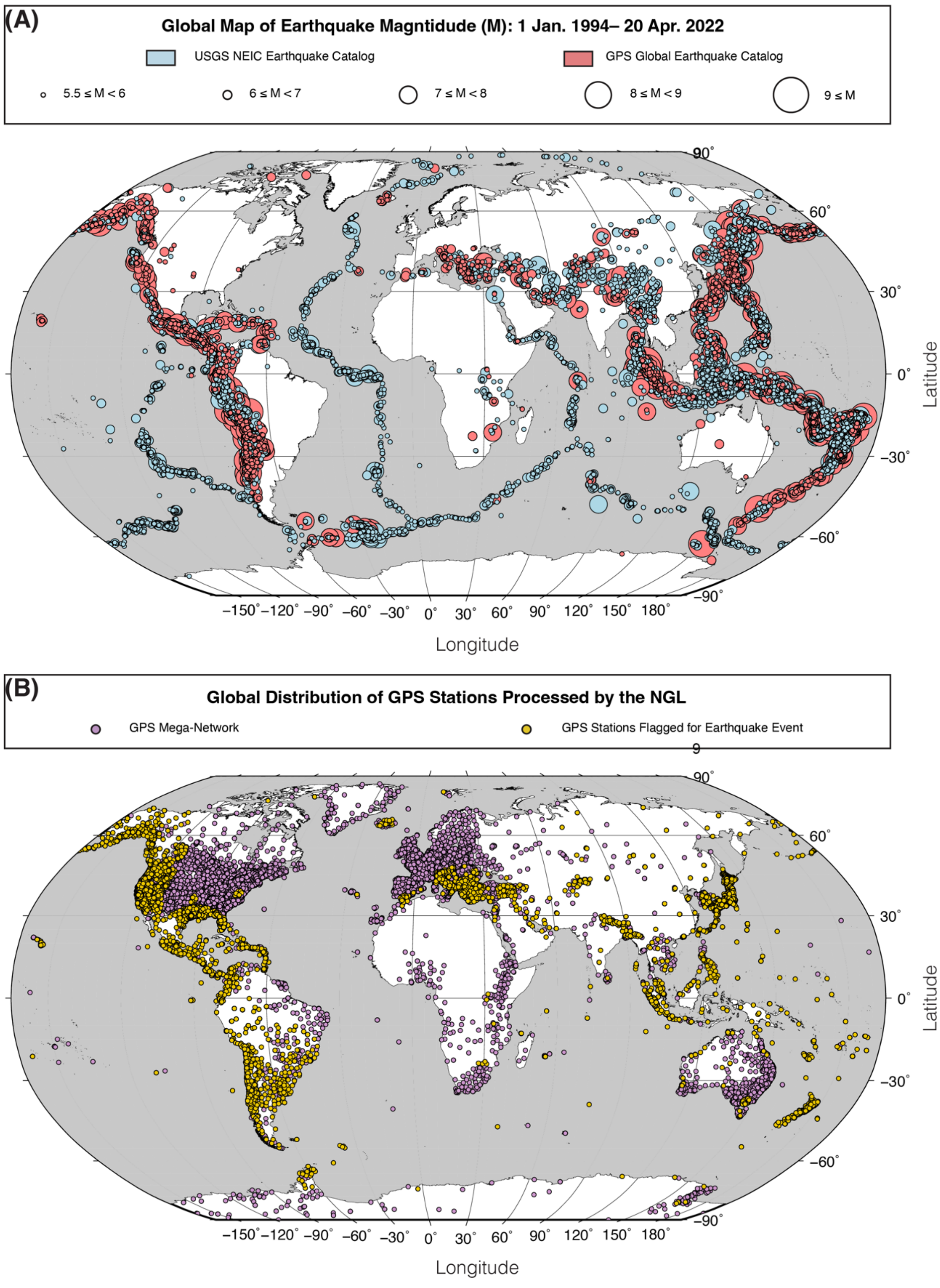

Figure 4.1. **(A)** Global map of all earthquakes occurring between 1 Jan. 1994 and 20 Apr. 2022. Earthquakes with estimated GPS coseismic displacements available (red) and

all other earthquakes recorded in the USGS NEIC catalog (blue) (U.S. Geological Survey, 2017) have magnitudes distinguished by circle size. Mid-ocean ridge earthquakes seldom have coseismic displacement availability for the GPS Mega-Network because of a paucity of geodetic instrumentation on the seafloor. **(B)** GPS stations flagged for earthquake displacements (yellow) contrasted against the remaining GPS stations in the GPS Mega-Network (purple).

To provide objective and timely earthquake displacement information derived from the NGL time series holdings, I have developed a new strategy to provide automated displacement estimation for all earthquake displacements affecting the GPS Mega-Network. The system relies on a first step of flagging all GPS stations that are potentially affected by each earthquake event. Next, I estimate 3-component displacements at each affected station and time using the GPS position time series data. Below I describe the methods employed for each step. I evaluate several different methodologies for estimating displacements using 24-hour and 5-minute GPS positioning time series to calculate coseismic displacements with the lowest uncertainties and misfit and find that different methodologies are needed depending on the completeness of the time series. I then construct a database of earthquake events $M \geq 5.5$ with associated GPS data: magnitude and epicenter of the earthquake event, GPS stations with potential displacements and their locations, estimated GPS displacements in east, north, and up components. This database allows us to evaluate the spatiotemporal completeness of the GPS Mega-Network Global Earthquake Catalog, which has implications for future reference frames, and comparisons with data from seismic networks.

4.4 Data

4.4.1 GPS Data

East, north, and up component GPS position time series from the 20,224 stations that comprise the GPS Mega-Network as of 20 Apr. 2022 were obtained from NGL's open access archive (all dots shown in Fig. 4.1B) (Blewitt et al., 2018). Position time series for 24-hour and 5-minute sample rate final solutions span between 1 Jan. 1994 and 20 Apr. 2022. Positioning data was processed using the GipsyX 1.0 software made available by the Jet Propulsion Laboratory (JPL), and JPL final orbit and clock products (Bertiger et al., 2020). All GPS time series solutions were aligned to the IGS14 global reference frame, which has the center of mass of the Earth system as its origin (Altamimi et al., 2016). GPS estimates of crustal motion are further improved by modeling atmospheric signal delays with the Vienna Mapping Function (VMF1) using gridded a priori data modeled by the European Center for Medium-Range Weather Forecasts (ECMWF) (Boehm et al., 2006). Further GPS processing details, e.g., regarding the treatment of metadata, data editing, ambiguity resolution, antenna phase center calibrations, and estimation strategy can be found in Blewitt et al. (2013) and Kreemer et al. (2020) and are documented at http://geodesy.unr.edu/gps/ngl.acn.txt.

To track the effect of geodetic station equipment changes on the position time series, I tabulate metadata from IGS log files so that apparent displacements not attributable to solid Earth movement may be recognized and accounted for. By gathering files from the GPS data archives, I have obtained 11,378 unique IGS log files, omitting those other than the most recent available for each station. From each log file I deduced times for changes in receiver and antenna makes and models, radomes, and receiver elevation cutoff angle setting. When a change event occurs, a record is generated that includes site name, date, and the type of equipment change event that occurred. These records mark the times of potential apparent equipment related discontinuities on the position time series. Equipment change displacements are generally less than a few millimeters, but can be much larger in cases where, e.g., the antenna was physically moved. Importantly, the equipment change times must be accounted for when selecting the interval of time used to compute earthquake displacements. In what follows, I use the equipment change times to truncate the time series so that displacement estimates are not biased by the equipment change.

4.4.2 National Earthquake Information Center Data

Earthquake time, magnitude, and epicentral location in latitude, longitude, and depth for the 14,059 earthquakes M≥5.5 that occurred between 1 Jan. 1994 and 20 Apr. 2022 were obtained from the NEIC data archive (all dots shown in Fig. 4.1A) (U.S. Geological Survey, 2017). Magnitude ranges from the minimum M5.5 to the largest recorded magnitude in the date range, M9.1 for the 2004 Great Sumatra–Andaman and the 2011 Great Tohoku-oki earthquakes. I include earthquakes with minimum magnitudes as low as M5.5 because, though the largest earthquakes contribute the greatest deformation in a single event (Tregoning et al., 2013), lower magnitude events measurably deform the crust and occur in far greater numbers, and hence contribute to surface movement that present as position time series displacements. Smaller magnitude earthquakes have a greater number of occurrences than larger magnitudes; 9,740 for 5.5≤M<6, 3,892 for 6≤M<7, 394 for 7≤M<8, 31 for 8≤M<9, and two M≥9.

The global geographic distribution of the earthquake epicenters is largely focused along tectonic plate boundaries, with a majority of the smallest magnitude earthquakes occurring along mid-oceanic ridges. Offshore earthquakes constitute 81% of the 5.5≤M<6, 80% of the 6≤M<7, 79% of the 7≤M<8, 87% of the 8≤M<9, and 100% of the M≥9 (Fig. 4.1A). Because there is a paucity of GPS instrumentation located on the seafloor, measurements of displacements for earthquakes with offshore epicenters are performed by GPS sites on-shore potentially far from the epicenters. However, the global distribution of earthquakes includes continental seismic sources as well. I define on-shore earthquakes in this study as earthquakes that occurred within the bounds of the continents and island land masses as defined by Matlab Mapping Toolbox's coastlines.mat database comprised of data from Wessel and Smith (1996). Using these criteria, on-shore earthquakes comprise 19% for 5.5≤M<6, 20% for 6≤M<7, 21% for 7≤M<8, and 13% occurrences for 8≤M<9 (Fig. 4.1A). Both M9.1 earthquakes occurred offshore (Fig. 4.1A).

4.5 Analysis

Coseismic displacement is the difference in position before and after an earthquake, but which part and how much of the GPS time series data is used in that estimation can influence the displacement amplitude. Differences in analysis strategy can play a significant role (e.g., Gazeaux et al., 2013). In this study, I focus on estimating the amplitudes of displacement discontinuities for earthquakes with known earthquake times. Here, I explore the utility of two different coseismic displacement estimation strategies that adapt to the degree of completeness of the data resources available. Which method is best to use depends on the content of the time series, particularly the presence of gaps in data at the time of the event which can make one class of estimation strategy impossible.

4.5.1 Estimating Coseismic Displacement – Data Near Event

The first method is the Data Near Event (DNE) model (Fig. 4.2B) which uses data immediately before and after an earthquake to estimate displacements. This method is designed for permanent stations in the GPS Mega-Network which are operating continuously and ideally have GPS data available for each 24-hour period following their installation. For this style estimation, I use the date of the earthquake provided by the USGS NEIC Earthquake Catalog (U.S. Geological Survey, 2017) to estimate the displacement from the data. First, the position time series is detrended using a Theil-Sen estimator which excludes pairs crossing the time of the displacement (Thiel, 1950; Sen, 1968). I then detrend the whole time series and estimate the difference between median positions before and after the event to obtain a robust estimate of the displacement amplitude using:

Eq. 4.1) $$D_{eq,i} = median(x(t_{i,after})) - median(x(t_{i,before}))$$

Where $D_{eq,i}$ are the displacements amplitudes for event i and $t_{i,\ before}$ and $t_{i,\ after}$ are the sets of discrete times before and after the earthquake used in the estimation. Because it is based on medians, this method has the strength of being insensitive to outlier positions within the time windows defined by $t_{i,\ before}$ and $t_{i,\ after}$, and is insensitive to movements of the station outside the time window that may be difficult to model explicitly. Formal uncertainties for the DNE method are calculated as if the problem were a least squares linear inversion of the times series for the displacement using the position uncertainties at times $t_{i,\ before}$ and $t_{i,\ after}$. The residual scatter is calculated from the median absolute deviation of the observed positions minus the positions predicted from the trend and coseismic displacement amplitude.

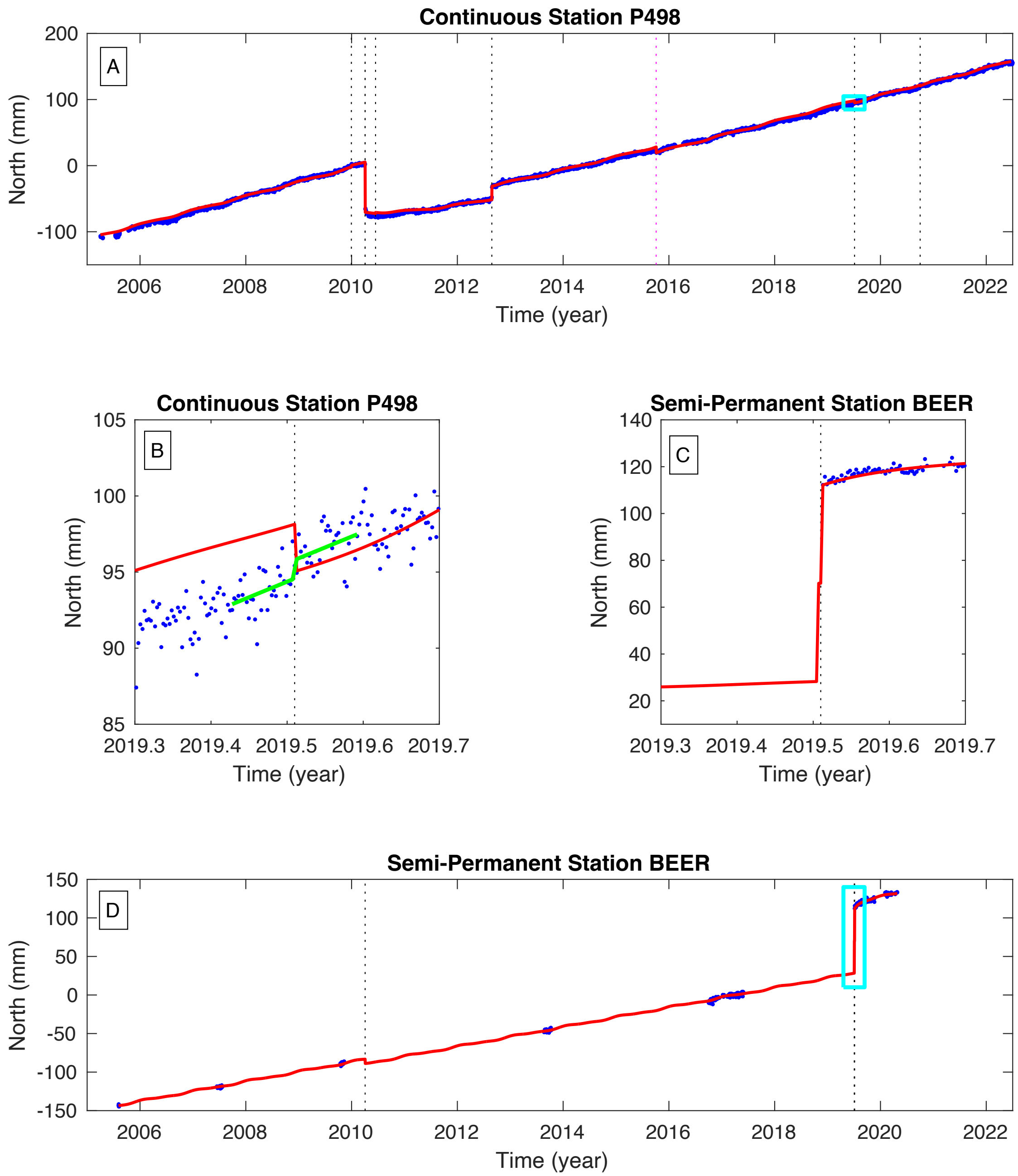

Figure 4.2. Example time series data (blue dots) with Time Series Models (red lines) that estimate coseismic displacements for the 2019 M7.1 Ridgecrest earthquake which occurred on day 2019.51. Vertical dotted lines are times of earthquakes (gray) and equipment changes (magenta). **(A)** Continuous station P498, where cyan box indicates time interval shown in **(B)**. The red line in (B) matches the red line in (A) and shows

how the TSM method poorly solves for the coseismic displacement. The green line is the result of the DNE method which makes a superior estimate for the displacement. **(D)** Semi-permanent MAGNET station BEER, where cyan box indicates time interval shown in **(C)**. The DNE method is not feasible for the Ridgecrest earthquake using data from station BEER because there is no data immediately before the event. See text for discussion.

4.5.2 Data Near Event Time Window Testing

Determining the size of the time window, i.e., how much time before and time after the earthquake to use when estimating coseismic displacement, is complicated by the potential presence of signals other than the coseismic displacement. The quantity of data centered in time around the earthquake, presence of foreshocks, aftershocks, or postseismic signals in the position data surrounding the event can affect the precision and accuracy of the displacement estimate. Using data from a fixed number of days before and after an earthquake event may not be the most appropriate depending on these factors. Longer time windows can reduce formal uncertainty by introducing a greater number of station data, but may increase residual scatter if the window contains other signals besides the coseismic displacement. For example, postseismic deformation can introduce bias in the estimation if it causes a change in station movement rate after the earthquake. Similarly, time series with non-linear signals may not be well-fit by linear trends for long durations that are adequate for a short duration window. To further improve the estimation, I seek a method that optimizes the duration of the time windows before and after the earthquake. Finding an optimum requires balancing the need for a low formal uncertainty and a low residual scatter. The time interval should be sufficiently long enough to reduce uncertainty, but short enough to minimize bias from non-linear signals.

The DNE method uses data within 30 days before and 30 days after an event when estimating displacements to reduce the influence of longer duration signals unrelated to the coseismic displacement possibly occurring concurrently at a given site. If no data is available within that time frame, it is impossible to estimate a DNE displacement and I use a different method discussed in the next section. If there is data within 30 days both before and after the event, however, a 30 x 30 array is built where each element represents a displacement estimate from data durations $1 \leq t_{i\ days,\ before} \leq 30$ and $1 \leq t_{i\ days,\ after} \leq 30$ the earthquake. The position data within each interval duration is used to calculate displacements for every combination. If there are earthquake events or equipment changes within either the pre- or post-event intervals, then the intervals are truncated so only data between the last event before, or first event after the target earthquake are used.

To decide which of the estimated displacements in the resulting array is the best, I use the formal uncertainty and median absolute deviation of the residual. This evaluation is based only on the horizontal magnitude of displacement rather than vertical because vertical position solutions have greater uncertainties and greater influence from other signals, e.g., bias introduced in imperfect modeling of refractivity of the atmosphere (Tregoning and Watson, 2009). The formal uncertainty is smaller when more data (long duration intervals) are used. The median absolute deviation of the residual increases when the misfit increases, which can occur, e.g., when postseismic deformation or other processes drive continuing change in station position. I normalize the formal uncertainty (Fig. 4.3A) and median absolute deviation (Fig. 4.3B) before summing them to make an objective parameter that represents a single integrated measure of displacement quality. I find the minimum value of this parameter for the horizontal magnitude that represents the best position window time interval combination $t_{i,\ before}$ and $t_{i,\ after}$ (Fig. 4.3C). Taking that optimal time window, I apply it to the time series to estimate DNE method displacement for east, north, and up components.

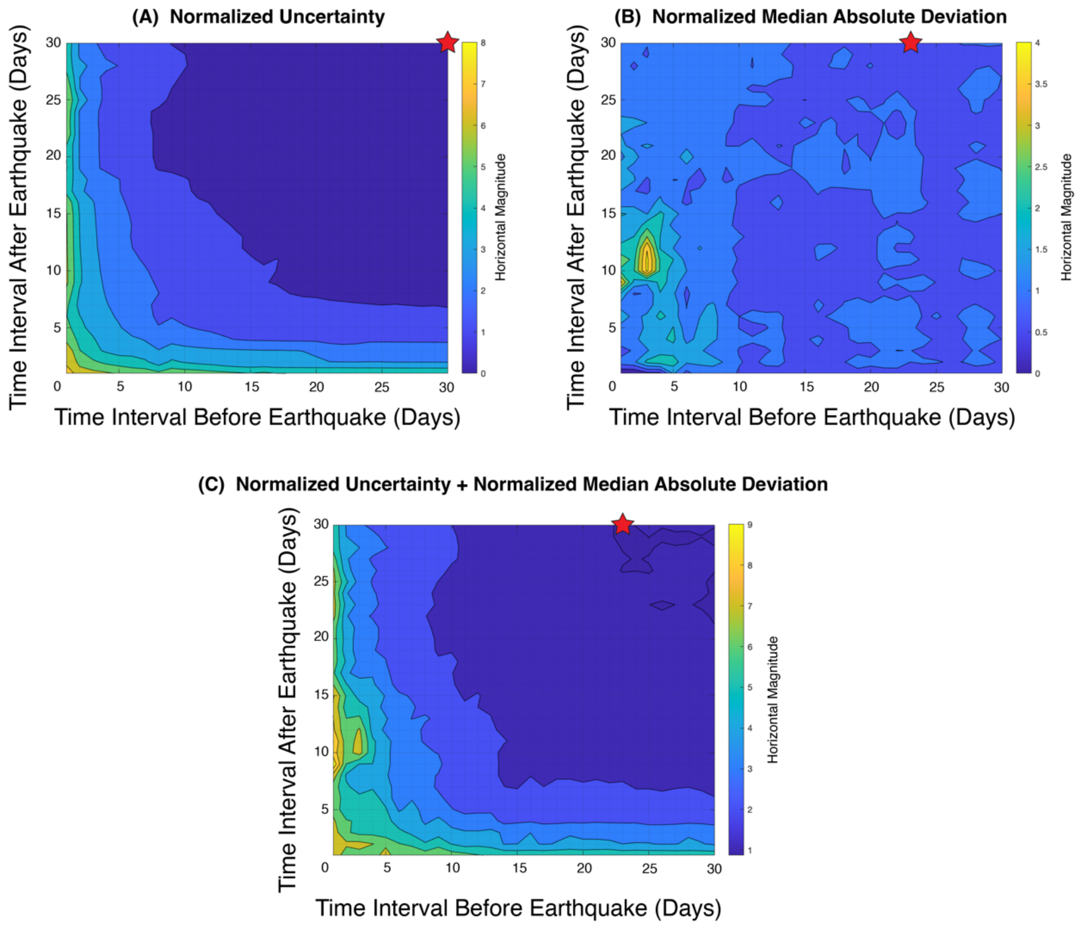

Figure 4.3. Example duration window optimization for the magnitude of horizontal components at GPS station ALAM for the 2020 M6.5 Monte Cristo Range mainshock. Lowest normalized value per $t_{i,\,before}$ and $t_{i,\,after}$ combination (red star) shown for **(A)** formal uncertainty, **(B)** median absolute deviation of residual, and **(C)** their normalized sum defines the optimal duration windows used to estimate coseismic displacement using the DNE model.

4.5.3 Accounting for Multiple Displacements in a 24-Hour Period

The DNE method can also be readily applied to 5-minute time series which are available for all stations for which there are 24-hour solutions in the NGL database. Using 5-minute time series is desirable in cases where multiple significant earthquakes occur in the same 24-hour period. This typically occurs during sequences with very large earthquakes, where foreshocks, the mainshock, or aftershocks occur very close in time to each other, affecting the GPS station at multiple times on the same day. In these cases, the DNE displacements based on 24-hour solutions are indeterminable since the displacements from different events cannot be distributed into the separate earthquakes. For these cases, I apply the DNE method to the 5-minute time series since I can divide the solutions into times before and after the events. The maximum amount of data, which depends on the time between events, is used to calculate the displacements for the multiple events in the 24-hour period since I am more concerned by data availability than potential short-term bias. If there are multiple days on either side of the day of the events, the 24-hour medians of the 5-minute data are used and the roving window strategy is employed as though it were regular 24-hour data to optimize the trade-off between low misfit and low formal uncertainty.

For example, if a large earthquake with no foreshocks in the 30 days preceding an event has one aftershock that occurs two hours after the main event, with no further aftershocks in the following 30 days, the mainshock displacement estimation uses 5-minute time series data grouped into 30 24-hour periods before the event to search for the $t_{i,\,before}$ with the lowest combined formal uncertainty and median absolute deviation. The

$t_{i,\,after}$ uses 5-minute time series only for the two hours after the mainshock and preceding the aftershock. Similarly, the aftershock displacement estimation uses the full two hours of 5-minute time series data before the event for the $t_{i,\,before}$ and 5-minute solutions grouped into 30 days of 24-hour periods after the event to find the ideal $t_{i,\,after}$. Essentially, instead of the 30 x 30 day array, the mainshock would appear as a 30 day search x 2 hour fixed array, and the aftershock would work as a 2 hour fixed x 30 day search array to estimate the time interval used in the displacement estimation.

4.5.4 Estimating Coseismic Displacement – Time Series Model

Some stations do not have continuous observations, and may have periods where they do not function, or are operated as semi-permanent stations where observations are clustered in time when the receiver occupies the station. One example is the semi-permanent Mobile Array of GPS for Nevada Transtension (MAGNET), a subset of the GPS Mega-Network where permanently installed GPS monuments are surveyed with mobile GPS receivers for one to several months at a time and usually have time gaps of months to years in the time series (Blewitt et al., 2009). Semi-permanent stations are more likely to have gaps during an earthquake event that make the DNE model unfeasible. In this case, a model is fit to the time series that includes a parameter for the amplitude of a Heaviside step function at the time of the earthquake. I call this style of time series displacement estimation strategy the Time Series Model (TSM) method, and an example of its use is shown in Figure 4.2C.

The TSM style of estimation solves for parameters representing the time series by using a model that includes terms for a trend, seasonality, displacements for known earthquake and equipment changes, and exponential terms for postseismic relaxation from large earthquakes (M≥6.5). The resolvability of the model parameters depends on the total length of the time series and how well the time series is modeled by:

Eq. 4.2)

$$x(t) = b + v(t) + C_1 cos(\omega t) + S_1 sin(\omega t) + C_2 cos(2\omega t) + S_2 sin(2\omega t) +$$
$$+\sum_i D_i \mathcal{H}(t - t_i) + \sum_j A_j (1 - e^{(\frac{-(t-t_j)}{\tau_j})}) \mathcal{H}(t - t_j)$$

where x is the position as a function of time t, b is the intercept, v is the slope (or velocity), and coefficients C_1, S_1, C_2, S_2 are the amplitudes of the sine and cosine terms for annual and semiannual constituents, respectively. I solve for the velocity term first using the MIDAS algorithm (Blewitt et al., 2016), then the remaining terms are found from the residual time series via least squares inversion. For a subset of the earthquake displacement terms when the earthquake is M≥6.5 and is within half the radius of influence ($0.5r_0$, a concept I will explain in greater detail in Analysis 4.5.6), I include the last term of Eq. 4.2 to solve for postseismic relaxation terms: A_j for the magnitude of the relaxation and τ_j for the relaxation time. The j are a subset of the i which meet the magnitude and distance criteria. A solution for A_j and τ_j is obtained, if needed, with a non-linear algorithm that converges within a few iterations. The predictions of the resulting TSM displacement model found for each time series are presented as the red line on the NGL station page time series plots, e.g., as shown by time series in Figure 4.2 and for station CCCC in Figure 4.4. This method has the strength of being constrained by all data in the entire time series, but some components may be sensitive to outliers or other unmodeled movements of the station that are not well fit by the parameterization in Eq. 4.2 (Fig. 4.2B). The uncertainties for the magnitude of the coseismic displacement are obtained from the formal uncertainty in the least squares estimate of the displacement amplitude.

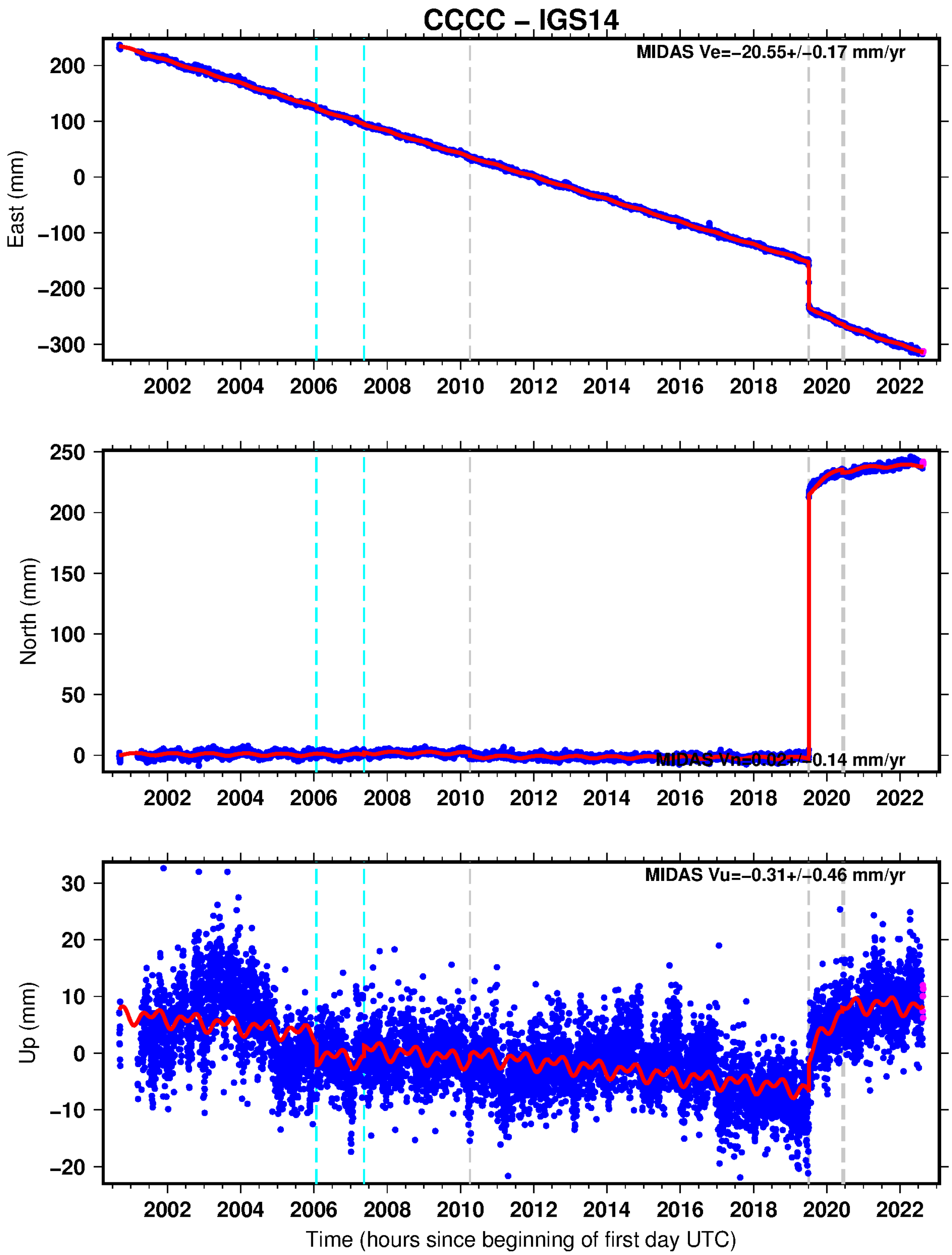

Figure 4.4. GPS time series for station CCCC near Ridgecrest, California. Potential coseismic displacements (gray dash) and equipment changes (cyan dash) are marked along the time axis. Time Series Model (red line) is plotted for each component.

4.5.5 Data Near Event Model Compared to Time Series Model

I compare TSM and DNE horizontal displacements and uncertainties for the 2019 M7.1 Ridgecrest and the 2020 M6.5 Monte Cristo Range mainshocks. The horizontal displacements were the primary consideration when determining displacement estimation improvement because vertical position solutions have greater uncertainties due to several processes that contribute to lower signal-to-noise ratios (Bennett and Hreinsdóttir, 2007; Mazzotti et al., 2007; Beavan et al., 2010). The expectation when evaluating these methods was that the largest displacements are located closest to the epicenter and that displacement decreases with distance from the epicenter. Vector plots of horizontal displacement indicate whether DNE displacements are in line with TSM solutions.

To decide which coseismic displacement estimation method is most appropriate for a given GPS station, I adopt a tiered strategy using 24-hour DNE when possible, resorting to 5-minute DNE when multiple events occur in the same day, and ultimately TSM should either of the DNE methods be unfeasible. This can happen when there are gaps in the time series >30 days surrounding the earthquake event, or when multiple earthquakes happen within a 5-minute period. In such cases, TSM becomes a more viable displacement estimation method. Usually at least one of the strategies, whether 24-hour DNE, 5-minute DNE, or TSM can provide valuable information on coseismic deformation at a given site. However, in some cases estimates are clearly outliers and not representative of the coseismic displacement field (Fig. 4.2).

DNE estimates appear to be slightly shifted compared to their TSM counterparts that benefit, in this case, from utilizing the full time series in their estimations that act as a stable reference frame (Fig. 4.5 and Fig. 4.7). I therefore apply a shift step to 24-hour DNE and 5-minute DNE far-field estimations to align these estimates to those made using TSM which have a more stable reference frame owing to their being constrained by the entire time series. In this instance, I take the difference in median east and north displacements for all positions as the alignment shift, and apply it to the DNE estimates, ensuring coseismic displacements have equivalent median displacements between strategies.

Outlier displacement estimates located far away from the epicenter can distort the pattern of coseismic deformation by appearing to be much greater than surrounding stations. These are likely owing to station defects or very localized site effects (Fig. 4.5D and Fig. 4.6D). I reduce the effect of these outlier displacement estimates uncorroborated by the displacement values at its nearest neighbors by applying median spatial filtering to displacements located in the far-field (>$0.33r_0$, see Analysis 4.5.6 for details) (Fig. 4.7F and Fig. 4.7F). Once an alignment vector is applied to DNE coseismic displacements, median spatial filtering is applied to the east and north components before calculating the horizontal displacement magnitudes and uncertainties to minimize the effects of noise and outliers in the far-field. These displacements located furthest from the epicenter are unlikely to experience significant movement, and outlying large magnitude displacements are probably caused by localized site effects unrelated to coseismic movement.

Comparisons of TSM and DNE combined 24-hour and 5-minute estimated displacements were performed for the two earthquake case studies for evaluation. First, I compared DNE and TSM displacement estimates for the 2019 M7.1 Ridgecrest earthquake using 1,271 GPS time series in the region (Fig. 4.5). An alignment shift of

0.51 mm is applied to the east and 1.18 mm is applied to the north components for the event, shifting displacements for 1,036 stations. For the 2020 Monte Cristo Range, Nevada M6.5 mainshock, I estimated displacements for 372 GPS time series (Fig. 4.7). Here I apply alignment scalars of 0.34 mm to the east and –0.11 mm to the north for 238 time series to shift the DNE estimates.

For both estimation strategies, horizontal displacement plots for the Ridgecrest and Monte Cristo Range earthquakes show largest displacement magnitudes are located nearest to the epicenter then grow smaller as distance from the epicenter increases. For the TSM strategy (Fig. 4.5A–4.5B and Fig. 4.7A–4.7B), Ridgecrest and Monte Cristo Range earthquakes plot higher uncertainty values in the horizontal displacement magnitudes north of the epicenters. These GPS stations include part of the MAGNET network which can have months to years-long gaps in their time series, possibly during the time of the earthquake, that increase the uncertainty in the displacement estimates. Because DNE cannot estimate displacements without data within ±30 days on either side of the earthquake origin time, these stations are not included on the DNE plots (Fig. 4.5C–4.5F and Fig. 4.7C–4.7F). In general, however, the DNE uncertainties are lower than the TSM uncertainties and have comparable magnitudes. Horizontal magnitude estimates in the far-field also have fewer large magnitude outliers for the DNE strategy compared to TSM. Once an alignment vector and median spatial filtering is applied to DNE displacement estimates (Fig. 4.5E–4.5F and Fig. 4.7E–4.7F), far-field outliers are further reduced. One noisy outlier on the outer boundary of $0.33r_0$ remains southwest of the epicenter and pointing north for the Ridgecrest event (Fig. 4.5E).

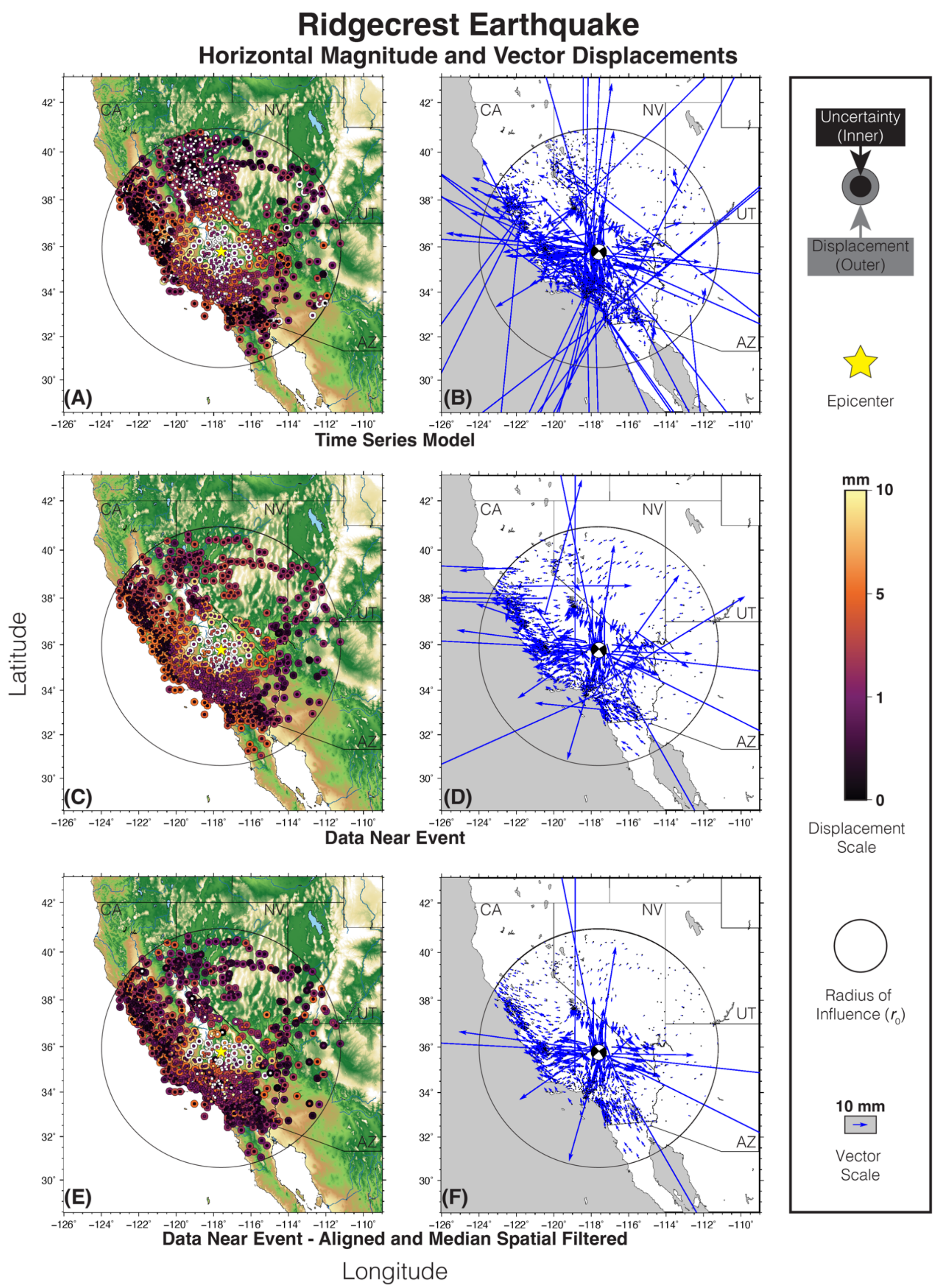

Figure 4.5. Horizontal displacements, corresponding uncertainties, and vector plots for the 2019 M7.1 Ridgecrest Earthquake. TSM displacement estimation strategy (**A & B**)

has higher uncertainties and higher scatter compared to the DNE displacement estimates (**C** & **D**). An alignment vector is applied to the DNE displacements (**E** & **F**) to correct for a systematic difference between TSM and DNE and outliers visible in the far-field. A comparison plot shows a detailed examination of the three strategies (Fig. 4.6).

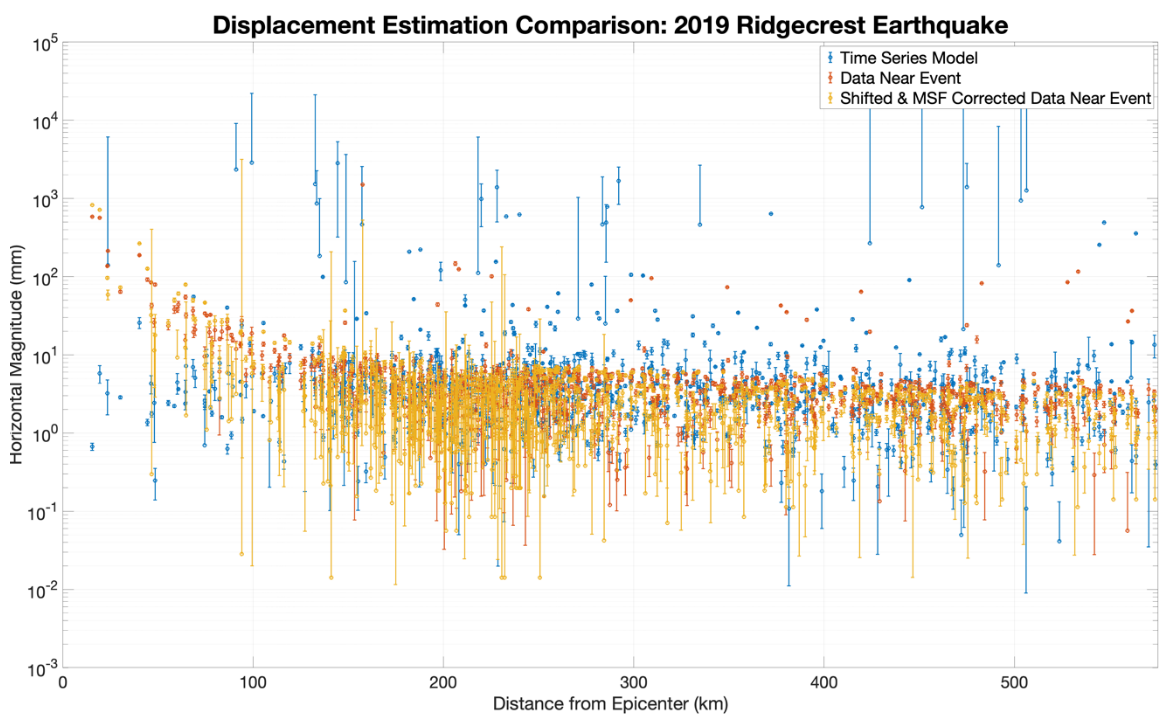

Figure 4.6. Comparison of the horizontal magnitudes produced by the Time Series Model (blue), Data Near Event (red) and median spatial filtered and aligned (yellow) displacement estimation strategies for the 2019 M7.1 Ridgecrest Earthquake. TSM horizontal magnitudes exhibit greater scatter likely caused by bias from unmodeled signals. The alignment correction factor is applied to all GPS time series for the median spatial filtered and reference frame shift corrected displacement estimates, but stations >$0.33r_0$ distance from the epicenter are median spatial filtered.

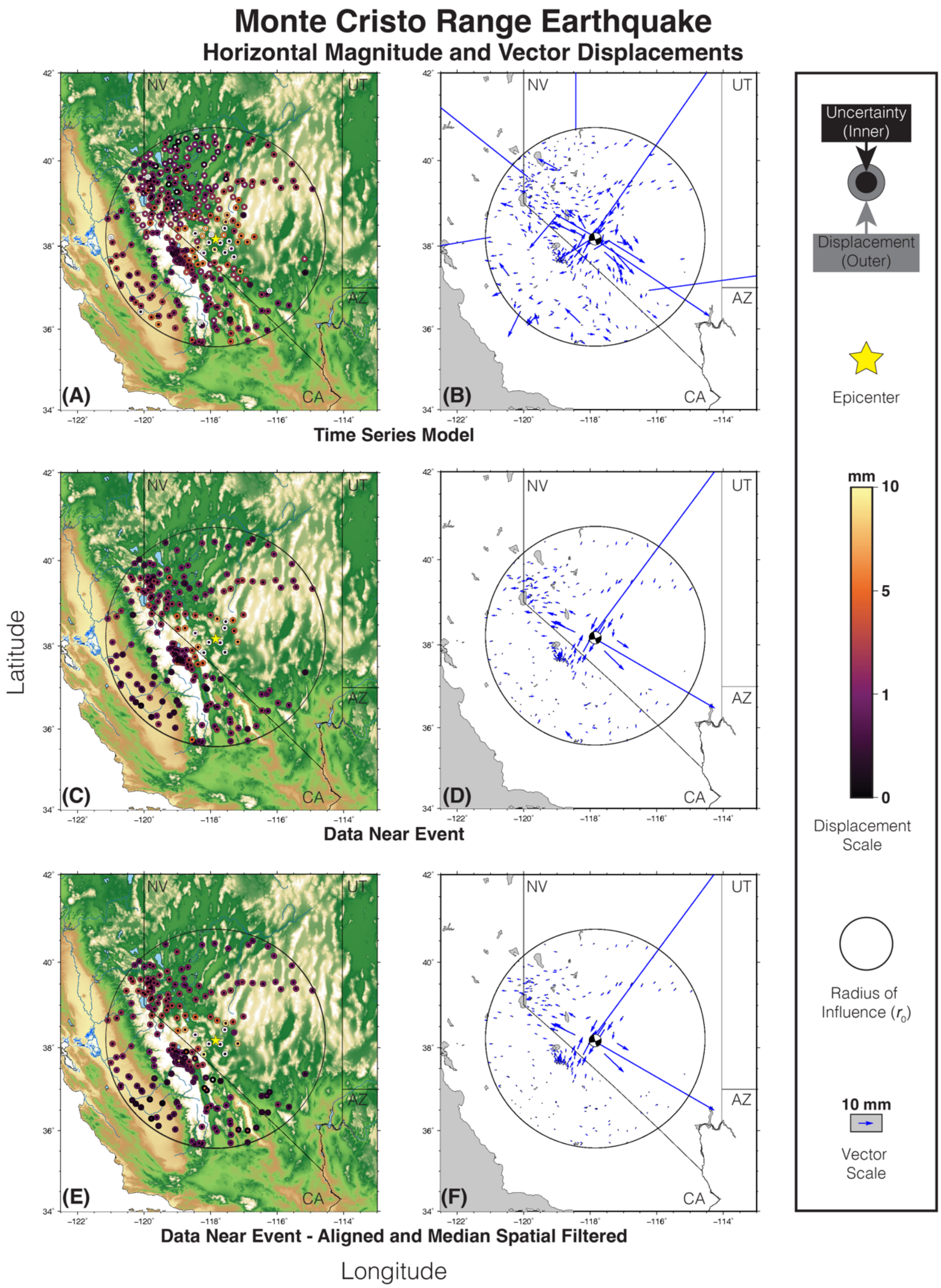

Figure 4.7. Horizontal displacements and corresponding uncertainties for the 2020 Monte Cristo Range, Nevada M6.5 mainshock. TSM displacement estimation strategy (**A**

& **B**) has higher uncertainties and higher scatter compared to the DNE estimates (**C** & **D**). Aligned DNE displacements (**E** & **F**) corrected for a slight systematic shift in the displacements, noise, and/or outliers in the far-field. A comparison plot shows a detailed examination of the three strategies (Fig. 4.8).

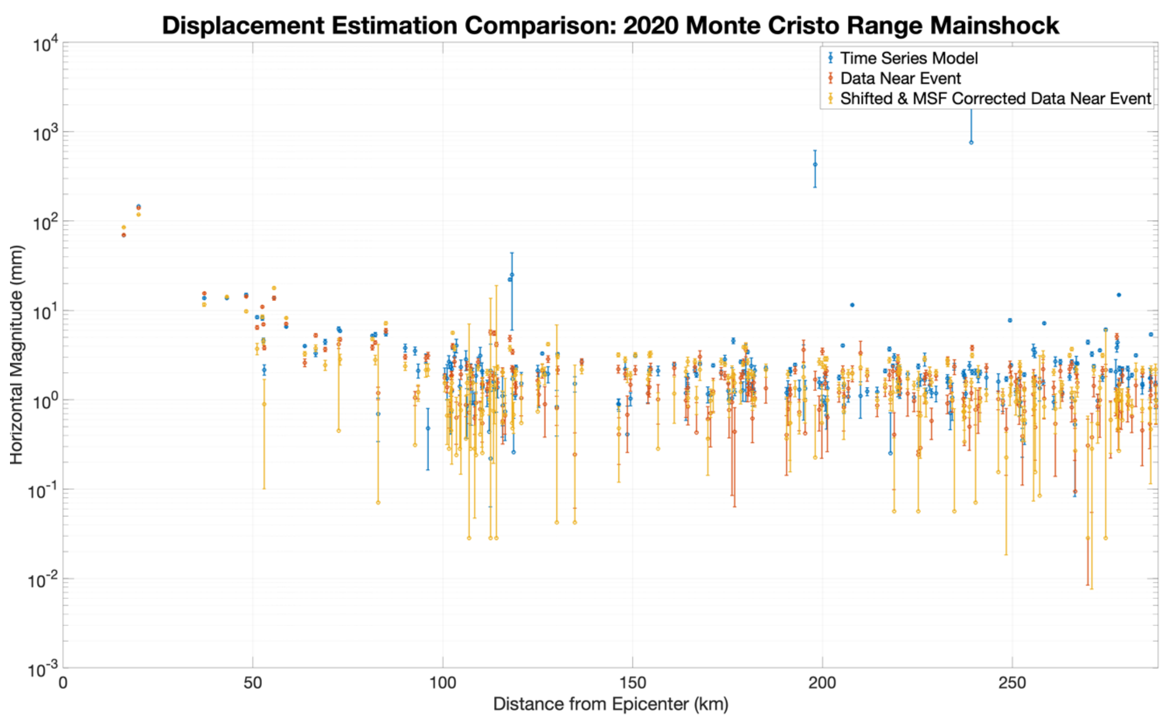

Figure 4.8. Comparison of the horizontal magnitudes produced by the Time Series Model (blue), Data Near Event (red) and median spatial filtered and aligned (yellow) displacement estimates for the 2020 M6.5 Monte Cristo Range mainshock. TSM horizontal magnitudes exhibit greater scatter likely caused by its bias from unmodeled signals.

4.5.6 Defining an Earthquake's Radius of Influence

When designing a strategy for estimating coseismic displacement, I assume that stations in the GPS Mega-Network nearest to the epicenter are more likely to have measurable deformation. Rather than estimating displacements after every M≥5.5 earthquake for all stations worldwide, which can degrade the quality of the position time series unaffected by the earthquake (Williams et al., 2003; Gazeaux et al., 2013), I need a method to identify GPS time series potentially affected by earthquake deformation before displacement estimation occurs. In general, the extent of coseismic displacement regionally depends on the source parameters, slip complexity, and Earth structure and response. However, I here define a simple method that can be easily and uniformly applied to all event station pairs, which uses only the magnitude (M) to approximate the extent of the area affected by an earthquake.

To define a radius of influence (r_0) for a given magnitude, I must first understand how the size of displacements decrease as distance from the epicenter increases. I empirically design the mathematical expression between magnitude and distance by relating horizontal displacement magnitudes for earthquakes 5.5≤M≤9.1 to an experimentally large radius that ideally encompasses many GPS stations. Horizontal displacement magnitudes were estimated per GPS station for each earthquake cataloged by the USGS NEIC (U.S. Geological Survey, 2017) between 1 Jan. 1994 and 20 Apr. 2022.

To estimate r_0, I begin with the observation that horizontal displacement magnitudes decrease with distance from the epicenter until reaching a distance beyond which the displacement magnitude levels taper off. I call this distance from the epicenter the empirical r_0 for the earthquake. To characterize the fall of displacement with distance, each event used to define r_0 is required to have at least one data point near the epicenter and a minimum of three displacements total. I use the combined model of DNE 24-hour, DNE 5-minute, and TSM displacements from a provisionally large radius surrounding each event (Fig. 4.9A). East and north components outside the near-field are median spatial filtered to reduce the effect of outliers and noise before computing horizontal displacement magnitudes and plotting them against distance from the epicenter (Fig. 4.9B and Fig. 4.10). Because each station has its own site effects and GPS station spacing is non-homogenous throughout the earthquake regions, stations are binned into 10 km distance intervals from the epicenter. The goal is to locate the distance where 90% of displacement magnitudes in each bin stabilize to the level of displacements magnitudes in the far-field. Beyond this distance, displacement magnitudes were considered unlikely to be affected by coseismic deformation. The threshold magnitude value is specific to each event's characteristics. For example, the Ridgecrest earthquake magnitudes stabilized below a threshold of 2.2 mm, which corresponded to an r_0 distance of 571 km (Fig. 4.9B). This process was repeated for the other earthquakes (e.g., Fig. 4.10) to establish their empirical r_0 values. Details about the earthquakes, threshold magnitudes, and their radii can be found in Sup. Table S4.1.

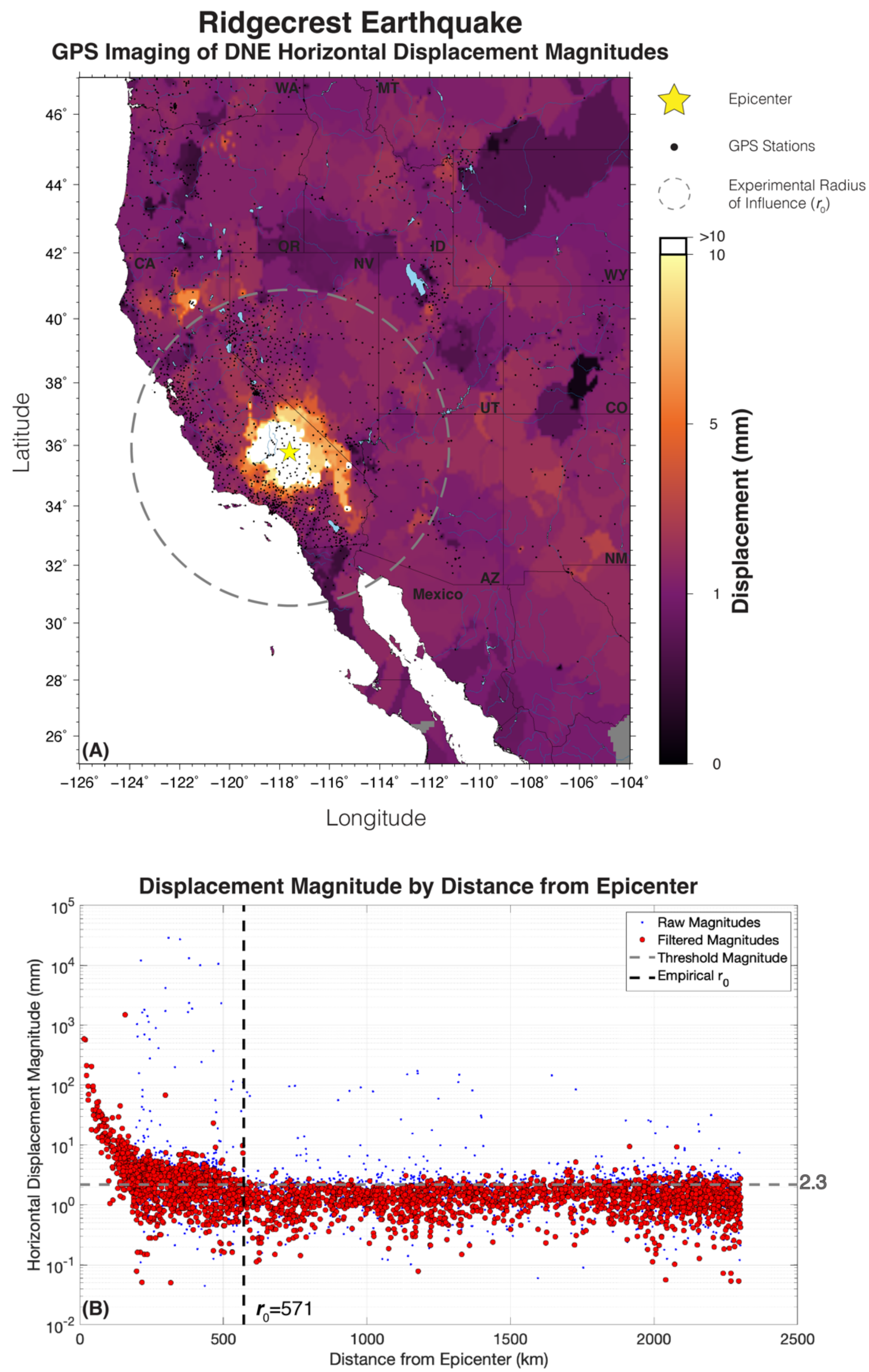

Figure 4.9. Horizonal displacement magnitudes within an experimentally large radius plotted for the M7.1 Ridgecrest earthquake. **(A)** GPS Imaging of displacements

compared to the empirical r_0 (gray circle). **(B)** Displacements (blue dots) and filtered displacements (red dots) as a function of distance from epicenter. Approximate threshold magnitude (horizontal gray dashed line) is used to find the empirical r_0 (vertical black dashed line) for each respective earthquake magnitude.

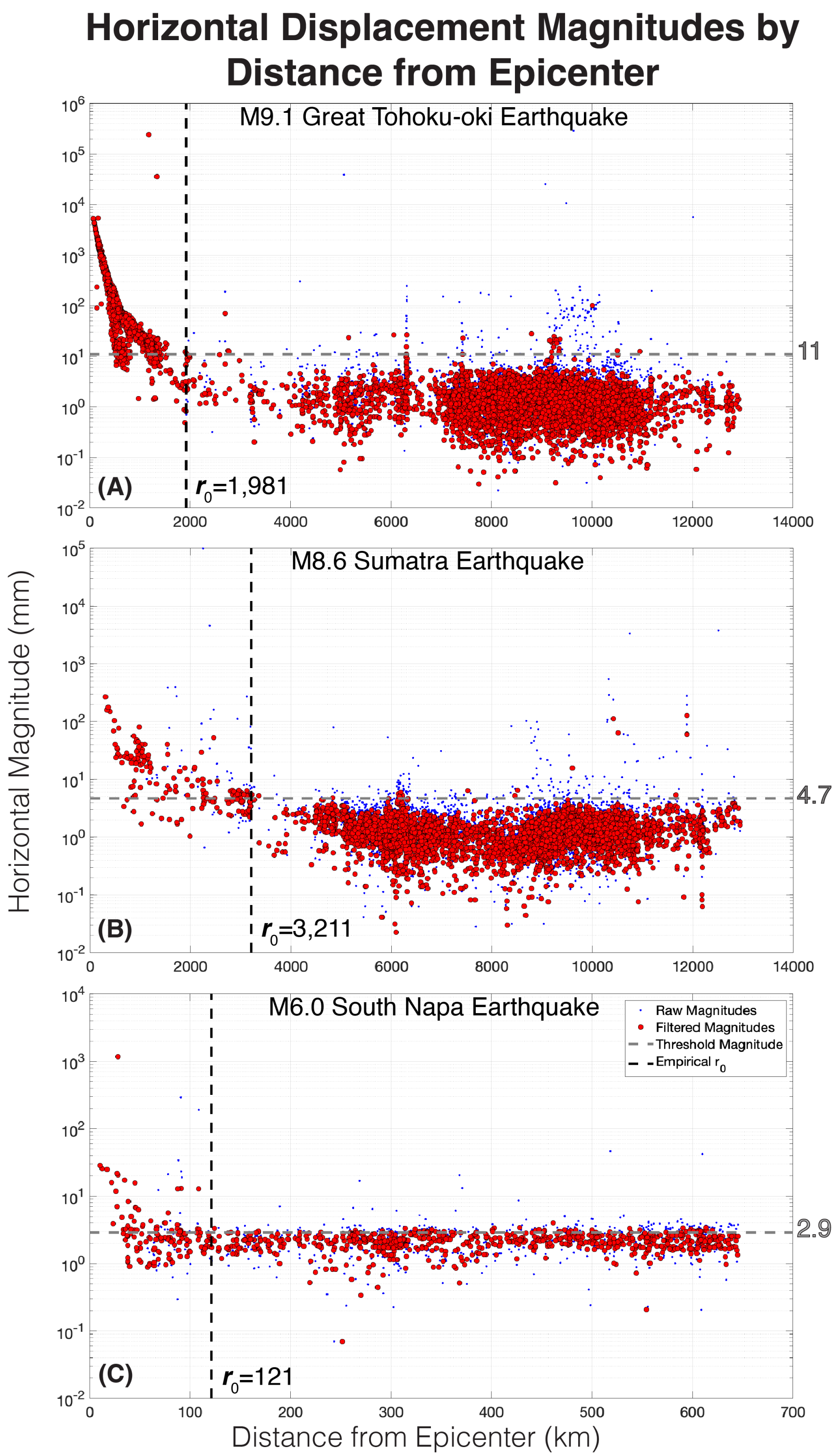

Figure 4.10. Median spatial filtered horizontal displacement magnitudes (red) are compared to their raw counterparts (blue) and plotted against distance from epicenter for

the **(A)** M9.1 Great Tohoku-oki, **(B)** M8.6 Sumatra, and **(C)** M6.0 South Napa earthquakes. Threshold magnitude (horizontal gray dashed line) is used to find the empirical r_0 (vertical black dashed line) for each earthquake.

Of the 14,059 earthquakes in the NEIC dataset, only 337 fulfilled the criteria required to define the empirical r_0 distances. I design the radius of influence equation with these 337 earthquakes to describe the relationship between significant coseismic displacement, distance from the epicenter, and the magnitude of the earthquake observed in the data. I chose an exponential function of the form $r_0 = 10^{(A*M + B)}$ inspired by the form of moment magnitude in Hanks and Kanamori (1979). The empirical r_0 for each earthquake was plotted against magnitude, and a function was fit to the data within a 95% confidence interval to estimate *A* and *B* (Fig. 4.11). The influence of earthquake depth on the curve fit was analyzed and 294 earthquakes were considered to be at shallow depths (0 km≤z≤70 km), 40 earthquakes at moderate depths (70 km<z≤300 km), and only 3 were deep earthquakes (300 km<z<750 km). I also examined the effect that the largest magnitude events had on the curve fit and determined that events M>8.6 had empirical radii that were considerably lower compared to the rest of the dataset. Taken as a whole, I decided the best fit equation would require a function below which all empirical r_0 values in the dataset were encompassed. That equation is described as a piecewise function:

Eq. 4.3
$$r_0 = \begin{cases} 10^{0.5M-0.79}, & 5.5 \leq M \leq 8.6 \\ 3235.94, & M > 8.6 \end{cases}$$

Where M is magnitude. Some stations within the radius may have displacements not significantly different than zero. The displacement size may be effectively zero, e.g., if the station is a large enough distance from the earthquake epicenter or in a direction along the azimuth of rupture, but this still places strong constraints on where most of the coseismic displacement occurs. Using a simple circular domain defined by r_0, with a piecewise ceiling placed on earthquakes M>8.6, is practical because for most applications displacements need not be estimated beyond this distance, saving computing time and resources.

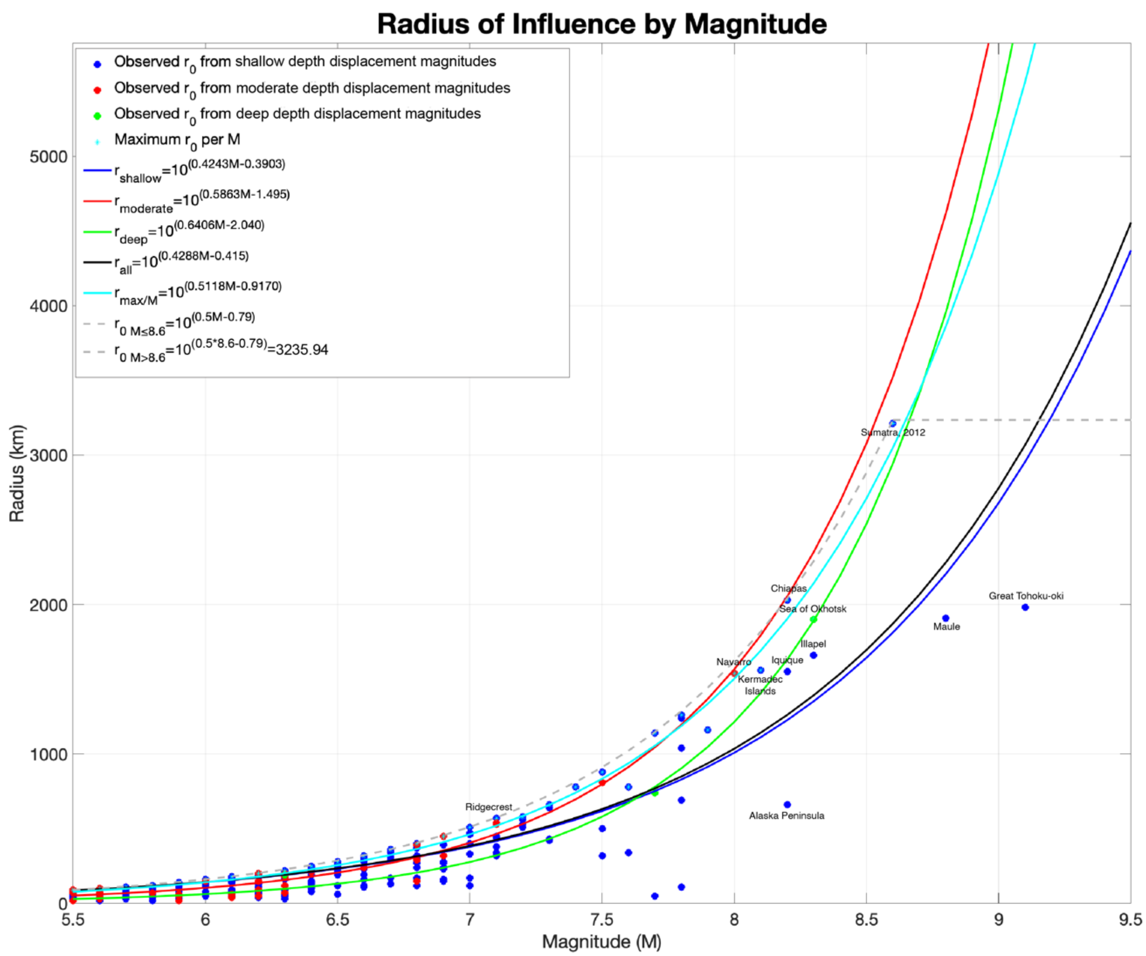

Figure 4.11. Empirical r_0 values for 337 earthquakes (dots). An exponential function of the form $r_0 = 10^{(A*M + B)}$ was fit to earthquake radii for all (black), shallow depth (blue), moderate depth (red), deep (green) earthquakes, and the maximum r_0 per magnitude with M>8.6 excluded (cyan). The best fit curve (gray dash) was defined by fitting the cyan curve to coefficients so that all r_0 values below the curve are contained (see Eq. 4.3).

4.5.7 *Evaluating the Radius of Influence*

To test the relation described in Eq. 4.3, I applied r_0 to the 2020 M6.5 Monte Cristo Range mainshock. I tested the ability of r_0 for M=6.5 to encompass displacements by interpolating the horizontal magnitude of the combined DNE 24-hour, DNE 5-minute, and TSM displacement estimates to a grid using the GPS Imaging technique (Fig. 4.9A and Fig. 4.12). The GPS Imaging technique reduces speckle noise from displacements during interpolation and enhances the signal of small displacements in the far-field by applying weighted median spatial filtering (Hammond et al., 2016). In this instance, I apply it to the horizontal magnitudes of displacement for each earthquake to build the interpolated grid of coseismic displacement.

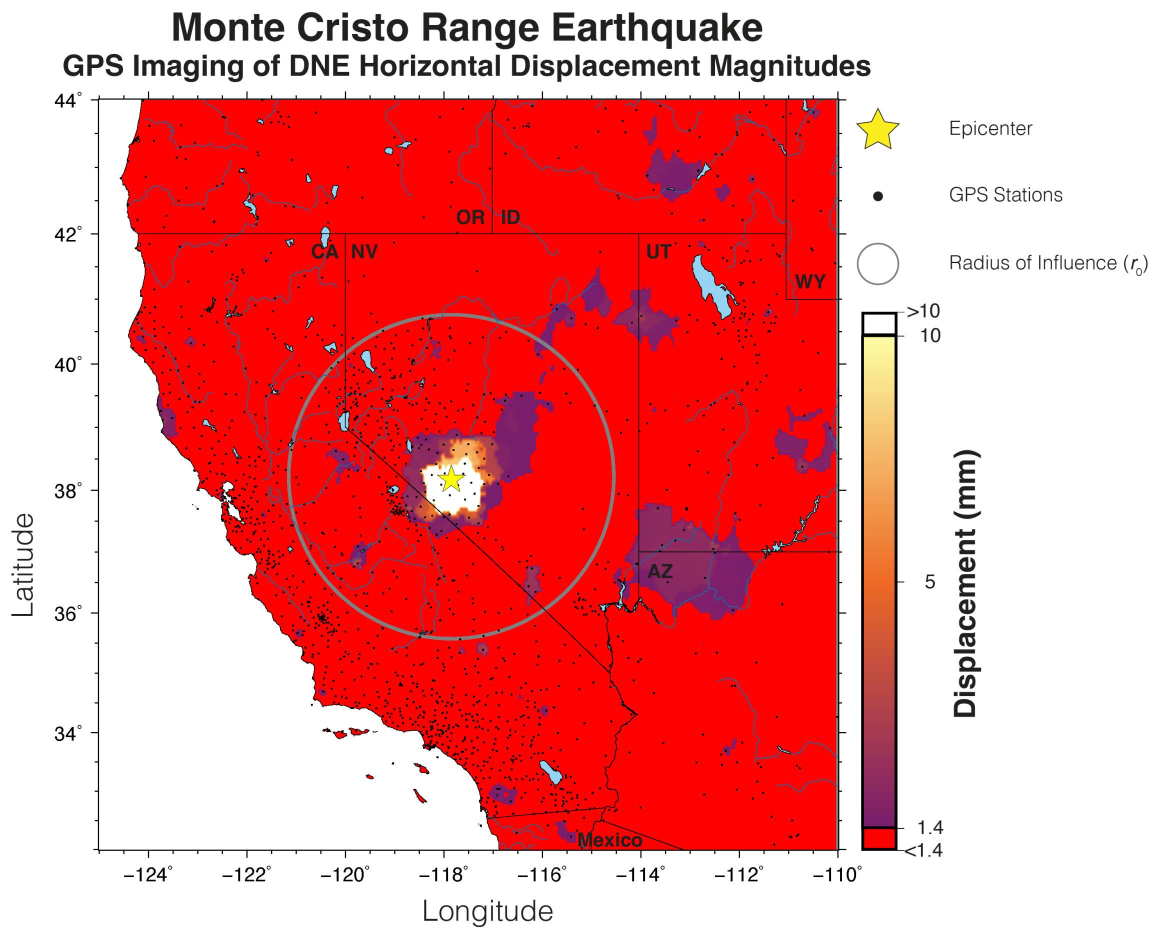

Figure 4.12. Testing the empirical radius of influence (r_0) using interpolated horizontal displacement magnitudes for the 2020 M6.5 Monte Cristo Range mainshock and radius of influence r_0=288 km. Dots represent station locations, and magnitudes less than the threshold value of 1.45 mm (Sup. Table S4.1) are shown with a saturated color bar (red).

The results (Fig. 4.12) show significant displacements in the near and medium field tapering to lower values in the far-field until no convincing signal exists near the boundary of the interpolated image. Here, I delineate where displacements are above a 1.45 mm horizontal displacement magnitude threshold, i.e., where horizontal magnitudes stabilized (Sup. Table S4.1). Slightly elevated magnitude values ≥1.45 mm at the northeast boundary of the radius are believed to be a border artifact from station density sparsity when constraining the interpolation in this region. Elevated values outside r_0 are attributable to localized site effects/station design that are unlikely to be related to coseismic movement. Based on this result, I consider that radius r_0 successfully encompassed all displacements affected by coseismic deformation without extending so far out that it degraded time series unaffected by the event.

4.6 Results

4.6.1 Improved Estimates Using the Data Near Event Model

The TSM strategy can estimate coseismic displacements for all position time series in the GPS Mega-Network, but when data are available within the 60-day time window surrounding an earthquake event, I prefer the DNE model. The DNE estimates match expected patterns of rupture described by the focal mechanisms for both the Ridgecrest and Monte Cristo Range earthquakes while providing data with fewer outliers and lower uncertainties than the TSM model (Fig. 4.5 and Fig. 4.7). When aligned to the more stable TSM reference frame and after applying median spatial filtering, the DNE strategy provides offsets with reduced noise and fewer outliers in the far-field. This makes for a cleaner displacement pattern that is more representative of coseismic Earth deformation. When the DNE model is used in conjunction with TSM to maximize available data, GPS displacements and their associated uncertainties improve knowledge of the scope, distribution, and style of coseismic Earth deformation.

4.6.2 Applying the Radius of Influence to Earthquake Events Worldwide

Of the 14,059 earthquakes cataloged by the USGS NEIC (U.S. Geological Survey, 2017) between 1 Jan. 1994 and 20 Apr. 2022, 3,451 earthquakes (24.5%) had at least one GPS station with displacements estimated, and hence were considered to have available displacement estimates in the GPS Mega-Network. To identify which GPS stations may be affected by a given earthquake, and thus have earthquake displacements marked in the GPS position time series, I apply Eq. 4.3 to each event M≥5.5 to determine their r_0. Times when the station possibly experienced coseismic deformation are flagged for displacement estimation if the station-to-epicenter distance is less than r_0. The radius of influence flagged 7,486 unique GPS stations (Fig. 4.1B) as being possibly affected by at least one of the 14,059 earthquakes (Fig. 4.1A), with these sites requiring 63,122 total coseismic displacement estimates.

This information comprises part of NGL's database that identifies two types of displacement events; those associated with GPS station equipment changes, as previously mentioned, and those from earthquakes derived from the radius of influences for each earthquake for its worldwide GPS data holdings. The earthquake records in the database include site name, date, estimated radius of earthquake zone of influence, distance from epicenter to station, magnitude, and the unique USGS event ID for each earthquake. As of 20 Apr. 2022, there were a total of 77,488 potential equipment-related and earthquake displacements in the time series (http://geodesy.unr.edu/NGLStationPages/steps.txt). The records in this file are called "potential displacements" because it is not necessarily the case that the time series are observed to have a significant displacement at these times.

4.7 Discussion

4.7.1 Fundamental Properties of the GPS Global Earthquake Catalog

To be considered to have available displacement estimates, an earthquake is required to have at least one GPS station located within its radius of influence at a point in time when data are available both before and after the event, allowing for successful estimation by one of the three strategies. Even if a displacement was estimated to be zero within uncertainty, it was still considered to have available displacement estimates because that data places a constraint on the physical source. Earthquakes $M \geq 7$ have the greatest likelihood of available displacement estimates over time with 302 of 394 (76.6%) $7 \leq M < 8$ earthquakes with available estimations by GPS since 1994, and all earthquakes (100%) $M \geq 8$ with available displacements estimates (Fig. 4.15). Earthquakes $M < 7$ were less likely to have available displacement estimates in the GPS Mega-Network. This is in part because their radius of influence is smaller, but also because many of the lower magnitude earthquakes originated at mid-oceanic ridges where there is a lack of GPS instrumentation. However, the number of lower magnitude earthquakes with estimated displacement availability is much greater for on-shore earthquakes (shown in maroon in Fig. 4.14 and Fig. 4.15, and Fig. 4.16B). The number of earthquakes with available displacement estimates exceed the number that occur on land (18%) for all earthquakes M≥6.

The number of earthquakes with displacement estimates available increased over time for all magnitudes as the GPS Mega-Network grew (Fig. 4.15 and Fig. 4.16). The percentage of total earthquakes with available displacement estimates in the GPS Mega-Network compared to the NEIC catalog exceeded single-digits four years after the inception of NGL's data holdings (Fig. 4.15). Available displacement estimate percentage has not dropped below 20% since 2005, approximately the beginning of the great GPS expansion (Fig. 4.13), and has an average estimated displacement availability percentage of 34% since 2004 (Fig. 4.15). The best year on record so far for available displacement estimates is 2015 at 46%, however, it's noteworthy that the availability percentage depends on the magnitude of the events that occurred. Years with a greater number of M≥7 earthquakes are more likely to have a greater total number of events with available displacement estimates in the GPS Mega-Network. Looking closer at the catalog comparison by magnitude per year, there is a noticeable increase in earthquakes M≤6.5 with available displacement estimates in the GPS Mega-Network starting in 2004, with events 5.5≤M<6.5 improving from single digits in the first five years of the data holdings to averaging over 28% in the years following 2004 (Fig. 4.16). Earthquakes 6.5≤M<7.5 follow a similar pattern of improvement as the GPS Mega-Network grows (Fig. 4.16). All earthquakes M≥8 have available displacement estimates in the GPS Mega-Network since the inception of NGL's data holdings.

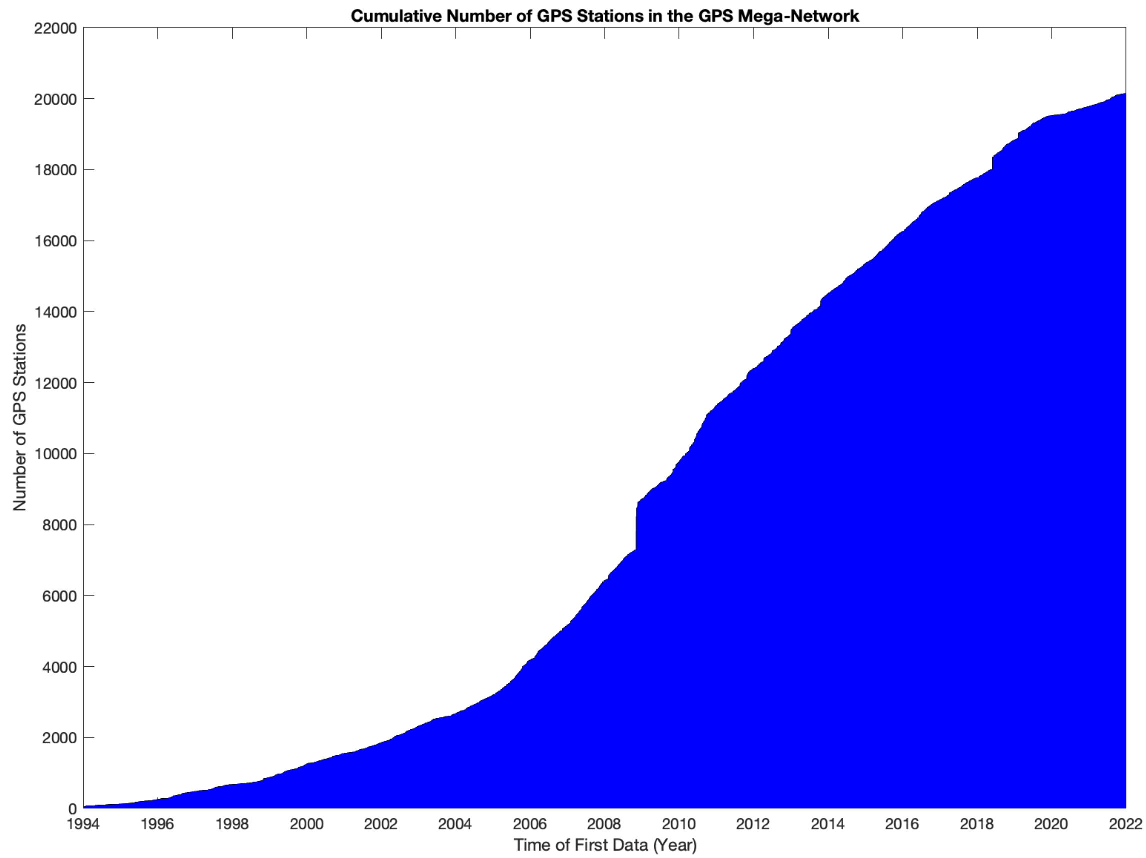

Figure 4.13. Cumulative number of GPS stations in the GPS Mega-Network as a function of time. The great GPS network expansion ramped up especially from 2004–2009 with the addition of UNAVCO's Network of the Americas.

The number of on-shore earthquakes cataloged by the USGS NEIC (U.S. Geological Survey, 2017) has remained fairly consistent since 1994, with an average of 92 on-shore earthquakes M≥5.5 occurring per year. Up until 2004, the number of earthquakes with available displacement estimates did not exceed the number of earthquakes that occurred on-shore. After the great GPS network expansion (Fig. 4.13), the number of earthquakes with estimated displacements expanded past the number of earthquakes that occurred on-shore and captured a greater number of offshore events for all magnitudes (Fig. 4.15).

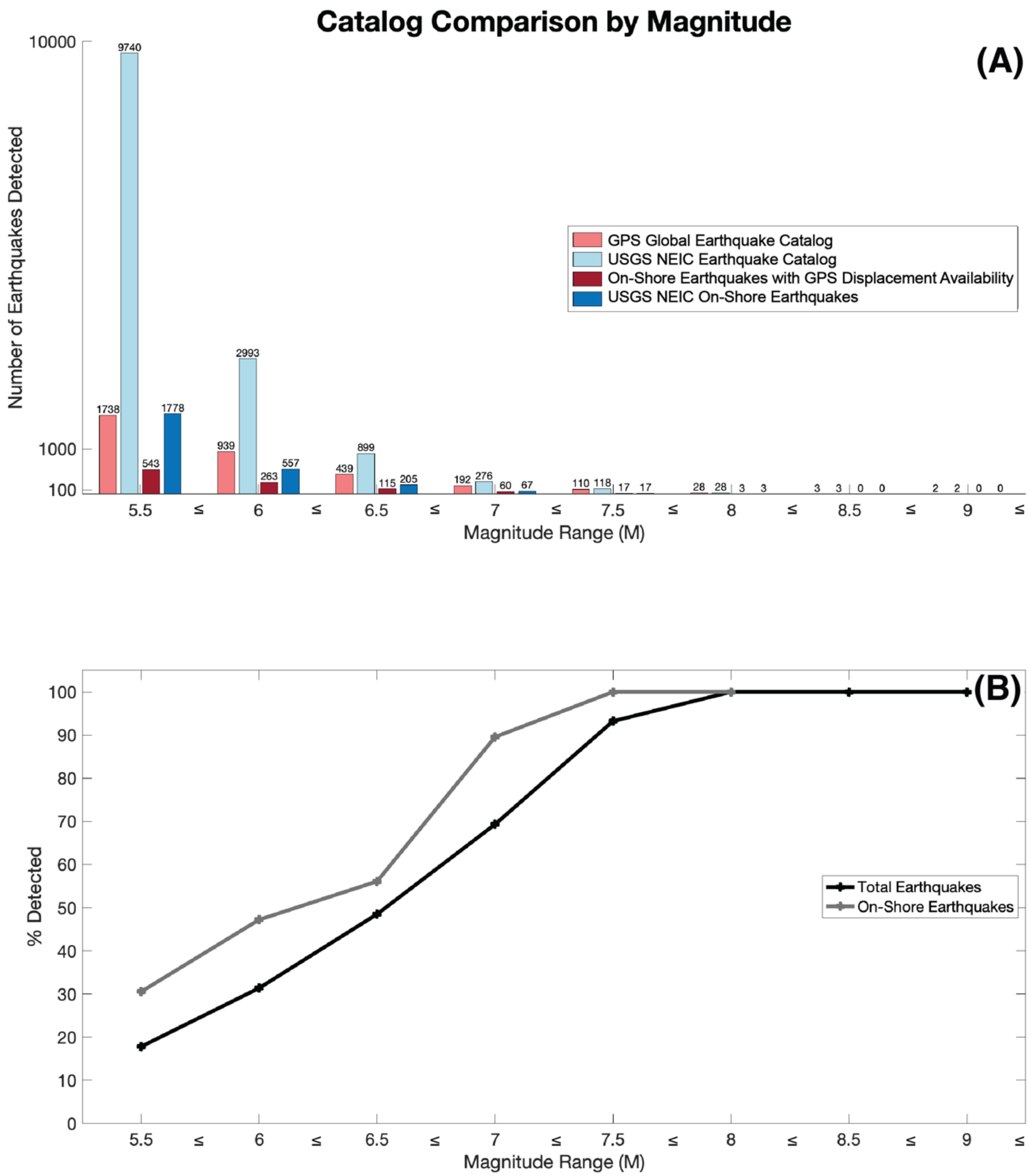

Figure 4.14. Catalog comparison by magnitude. Magnitude range is listed on horizontal axis label by minimum bound, e.g., 5.5 contains magnitudes 5.5≤M<6, etc. **(A)** Bar

charts of global earthquakes by magnitude having at least one displacement calculated for GPS time series in total (red), and on-shore (maroon), and all earthquakes occurring between 1 Jan. 1994 and 20 Apr. 2022 identified by the USGS NEIC (light blue) (U.S. Geological Survey, 2017) and those that occurred on-shore (dark blue). **(B)** Percentage of earthquakes with estimated displacement availability by the GPS Global Earthquake Catalog vs. the USGS NEIC Earthquake Catalog (U.S. Geological Survey, 2017) as a function of magnitude and subdivided by total earthquakes (black) compared to only earthquakes with epicenters located on-shore (gray).

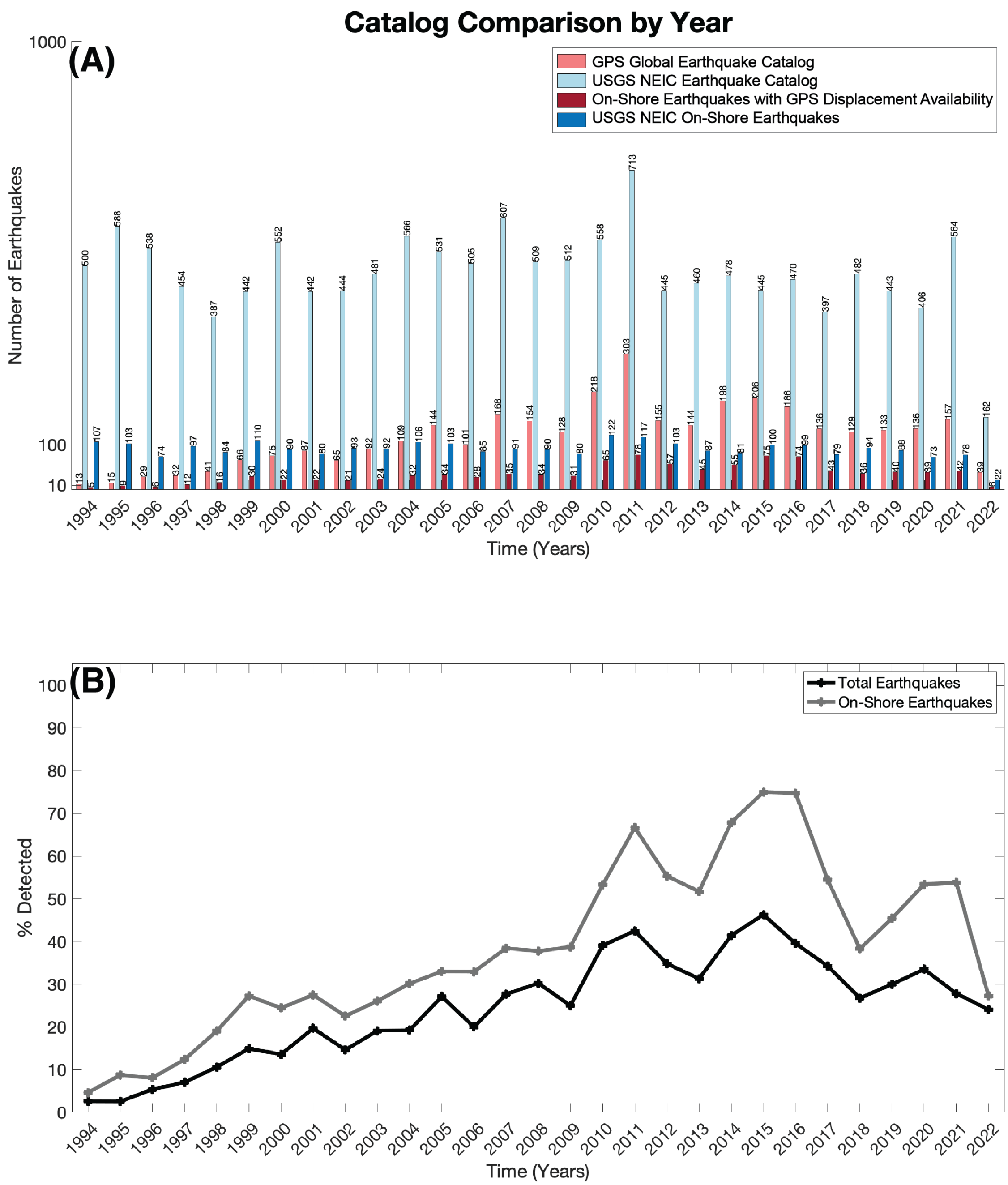

Figure 4.15. Catalog comparison by year. **(A)** Number of earthquakes having at least one displacement calculated from GPS time series in total (red) and on-shore (maroon) as a function of time vs. all earthquakes occurring between 1 Jan. 1994 and 20 Apr. 2022 identified by the USGS NEIC (light blue) (U.S. Geological Survey, 2017) and those that

occurred on-shore (dark blue). The peak in 2011 is attributable to the Great Tohoku-oki earthquake sequence. **(B)** Percentage of earthquakes with estimated displacement availability by the GPS Global Earthquake Catalog vs. the USGS NEIC Earthquake Catalog (U.S. Geological Survey, 2017) as a function of year and subdivided by total earthquakes (black) compared to only earthquakes with epicenters located on-shore (gray).

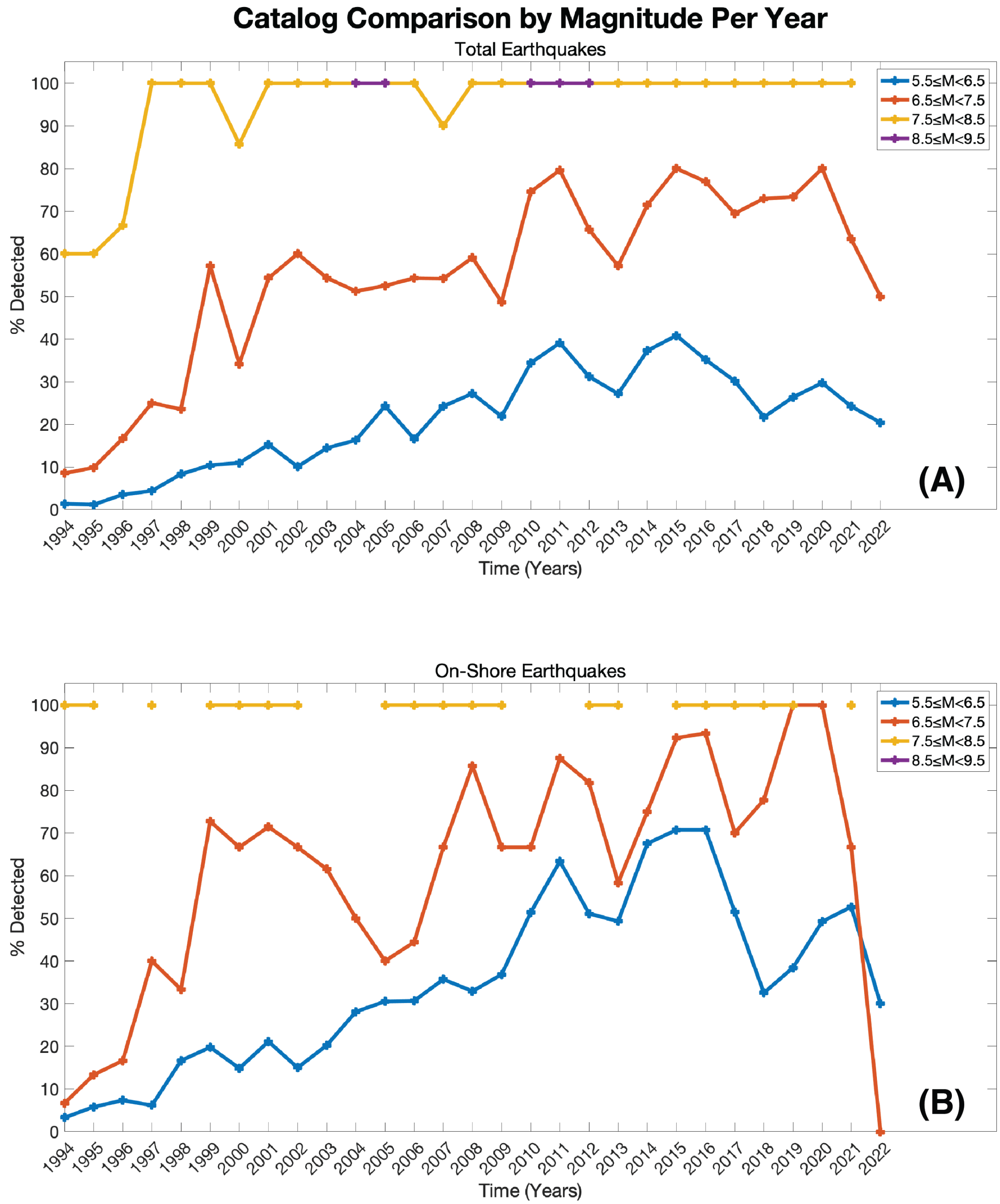

Figure 4.16. Percentage of earthquakes with estimated displacement availability by the GPS Global Earthquake Catalog vs. the USGS NEIC Earthquake Catalog (U.S. Geological Survey, 2017) occurring between 1 Jan. 1994 and 20 Apr. 2022 as a function of magnitude. The GPS Global Earthquake Catalog is comprised of stations having at

least one displacement calculated from GPS time series. Overall trend shows improvement in available displacement estimates over time for all earthquakes **(A)** and on-shore earthquakes **(B)**. Smaller magnitude earthquakes ($5.5 \leq M < 6.5$ in blue, $6.5 \leq M < 7.5$ in orange) occur at a higher rate, but their epicenters are often offshore, explaining their comparably lower estimated displacement availability percentage. Larger magnitude earthquakes ($7.5 \leq M < 8.5$ in yellow, $8.5 \leq M < 9.5$ purple) occur less frequently, leading to breaks in the time series, and typically originate offshore.

Because GPS stations must be within the radius of influence for an earthquake to be considered to have estimated displacement availability, there is still a sizable deficit between the GPS Global Earthquake Catalog and the USGS NEIC Earthquake Catalog (U.S. Geological Survey, 2017). If the earthquake has a small magnitude and/or is located offshore, it is less likely to have displacement estimates for a GPS station. The largest magnitude events nearly always have available displacement estimates in the GPS Mega-Network, however, especially later in the global expansion of GPS networks which ramped up after 2004 (Fig. 4.13). For every $M \geq 8$ modern event, there are hundreds to thousands of GPS time series with available displacement estimates for the earthquake. The larger the magnitude of the earthquake, the greater number of displacements estimated per event (Fig. 4.17). Though $M < 6$ has the greatest number of earthquakes with available displacement estimates in the GPS Mega-Network Global Earthquake Catalog, there are on average only 8 GPS stations with estimated displacements per event. Compare that to the number for the average $M \geq 9$ which is 952. The 2011 M9.1 Great Tohoku-oki earthquake alone had 1,701 stations with displacements estimated, indicating that the date and station distribution in Japan around the event also contributes to the total number of GPS stations affected.

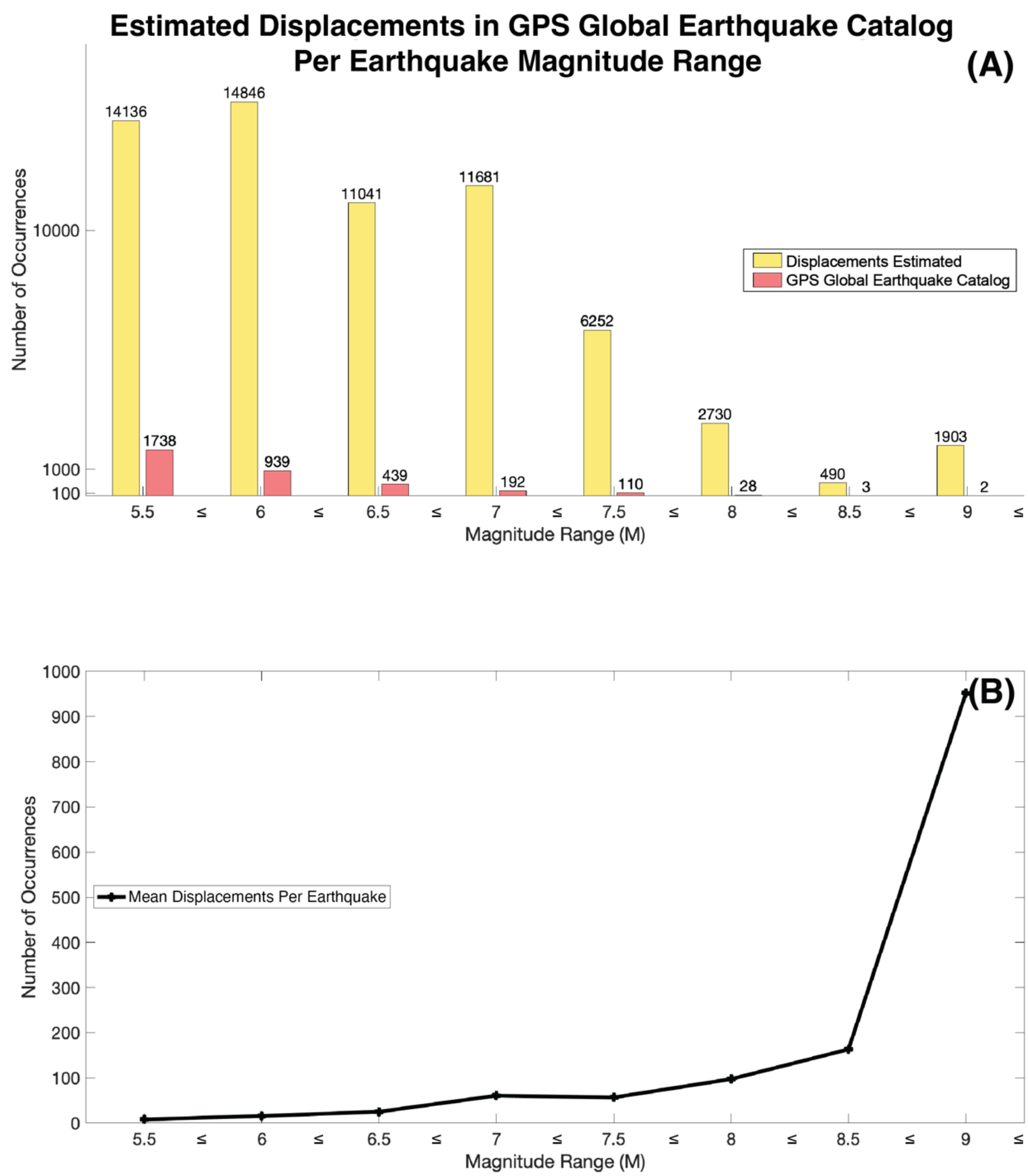

Figure 4.17. Displacements estimated per earthquake available in the GPS Global Earthquake Catalog according to magnitude. Magnitude range is listed on horizontal axis

label by minimum bound, e.g., 5.5 contains magnitudes 5.5≤M<6, etc. **(A)** Number of GPS stations with displacements estimated (yellow) by magnitude and number of earthquakes with available displacement estimates in the GPS Mega-Network Global Earthquake Catalog (red) occurring between 1 Jan. 1994 and 20 Apr. 2022. **(B)** The black curve represents the mean number of displacements estimated per event as a function of magnitude.

In addition to the GPS Global Earthquake Catalog, I identified stations in the GPS Mega-Network flagged for earthquake displacements from statistics collected during displacement estimation. Of the 20,224 GPS stations in the GPS Mega-Network as of 20 Apr. 2022, 7,486 stations account for the 63,122 potential displacements flagged for earthquake displacement estimation (Fig. 4.1B). Since GPS stations are often installed near plate boundaries and in tectonically active regions, this is a reasonable result, but this information could also serve other interests beyond earthquake applications. Knowing which GPS time series are serially affected by earthquake displacements is important to geodesists designing regional and global reference frames. By having a database of stations impacted by earthquake displacements, and the size of the displacements, geodesists have a source for which stations to correct for or potentially avoid when defining tectonic plate stable interiors.

4.7.2 Future Prospects for the Growth and Utility of the GPS Global Earthquake Catalog

Coseismic displacements provide fundamental constraints on processes that drive earthquakes in the solid Earth system. By refining coseismic displacement analysis, I can improve the accuracy and utility of data that reveals properties of the earthquake source, physical process, scope, style and direction of surface deformation. However, future improvements are predicated on the availability of data. Currently, these strategies are limited to continuous or semi-continuous GPS networks processed by the NGL as part of the GPS Mega-Network, and do not include stations in campaign GPS networks, seafloor geodetic stations, or stations in networks for which the data are not openly available. Furthermore, these estimation strategies will only be viable with the continued sharing of data and operation of stations within the GPS Mega-Network.

Though earthquake estimated displacement availability by stations within the GPS Mega-Network has improved over time, there is still a sizeable deficit between earthquakes detected by the USGS NEIC Earthquake Catalog (U.S. Geological Survey, 2017) and estimated displacement availability by the GPS Global Earthquake Catalog. As previously discussed, this is especially true for lower magnitude earthquakes. The continued growth and maintenance of the GPS Mega-Network can help close this gap. Though there were large strides in network growth, especially in the mid-2000s, the rate of station growth has decreased in recent years (Fig. 4.13). Increasing the number of operational GPS stations in the network will help improve the resolvability of earthquakes by increasing the number of available coseismic displacement estimates.

Similarly, when discussing the limitations on the GPS Mega-Network, the distinction between on-shore and offshore events is the single most important factor. Though many offshore earthquakes are powerful enough to have on-shore GPS instrumentation located within the radius of influence, the difference in average available displacements estimates for offshore earthquakes is huge. To address this, I see sea-floor geodesy (Bürgmann and Chadwell, 2014; Newman et al., 2021) as having special potential to eventually place a greater number of sensors near those sources. Potentially fiber optic cables that cross the seafloor could allow distributed acoustic sensing of strain (Zumberge et al., 2018; Jousset et al., 2018) near spreading centers where available displacement estimates are currently very low, and in the future could illuminate more of the seafloor. Additionally, on-shore GPS instrumentation and data communications infrastructure will become less expensive and continue to fill the gaps in remote locations where station coverage is currently sparse. Access to low-latency telemetry capabilities have been identified as a near-frontier priority by NSF geophysical facility instrumentation portfolio review (Arrowsmith et al., 2021).

Finally, I hope future earthquake research will continue to collaborate with other complementary data sources from this and other catalogs including, for example, seismic data from moment tensor catalogs (Ekstrom et al., 2012), InSAR products from the Geodetic Centroid (gCent) Catalog (Shea and Barnhart, 2022), catalogs of afterslip (Churchill et al., 2022), and geologic data (e.g., USGS, 2023). At minimum, cross-referencing global earthquake data from the seismology, geology, and geodesy disciplines can help solve big science questions about these dynamic Earth processes.

4.8 Conclusions

This analysis quantifies the sensitivity and scope of coverage that continuous GPS networks have for capturing coseismic displacements. I present an analysis method for estimating coseismic displacements that uses an adaptable time window to optimize the balance between uncertainty and data misfit, and a hierarchical strategy to account for gaps and non-linear signals in GPS time series data before and after earthquakes. These methods improve coseismic displacement estimates and support objective application of the algorithm to the entirety of the GPS Mega-Network affected by earthquake events $M \geq 5.5$.

I define an empirical earthquake radius of influence that is a function of magnitude and ensures most all stations potentially having coseismic displacements are considered for displacement estimation. The adaptable time window customizes the interval of data used to estimate each displacement potentially affected by an event to account for missing data, other earthquake events within the time window, and reduces the possible influence of postseismic relaxation during larger magnitude events. Additionally, the hierarchical strategy that prioritizes the DNE 24-hour and DNE 5-minute solutions over the TSM solutions using the data closest to the earthquake allows for the estimation of multiple coseismic displacements within a 24-hour period.

These strategies improve estimates of coseismic displacements for all GPS stations in the global GPS Mega-Network, which has implications for earthquake science, crustal deformation studies, and defining future geodetic reference frames. GPS stations that experience coseismic movement give details about the direction and style of deformation that can further describe the earthquake source. Other researchers who might treat earthquakes as an unwanted disturbance while examining other crustal signals can also use the displacements to "correct" the GPS positions. Knowing which stations are affected by earthquakes and having estimates of that deformation can pinpoint relatively stable stations for reference frames. The GPS Global Earthquake Catalog identifies which earthquakes have available GPS displacement estimates, which GPS stations may be influenced by earthquakes, and allows for comparisons to or integrations with seismic catalogs.

4.9 Acknowledgements

I am grateful to NASA for supporting this research with grants NNX16AK89G and 80NSSC19K1044 via its Earth Surface and Interior program. Support for the MAGNET GPS network operations came from the USGS Geodetic Networks program grant G20AC00046. GPS data processes was performed with the GipsyX software provided by the Jet Propulsion Laboratory. Some figures in this manuscript were made with the Generic Mapping Tools software (Wessel et al., 2013). The seismic catalog of earthquake data was obtained from: https://www.usgs.gov/natural-hazards/earthquake-hazards/earthquakes. The GPS analysis would not have been possible without the network maintenance and open access of data archives by those in the International GNSS Service and all GPS network administrators. I particularly thank the following

networks/archives: AFREF; Alabama Department of Transportation (DOT) CORS network, USA; Albuquerque Real Time GNSS Network, USA; Arpa Piemonte, Italy; Asia Pacific Crustal Monitoring System; AZGPS, USA; BANIAN, New Caledonia; BARD, USA; Bureau of Meteorology, Australia; Canary GNSS Center; CDDIS, USA; CORS-NGS, USA; Danish GPS Center; DPGA-TUDELFT, The Netherlands; EarthScope Plate Boundary Observatory, USA; ERVA Instituto Geográfico Valencia, Spain; EUREF; FLEPOS, Belgium; FREDNET, Italy; GEODAF, Italy; Geodetic Observatory Pecny, Czech Republic; GeoNet, New Zealand; Geosciences Australia; Gobierno de la Rioja, Spain; GREF-BKG; GPSCOPE-INSU; HEMUNET, Bulgaria; Idaho National Laboratory, USA; Indiana DOT CORS network, USA; Institut Teknologi Bandung, Indonesia; Instituto Geográfico Nacional, Spain; Instituto Geográfico Nacional, Tommy Guardia, Panama; Instituto Geográfico Português, Portugal; Instituto Technologico Agrario, Castilla y León, Spain; Institut Cartogràfic de Catalunya, Spain; Iowa DOT CORS network, USA; KARA, USA; Laboratorio di Topografia, Università degli Studi di Perugia, Italy; LATPOS, Latvia; Leica Kazachstan; Leica SmartnetUSA, USA and Canada; Lower Colorado River Authority, USA; MAGNA-ECO, Colombia; Maine DOT CORS network, USA; Mesa county, Colorado, USA; Missouri DOT CORS network, USA; Minnesota DOT CORS network, USA; Natural Resources Canada; NEGAR, California Institute of Technology, USA; MAGNET/NEARNET, University of Nevada, Reno, USA; NOANET, Greece; Norwegian Mapping Authority; OLGGPS, Austria; Pacific Geoscience Centre, Canada; Pacific GPS Facility, Hawaii, USA; Panamá Canal Authority, Panama; PANGA, USA; Provincia di Milano, Italy; RAMSAC, Argentina; RBMC Brasil; Red Andaluza de Poscionamiento, Spain; Red de Estaciones de

Referencia GNSS de Euskadi, Spain; Red Extremeña de Posicionamiento, Spain; Red de Geodesia Activa de Navarra, Spain; Regione Autonoma Friuli Venezia Giulia, Italy; Regione Campania, Italy; Regione Emilia Romagna, Italy; Regione Liguria, Italy; Región de Murcia, Spain; REMOS, Venezuela; RENAG, France; Réseau GNSS Permanent, France; Rete GPS Veneto, Italy; RING-INGV, Italy; SCIGN, USA; Seiler Instrument Company, USA; SONEL, France; SOPAC, USA; South Carolina DOT CORS network, USA; STPOS Bolzano, Italy; SUGAR-NTU, Singapore; Survey of Israel; TAZNET, Arizona, USA; Texas DOT CORS network, USA; TGRef, Romania; TRIGNET, South Africa; UNAVCO, USA; Universidad de Cantabria; Universidad Politécnica de Madrid, Spain; University of Western Ontario, Canada; Washoe County, Nevada, U.S; and West Virginia DOT CORS network, USA. I appreciate the efforts of all Principal Investigators in the following NSF-funded networks or regions for making data available: Africa Array, Andes (CAP), Antarctica (PoleNet), Bhutan, Calabria, CocoNET, Costa Rica, El Salvador, Eritrea, Ethiopia, Greenland (PoleNet), Hawaii, Iceland, Mediterranean, Mexico, Mid-America (GAMA), New Zealand (SAGE). Pamir Mountains, Puerto Rico, Rio Grande Rift, SUOMI-NET, Tanzania, and Uganda. Many thanks to these Institutions/networks which provided raw RINEX data not otherwise available: British Columbia Active Control System, Canada; British Isles continuous GNSS Facility (BIGF), U.K.; Central-Asian Institute for Applied Geosciences (CAIAG), Kirghistan; GEONET, GSI, Japan; Instituto Nacional de Estadística y Geografía (INEGI), Mexico; Jeddah Municipality, Saudia Arabia; Las Vegas Valley Water Authority, Nevada, USA; Leica SmartNet, Australia; Leica SmartNet (ITALPOS), Italy; Linz AG, Austria; LITPOS, Lithuania; Low-Latitude Ionospheric Sensor Network (LISN); Provincia

Autonoma di Trento, Italy; REGNA, Servicio Geográfico Militar, Uruguay; and WALCORS, Belgium.

4.10 References

Arrowsmith, R. J., Brodsky, E., Cooper, C. M., Elliot, J. L., Fee, D., Fischer, K., Hammond, W. C., La Femina, P., Lekic, V., Wang, H., & Worthington, L.L. (2021) Recommendations for enabling Earth science through NSF's geophysical facility - A portfolio review of EAR seismology and geodesy instrumentation, Report from the NSF SAGE/GAGE Instrumentation Portfolio Review Committee, https://www.nsf.gov/geo/adgeo/ear-instrumentation-review/AC-GEO-EAR-Instrumentation-Portfolio-Review-April-2021%20Report.pdf.

Altamimi, Z., Rebischung, P., Métivier, L., & Collilieux, X. (2016). ITRF2014: A new release of the International Terrestrial Reference Frame modeling nonlinear station motions. *J. of Geophys. Res. - Solid Earth*, *121*(8), 6109-6131.

Amos, C. B., Audet, P., Hammond, W. C., Bürgmann, R., Johanson, I. A., & Blewitt, G. (2014). Uplift and seismicity driven by groundwater depletion in central California. *Nature*, *509*(7501), 483–486, https://doi.org/10.1038/nature13275.

Argus, D. F., Fu, Y., & Landerer, F. W. (2014). Seasonal variation in total water storage in California inferred from GPS observations of vertical land motion. *Geophys. Res. Lett.*, *41*, 1971–1980, https://doi.org/10.1002/2014GL059570.

Beavan, J., Denys, P., Denham, M., Hager, B., Herring, T., & Molnar, P. (2010). Distribution of present-day vertical deformation across the Southern Alps, New Zealand, from 10 years of GPS data. *Geophys. Res. Lett.*, *37*, L16305, https://doi.org/10.1029/2010GL044165.

Becker, T. W., Lowry, A. R., Faccenna, C., Schmandt, B., Borsa, A., & Yu, C. (2015). Western US intermountain seismicity caused by changes in upper mantle flow. *Nature*, *524*(7566), 458-461.

Bennett, R., & Hreinsdóttir, S. (2007). Constraints on vertical crustal motion for long baselines in the central Mediterranean region using continuous GPS. *Earth Planet. Sci. Lett.*, *257*, 419–434.

Bertiger, W., Bar-Sever, Y., Dorsey, A., Haines, B., Harvey, N., Hemberger, D., et al. (2020). GipsyX/RTGx, a new tool set for space geodetic operations and research. *Advances in Space Research*, *66*(3), 469–489, https://doi.org/10.1016/j.asr.2020.04.015.

Blewitt, G., Kreemer, C., Hammond, W.C., & Gazeaux, J. (2016). MIDAS Robust Trend Estimator for Accurate GPS Station Velocities Without Step Detection. *J. Geophys. Res. - Solid Earth*, *121*(30), 2054-2068, https://doi.org/10.1002/2015JB012552.

Blewitt, G., Kreemer, C., Hammond, W. C., & Goldfarb, J. M. (2013). Terrestrial reference frame NA12 for crustal deformation studies in North America. *Journal of Geodynamics*, *72*, 11-24.

Blewitt, G., Hammond, W. C., & Kreemer, C. (2009). Geodetic observation of contemporary deformation in the northern Walker Lane: 1. Semipermanent GPS strategy. *Geol. Soc. Am.*, *447*, 1-15.

Blewitt, G., Hammond, W.C., & Kreemer, C. (2018). Harnessing the GPS data explosion for interdisciplinary science. *Eos*, *99*, https://doi.org/10.1029/2018EO104623.

Boehm, J., Werl, B., & Schuh, H. (2006). Troposphere mapping functions for GPS and very long baseline interferometry from European Centre for Medium-Range Weather Forecasts operational analysis data. *J. of Geophys. Res. - Solid Earth*, *111*, B02406, https://doi.org/10.1029/2005JB003629.

Borsa, A., Agnew, D.C., & Cayan, D.R. (2014). Ongoing drought-induced uplift in the western United States. *Science*, *345*(6204), 1587-1590.

Bürgmann, R., & Chadwell, D. (2014). Seafloor geodesy. *Annu. Rev. Earth Planet. Sci.*, *42*, 509-534.

Bürgmann, R. & Dresen, G. (2008). Rheology of the lower crust and upper mantle: Evidence from rock mechanics, geodesy, and field observations. *Annu. Rev. Earth Planet. Sci.*, *36*, 531-567.

Churchill, R. M., Werner, M. J., Biggs, J., & Fagereng, Å. (2022). Afterslip moment scaling and variability from a global compilation of estimates. *J. Geophys. Res. - Solid Earth*, *127*(4), e2021JB023897.

Dzurisin, D., Lisowski, M., & Wicks, C. W. (2009). Continuing inflation at Three Sisters volcanic center, central Oregon Cascade range, USA, from GPS, leveling, and InSAR observations. *Bulletin of Volcanology*, *71*(10), 1091-1110, https://doi.org/10.1007/s00445-009-0296-4.

Ekström, G., M. Nettles, A.M. Dziewoński, (2012). The global CMT project 2004–2010: Centroid-moment tensors for 13,017 earthquakes. *Phys. Earth Planet. Int.*, *200*, 1-9, https://doi.org/10.1016/j.pepi.2012.04.002.

Fialko, Y. (2004), Evidence of fluid-filled upper crust from observations of postseismic deformation due to the 1992 Mw7.3 Landers earthquake. *J. of Geophys. Res. - Solid Earth*, *109*, B08401, https://doi.org/10.1029/2004JB002985.

Flesch, L.M., Holt, W. E. Haines, A.J., & Shen-Tu, B. (2000), Dynamics of the Pacific–North American Plate Boundary in the Western United States. *Science*, *287*, 834-836.

Freed, A. (2005). Earthquake triggering by static, dynamic, and postseismic stress transfer. *Annu. Rev. Earth Planet. Sci.*, *33*, 335–367, https://doi.org/10.1146/annurev.earth.33.092203.122505.

Freed, A. M., Bürgmann, R., & Herring, T. (2007). Far-reaching transient motions after Mojave earthquakes require broad mantle flow beneath a strong crust. *Geophysical Research Letters*, *34*(19).

Fu, Y., & Freymueller, J. T. (2012). Seasonal and long-term vertical deformation in the Nepal Himalaya constrained by GPS and GRACE measurements. *J. of Geophys. Res. - Solid Earth*, *117*, B03407, https://doi.org/10.1029/2011JB008925.

Gazeaux, J., Williams, S., King, M., Bos, M., Dach, R., Deo, M., … & Webb, F. H. (2013). Detecting offsets in GPS time series: First results from the detection of offsets in GPS experiment. *J. Geophys. Res. - Solid Earth*, *118*(5), 2397-2407: https://doi.org/10.1002/jgrb.50152.

Gomberg, J., Beeler N.M., & Blanpied M.L. (1998). Earthquake triggering by transient and static deformations. *J. Geophys. Res. - Solid Earth*, *103*, 24411–24426.

Hammond, W. C., Blewitt, G., & Kreemer, C. (2016). GPS Imaging of vertical land motion in California and Nevada: Implications for Sierra Nevada uplift. *J. Geophys. Res. - Solid Earth*, *121*, 7681–7703, https://doi.org/10.1002/2016JB013458.

Hanks, T. C., & Kanamori, H. (1979). A moment magnitude scale. *J. Geophys. Res. - Solid Earth*, *84*(B5), 2348-2350.

Harris, R.A., & Simpson, R.W. (1998). Suppression of large earthquakes by stress shadows; a comparison of Coulomb and rate-and-state failure. *J. Geophys. Res. - Solid Earth*, *103*, 24439–24451.

Jousset, P., Reinsch, T., Ryberg, T. *et al.* (2018). Dynamic strain determination using fibre-optic cables allows imaging of seismological and structural features. *Nat. Commun.*, *9*, 2509, https://doi.org/10.1038/s41467-018-04860-y.

Kreemer C., Haines, A. J., Holt, W.E., Blewit, G., & Lavallee, D. (2000), On the determination of a global strain rate model. *Earth Planets Space, 52*, 765–770.

Kreemer, C., Blewitt, G., & Davis, P. M. (2020). Geodetic Evidence for a Buoyant Mantle Plume Beneath the Eifel Volcanic Area, NW Europe. *Geophysical Journal International*, *222*(2), 1316-1332, https://doi.org/10.1093/gji/ggaa227.

Kreemer, C., Hammond, W.C., Blewitt, G. (2018). A robust estimation of the 3D intraplate deformation of the North American plate from GPS. *J. Geophys. Res. - Solid Earth*, *123*, 4388-4412*,* https://doi.org/10.1029/2017JB015257.

Larochelle, S., Chanard, K., Fleitout, L., Fortin, J., Gualandi, A., Longuevergne, L., ... & Avouac, J. P. (2022). Understanding the geodetic signature of large aquifer systems: Example of the Ozark Plateaus in central United States. *J. Geophys. Res. - Solid Earth*, *127*(3), e2021JB023097, https://doi.org/10.1002/essoar.10507870.1.

Martens, H.R., M. Simons, S. Owen, L Rivera, (2016), Observations of ocean tidal load response in South America from subdaily GPS positions. *Geophysical Journal International*, *205*, 1637–1664, https://doi.org/10.1093/gji/ggw087.

Mazzotti, S., Lambert, A., Courtier, N., Nykolaishen, L., & Dragert, H. (2007). Crustal uplift and sea level rise in northern Cascadia from GPS, absolute gravity, and tide gauge data. *Geophys. Res. Lett.*, *34*, L15306, https://doi.org/10.1029/2007GL030283.

Métivier, L., Collilieux, X., Lercier, D., Altamimi, Z., & Beauducel, F. (2014). Global coseismic deformations, GNSS time series analysis, and earthquake scaling laws. *J. Geophys. Res. - Solid Earth*, *119*(12), 9095-9109.

Montgomery-Brown, E. K., Wicks, C. W., Cervelli, P. F., Langbein, J. O., Svarc, J. L., Shelly, D. R., ... & Lisowski, M. (2015). Renewed inflation of long valley caldera, California (2011 to 2014). *Geophys. Res. Lett.*, *42*(13), 5250-5257. https://doi.org/10.1002/2015GL064338.

Newman, A., Bartlow, N., Schmidt, D., Charlevoix, D., Foster, J., Haines, B., Araki, E., Bürgmann, R., Chadwick, W., Gomberg, J., Melgar, D., Wallace, L. Wei, M., & Wilcock, W. (2021). Future Directions in Seafloor Geodesy 2021 Community Workshop held 6-9 Apr. 2021, Online.

Overacker, J., Hammond, W. C., Blewitt, G., & Kreemer, C. (2022). Vertical land motion of the High Plains Aquifer region of the United States: Effect of aquifer confinement style, climate variability, and anthropogenic activity. *Water Resources Research*, e2021WR031635, https://doi.org/10.1029/2021WR031635.

Peltier, W. R., Argus, D. F., & Drummond, R. (2015). Space geodesy constrains ice age terminal deglaciation: The global ICE-6G_C (VM5a) model. *J. Geophys. Res. - Solid Earth*, *120*, 450–487, https://doi.org/10.1002/2014JB011176.

Perfettini, H., & Avouac, J.P. (2004). Stress transfer and strain rate variations during the seismic cycle. *J. of Geophys. Res. - Solid Earth*, *109*, B06402, https://doi.org/10.1029/2003JB002917.

Pollitz, F. F. (1997). Gravitational viscoelastic postseismic relaxation on a layered spherical Earth. *J. of Geophys. Res. - Solid Earth*, *102*(B8), 17921-17941.

Sen, P. K. (1968). Estimates of the regression coefficient based on Kendall's tau, *J. Am. Stat. Assoc.*, *63*, 1379–1389.

Shea, H. N., & Barnhart, W. D. (2022). The Geodetic Centroid (gCent) Catalog: Global earthquake monitoring with satellite imaging geodesy. *Bulletin of the Seismological Society of America*, *112*(6), 2946-2957.

Stein, R. S. (1999). The role of stress transfer in earthquake occurrence. *Nature*, *402*(6762), 605-609.

Theil, H. (1950). A rank-invariant method of linear and polynomial regression analysis, *Indag. Math.*, *12*, 85–91.

Tregoning, P., Burgette, R., McClusky, S. C., Lejeune, S., Watson, C. S., & McQueen, H. (2013). A decade of horizontal deformation from great earthquakes. *J. of Geophys. Res. - Solid Earth*, *118*(5), 2371-2381.

Tregoning, P., & Watson, C. (2009). Atmospheric effects and spurious signals in GPS analyses, *J. of Geophys. Res. - Solid Earth*, *114*, B09403, https://doi.org/10.1029/2009JB006344.

U.S. Geological Survey, Earthquake Hazards Program (2017). Advanced National Seismic System (ANSS) Comprehensive Catalog of Earthquake Events and Products: Various, https://doi.org/10.5066/F7MS3QZH.

U.S. Geological Survey. (2023). Quaternary fault and fold database for the United States, accessed at: https://www.usgs.gov/natural-hazards/earthquake-hazards/faults.

Wessel, P., & Smith, W. H. F. (1996). A global, self-consistent, hierarchical, high-resolution shoreline database. *J. of Geophys. Res. - Solid Earth*, *101*(B4), 8741–8743.

Wessel, P., Smith, W. H. F., Scharroo, R., Luis, J., & Wobbe, F. (2013). Generic Mapping Tools: Improved version released. *Eos, Trans. Am. Geophys. Union*, *94*, 409–410, https://doi.org/10.1002/2013EO450001.

Williams, S. D. (2003). Offsets in global positioning system time series. *J. of Geophys. Res. - Solid Earth*, *108*(B6), https://doi.org/10.1029/2002JB002156.

Zumberge, M. A., Hatfield, W., & Wyatt, F. K. (2018). Measuring seafloor strain with an optical fiber interferometer. *Earth and Space Science, 5*(8), 371-379, https://doi.org/10.1029/2018EA000418.

4.11 Supplemental Tables

Table S4.1. Earthquakes used in the empirical estimation of the radius of influence (r_0).

M	Date	USGS NEIC Earthquake ID	Approximate Location	Epicenter Latitude (°)	Epicenter Longitude (°)	Depth (km)	r_0 (km)	Horizontal Displacement Magnitude Threshold (mm)
9.1	11-Mar-2011	official20110311054624120_30	Great Tohoku Earthquake, Japan	38.2970	142.3730	29.0	1921	11.02
8.8	27-Feb-2010	official20100227063411530_30	Quirihue, Chile	-36.1220	-72.8980	22.9	1911	6.02
8.6	11-Apr-2012	official20120411083836720_20	Sumatra, Indonesia	2.3270	93.0630	20.0	3211*	4.69
8.3	24-May-2013	usb000h4jh	Sea of Okhotsk	54.8920	153.2210	598.1	1901*	2.40
8.3	16-Sep-2015	us20003k7a	Illapel, Chile	-31.5729	-71.6744	22.4	1661	2.39
8.2	1-Apr-2014	usc000nzvd	Iquique, Chile	-19.6097	-70.7691	25.0	1551	4.24
8.2	8-Sep-2017	us2000ahv0	Chiapas, Mexico	15.0222	-93.8993	47.4	2031*	2.79
8.2	29-Jul-2021	ak0219neiszm	Alaska Peninsula, USA	55.3635	-157.8876	35.0	661	3.48
8.1	4-Mar-2021	us7000dflf	Kermadec Islands, New Zealand	-29.7228	-177.2794	28.9	1561*	7.06
8.0	26-May-2019	us60003sc0	Navarro, Peru	-5.8119	-75.2697	122.6	1541*	5.48
7.9	23-Jan-2018	us2000cmy3	Chiniak, Alaska, USA	56.0039	-149.1658	14.1	1161*	2.19
7.8	15-Jul-2009	usp000gz8j	Te Anau, New Zealand	-45.7620	166.5620	12.0	1241	1.04
7.8	28-Oct-2012	usp000juhz	Prince Rupert, Canada	52.7880	-132.1010	14.0	1041	3.16
7.8	25-Apr-2015	us20002926	Bharatpur, Nepal	28.2305	84.7314	8.2	111	1.69
7.8	16-Apr-2016	us20005j32	Muisne, Ecuador	0.3819	-79.9218	20.6	1261*	2.87
7.8	13-Nov-2016	us1000778i	Amberley, New Zealand	-42.7373	173.0540	15.1	691	4.41
7.8	22-Jul-2020	us7000asvb	Perryville, Alaska, USA	55.0715	-158.5960	28.0	1261*	1.78
7.7	11-Mar-2011	usp000hvpg	Kamaishi, Japan	38.0580	144.5900	18.6	1141*	35.54
7.7	14-Aug-2012	usp000jq9h	Poronaysk, Russia	49.8000	145.0640	583.2	741	2.65
7.7	3-Apr-2014	usc000p27i	Iquique, Chile	-20.5709	-70.4931	22.4	51	11.10
7.6	5-Sep-2012	usp000jrsw	Hojancha, Costa Rica	10.0850	-85.3150	35.0	341	3.13

7.6	19-Oct-2020	us6000c9hg	Sand Point, Alaska, USA	54.6020	-159.6258	28.4	781*	1.76
7.5	5-Jan-2013	ak0138esnzr	Edna Bay, Alaska, USA	55.2280	-134.8591	8.7	501	3.53
7.5	10-Jan-2018	us1000c2zy	Barra Patuca, Honduras	17.4825	-83.5200	19.0	881*	2.41
7.5	5-Dec-2018	us1000i2gt	Tadine, New Caledonia	-21.9496	169.4266	10.0	321	3.37
7.5	22-Feb-2019	us2000jlfv	Palora, Ecuador	-2.1862	-77.0505	145.0	811	1.70
7.4	23-Jun-2020	us6000ah9t	Santa María Xadani, Mexico	15.8861	-96.0077	20.0	781*	3.25
7.3	9-Mar-2011	usp000hvhj	Ōfunato, Japan	38.4350	142.8420	32.0	661*	2.15
7.3	27-Aug-2012	usp000jqvm	El Triunfo, El Salvador	12.1390	-88.5900	28.0	431	4.12
7.3	7-Dec-2012	usp000jwjn	Ōfunato, Japan	37.8900	143.9490	31.0	641	2.76
7.3	16-Mar-2022	us6000h519	Namie, Japan	37.7302	141.5951	59.9	421	3.54
7.2	15-Jun-2005	usp000dt25	Big Lagoon, California, USA	41.2920	-125.9530	16.0	511	3.34
7.2	16-Aug-2005	usp000dxe2	Ishinomaki, Japan	38.2760	142.0390	36.0	531	2.95
7.2	4-Apr-2010	ci14607652	Delta, Baja California, Mexico	32.2862	-115.2953	10.0	581*	2.55
7.2	18-Apr-2014	usb000pq41	Coyuquilla Norte, Mexico	17.3970	-100.9723	24.0	561	2.12
7.1	9-Aug-2009	usp000h04j	Ōyama, Japan	33.1670	137.9440	292.0	531	2.90
7.1	7-Apr-2011	usp000hzf6	Ishinomaki, Japan	38.2760	141.5880	42.0	321	2.53
7.1	23-Oct-2011	usp000j9rr	Van, Turkey	38.7210	43.5080	18.0	381	1.73
7.1	25-Mar-2012	usp000jgsw	Constitución, Chile	-35.2000	-72.2170	40.7	541	1.24
7.1	24-Jan-2016	ak01613v15nv	Pedro Bay, Alaska, USA	59.6204	-153.3392	125.6	541	3.05
7.1	19-Sep-2017	us2000ar20	Matzaco, Mexico	18.5499	-98.4887	48.0	341	3.51
7.1	30-Nov-2018	ak018fcnsk91	Point MacKenzie, Alaska, USA	61.3464	-149.9552	46.7	451	4.67
7.1	6-Jul-2019	ci38457511	Ridgecrest, California, USA	35.7695	-117.5993	8.0	571*	2.19
7.1	13-Feb-2021	us6000dher	Namie, Japan	37.7265	141.7751	44.0	441	2.61
7.0	19-Jul-2008	usp000gcjg	Namie, Japan	37.5520	142.2140	22.0	471*	3.17
7.0	26-Feb-2010	usp000h7qu	Katsuren-haebaru, Japan	25.9300	128.4250	25.0	121	2.35
7.0	3-Sep-2010	usp000hk46	Methven, New Zealand	-43.5220	171.8300	12.0	171	2.40

7.0	10-Jul-2011	usp000j4gp	Ishinomaki, Japan	38.0340	143.2640	23.0	461	3.74
7.0	16-Sep-2015	us20003k7w	Illapel, Chile	-31.5622	-71.4262	28.4	511	10.13
7.0	15-Apr-2016	us20005iis	Kumamoto, Japan	32.7906	130.7543	10.0	401	3.38
7.0	1-Sep-2016	us10006jbi	Gisborne, New Zealand	-37.3586	179.1461	19.0	331	2.38
7.0	30-Oct-2020	us7000c7y0	Néon Karlovásion, Greece	37.8973	26.7838	21.0	471*	2.33
7.0	20-Mar-2021	us7000dl6y	Ishinomaki, Japan	38.4515	141.6477	43.0	401	2.37
6.9	14-Feb-2008	usp000fyw4	Methóni, Greece	36.5010	21.6700	29.0	271	2.09
6.9	7-May-2008	usp000g5rx	Hasaki, Japan	36.1640	141.5260	27.0	391	2.73
6.9	13-Jun-2008	usp000g9h6	Mizusawa, Japan	39.0300	140.8810	7.8	161	2.15
6.9	2-Feb-2013	usc000f03a	Obihiro, Japan	42.7700	143.0920	107.0	451*	3.07
6.9	9-Feb-2013	usc000f4ij	Yacuanquer, Colombia	1.1350	-77.3930	145.0	321	1.49
6.9	1-Apr-2014	usc000nzwm	Iquique, Chile	-19.8927	-70.9455	28.4	391	3.42
6.9	24-May-2014	usb000r2hc	Kamariótissa, Greece	40.2893	25.3889	6.4	231	2.97
6.9	11-Nov-2015	us10003x8t	Coquimbo, Chile	-29.5067	-72.0068	12.0	151	12.20
6.9	21-Nov-2016	us10007b88	Namie, Japan	37.3931	141.3870	9.0	281	1.75
6.9	24-Apr-2017	us10008kce	Valparaíso, Chile	-33.0375	-72.0617	28.0	321	3.46
6.9	1-May-2021	us7000dz5t	Onagawa Chō, Japan	38.1997	141.5973	43.0	281	1.96
6.9	11-Oct-2021	ak021d1u1nos	Chignik, Alaska, USA	56.2954	-156.5810	51.6	241	3.04
6.8	15-Oct-2007	usp000fqks	Te Anau, New Zealand	-44.7960	167.5530	18.0	241	4.10
6.8	23-Jul-2008	usp000gczp	Morioka, Japan	39.8020	141.4640	108.0	151	3.13
6.8	11-Sep-2008	usp000ggu8	Obihiro, Japan	41.8920	143.7540	25.0	271	1.09
6.8	10-Mar-2014	nc72182046	Indianola, California, USA	40.8287	-125.1338	16.4	401*	3.57
6.8	12-May-2015	us20002et4	Ōfunato, Japan	38.9056	142.0317	35.0	171	2.21
6.8	29-May-2015	ak0156uj8rk3	Ugashik, Alaska, USA	56.5940	-156.4301	72.6	291	3.14
6.8	7-Nov-2015	us10003vgt	Ovalle, Chile	-30.8796	-71.4519	46.0	301	4.30
6.8	25-Oct-2018	us1000hhb1	Lithakiá, Greece	37.5203	20.5565	14.0	291	3.49
6.8	1-Aug-2019	us60004yps	San Antonio, Chile	-34.2364	-72.3102	25.0	371	1.90

6.8	3-Jun-2020	us6000a4yi	San Pedro de Atacama, Chile	-23.2740	-68.4677	112.0	391	2.11
6.8	1-Sep-2020	us7000bfjr	Vallenar, Chile	-27.9686	-71.3062	21.0	121	4.44
6.8	11-Jan-2022	us7000gavu	Nikolski, Alaska, USA	52.3415	-167.7554	20.0	321	6.42
6.7	8-Jan-2006	usp000e7u3	Kýthira, Greece	36.3110	23.2120	66.0	131	1.88
6.7	25-Mar-2007	usp000f7b5	Nanao, Japan	37.3360	136.5880	8.0	361*	19.82
6.7	14-Feb-2011	usp000hugg	Constitución, Chile	-35.3800	-72.8340	21.0	341	5.06
6.7	22-Jun-2011	usp000j3k6	Miyako, Japan	39.9550	142.2050	33.0	351	3.58
6.7	16-Sep-2011	usp000j84y	Miyako, Japan	40.2730	142.7790	30.0	171	4.70
6.7	17-Apr-2012	usp000jj3u	Hacienda La Calera, Chile	-32.6250	-71.3650	29.0	351	1.58
6.7	16-Mar-2014	usc000ndnj	Iquique, Chile	-19.9807	-70.7022	20.0	341	3.44
6.7	16-Feb-2015	usb000tpvj	Miyako, Japan	39.8558	142.8808	23.0	361*	2.53
6.7	17-Sep-2015	us20003kfv	Illapel, Chile	-31.5173	-71.8040	23.0	311	7.70
6.7	14-Jan-2016	us10004ebx	Shizunai-furukawachō, Japan	41.9723	142.7810	46.0	351	1.98
6.7	20-Jan-2019	us2000j6hy	Coquimbo, Chile	-30.0404	-71.3815	63.0	291	2.68
6.6	16-Jul-2007	usp000fg9t	Kashiwazaki, Japan	37.5350	138.4460	12.0	281	12.16
6.6	20-Dec-2007	usp000fuvt	Gisborne, New Zealand	-39.0110	178.2910	20.0	301	2.24
6.6	12-Aug-2009	usp000h093	Tateyama, Japan	32.8210	140.3950	53.0	231	4.66
6.6	14-Jul-2010	usp000hf8z	Cañete, Chile	-38.0670	-73.3100	22.0	121	3.18
6.6	11-Mar-2011	usp000hvuu	Ōtsuchi, Japan	39.2410	142.4630	25.7	321*	157.05
6.6	11-Apr-2011	usp000hzq8	Ishikawa, Japan	37.0010	140.4010	11.0	111	4.83
6.6	12-Oct-2013	usb000kbn7	Kíssamos, Greece	35.5142	23.2523	40.0	311	2.01
6.6	11-Apr-2014	usc000pgsi	Belén, Nicaragua	11.6420	-85.8779	135.0	241	3.01
6.6	21-Sep-2015	us20003mi0	Illapel, Chile	-31.7275	-71.3792	35.0	191	5.84
6.6	1-Jun-2016	us20005zt1	Sungai Penuh, Indonesia	-2.0967	100.6654	50.0	231	1.48
6.6	30-Oct-2016	us1000731j	Preci, Italy	42.8621	13.0961	8.0	291	7.61
6.6	20-Jul-2017	us20009ynd	Kos, Greece	36.9293	27.4139	7.0	291	1.73
6.6	5-Sep-2018	us2000h8ty	Chitose, Japan	42.6861	141.9294	35.0	161	3.14

6.6	11-Jan-2022	us7000gaqu	Pólis, Cyprus	35.2267	31.9435	21.0	311	2.86
6.5	22-Dec-2003	nc21323712	San Simeon, California, USA	35.7005	-121.1005	8.4	281*	2.36
6.5	14-Feb-2008	usp000fywh	Koróni, Greece	36.3450	21.8630	28.0	271	3.46
6.5	13-Oct-2009	usp000h2u7	Nikolski, Alaska	52.7540	-166.9970	24.0	191	2.26
6.5	10-Jan-2010	nc71338066	Ferndale, California, USA	40.6520	-124.6925	28.7	261	2.90
6.5	14-Mar-2010	usp000h9cg	Namie, Japan	37.7450	141.5900	32.0	251	2.33
6.5	24-Oct-2012	usp000jucg	Nandayure, Costa Rica	10.0860	-85.2980	17.0	61	3.61
6.5	15-Jun-2013	usc000hrnr	Masachapa, Nicaragua	11.7630	-86.9260	30.0	261	3.44
6.5	21-Jul-2013	usb000iivv	Blenheim, New Zealand	-41.7040	174.3370	17.0	281*	4.26
6.5	16-Aug-2013	usb000j4iz	Blenheim, New Zealand	-41.7340	174.1520	8.2	281*	2.89
6.5	3-Apr-2014	usc000p26f	Iquique, Chile	-20.3113	-70.5756	24.1	271	4.34
6.5	24-Apr-2014	usb000px6r	Vernon, Canada	49.6388	-127.7316	10.0	191	1.62
6.5	17-Nov-2015	us10003ywp	Lefkáda, Greece	38.6700	20.6000	11.0	121	4.48
6.5	13-Nov-2016	us10007795	Blenheim, New Zealand	-42.3205	173.6694	10.0	281*	14.65
6.5	14-Nov-2016	us100077hw	Amberley, New Zealand	-42.6058	173.2543	9.0	221	11.94
6.5	31-Mar-2020	us70008jr5	Stanley, Idaho, USA	44.4646	-115.1175	12.1	211	2.37
6.5	15-May-2020	nn00725272	Monte Cristo Range, Nevada, USA	38.1689	-117.8497	2.7	261	1.45
6.4	8-Jun-2008	usp000g8vs	Várda, Greece	37.9630	21.5250	16.0	101	2.64
6.4	5-Jun-2009	usp000gxvt	Shizunai-furukawachō, Japan	41.8240	143.4450	29.0	111	1.44
6.4	9-Sep-2011	usp000j7ur	Vernon, Canada	49.5350	-126.8930	22.0	131	2.36
6.4	23-Aug-2014	usb000s5rc	Hacienda La Calera, Chile	-32.6953	-71.4416	32.0	251*	2.18
6.4	20-Jun-2015	us10002ke8	Talcahuano, Chile	-36.3601	-73.8120	11.0	231	2.79
6.4	29-Jul-2015	ak0159nc9dk8	Pedro Bay, Alaska, USA	59.8935	-153.1962	119.3	211	1.68
6.4	16-Sep-2015	us20003k8b	Illapel, Chile	-31.6180	-71.7450	26.7	141	58.18
6.4	17-Sep-2015	us20003kcn	Ovalle, Chile	-31.1043	-71.6504	42.3	81	50.32
6.4	18-Jun-2019	us600042fx	Tsuruoka, Japan	38.6391	139.4769	12.0	151	2.07

6.4	4-Jul-2019	ci38443183	Ridgecrest, California, USA	35.7053	-117.5038	10.5	191	4.67
6.4	26-Nov-2019	us70006d0m	Mamurras, Albania	41.5138	19.5256	22.0	191	2.10
6.4	7-Jan-2020	us70006vll	Maria Antonia, Puerto Rico	17.8686	-66.8266	8.9	111	5.69
6.4	19-Jan-2021	us7000d18q	Pocito, Argentina	-31.8334	-68.7992	20.8	221	2.16
6.4	21-Sep-2021	us7000fd4k	Talcahuano, Chile	-36.7771	-73.9329	18.8	241	1.54
6.3	6-Apr-2009	usp000gvtu	Sassa, Italy	42.3340	13.3340	8.8	161	2.67
6.3	11-Apr-2010	usp000hb7n	Nigüelas, Spain	36.9650	-3.5420	609.8	191	1.82
6.3	4-Jul-2010	usp000heww	Miyako, Japan	39.6970	142.3690	27.0	71	2.13
6.3	11-Mar-2011	usp000hvnv	Namie, Japan	37.7120	141.1840	32.3	201	950.30
6.3	23-Jul-2011	usp000j5by	Ōfunato, Japan	38.8980	141.8150	41.0	61	10.24
6.3	24-Jul-2011	usp000j5ed	Namie, Japan	37.7300	141.3900	40.0	171	4.04
6.3	30-Jul-2011	usp000j5rk	Iwaki, Japan	36.9420	140.9550	38.0	31	4.32
6.3	17-Jun-2012	usp000jmwc	Ōfunato, Japan	38.9190	141.8310	36.0	91	2.52
6.3	13-Mar-2014	usc000nabv	Hikari, Japan	33.6842	131.8249	79.0	71	2.42
6.3	26-Sep-2015	us20003p9y	Ovalle, Chile	-30.8148	-71.3217	46.0	51	5.08
6.3	10-Feb-2016	us20004z5b	Ovalle, Chile	-30.5723	-71.5838	29.0	221*	1.64
6.3	11-Jul-2016	us100062hg	Rosa Zarate, Ecuador	0.5812	-79.6380	21.0	201	6.73
6.3	4-Nov-2016	us1000744u	Curicó, Chile	-35.0945	-71.0457	90.0	121	3.35
6.3	12-Jun-2017	us20009ly0	Plomári, Greece	38.9296	26.3650	12.0	221	2.61
6.3	10-Oct-2017	us2000b3dm	Arica, Chile	-18.5715	-69.7526	85.0	201	1.20
6.3	21-Jan-2018	us2000cm0f	Arica, Chile	-18.8806	-69.4445	116.0	181	1.79
6.3	8-Jan-2019	us2000j1d4	Nishinoomote, Japan	30.5872	131.0441	35.0	191	1.69
6.3	4-Aug-2019	us600050if	Namie, Japan	37.7594	141.6031	38.0	201	3.23
6.3	19-Apr-2020	us7000903m	Ōfunato, Japan	38.8953	142.0049	38.0	211	2.91
6.3	3-Mar-2021	us7000df40	Týrnavos, Greece	39.7546	22.1757	8.0	221*	1.49
6.3	21-Jan-2022	us7000gdwz	Saiki, Japan	32.7282	132.0386	39.0	221*	2.57
6.2	6-Jan-2008	usp000fw2w	Leonídio, Greece	37.2160	22.6930	75.0	151	2.26

6.2	10-Aug-2009	usp000h05y	Sagara, Japan	34.7430	138.2640	40.4	201*	7.04
6.2	3-Sep-2009	usp000h16f	Makurazaki, Japan	31.1400	130.0140	163.0	51	2.69
6.2	9-Sep-2010	usp000hkg9	Lota, Chile	-37.0340	-73.4120	16.0	41	2.03
6.2	17-Mar-2011	usp000hxmc	Miyako, Japan	40.1360	142.1680	29.0	131	168.35
6.2	25-Mar-2011	usp000hyjm	Ōfunato, Japan	38.7720	141.8800	39.0	111	5.40
6.2	27-Mar-2011	usp000hyrs	Ishinomaki, Japan	38.4150	142.0110	19.0	201*	7.56
6.2	11-Apr-2011	usp000hzsk	Tōgane, Japan	35.4170	140.5750	15.0	131	4.85
6.2	21-Apr-2011	usp000j0c3	Tōgane, Japan	35.5790	140.3050	43.0	201*	4.08
6.2	19-Aug-2011	usp000j6nx	Namie, Japan	37.6710	141.6520	47.0	181	4.78
6.2	11-Apr-2014	usc000pfgr	Iquique, Chile	-20.6590	-70.6472	13.8	81	3.35
6.2	25-Sep-2014	ak014cbigci8	Skwentna, Alaska, USA	61.9449	-151.8160	108.9	91	3.25
6.2	22-Nov-2014	usb000syza	Hakuba, Japan	36.6408	137.8875	9.0	61	5.31
6.2	18-Mar-2015	us10001nj1	Tomé, Chile	-36.1167	-73.5219	13.0	111	1.25
6.2	19-Sep-2015	us20003luw	La Ligua, Chile	-32.3335	-72.0629	18.0	201*	3.88
6.2	11-Jan-2016	us10004djn	Rumoi, Japan	44.4761	141.0867	238.8	201*	2.01
6.2	14-Apr-2016	us20005hzn	Kumamoto, Japan	32.7880	130.7042	9.0	61	6.49
6.2	24-Aug-2016	us10006g7d	Accumoli, Italy	42.7230	13.1877	4.4	201*	2.60
6.2	21-Oct-2016	us20007fta	Kurayoshi, Japan	35.3743	133.8092	5.6	191	1.63
6.2	13-Nov-2016	us100077aj	Blenheim, New Zealand	-42.3093	173.6961	2.1	201*	32.02
6.2	10-Apr-2018	us2000dxfc	Ovalle, Chile	-31.0258	-71.5292	66.0	71	2.73
6.2	9-May-2019	us70003j46	Miyazaki, Japan	31.7772	131.8483	22.0	201*	1.76
6.2	11-Sep-2020	us7000blm2	Tocopilla, Chile	-21.3968	-69.9096	51.0	141	2.28
6.2	20-Dec-2021	nc73666231	Petrolia, California, USA	40.3902	-124.2980	27.0	191	3.91
6.1	8-Mar-2010	usp000h8x1	Karakoçan, Turkey	38.8640	39.9860	12.0	151	4.01
6.1	12-Feb-2011	usp000hucz	Chiguayante, Chile	-37.0270	-72.9540	16.0	91	3.02
6.1	12-Mar-2011	usp000hwfv	Namie, Japan	37.2490	141.1590	38.0	181*	22.17
6.1	12-Mar-2011	usp000hwnq	Ishinomaki, Japan	38.0470	141.7200	15.0	181*	14.25
6.1	13-May-2011	usp000j1jk	Namie, Japan	37.3960	141.3410	35.0	51	5.86

6.1	21-Oct-2011	usp000j9mz	Asahikawa, Japan	43.8920	142.4790	187.0	61	1.48
6.1	23-Nov-2011	usp000jbaf	Namie, Japan	37.3650	141.3680	34.0	61	3.03
6.1	23-Jan-2012	usp000jdvv	Tomé, Chile	-36.4090	-73.0300	20.0	51	2.32
6.1	27-Mar-2012	usp000jgv9	Miyako, Japan	39.8590	142.0170	15.0	61	2.77
6.1	20-Jan-2014	usb000m4i4	Masterton, New Zealand	-40.6595	175.8144	28.0	81	2.44
6.1	26-Jan-2014	usb000m8ch	Lixoúri, Greece	38.2082	20.4528	8.0	171	2.60
6.1	16-Sep-2015	us20003k7m	Illapel, Chile	-31.7502	-71.7425	19.1	181*	196.98
6.1	10-Jun-2016	us200063cy	Puerto Morazán, Nicaragua	12.8318	-86.9633	10.0	61	2.58
6.1	26-Oct-2016	us1000725y	Visso, Italy	42.9564	13.0666	10.0	141	2.77
6.1	11-Nov-2016	us1000770m	Ishinomaki, Japan	38.4973	141.5658	42.4	141	1.42
6.1	13-Nov-2016	us1000779b	Blenheim, New Zealand	-42.1762	173.6227	14.0	181*	27.77
6.1	30-Oct-2018	us1000hiup	Waitara, New Zealand	-39.0570	174.9584	225.5	41	2.42
6.1	12-Sep-2020	us7000bm9m	Ōfunato, Japan	38.7482	142.2446	34.0	71	2.66
6.1	6-Jan-2022	us7000g9nb	Corinto, Nicaragua	11.9367	-87.1371	17.0	91	1.63
6.0	13-Feb-2011	usp000huey	Talcahuano, Chile	-36.6490	-73.1760	17.0	161*	3.01
6.0	15-Mar-2011	usp000hxc7	Fujinomiya, Japan	35.2720	138.5820	9.0	61	6.88
6.0	31-Mar-2011	usp000hyzj	Ōfunato, Japan	38.9220	141.8210	42.0	131	8.48
6.0	16-Jul-2011	usp000j4zz	San Antonio, Chile	-33.8190	-71.8320	20.0	151	3.52
6.0	14-Mar-2012	usp000jg80	Asahi, Japan	35.6870	140.6950	10.0	161*	4.45
6.0	20-May-2012	usp000jkn8	Massa Finalese, Italy	44.8900	11.2300	6.3	141	1.56
6.0	7-Jun-2012	usp000jmf2	Namie, Japan	-36.0740	-70.5700	8.0	151	4.06
6.0	18-May-2013	usb000gy67	Namie, Japan	37.7390	141.4710	39.0	121	1.70
6.0	3-Feb-2014	usc000mfuh	Lixoúri, Greece	38.2637	20.3897	5.0	81	2.20
6.0	4-May-2014	usb000q9sv	Itō, Japan	34.9118	139.4186	153.0	151	2.15
6.0	24-Aug-2014	nc72282711	South Napa, California, USA	38.2152	-122.3123	11.1	121	2.89
6.0	14-Apr-2016	us20005i1a	Uto, Japan	32.6973	130.7204	8.0	51	5.22
6.0	8-Jul-2021	nc73584926	Antelope Valley, California, USA	38.5075	-119.4998	7.5	111	1.99

5.9	24-Jan-2009	ak00913zo63t	Southern Alaska, USA	59.4302	-152.8875	97.9	51	4.71
5.9	5-Aug-2010	usp000hhjy	Curanilahue, Chile	-37.4430	-73.2810	18.0	61	2.07
5.9	11-Feb-2011	usp000hucn	Arauco, Chile	-37.1960	-73.1980	15.0	61	4.70
5.9	1-Apr-2011	usp000hz2b	Ōtsuchi, Japan	39.3230	141.9500	41.0	111	5.37
5.9	12-Apr-2011	usp000hzt4	Ishikawa, Japan	37.1070	140.3680	11.0	41	6.87
5.9	1-Aug-2011	usp000j5ua	Ōyama, Japan	34.6310	138.4330	13.0	41	3.50
5.9	23-Dec-2011	usp000jch9	Christchurch, New Zealand	-43.5300	172.7430	6.9	21	3.69
5.9	25-Aug-2012	usp000jqqj	Shizunai-furukawachō, Japan	42.4190	142.9130	54.5	61	1.94
5.9	17-Apr-2013	usb000g940	Ishinomaki, Japan	38.4750	141.6300	50.5	121	2.33
5.9	16-Aug-2013	usb000j4kk	Blenheim, New Zealand	-41.7420	174.0500	8.5	131	5.82
5.9	16-Aug-2013	usb000j4n4	Blenheim, New Zealand	-41.6688	174.2623	14.3	141*	7.37
5.9	1-Apr-2016	us20005du0	Shingū, Japan	33.3807	136.3901	14.0	81	1.51
5.9	23-Nov-2016	us10007bwb	Namie, Japan	37.2143	141.3209	9.0	111	3.02
5.9	28-Dec-2016	us10007naf	Daigo, Japan	36.8604	140.4421	7.0	61	1.77
5.9	28-Apr-2017	us10008llg	Valparaíso, Chile	-33.2190	-71.9694	22.0	141*	5.16
5.9	24-Jun-2020	us7000aabt	Hasaki, Japan	35.4711	141.0738	29.1	91	1.91
5.9	17-Jul-2020	us7000aq5p	Iquique, Chile	-20.2355	-70.1328	73.6	21	2.11
5.9	21-Sep-2021	us7000fd9v	Mount Buller, Australia	-37.4920	146.3534	12.0	91	2.58
5.9	7-Oct-2021	us6000fsl6	Chiba, Japan	35.5736	140.0705	62.0	31	1.92
5.9	21-Dec-2021	ak021gbh4rso	Port Alsworth, Alaska, USA	60.1237	-153.2742	151.2	61	3.18
5.8	23-Oct-2007	usp000fr4d	Padang, Indonesia	-1.9960	99.8960	30.0	121*	4.70
5.8	5-Apr-2009	usp000gvsp	Miyazaki, Japan	32.0070	131.4170	26.0	111	1.32
5.8	6-Jun-2009	usp000gxx2	Hasaki, Japan	35.4830	140.9140	34.0	121*	2.24
5.8	13-Feb-2011	usp000huet	Talcahuano, Chile	-36.5650	-73.1780	20.7	111	4.33
5.8	11-Mar-2011	usp000hvpr	Tōno, Japan	39.5990	141.5760	35.0	121*	719.21
5.8	12-Mar-2011	usp000hwgq	Yamada, Japan	39.4650	142.4050	35.0	91	2779.84
5.8	17-Mar-2011	usp000hxny	Kitaibaraki, Japan	36.7570	141.2020	29.0	81	10.72
5.8	20-Mar-2011	usp000hy1v	Ōtsuchi, Japan	39.3500	141.8240	42.0	61	2.81

5.8	24-Mar-2011	usp000hyfh	Kamaishi, Japan	39.0790	142.0840	27.0	101	5.15
5.8	11-Apr-2011	usp000hzq9	Marumori, Japan	37.7910	140.8120	10.0	121*	8.94
5.8	20-May-2011	usp000j1v8	Hasaki, Japan	35.7610	140.8430	29.0	41	7.29
5.8	23-Dec-2011	usp000jch0	Christchurch, New Zealand	-43.4900	172.8000	9.7	21	3.27
5.8	29-Apr-2012	usp000jjs6	Tōgane, Japan	35.5960	140.3490	44.0	51	1.94
5.8	29-May-2012	usp000jm2n	Medolla, Italy	44.8510	11.0860	10.2	111	5.00
5.8	25-Feb-2013	usc000fd56	Numata, Japan	36.8440	139.2450	10.0	41	4.65
5.8	12-Apr-2013	usb000g5yg	Sumoto, Japan	34.3690	134.8280	14.0	21	2.70
5.8	4-Aug-2013	usb000iv4w	Ishinomaki, Japan	38.2133	141.8621	56.0	121*	1.89
5.8	1-Apr-2014	usb000pmkl	Iquique, Chile	-19.4928	-70.1660	21.6	121*	104.08
5.8	10-May-2014	ak0145z8amwh	Happy Valley, Alaska, USA	60.0101	-152.1260	89.1	71	2.45
5.8	14-Feb-2016	us20005019	Christchurch, New Zealand	-43.4798	172.7715	7.6	21	3.92
5.8	30-Nov-2018	ak018fcntv5m	Anchorage, Alaska, USA	61.2822	-149.9571	40.8	61	6.50
5.8	23-Nov-2019	us70006c81	Whakatane, New Zealand	-37.3696	177.2566	120.5	71	2.77
5.8	24-Jun-2020	ci39493944	Lone Pine, California, USA	36.4468	-117.9752	4.7	111	2.19
5.8	28-Oct-2020	us7000c6u9	La Serena, Chile	-29.3186	-71.2397	50.0	121*	3.52
5.8	4-Mar-2021	us7000dfku	Verdikoússa, Greece	39.7865	22.1157	10.0	121*	5.39
5.8	2-May-2021	us7000dzfk	Coquimbo, Chile	-30.1366	-71.5825	33.0	61	0.79
5.7	31-Jan-2009	usp000gtaz	Kitaibaraki, Japan	36.7190	141.1480	34.0	111*	2.92
5.7	15-Jun-2010	ci14745580	Ocotillo, California, USA	32.7050	-115.9113	8.8	71	1.32
5.7	11-Mar-2011	usp000hvug	Hasaki, Japan	35.6840	140.9330	35.0	111*	34.74
5.7	11-Mar-2011	usp000hw1n	Honshu, Japan	36.9430	138.3000	12.4	111*	249.45
5.7	16-Mar-2011	usp000hxfe	Miyako, Japan	39.8870	142.0190	36.0	111*	97.92
5.7	1-Aug-2011	usp000j5u4	Miyako, Japan	39.8370	142.0830	40.0	31	2.31
5.7	1-Apr-2012	usp000jh3k	Iwaki, Japan	37.1160	140.9570	48.0	111*	4.36
5.7	13-Apr-2012	usp000jhus	Iwaki, Japan	36.9880	141.1520	11.0	111*	3.32
5.7	24-May-2013	nc71996906	Canyondam, California, USA	40.1918	-121.0595	8.0	111*	2.45

5.7	4-Jul-2014	usc000rqix	Miyako, Japan	39.6480	142.0802	50.3	71	4.15
5.7	28-Jan-2015	nc72387946	Ferndale, California, USA	40.3178	-124.6067	16.9	101	1.99
5.7	15-Apr-2016	us20005ija	Kikuchi, Japan	32.9241	130.8091	10.0	111*	15.71
5.7	13-Nov-2016	us10007798	Blenheim, New Zealand	-42.4063	173.6606	9.9	91	168.24
5.7	13-Nov-2016	us10007797	Blenheim, New Zealand	-41.6877	174.2061	14.6	51	269.64
5.7	18-Jan-2017	us10007twj	Cittareale, Italy	42.6012	13.2268	7.0	111*	6.27
5.7	28-Feb-2017	us20008mw4	Namie, Japan	37.5666	141.3347	47.0	81	1.33
5.7	8-Apr-2018	us2000dwh6	Ōdachō-ōda, Japan	35.2588	132.5528	10.3	61	1.53
5.7	25-Oct-2018	us1000hh6r	Ishinomaki, Japan	38.3158	141.7850	40.0	51	1.96
5.7	18-Mar-2020	uu60363602	Magna, Utah, USA	40.7510	-112.0783	11.9	51	2.31
5.7	5-Oct-2021	us6000frzg	Miyako, Japan	40.0529	142.1410	55.0	61	2.44
5.7	20-Dec-2021	nc71127029	Petrolia, California, USA	40.2978	-124.6260	16.5	41	5.84
5.6	16-Oct-1999	ci10180015	Running Springs, California, USA	34.2400	-117.0400	6.0	101*	8.23
5.6	13-Mar-2010	usp000h9ap	Namie, Japan	37.5940	141.2990	76.7	101*	3.33
5.6	14-Oct-2010	usp000hn3m	Shizunai-furukawachō, Japan	42.3110	142.8710	59.0	31	1.74
5.6	13-Mar-2011	usp000hwup	Ōfunato, Japan	38.8490	141.8580	33.0	91	1540.04
5.6	21-May-2011	usp000j1zc	Narutō, Japan	35.5970	140.4920	37.0	21	6.06
5.6	10-Oct-2011	usp000j95h	Namie, Japan	37.5470	141.2570	46.0	101*	3.66
5.6	29-Apr-2012	usp000jjsh	Miyako, Japan	39.7450	142.0370	10.0	101*	1.34
5.6	16-Oct-2012	usp000ju2g	Taupo, New Zealand	-38.6390	176.1670	110.5	31	2.54
5.6	17-Apr-2013	usb000g9yi	Shimoda, Japan	33.9580	139.3520	8.8	91	2.14
5.6	9-Nov-2013	usb000kvca	Moriya, Japan	35.9187	139.9684	64.3	101*	3.35
5.6	15-Jun-2014	usc000rfv0	Iwaki, Japan	37.0961	141.1141	45.0	71	7.93
5.6	23-Aug-2014	usb000s5lt	Iquique, Chile	-20.1745	-69.0385	100.0	101*	2.21
5.6	22-Nov-2014	usb000sz38	Panciu, Romania	45.8977	27.1505	32.0	91	2.10
5.6	19-Dec-2014	usc000t8gv	Pointe-Noire, Guadeloupe	16.1951	-61.8091	118.1	41	3.39

5.6	12-Oct-2015	us10003mxv	Castlepoint, New Zealand	-40.5837	176.2884	22.0	31	1.69
5.6	28-Dec-2015	us10004a1v	Saint-Pierre, Martinique	14.6571	-61.3454	150.0	31	4.55
5.6	24-Aug-2016	us10006g7w	Castelsantangelo sul Nera, Italy	42.8413	13.1533	3.2	101*	5.25
5.6	23-Sep-2016	us10006s5c	Nereju Mic, Romania	45.7275	26.6097	92.0	91	1.29
5.6	18-Oct-2016	us20007f6l	Pointe Michel, Dominica	15.2230	-61.5065	146.0	71	3.65
5.6	28-Dec-2016	nn00570709	Hawthorne, Nevada, USA	38.3755	-118.8989	11.3	101*	3.81
5.6	28-Dec-2016	nn00570710	Hawthorne, Nevada, USA	38.3904	-118.8972	12.2	101*	3.27
5.6	18-Jan-2017	us10007twn	Cittareale, Italy	42.5855	13.1904	10.0	41	7.57
5.6	6-Oct-2017	us2000b20f	Iwaki, Japan	37.0959	141.0771	44.0	41	3.77
5.6	23-Jun-2019	nc73201181	Petrolia, California, USA	40.2735	-124.3003	9.4	61	2.25
5.6	21-Sep-2019	us60005lrf	Shijak, Albania	41.3375	19.5303	20.0	91	1.14
5.5	28-Feb-2009	usp000gufa	Shizunai-furukawachō, Japan	42.6100	142.1040	105.0	71	2.24
5.5	7-Apr-2009	usp000gvvw	San Panfilo d'Ocre, Italy	42.2750	13.4640	15.1	31	3.19
5.5	18-Jan-2010	usp000h6a0	Náfpaktos, Greece	38.4040	21.9610	0.8	21	2.80
5.5	29-Sep-2010	usp000hmb0	Kuroiso, Japan	37.2570	139.8830	33.3	71	1.90
5.5	11-Mar-2011	usp000hw1j	Honshu, Japan	35.6850	140.6580	2.2	21	21.02
5.5	14-Mar-2011	usp000hx1e	Ōarai, Japan	36.4080	140.8940	11.0	71	8.13
5.5	22-Mar-2011	usp000hyb1	Ishikawa, Japan	37.0650	140.6380	18.0	41	4.92
5.5	22-Mar-2011	usp000hyb2	Iwaki, Japan	37.0140	140.6790	40.7	41	4.92
5.5	22-Mar-2011	usp000hyb4	Ishikawa, Japan	37.1110	140.5800	37.5	91*	2.99
5.5	11-Apr-2011	usp000hzsf	Iiyama, Japan	36.8090	138.2840	17.1	41	4.23
5.5	3-Jun-2011	usp000j2nd	Iwaki, Japan	37.0670	140.9120	17.0	91	4.65
5.5	24-Jun-2011	usp000j3pk	Shizunai-furukawachō, Japan	42.0490	142.5530	58.1	41	8.05
5.5	7-Jul-2011	usp000j4b1	Iwaki, Japan	37.1250	140.8690	35.0	21	4.52
5.5	15-Mar-2012	usp000jgaf	Ōme, Japan	35.8020	139.2790	103.8	81	3.89
5.5	24-Apr-2012	usp000jjhz	Narutō, Japan	35.6220	140.4720	54.3	41	2.79

5.5	29-May-2012	usp000jm2z	San Possidonio, Italy	44.8880	11.0080	6.8	51	4.63
5.5	16-Aug-2013	usb000j4j6	Blenheim, New Zealand	-41.7640	174.1170	5.8	81	7.46
5.5	16-Nov-2013	usb000kzuj	Chiba, Japan	35.6039	140.1529	59.4	91*	2.50
5.5	21-Dec-2013	usc000lpah	Asahi, Japan	35.6065	140.6497	35.4	61	2.75
5.5	2-Apr-2014	usc000p20r	Ōfunato, Japan	39.1648	141.8049	58.1	91*	1.70
5.5	14-Jun-2014	usc000rfj5	Hanamaki, Japan	39.4384	140.9876	92.0	91*	7.15
5.5	9-Jul-2015	us20002wd2	Hachinohe, Japan	40.3631	141.4646	81.0	21	1.58
5.5	12-Jul-2015	us20002wz9	Usuki, Japan	33.0229	131.7493	53.0	81	2.27
5.5	15-Apr-2016	us20005inz	Aso, Japan	33.0051	131.1569	13.2	91*	49.53
5.5	18-Apr-2016	us20005jgz	Aso, Japan	33.0143	131.0991	10.5	41	9.39
5.5	26-Oct-2016	us20007guy	Preci, Italy	42.8580	13.0528	6.0	71	4.18
5.5	13-Nov-2016	us10007db8	Blenheim, New Zealand	-42.2132	173.4319	10.0	91*	121.78
5.5	14-Nov-2016	us100077l5	Blenheim, New Zealand	-41.7598	174.2992	17.2	91*	12.67
5.5	15-Nov-2016	us1000780y	Blenheim, New Zealand	-41.7875	174.3064	10.0	91*	14.84
5.5	28-Dec-2016	nn00570744	Hawthorne, Nevada, USA	38.3777	-118.8957	8.8	31	8.88
5.5	24-Apr-2018	us1000dr71	Nemuro, Japan	43.3482	145.7259	83.0	71	1.46
5.5	17-Jun-2018	us1000eu1c	Honshu, Japan	34.8246	135.6389	10.3	31	1.90
5.5	20-Nov-2018	us1000hujf	Nagata, Japan	30.4200	130.0667	123.0	91*	1.34
5.5	6-Jul-2019	ci38457687	Ridgecrest, California, USA	35.9012	-117.7495	5.0	91*	28.17
5.5	4-Jun-2020	ci39462536	Ridgecrest, California, USA	35.6148	-117.4282	8.4	41	1.80
5.5	17-Feb-2021	us6000diae	Kamárai, Greece	38.4057	22.0190	5.3	21	2.53

* Maximum empirical radius of influence per earthquake magnitude interval (shown as cyan stars in Fig. 4.11), e.g., M5.5=91 km

5

Conclusions

The research presented in this dissertation demonstrates applications of the GPS Imaging technique that increases understanding of geophysical signals detected by the GPS Mega-Network in the United States and globally. Distinguishing common geophysical signals in complex geologic regions can reveal underlying geodynamic processes occurring at different time scales. Each of the chapters present strategies to visualize and identify sources of crustal motion. The major conclusions for each chapter are summarized in the following paragraphs.

Two chapters particularly focus on using GPS Imaging in unison with interdisciplinary methods to analyze loading and unloading signals. The first chapter used GPS Imaging to identify a –2 mm/year signal of subsidence in the interior Pacific Northwest United States that spanned the approximate length of the Cascadia subduction zone latitudes. Velocity profiles from GPS Imaging and MIDAS compared to topographic profiles suggested that the subsidence feature was centralized approximately around the Cascade Arc longitudes. I investigated plate tectonic iterations, postseismic relaxation, volcanic processes, climatological tends related to orographic precipitation, and GIA due to the region's proximity to the former Laurentide ice sheet and Western Cordilleran deglaciation as possible sources for the subsidence feature. Models of lithospheric flexure with realistic geologic parameters for the region and GPS Imaging of the subsidence feature were used as constraints. Both Juan de Fuca plate subduction end loading and volcanic loading model results were capable of producing the subsidence feature. Climatological and GRACE data imply a potential, though relatively minor, contribution from hydrological loading. Postseismic relaxation models from the 1700 M9.1 Cascadia Earthquake removed approximately half of the subsidence feature rate.

By combining it with the GIA postglacial rebound corrections, the majority of the subsidence signal was accounted for north into Canada. This suggests lithospheric flexure from postseismic relaxation and GIA are likely the primary sources for the subsidence feature.

The second chapter studies an enigmatic uplift signal of ~2 mm/year revealed by GPS Imaging in the Great Plains region of the United States after GIA corrections for forebulge collapse. This area is in the relatively stable interior, and there was no topographic correlation with velocity profiles from GPS Imaging or MIDAS velocities. However, uplift extends throughout the southern High Plains aquifer and the greatest uplift rate is centralized where groundwater levels have experienced the greatest declines, so we therefore investigated a possible hydrological source for the uplift. GRACE data corroborate the spatial extent of hydrologic mass loss observed by GPS Imaging. Climatic, hydrologic, and GPS time series comparisons reveal a connection between vertical land motion and anthropogenic hydrological mass unloading exacerbated by drought. The simple hydrological unloading model constrained by GPS Imaging indicates that a water volume loss of –5.1 km^3/year is sufficient to cause the uplift, similar to GRACE estimates and previous studies. Generally, geophysical signals from anthropogenic aquifer depletion are associated with subsidence, but the High Plains aquifer is unconfined, meaning the reservoir will not compress with groundwater removal as it is at atmospheric pressure, and crustal response for hydrological mass unloading might therefore appear as uplift.

The final project details new strategies to estimate earthquake displacements in the GPS Mega-Network, and examines the scope and sensitivity of the network through time by building the GPS Global Earthquake Catalog from the coseismic displacement estimates. I tested coseismic displacements using two strategies: the DNE model comprised of GPS time series data in a 30 day adaptable time window before and after an earthquake event, and the TSM method that estimates displacements with the entire GPS time series. The DNE model was preferred, and a hierarchy of methodologies to estimate coseismic displacements was established: 24-hour DNE, 5-minute DNE, and then TSM estimations. Four earthquakes M≥6 helped define the empirical radius of influence equation which is used to flag GPS stations potentially affected by coseismic deformation. The new equation was vetted with the aid of GPS Imaging which created a field of coseismic displacements for the 2019 M7.1 Ridgecrest earthquake and the 2020 M6.5 Monte Cristo range mainshock events. Global coseismic displacements were estimated for 14,059 earthquakes M≥5.5 between 1. Jan. 1994 and 20 Apr. 2022 which comprise the GPS Global Earthquake Catalog. Comparisons with the USGS NEIC Earthquake Catalog confirm that the ability of the GPS Mega-Network to estimate displacements for earthquake events increases with magnitude and improves over time.